Electrical and Computer Engineering

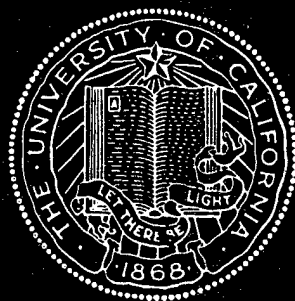## Low-Power VCSEL-Based Smart Pixels with Simplified Optics

Final Technical Report
8/1/96 – 3/31/00

PI - L.A. Coldren

ECE Technical Report # 00-06

Air Force Office of Scientific Research
Contract No. F49620-1-0342

TECHNICAL REPORT

UNIVERSITY OF CALIFORNIA
SANTA BARBARA, CA 93106

Low-Power VCSEL-Based Smart Pixels
with Simplified Optics

Final Technical Report
8/1/96 – 3/31/00

PI - L.A. Coldren

ECE Technical Report # 00-06

Air Force Office of Scientific Research
Contract No. F49620-1-0342

Department of Electrical and Computer Engineering

University of California at Santa Barbara, CA 93106-9560

20000509 041

REPORT DOCUMENTATION PAGE

AFRL-SR-BL-TR-00-

0173

1. AGENCY USE ONLY *(Leave blank)*	2. REPORT DATE	3. REPORT TYPE AND DATES COVERED
		Final 01 Jul 96 to 31 Dec 01

4. TITLE AND SUBTITLE
Low-Power VCSEL-based smart pixels with simplified optics

5. FUNDING NUMBERS
61102F
2305/DX

6. AUTHOR(S)
Professor Coldren

7. PERFORMING ORGANIZATION NAME(S) AND ADDRESS(ES)
University of California, Santa Barbara
Cheadle Hall
Santa Barbara CA 93106-6150

8. PERFORMING ORGANIZATION REPORT NUMBER

9. SPONSORING/MONITORING AGENCY NAME(S) AND ADDRESS(ES)
AFOSR/NE
801 N Randolph Street Rm 732
Arlington, VA 22203-1977

10. SPONSORING/MONITORING AGENCY REPORT NUMBER

F49620-96-1-0342

11. SUPPLEMENTARY NOTES

12a. DISTRIBUTION AVAILABILITY STATEMENT
APPROVAL FOR PUBLIC RELEASE, DISTRIBUTION UNLIMITED

12b. DISTRIBUTION CODE

13. ABSTRACT *(Maximum 200 words)*

Over the last four years, vast improvements have been made in the area of VCSEL technology, moving them toward integration as smart pixels. VCSEL design such as tapered oxide apertures, mirror doping schemes, and improved active regions have benefited greatly during this time period. Finally, an easy to use graphical user interface and modeling program has been developed to estimate the optical scattering losses in oxide-defined VCSELs.

14. SUBJECT TERMS

15. NUMBER OF PAGES

16. PRICE CODE

17. SECURITY CLASSIFICATION OF REPORT	18. SECURITY CLASSIFICATION OF THIS PAGE	19. SECURITY CLASSIFICATION OF ABSTRACT	20. LIMITATION OF ABSTRACT
UNCLASSIFIED	UNCLASSIFIED	UNCLASSIFIED	UL

Low-Power VCSEL-Based Smart Pixels
with Simplified Optics

Professor Larry A. Coldren

Final Technical Report
Aug. 1, 1996 to March 31, 2000

University of California, Santa Barbara
Electrical and Computer Engineering Department
Santa Barbara, CA 93106-9560

ph: (805) 893-4486
fax: (805) 893-4500
email: coldren@ece.ucsb.edu

Abstract

Over the last four years, vast improvements have been made in the area of VCSEL technology, moving them toward integration as smart pixels. VCSEL design such as tapered oxide apertures, mirror doping schemes, and improved active regions have benefited greatly during this time period. 850-nm VCSELs with strained AlInGaAs/AlGaAs active layers were fabricated with current thresholds as low as 156 A from a 2.8 m device. Tapered apertures have been successfully integrated into 980-nm devices for use in free-space optical links with data transmission at 3 Gbit/s with a BER $<10^{-12}$. Tapered apertures as well as improved doping schemes were used to improve broad area VCSEL characteristics and achieve slope efficiencies of 55 and 58% for devices of 1.5 A and 2.5 m respectively. And, for devices 2-3 m in diameter, wall-plug efficiencies as high as 20% at only 150 W were obtained. Finally, an easy to use graphical user interface and modeling program has been developed to estimate the optical scattering losses in oxide-defined VCSELs.

Subject terms

Semiconductor lasers, VCSEL, smart pixels, microlens, free-space interconnects, tapered apertures.

Introduction

The goal of this AFOSR program was to develop a new generation of very low-power, high-speed devices and circuits for use in free-space interconnect architectures. The transceivers used in these free-space links were ultralow-threshold, high-efficiency VCSELs with integrated microlenses. The VCSELs, along with low-power, high-speed transceiver circuits, and compatible detector arrays form the smart pixel building block. Wavelength encoding of the arrays for lower crosstalk, higher packing density and wavelength routing was also studied.

Much of the work on these VCSEL-based smart pixels is included in Dr. Eric Hegblom's Ph.D. thesis which we included as Appendix 1 to serve as the detailed content of this report. However, in order to provide an introduction to its contents we here briefly summarize the material contained in its various chapters.

Thesis summary

Chapter 1
This chapter describes the key applications for ultralow-threshold, high-efficiency VCSELs for use in free-space optics. It describes the evolution of VCSELs from channel links over multimode fiber to board-to-board and ultimately chip-to-chip interconnects within computers. It also depicts the use of VCSELs as smart pixels for improved speed in laser printing..

Chapter 2

Chapter 2 describes the benefits of scaling VCSELs to smaller sizes. Proper scaling is essential for ultralow-threshold, high-efficiency smart pixels. The chapter introduces methods for improved scaling by using oxide apertures to confine both the current and the optical mode.

Chapter 3

In order to achieve ideal scaling of VCSELs, it is necessary to improve the broad-area characteristics of VCSELs. This chapter focuses on the design of VCSELs, particularly the design of the mirrors. It describes the tradeoffs between increased free carrier absorption loss and lower electrical resistance, and for the first time derives the ideal carrier profile based on the loss-resistance product.

Chapter 4

Chapter 4 contains the bulk of the theoretical calculations for apertured VCSELs. The calculations are intended to estimate the reduction of optical scattering losses due to tapered apertures. Figure 1 illustrates the concept of optical scattering losses at the oxide aperture.
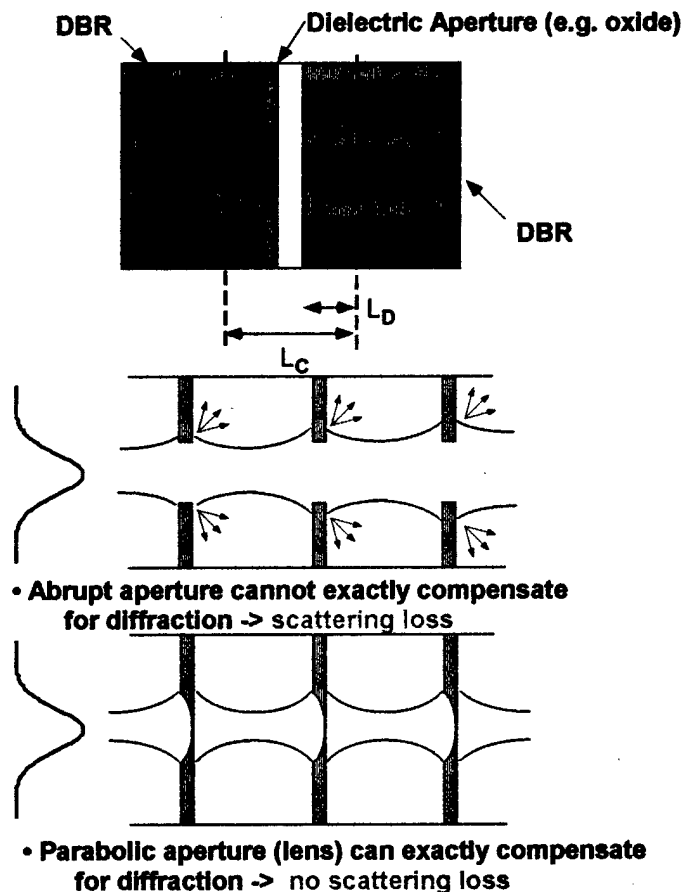

Figure 1. Schematic of a propagating mode inside a VCSEL with an abrupt aperture and with a tapered aperture to form a lens.

As illustrated in Figure 1, when a mode propagates through the structure, an abrupt aperture cannot perfectly refocus the mode. A perfect, parabolic lens can exactly compensate for the mode's diffraction, however, making an actual lens is not possible if current is to flow through the aperture.

An iterative approach was used to solve for the optical losses in the VCSEL structure due to diffraction. The results are summarized in Figure 2. From the figure, it is apparent that thin apertures with tapers ~1 μm can reduce the optical losses to negligible values.

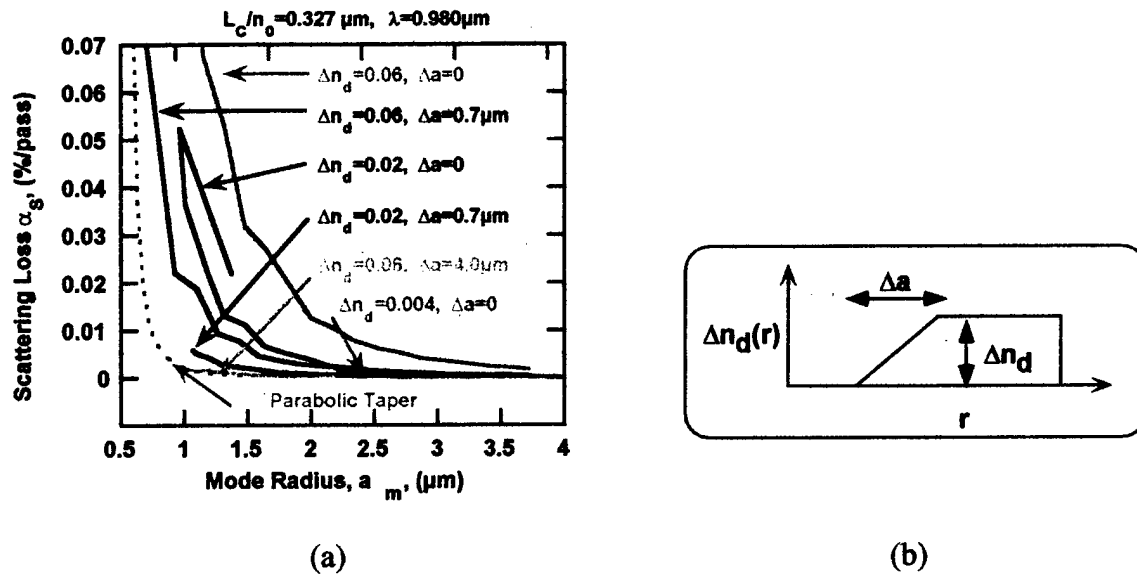(a)   (b)

Figure 2. Theoretical results of an iterative model for the optical mode in a VCSEL. (a) Scattering (excess) loss versus mode radius for various aperture shapes (b) Schematic showing the aperture effective thickness.

The chapter ends by explaining how ultimately designs with single apertures can not confine the smallest of modes without being limited by the angular stop-band of the DBR mirrors. An effective mirror length model called the *ray penetration depth*, is introduced to describe this effect.

Chapter 5

Chapter 5 addresses the limit on device scaling due to current spreading. Current spreads between the aperture and the active region, as illustrated in Figure 3a. This spreading affects both the threshold current density and the injection efficiency above threshold. The analysis of Chapter 5 quantifies these two effects with a simple formula that can easily be applied to device designs. Figure 3b. shows measured threshold currents for various device sizes and fits the data to the current spreading model developed in this chapter.
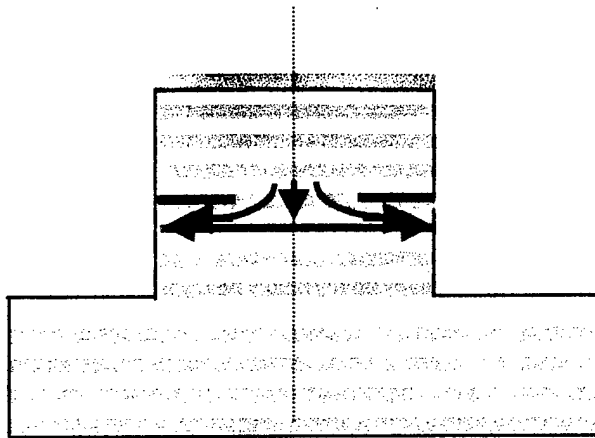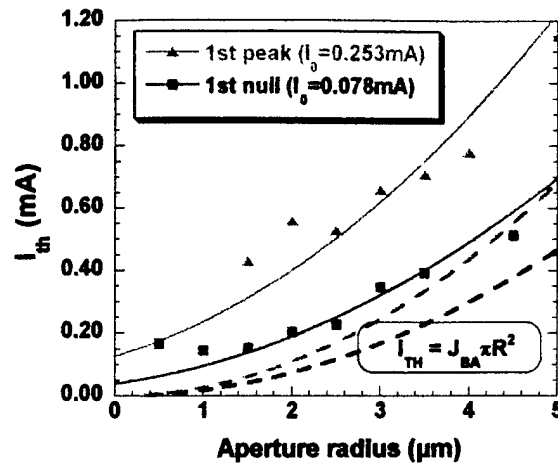
Figure 3. (a) Current spreads between the aperture and the active region
(b) Threshold currents increase for small sizes due to current spreading

Chapter 6

Chapter 6 summarizes the device results for the fabricated VCSELs. Analysis from Chapter 4 directed device designs toward thin apertures or tapered apertures at a standing wave null. With these designs, scattering losses have been virtually eliminated, resulting in record efficiencies for devices smaller than 2μm in diameter. Equally as important, devices 2-3μm in diameter reached wall-plug efficiencies for 20% at only 150μW of output power. Figure 4 below, depicts these results.
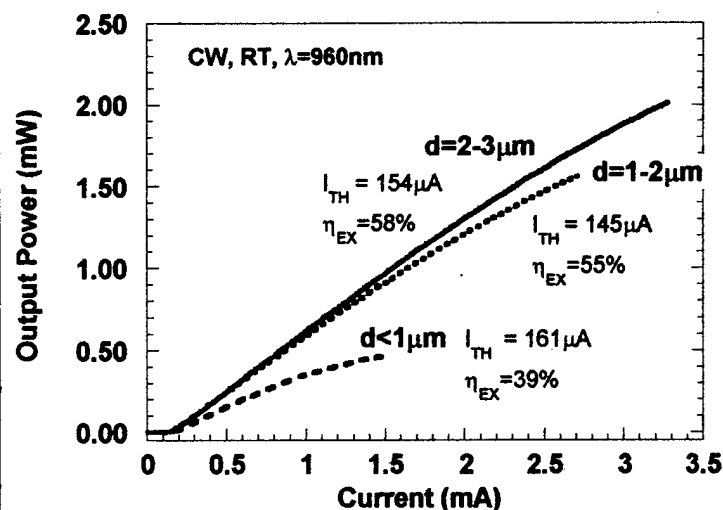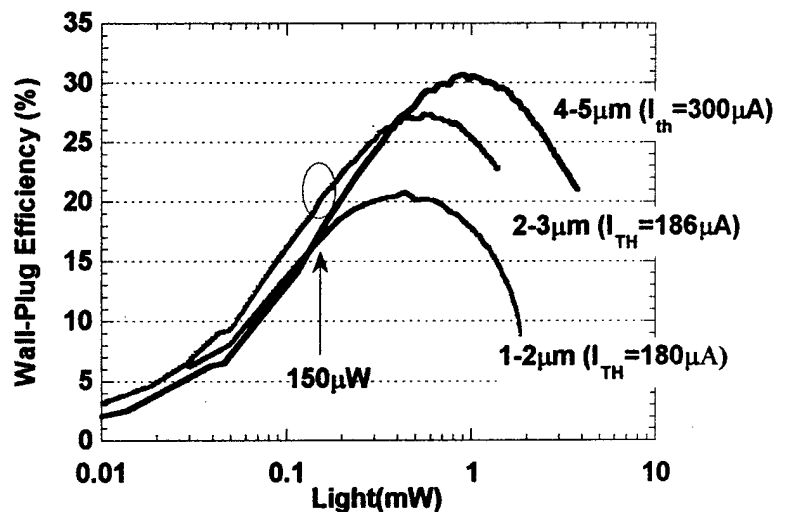
Figure 4. (a) Light versus current for devices <3μm differential efficiencies are
labeled for each curve (b) Wall-plug efficiencies for devices 1-5μm in diameter

4

Chapter 7

This chapter describes how tapered apertures are formed. The combination of fast lateral oxidation along with slow vertical oxidation in an AlGaAs layer with varying Al composition forms the taper. In addition, other issues such as stress due to the oxide and re-oxidation issues are discussed.

Chapter 8

The final chapter in this thesis provides some conclusions for the work done in designing and realizing ultra-low threshold, high-efficiency VCSELs. The chapter finishes by forecasting the major impact better current and carrier confinement could have on the wall-plug efficiency at smaller sizes and examines the other potential benefits of tapered apertures.

Summary of Results

Initially 850-nm VCSELs with strained AlInGaAs/AlGaAs active layers were fabricated using thin (200Å) oxide aperture layers. Threshold currents as low as 156μA were measured from a 2.8μm diameter device. Additionally, a burn-in study was performed on these VCSELs. No observable degradation in device performance was found after 30 hours of testing at a constant current density of 22kA/cm^2 and a junction temperature of 140°C. Figure 5 below depicts these results.
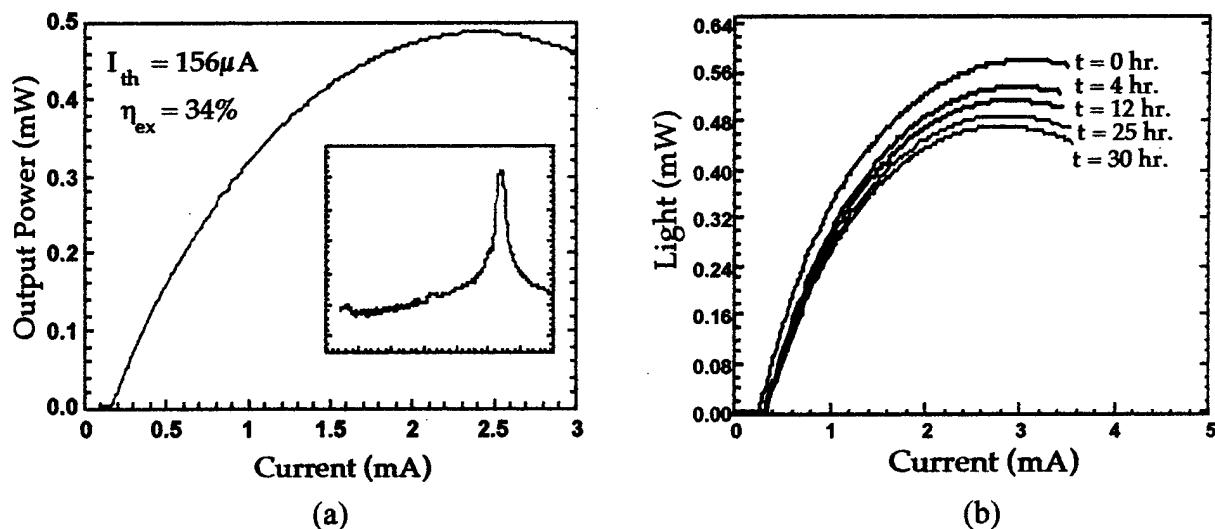
Figure 5. (a) Light versus current plot for a 2.8μm diameter device along with the measured optical spectrum (b) Light versus current curves as a function of time during the burn-in study.

Low-threshold 980-nm VCSELs were then investigated for use in free-space optical interconnects between boards. A VCSEL-based free-space optical link was demonstrated and the alignment tolerances for the link where characterized. Limitations due to device sizes, interconnect dimensions, crosstalk, and insertion loss levels were also studied. A data transmission at 500 Mbit/s per channel with a lateral alignment tolerance of ± 50μm

was demonstrated. By launching the signal from the microlensed VCSEL directly into a fiber-coupled receiver, a data transmission at 3 Gbit/s with a BER < 10^{-12} was obtained. These results are illustrated in Figure 6.

Figure 6. (a) Measured insertion loss and crosstalk for the free-space link as a function of lateral misalignment for varied interconnect lengths (b) Measured Bit Error Rate (BER) for the free-space link for various received powers.
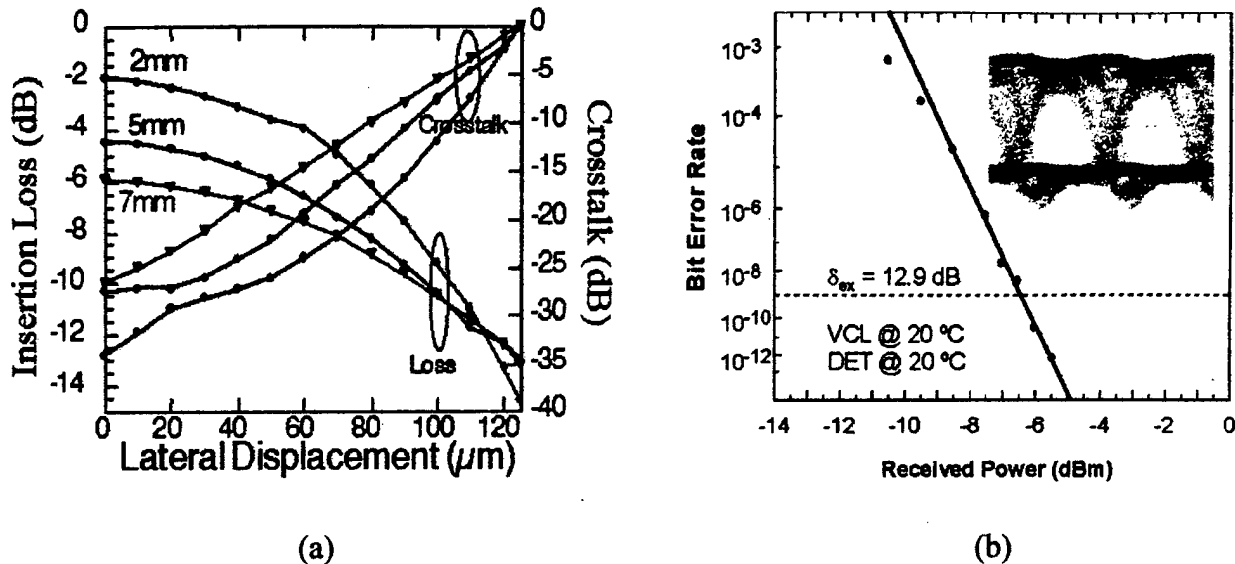
Focus was then placed on improving aperture design by using tapered apertures and improving broad area characteristics by optimizing the mirror doping. As a result of these design improvements, devices with diameters less than 1μm lased with output powers greater than 0.5mW. Additionally, devices of ~1.5μm and ~2.5μm diameters lased with slope efficiencies of 55 and 58% respectively--nearly equal to the broad area value. More importantly, peak wall-plug efficiencies of 21% and 27% were achieved for the 1.5μm and 2.5μm devices. And, at low output powers of 150μW, wall-plug efficiencies > 20% were demonstrated for all devices.

Finally, a user-friendly Graphical User Interface (GUI) software package that aids in calculating the optical losses in VCSEL structures has been developed. The program is available for download with the disclaimer that UCSB be recognized with its use.

Future work

Although this grant has officially ended, research is still being conducted on these device structures. Even though the current is well confined by placing the aperture at the first standing wave null, the carriers still diffuse once they enter the quantum wells. This accounts for the majority of the threshold current for diameters <3μm. Schemes for carrier confinement such as etching and regrowth and quantum well disordering by implantation and subsequent Rapid Thermal Annealing (RTA) are currently underway.

6

With the improved scaling of these devices, it is conceivable that even higher wall-plug efficiencies can be achieved due to the decrease in the threshold current.

Conclusions

Over the span of this grant, significant improvements have been made in the design of VCSELs for use as smart pixels. 850-nm VCSELs with threshold currents as low as 156μA were fabricated using strained AlInGaAs/AlGaAs active layers. Improved 980-nm VCSELs were fabricated and used in free-space optical links yielding BER < 10^{-12} at 3 Gbit/s. Devices employing the use of oxide apertures and improved mirror design demonstrated slope efficiencies as high as 58% and wall-plug efficiencies as high as 27% for output powers of 150 μW. Finally, a computer model for calculating optical losses in oxide-defined VCSELs has been integrated with a graphical user interface to aid in the design of VCSELs.

Engineering Oxide Apertures in Vertical Cavity Lasers

March, 1999

Electrical and Computer Engineering Department
University of California at Santa Barbara
Santa Barbara, CA 93106

Acknowledgements:

The work I present in this thesis would not have been possible without many resources (personnel, equipment and money) far beyond what I alone could supply. And it will be difficult to know I have acknowledged all involved, but so it goes:

I wish to thank my advisor, Larry Coldren, for providing a very good perspective on the direction and presentation best for my work and for trusting me with a relatively large amount of independence pursuing research and also for his effort seeking out the funding necessary to keep everything going.

I also am grateful to the other members of my committee for their comments and questions to improve this work.

I must acknowledge those who kept the labs running: John English, who can make MBE equipment behave by intimidation; Jack "Everyday is Christmas in the cleanroom" Whaley who maintained a steady stream of lab supplies; Dan Cohen for his support in the photonics lab, and Martin Vandenbroek for his assistance setting up the oxidation furnace.

I am indebted to Brian Thibeault and Bruce Young who spent much time teaching me about growth and processing and provided good insight when equipment or processes were not behaving "as usual". In addition, the loss measurements on pillars and thin and thick apertures by Brian Thibeault and Phil Floyd are a foundation for this work.

I benefited much from synergetic discussions with Near Margalit on VCSEL device results, processing and design. And I found lunchtime discussions with Near, Greg Fish, Ola Sjolund, Beck Mason and Duane Louderback not only a good break, but also frequently helpful to my own work.

I thank Dubravko Babic for passing to me a philosophy that modeling is generally useless unless one can reduce the results into something the device

"You can't always get what you want, but if you try sometimes you just might find you get what you need."
- M. Jagger

This dissertation is dedicated
To all those VCSEL makers still striving for their bumper stickers

Vita

March 18, 1972	Born in Boston, Massachusetts.
June, 1994	B.S., Applied and Engineering Physics, Cornell University.
May, 1996	M.S., Electrical and Computer Engineering, University of California, Santa Barbara.
June, 1999	Ph.D., Electrical and Computer Engineering, University of California, Santa Barbara.

Patent

U.S. Patent Application (filed by UCSB):
"Structures for Integration of Semiconductor Lasers and Photodetectors"
Inventors: Eric R. Hegblom and Duane A. Louderback

Publications:

First Authored Journal Papers [1-5]

[1]   E. R. Hegblom, N. M. Margalit, A. Fiore, and L. A. Coldren, "High Performance Small Vertical Cavity Lasers: A comparison of measured improvements in optical and current confinement in devices using tapered apertures," *Submitted to J. Selected Topics in Quantum Electronics*, 1999.

[2]   E. R. Hegblom, N. M. Margalit, A. Fiore, and L. A. Coldren, "Small, Efficient Vertical-Cavity Lasers with tapered oxide apertures," *Electron. Lett.*, vol. 34, pp. 895-897, 1998.

[3]   E. R. Hegblom, D. I. Babic, B. J. Thibeault, and L. A. Coldren, "Scattering Losses from Dielectric Apertures in Vertical Cavity Lasers," *IEEE J. Selected Topics in Quantum Electron.*, vol. 3, 1997.

[4]   E. R. Hegblom, B. J. Thibeault, R. L. Naone, and L. A. Coldren, "Vertical Cavity Lasers with tapered oxide apertures for low scattering loss," *Electron. Lett.*, vol. 33, pp. 869-879, 1997.

[5]   E. R. Hegblom, D. I. Babic, B. J. Thibeault, and L. A. Coldren, "Estimation of Scattering Losses in Dielectrically Apertured Vertical Cavity Lasers," *Appl. Phys. Lett.*, vol. 68, pp. 1757-1759, 1996.

First Authored Conference Papers [1-5]

[1]   E. R. Hegblom, N. M. Margalit, and L. A. Coldren, "Low Threshold, Efficient Vertical Cavity Lasers with tapered apertures," in *Proc. LEOS '98*, paper no. ThJ2 (INVITED), 1998.
[2]   E. R. Hegblom, R. L. Naone, N. M. Margalit, and L. A. Coldren, "Comparison of tapered apertures in vertical cavity lasers," in *Proc. LEOS '97*, Vol. 2, No. ThI3, p. 350-351, 1997.
[3]   E. R. Hegblom, N. M. Margalit, B. J. Thibeault, L. A. Coldren, and J. E. Bowers, "Current Spreading in apertured vertical cavity lasers," in *Proc. SPIE Photonics West*, Vol. 3003, paper no. 23, pp. 176-179, 1997.
[4]   E. R. Hegblom, B. J. Thibeault, and L. A. Coldren, "Towards microcavity vertical cavity lasers: aperture and cavity design for high efficiency and low threshold," in *Proc. LEOS Summer Topicals*, MB1 (Invited), 1997.
[5]   E. R. Hegblom, D. I. Babic, B. J. Thibeault, and L. A. Coldren, "Loss Limitations in Dielectrically Apertured Vertical Cavity Lasers," in *Proc. CLEO '96*, paper no. JTuH3, pp. 204-205, 1996.

Co-Authored Book Chapter

Larry A. Coldren and Eric R. Hegblom, "Fundamental Issues in VCSEL Design", Chapter 2 in Vertical Cavity Lasers, Eds. C. Wilmsen, H. Tempkin, and L. A. Coldren, *to be published*

Co-Authored Papers

[1]   L. A. Coldren, E. R. Hegblom, Y. A. Akulova, J. Ko, E. M. Strzelecka, and S. Y. Hu, "Vertical Cavity Lasers for Parallel Optical Interconnects," in *Proc. MPPOI '98*, 1998.

[2]   L. A. Coldren, E. R. Hegblom, Y. A. Akulova, J. Ko, E. M. Strzelecka, and S. Y. Hu, "VCSEL's in '98: What we have and What we can

expect," in *Proc. SPIE Photonics West*, INVITED paper no. 3286-100, 1998.

[3]   L. A. Coldren, E. R. Hegblom, E. Strzelecka, J. Ko, Y. A. Akulova, and B. J. Thibeault, "Recent Advances and Important Issues in Vertical Cavity Lasers," in *Proc. Photonics West '97*, paper no. 3003-01, pp. 2013, 1997.

[4]   L. A. Coldren, B. J. Thibeault, E. R. Hegblom, G. B. Thompson, and J. W. Scott, "Dielectric Apertures as Intracavity Lenses in Vertical Cavity Lasers," *Appl. Phys. Lett.*, vol. 68, pp. 313-315, 1996.

[5]   L. A. Coldren, T. Wipiejewski, B. J. Thibeault, E. R. Hegblom, J. Ko, and D. B. Young, "Novel Multiple Wavelength Single Frequency Vertical-Cavity Laser arrays and Techniques for improved performance," in *Proc. DoD Photonics '96*, paper no. 26.1, pp. 345-349, 1996.

[6]   K. A. Black, N. M. Margalit, E. R. Hegblom, P. Abraham, Y.-J. Chiu, J. Piprek, J. E. Bowers, and E. L. Hu, "Double-fused 1.5um vertical cavity lasers operating continuous-wave up to 70oC," in *Proc. 16th IEEE International Semiconductor Laser Conference*, 1998.

[7]   A. Fiore, Y. A. Akulova, E. R. Hegblom, J. Ko, and L. A. Coldren, "Postgrowth Tuning of Cavity Resonance for Multiple-Wavelength Laser and Detector Arrays," in *Proc. CLEO '98*, paper no. CThX3, 1998.

[8]   A. Fiore, Y. A. Akulova, J. Ko, E. R. Hegblom, and L. A. Coldren, "Multiple Wavelength Vertical Cavity Laser Arrays Based on a Postgrowth Lateral-Vertical Oxidation of AlGaAs," *Appl. Phys. Lett.*, vol. 73, pp. 282-284, 1998.

[9]   P. D. Floyd, B. J. Thibeault, E. R. Hegblom, J. Ko, and L. A. Coldren, "Comparison of Optical Losses in Dielectric Apertured Vertical-Cavity Lasers," *IEEE Photon. Technol. Lett.*, vol. 8, pp. 590-592, 1996.

[10]   S. Y. Hu, E. R. Hegblom, and L. A. Coldren, "Coupled-Cavity Resonant Photodetectors for High Performance Wavelength Demultiplexing Applications," *Appl. Phys. Lett.*, vol. 71, pp. 178-180, 1997.

[11]   S. Y. Hu, E. R. Hegblom, and L. A. Coldren, "Multiple-Wavelength Top-Emitting Vertical Cavity Laser Arrays for Wavelength Division Multiplexing Application," in *Proc. LEOS '97*, POST DEADLINE, paper no. PD1.5, 1997.

[12]   S. Y. Hu, E. R. Hegblom, and L. A. Coldren, "Multiple-Wavelength Top-Emitting Vertical-Cavity Photonic Integrated Emitter Arrays for Diect-Coupled Wavelength-Division Multiplexing Applications," *Electron. Lett.*, vol. 34, pp. 189-190, 1998.

[13]   S. Y. Hu, J. Ko, E. R. Hegblom, and L. A. Coldren, "High Performance Multiple-Wavelength Vertical Cavity Photonic Integrated Emitter Arrays for Direct Coupled Multimode Optical Links," in *Proc. CLEO '98*, INVITED paper no. CThK1, 1998.

[14]   S. Y. Hu, J. Ko, E. R. Hegblom, and L. A. Coldren, "Multimode WDM Optical Data Links with Monolithically-Integrated Multiple-Channel VCSEL and Photodetectors Arrays," *J. Quantum Electron.*, vol. 34, pp. 1403-1414, 1998.

[15]   J. Ko, E. R. Hegblom, Y. Akulova, N. M. Margalit, and L. A. Coldren, "AlInGaAs/AlGaAs Strained Active Layer 850nm Vertical-Cavity Lasers with Very Low Thresholds," *Electron. Lett.*, vol. 33, pp. 1550-1552, 1997.

[16]   J. Ko, E. R. Hegblom, Y. Akulova, N. M. Margalit, and L. A. Coldren, "Ultra Low Threshold 850nm Oxide-Apertured Vertical-Cavity Lasers Using AlInGaAs/AlGaAs Strained Active Layers"," in *Proc. SPIE Photonics West*, paper no. 3286-03, 1998.

[17]   J. Ko, E. R. Hegblom, Y. Akulova, B. J. Thibeault, and L. A. Coldren, "Record Low Threshold 840nm Laterally Oxidized Vertical Cavity Lasers Using AlInGaAs/AlGaAs Strained Active Layers," in *Proc. CLEO '97*, paper no. CWM3, pp. 289-290, 1997.

[18]   J. Ko, E. R. Hegblom, Y. A. Akulova, B. J. Thibeault, and L. A. Coldren, "Low-Threshold 840nm Laterally Oxidized Vertical Cavity Lasers Using AlInGaAs/AlGaAs Strained Active Layers," *IEEE Photon. Technol. Lett.*, vol. 9, pp. 863-865, 1997.

[19]   J. Ko, B. J. Thibeault, Y. Akulova, E. R. Hegblom, D. B. Young, and L. A. Coldren, "MBE-Grown Strained AlInGaAs/AlGaAs Vertical

Cavity Lasers with Low Threshold Currents and High Output Power," in *Proc. LEOS '96*, paper no. TuDD3, pp. 388-389, 1996.

[20]   D. A. Louderback, O. Sjolund, E. R. Hegblom, J. Ko, and L. A. Coldren, "Novel Integration of Substrate Input/Output Vertical Cavity Lasers and Resonant Photodetectors," in *Proc. Device Research Conference (DRC)*, Vol. I, paper B-4, p. 140, 1998.

[21]   N. M. Margalit, K. A. Black, Y. J. Chiu, E. R. Hegblom, K. Streubel, P. Abraham, M. Anzlowar, J. E. Bowers, and E. L. Hu, "Top-emitting double fused 1.5μm vertical cavity lasers.," *Electron. Lett.*, vol. 34, pp. 285-7, 1998.

[22]   N. M. Margalit, Y. J. Chiu, E. R. Hegblom, P. Abraham, J. Wesslmann, J. E. Bowers, and E. L. Hu, "120 Degrees C pulsed operation from a 1.55 μm vertical cavity laser," in *Proc. IEEE/LEOS Summer Topical Meeting*, p. 43-44, 1997.

[23]   N. M. Margalit, K. Streubel, Y. Chiu, E. R. Hegblom, H. Q. Hou, J. E. Bowers, and E. L. Hu, "High Temperature 1.55 μm vertical-cavity lasers through wafer fusion," in *Proc. Photonics West '97*, Paper no. 3003-22, pp. 169-175, 1997.

[24]   R. L. Naone, P. D. Floyd, D. B. Young, E. R. Hegblom, T. A. Strand, and L. A. Coldren, "Interdiffused Quantum Wells for Lateral Carrier Confinement in VCSELs," *J. of Selected Topics in Quantum Electron.*, vol. 4, pp. 1-9, 1998.

[25]   R. L. Naone, E. R. Hegblom, and L. A. Coldren, "Lateral Oxidation Rate Dependence of AlAs Thickness," in *Proc. Workshop on Native Oxides of Compound Semiconductors*, 1997.

[26]   R. L. Naone, E. R. Hegblom, B. J. Thibeault, and L. A. Coldren, "Oxidation of AlGaAs for tapered apertures in vertical cavity lasers," *Electron. Lett.*, vol. 33, pp. 300-301, 1997.

[27]   R. L. Naone, E. R. Hegblom, B. J. Thibeault, J. C. Ko, and L. A. Coldren, "Design of Graded AlxGa1-xAs Layers for Tapered Al-Oxide Apertures in Vertical Cavity Lasers," in *Proc. Electronic Materials Conference*, paper no. F3, p. 9, 1996.

[28]   O. Sjolund, D. A. Louderback, E. R. Hegblom, J. Ko, and L. A. Coldren, "Individually Optimized Bottom-Emitting Vertical Cavity

Lasers and Bottom-Illuminated Resonant Cavity Detectors," in *Proc. Optics in Computing '98*, pp. 6-9, 1998.

[29]   O. Sjolund, D. A. Louderback, E. R. Hegblom, J. Ko, and L. A. Coldren, "Novel Integration of Microlensed Resonant Photodetectors and Vertical Cavity Lasers," in *Proc. CLEO '98*, POSTDEADLINE paper no. CPD13-2, 1998.

[30]   B. J. Thibeault, K. Bertilsson, E. R. Hegblom, P. D. Floyd, and L. A. Coldren, "High-Speed Modulation Characteristics of Oxide-Apertured Vertical-Cavity Lasers," in *Proc. 15th IEEE Int. Semiconductor Laser Conference*, paper no. M3.2, pp. 17-18, 1996.

[31]   B. J. Thibeault, K. Bertilsson, E. R. Hegblom, E. M. Strzelecka, Y. Akulova, and L. A. Coldren, "High Speed Characteristics of Low Optical Loss oxide apertured Vertical Cavity Lasers," *IEEE Photon. Technol. Lett.*, vol. 9, pp. 11-13, 1997.

[32]   B. J. Thibeault, E. R. Hegblom, Y. A. Akulova, P. D. Floyd, J. Ko, R. Naone, and L. A. Coldren, "Electrical and optical losses in dielectrically-apertured vertical-cavity lasers," in *Proc. SPIE Photonics West '97*, Vol. 3003-12, 1997.

[33]   B. J. Thibeault, E. R. Hegblom, P. D. Floyd, Y. Akulova, R. L. Naone, and L. A. Coldren, "Reduced Optical Scattering Loss in Vertical Cavity Lasers with Thin or Tapered oxide apertures," in *Proc. IEEE LEOS '95*, POSTDEADLINE Paper no. PD2.1, 1995.

[34]   B. J. Thibeault, E. R. Hegblom, P. D. Floyd, R. Naone, Y. Akulova, and L. A. Coldren, "Reduced Optical Scattering Loss in Vertical-Cavity Lasers Using a Thin (300Å) Oxide Aperture," *IEEE Photon. Tech. Lett.*, vol. 8, pp. 593-596, 1996.

[35]   T. Wipiejewski, M. G. Peters, E. R. Hegblom, and L. A. Coldren, "Vertical Cavity Surface Emitting Laser Diodes with Post-Growth Wavelength Adjustment," *IEEE Photon. Technol. Lett.*, vol. 7, pp. 727-729, 1995.

Abstract:

Engineering Oxide Apertures in Vertical Cavity Lasers
by Eric R. Hegblom

This work focuses on analyzing and improving the performance of smaller vertical cavity lasers which employ transparent, insulating apertures (commonly made by lateral etching or oxidation) for optical and current confinement.

Improved performance of smaller vertical cavity lasers is important for applications which require arrays of vertical cavity lasers operating at low power such as free-space optical interconnections between computer boards or even computer chips or highly parallel laser printing schemes. And if properly scaled, smaller lasers have better characteristics at lower output powers.

We analyze two major barriers to shrinking the aperture size: optical scattering losses and current spreading. These analyses helped explain the observed drop in efficiency and rise of threshold current density in earlier oxide apertured, small lasers, and directed changes in the aperture design such as tapering the oxide front for a more lens-like shape. In addition, these analyses were reduced to simple formulas involving normalized parameters which can be applied to a variety of designs.

We also demonstrate experimentally the impact of improvements in aperture design which enabled small, single-mode, VCSELs $<2\mu m$ diameter to reach record efficiencies and enabled 2-3μm diameter devices to reach power conversion efficiencies of 20% at output powers as low as 150μW. And we discuss how these results can be improved with carbon doping and better tailoring of the doping profile to minimize resistance with the least absorptive loss.

Dissertation Overview and Summary of Contributions

Application Motivations and Background (Chapter 1)

Relatively large multimode vertical cavity surface emitting lasers (VCSELs) are presently manufactured by several companies for short distance (~200m), single-channel data links over multimode fiber. However, in the future, there are opportunities for arrays of VCSELs serving as the optical source for denser data links over shorter distances. As the array size is increased and VCSEL spacing reduced, the requirements on VCSEL performance become more stringent. The application scale may range from ~10 channel links over multimode fiber to link computers for high performance applications to board-to-board or ultimately to chip-to-chip interconnects within computers. In addition, dense arrays may also be desired to improve speed in lasers printers where the ultimate limit would be to have a VCSEL for every pixel across the row of a page. These application areas and requirements are discussed further in Chapter 1.

Applications like free-space optical interconnects require much less power than those over longer distances. To stay competitive with an electronic link one desires less than about $\Delta V^2/Z_0 \sim (0.4)^2/50\Omega = 3mW$ per connection for the laser itself. (Previously, it appeared optical connections would have a great advantage over electrical ones at short distances from a power consumption perspective, but lower voltage electronics are changing that.) This means that it is important to improve the efficiency of devices at lower output powers. In addition it is desired to have single-mode devices to reduce optical crosstalk between adjacent channels and modal competition noise. Finally, one would like low voltage for compatibility with CMOS/BiCMOS drivers.

Benefits of Scaling (Chapter 2)

This thesis aims to improve the characteristics of VCSELs at lower powers by improving the scaling of the broad-area properties to small sizes. If the broad area threshold current density and slope efficiency remain constant with device size, then smaller lasers will have higher wall-plug efficiency than larger lasers despite the electrical resistance increasing inversely with device size. In addition, smaller lasers would require less operating power for a given modulation bandwidth, and at the operating point for highest efficiency, the temperature rise, and drive voltage would also be lower in smaller lasers (assuming perfect scaling). The benefits and barriers to ideal scaling are described and quantified in Chapter 2.

Thesis Focus:

To improve the scaling of device characteristics, this thesis examines two basic issues in *apertured* vertical cavity lasers: optical confinement and current confinement and demonstrates improvements the to scaling using tapered Al-oxide apertures in 980nm VCSELs grown in the GaAs/AlGaAs material system. In addition, we formalize and pursue some ideas to improve the broad-area device characteristics.

Improving the broad-area VCSEL characteristics (Chapter 3)

The doping profile particularly in the mirrors of a vertical cavity laser is critical to device performance for all sizes. And there is always a trade off between increased free carrier absorption loss and lower electrical resistance. In Chapter 3, we introduce the loss-resistance product (which has been shown to be correlated to the wall-plug efficiency), and *use it for the first time to derive the ideal carrier profile*. We then compare various mirror interface doping and grading schemes to achieve this profile.

Analysis of Optical Confinement of Apertures (Chapter 4)

The lateral optical confinement provided by oxide apertures in vertical cavity lasers is not perfect. Analyzing the optical confinement and quantifying the

excess optical loss created by the apertures is a key contribution of this thesis. In fact, the conclusions and analysis in this area have already provided understanding and directed device design here and elsewhere. And you may have seen the simple formula for the loss estimates in the theses of Brian Thibeault and Yuliya Akulova. This analysis supported experimental evidence that the performance of small (<4μm) VCSELs was limited by significant excess optical losses in typical aperture designs at that time and showed that moving to optically weaker (thinner) apertures would provide improvement as Brian Thibeault demonstrated. In addition, the analysis showed that by tapering the aperture tip (which can be done by a combination of lateral and vertical oxidation as discussed in Chapter 7) could provide even further reduction of excess loss, but ultimately designs with single apertures could not confine the smallest of modes without being limited by the angular stop-band of the DBR mirrors. At the end of Chapter 4, we introduce another effective mirror length, the *ray penetration depth*, to describe this effect.

Current Confinement Analysis (Chapter 5)

Current can spread between the aperture and the active region. This spreading can effect both the threshold current and the injection efficiency above threshold. The analysis of Chapter 5 quantifies these two effects with simple formulae that can be easily applied to device designs. The key conclusions provided by this analysis are that current spreading can be a far greater contribution to threshold than lateral carrier diffusion and that current spreading does little to lower the injection efficiency above threshold. These points were key to understanding the device performance of VCSELs made by Thibeault and Margalit and the devices in this work and you may have already seen that analysis applied in their theses or in the thesis of Yuliya Akulova.

Device Results (Chapter 6)

The analysis of optical scattering losses and of current confinement directed device designs towards the use of thin or tapered apertures positioned at the standing wave null closest to the active region. With such modifications, we fabricated devices that benefited from the improvements in scaling of broad

area characteristics. Lowering of scattering loss has enabled record efficiencies for devices <2μm diameter. Equally important, 2-3μm diameter devices reach a wall-plug efficiency of 20% at only 150μW output power. The peak efficiency is higher, but the important result is being able to reduce the total operating power as desired for the shortest distance interconnect applications. We should note that with carbon doped VCSELs, researchers at Sandia Labs and the University of Ulm have achieved high wall-plug efficiencies of 50% and 57% at output powers of 1.3mW and 3.3mW, respectively. But these have been in larger 7μm and 5μm diameter devices and the improvements being touted here are for smaller, single-mode (as desired for free-space optical interconnects) devices at lower powers where the scaling issues are much more important and the efficiency of the devices in this work represent state of the art results for that low an output power and small a size. Only one other VCSEL (the 7μm Sandia hero device) has achieved an efficiency of 20% at 150μW.

After describing the major device results, we also compare experimental data to other structures to quantify how much the optical and current confinement benefited by the design changes. The best results were obtained in Be doped devices, but we expect to do even better with the use of a more controlled p dopant, like carbon. And the effort to use carbon as a p-dopant is described in Appendix A.

Wet Thermal Oxidation: Tapered Apertures and Related Issues (Chapter 7)

An original demonstration in this work (with some credit due to Brian Thibeault, Ryan Naone and Larry Coldren) is the formation of tapered oxide apertures through a combination of fast lateral and slow vertical oxidation in an AlGaAs layer with a varying Al composition. Chapter 7 shows how changes in the layer structure affect the taper shape. In addition, other issues such as stress in the oxide and re-oxidation are discussed.

Conclusions and Outlook (Chapter 9)

The major contributions of this work are the theoretical analysis and laboratory realization of VCSELs with lower parasitic optical and current losses. We look beyond the results achieved to forecast the major impact better current and carrier confinement could have on the wall-plug efficiency at smaller sizes and examine other potential benefits of tapered apertures.

MBE Growth with solid source Carbon doping (Appendix A)

For improved VCSEL performance, a p-dopant like carbon is preferable to Be which moves during growth and does not incorporate well into high aluminum content layers. Previous efforts at UCSB by Matt Peters using a graphite filament source installed in an MBE system here showed the carbon doped layers tended to roughen during growth (though such roughness has not been reported with gas source carbon doping). But after some effort, we found the proper conditions (a higher substrate temperature~650°C) necessary to correct this problem. While the performance frontier was not pushed further for 980nm VCSELs (as this appendix discusses), the mirror material was still good enough to offer the low resistance and low loss necessary for the $1.55\mu m$ fused VCSEL researchers (Alexis Black et al.) to achieve record high temperature (70°C) CW lasing in their devices. Possibly performance could be pushed further at 980nm even using the filament source.

Theoretical Odds and Ends (Appendix B)

This section contains some handy graphs like confinement factor and mode radius vs. V number and derives modifications to the expression for mirror length when there are extra spacers or grading in the DBR. In addition, a generalized form of the optical efficiency is given which is useful when writing a transmission matrix program. But a majority of this appendix is spent deriving the mathematical difference between periodic and uniform waveguiding under the Fresnel approximation.

Layer Specifications (Appendix C)

The actual MBE growth program for the 1st Null VCSELs is provided.

Table of Contents:

Chapter 3: Vertical Design Issues   57

Chapter 4: Analysis of Index Aperture Optical Confinement 87

Chapter 5: Current Spreading   141

Chapter 1 :
VCSEL Applications

Overview:

Over the past decade vertical cavity lasers have matured from a laboratory fascination to a wafer-scale manufactured product. Even just a few years ago (1994), people still wondered if VCSELs would ever be mass produced instead of in-plane lasers. But today several companies are selling either individual Vertical Cavity Surface Emitting lasers (VCSELs) or selling modules for data links which use VCSELs. The most common application for the VCSELs is gigabit Ethernet and Fibre channel link modules. Presently, total sales are on the order of over a million devices per year! VCSELs are definitely here to stay, but how will they change in the future? What new requirements will be placed upon the devices? What should be improved about them today? Where is this thesis relevant?

In the future, VCSELs may be used for other applications like high performance interconnects for parallel computing or in phone switching centers, or at smaller scales such as chip-to-chip interconnects within computers, laser printing and possibly in digital video disks (or other optical storage applications) with red or possibly, with (who knows?) blue VCSELs. In addition, many improvements may be made to VCSELs for the existing

data-link applications such as using wavelength division multiplexing, making modules with arrays of VCSELs, employing oxide apertured VCSELs, and manufacturing VCSELs which operate at 1.3 or 1.55μm. And beyond that VCSELs may start being integrated monolithically with other components like photodetectors (either for two-way communication or as a monitor for the output power), or less likely, with transistors. Pursuing these various developments will keep the VCSEL community well employed over the next few years.

VCSELs have a number of advantages touted over the years namely: a circular beam which is easy to couple to fiber, low power consumption even at relatively high modulation speeds, compatibility with LED manufacturing. In addition, the various attributes (like resistance, mode-size, number of modes, efficiency at lower powers) change with device size and with our ability to circumvent parasitics. As will be discussed further in the next chapter, the removal of parasitics mean that smaller VCSELs can provide higher power conversion efficiency at lower output power and higher modulation speed at lower operating powers. Furthermore, with proper scaling, smaller VCSELs are able to reach a higher output power density than larger ones which also implies that properly scaled smaller VCSELs will have a higher maximum modulation bandwidth. Unfortunately, shrinking the VCSEL size also means higher electrical resistance (although the scaling is better for apertured devices) and this is a limiting factor if one wants to match to low impedance transmission lines running to the device.

In the following sections we will examine the various requirements on VCSELs demanded by both data link applications (for LANs, chip-to-chip interconnects) and printing (where an electrical alternative is not a competitive solution). We will comment on device designs to meet those requirements and also examine where improved scaling of VCSELs will impact system performance in order to motivate that key objective of this thesis.

Optical Interconnect Regimes:

Before discussing the specifics about VCSEL interconnect applications let us examine the regimes where optical interconnects are competitive with

electrical interconnects based upon the limit of the transmission medium. *In this section, we are not considering what power or current is needed to send a signal in absence of electrical transmission losses. Such an issue becomes important for very short distance interconnects as we will discuss in that subsequent section.*

The traditional argument for the use of optical communication rather than electrical is the is attenuation of electrical media (coaxial cable) at high frequencies and long distances. Over shorter distances one would expect loss by the transmission medium to become less of an issue. This is roughly true, but packaging constraints which force much more closely spaced lines increase the attenuation. The limit is still difficult to beat at very short (~cm) distances, but there are other interconnect opportunities using closely spaced (~200μm) VCSELs operating at > Gbit/sec speeds over several meter lengths.

A metal transmission line is limited by losses of the metal (skin effect losses) and radiation losses. Let us consider here these limits from a microstrip transmission line as shown in Figure 1-1. Although such a geometry is not used over all length scales, it provides an excellent estimation to understand the limitations to within an order of magnitude. The same limitations discussed still exist for other transmission line shapes but values will not change dramatically assuming appropriate scaling dimensions are chosen.

Skin Effect Losses

Using the expression for skin-effect loss in a microstrip line given in [1] and assuming a few ordinary parameters (namely effective width, w_{eff}, = height and impedance of 50Ω, a copper thickness of 2μm), we find the frequency for the transmission to attenuate the signal by 3dB is,

$$f_{3dB}\big|_{\text{Microstrip Line}} = \frac{5\,\text{GHz-m}^2}{L^2}\left(\frac{w_{eff}}{0.5mm}\right)^2 = \frac{5\,\text{Ghz-m}^2/\text{mm}^2}{L^2\rho_l} \quad (1\text{-}1)$$

As expected, this loss is not significant at 1GHz until a 0.5mm wide line is over a meter long which is beyond the regime that free-space optical interconnects might compete; but we still need to consider radiation loss, crosstalk and most importantly, interconnect density. And other switching

power issues for free-space interconnects will be discussed in a subsequent section.
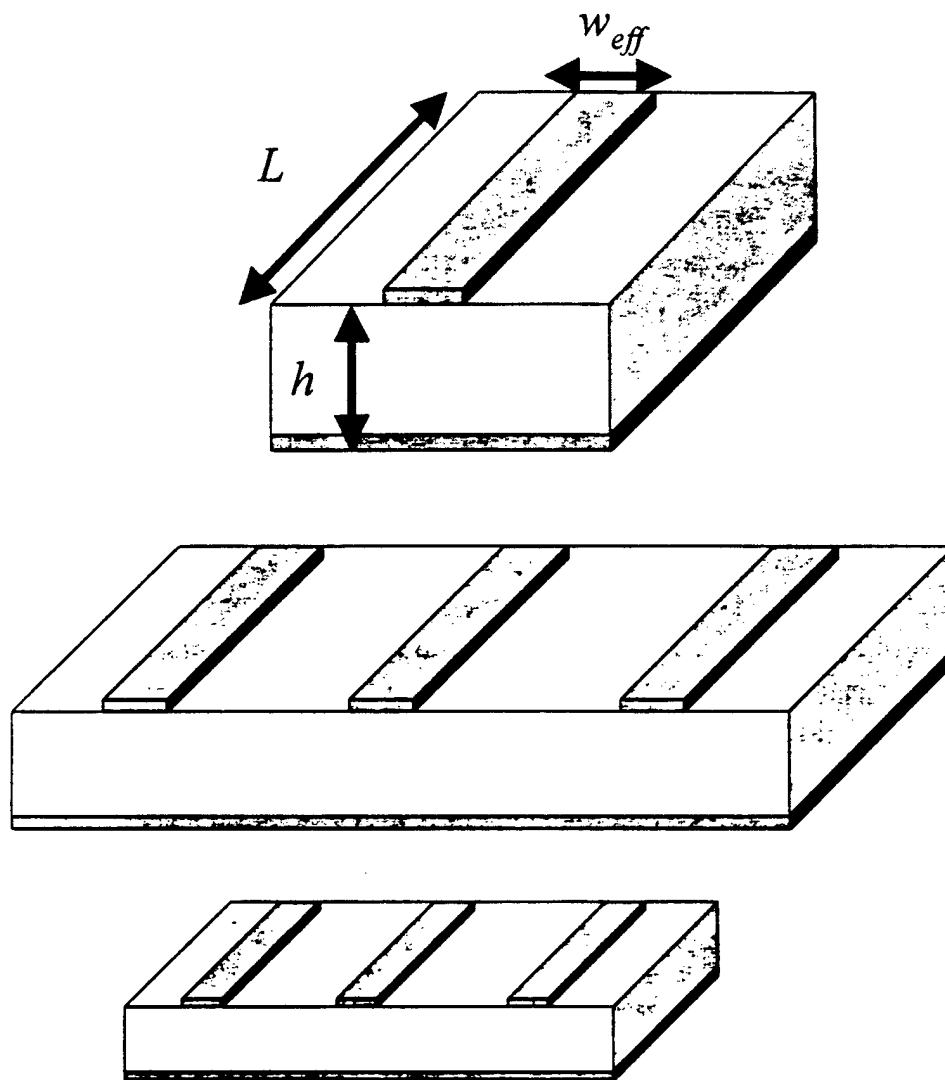
Figure 1-1: A Microstrip line. As the line is scaled to small size to avoid radiation loss or for packaging reasons, skin effect losses increase

Radiation Losses

So what about radiation losses? These do not happen to be the limit in the above example, but significant coupling to spurious modes occurs around a frequency of [2]

$$f_{RAD} = 50\,\text{GHz - mm}\Big/h \qquad (1\text{-}2)$$

using a typical ε_r=3.8. Thus, to avoid radiation losses it is necessary to scale the transmission line dimensions down as the frequency increases. Consider that we pick h so that f_{RAD} is five times the operating frequency, and scale w_{eff} with h, then the limit due to the skin effect losses can be rewritten as,

$$f_{3dB}\big|_{\text{Microstrip Line}} = 13\,\text{GHz}\left(\frac{1\,\text{m}}{L}\right)^{2/3} \qquad (1\text{-}3)$$

Allowing for the maximum height and width to avoid radiation losses, means it now takes ~50m long transmission line for a 3dB attenuation at 1GHz. However, that transmission line is now 1cm high and wide! Radiation losses do force the designer to scale the size of the line, but more likely packaging considerations will force the use of smaller lines (in which case radiation losses will be even less of a concern).

Crosstalk

We should also mention here that increasing cross-talk (which is obviously related to radiation losses) can be avoided if the height of the line, h, is scaled with the interconnect spacing. Then the amount of coupling between two lines will just depend on, L/λ the physical length over the wavelength. For a separation between microstrip lines on GaAs equal to $3h$, the coupling between them is <-20dB for lines about 2/3 the wavelength[3]. Thus, the coupling is avoidable at GHz speeds over distances < 1m, but over tens of meters (at 1GHz) crosstalk begins to dictate design changes (greater lateral spacing or use of a coaxial geometry).

2-D and 3-D Packaging Limitations

Let us consider scaling the effective width (and also height) for much more densely packed transmission lines as might be desired if there are many

interconnects over a short length. These interconnects need not only be arrayed laterally. They may stacked vertically. (Or they may be tipped up so that they send a signal vertically from a board. We will not limit ourselves to what packaging may be possible. We will just assume that somehow the transmission lines can be fabricated.) Essentially, what this analysis means is that the electrical limit due to attenuation should not be thought of as just as a length limit for a given frequency, but as a length limit at a given frequency and interconnect density, ρ_I, the number transmission lines/cm^2 crossing a planar boundary or equivalently the interconnect spacing (both laterally and vertically). Figure 1-2 plots the boundary given by Eq. (1-1) for different -3dB frequencies (i.e. for a given frequency and interconnect spacing, the length of line is calculated that would have 3dB attenuation). One can learn a lot from this plot; so let us look at the different regimes. First, lets look at interconnect lengths ~10^2 meters long and interconnect spacing on the order of centimeters. We see that this clearly lies in the "optics" region of the plot. This is where optical solutions for gigabit ethernet(GE) are competing. For an optical solution to be competitive with an electronic one over shorter distances, it must be able to packaged into a smaller form factor (interconnect spacing). If we scale down to a 1cm length, then the 3dB limit at 1GHz occurs at an interconnect spacing of ~30μm. Beating this limit with optics is still challenging because VCSELs communicating through free-space at a GHz speed on a 30μm pitch over a centimeter is a probably not possible without WDM techniques to avoid crosstalk. But other limit to consider for these links is the switching power and drive current to send a signal in absence of these skin effect losses.

But we do not have to try to scale the interconnect length to 1cm. What Figure 1-2 shows is that there is a different opportunity for VCSELs spaced ~200-500μm (compatible with fiber ribbon cable) which can send data at faster than 1Gbit/sec over lengths longer than 1 meter. Such an application is indicated by the POFI[1] (Parallel Optical Fiber Interconnects) label and will be discussed in the *VCSELs for HIPPIs* section.

---

[1] I don't intend to keep using the acronym; it just fit easily on the plot

With some idea of where these various optical interconnect regimes lie in comparison to the loss limitations from metal interconnects, let us proceed to examine the specific applications.
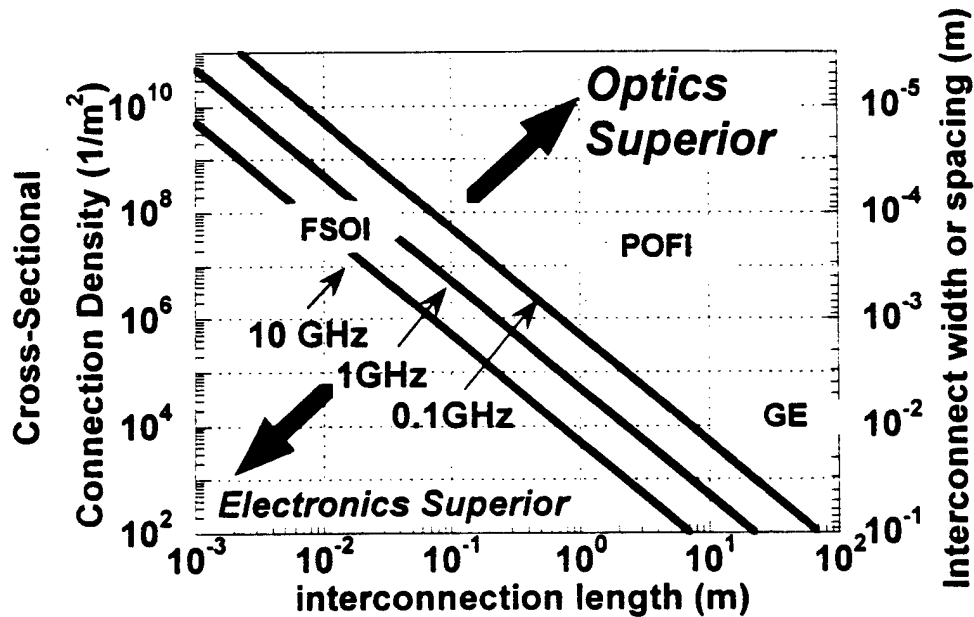
Figure 1-2: Attenuation limit from a microstrip transmission line due to skin effect losses which are dependent upon both the length of the line, the line density and the frequency. The limit approximately defines a dividing line where an optical interconnect could compete with an electrical interconnect. The blobs indicate the typical density and interconnection length of three different links. FSOI (Free-Space Optical Interconnects) have a difficult time competing with metallic interconnects purely on the bases of skin-effect losses - unless the interconnect density can be increased or a channel can operate over 10GHz. GE (Gigabit Ethernet) is already in a regime where fiber-based links have advantage over metal, and in the future, closely spaced POFI (Parallel Optical Fiber Interconnects) have a clear opportunity to compete with metal-based interconnects. Not shown on the chart are the km distances where $\lambda=1.3\mu m$ and $1.55\mu m$ laser based links have historically been preferred to coaxial cable at Gbit/sec speeds.

VCSELs for LANs (Single channel, ~10-100m interconnects)

From the previous discussion, the need for an optical-based interconnect operating at Gbit/s over distances of 100m is clear. (See Figure 1-2 again). And as mentioned this is the largest present application for VCSELs. In this high volume market, cost of manufacture is very important. Hence, the laser is used in conjunction with easy to couple to multimode fiber. Another major cost reduction comes from the ability to test and package VCSELs in a manner similar to the well developed (i.e. low cost) techniques used for LEDs. Such techniques could not be used for in-plane lasers. Furthermore, multimode VCSELs have a denser modal spectrum (from transverse modes) than in-plane lasers do (from longitudinal modes). The larger number of modes reduces the speckle patterns and consequently the higher bit error rate produced by interference of modes at junctions[4]. CD lasers also have reduced speckle because they are designed to be self-pulsating and they are cheap (~$0.5 in volume). However, commercial CD lasers have been found to be less reliable than VCSELs. (Although IBM has gone to great lengths to find techniques for fishing out reliable ones[5].)

The standard for gigabit Ethernet[6] specifies two different operating ranges of wavelengths: 770-860nm and 1270-1355nm. Although at 980nm, fibers have lower attenuation, the standard was written when 850nm VCSELs were more mature in industry and was written to allow 780nm CD lasers to compete with 850nm VCSELs[7]. The minimum length specified for a link around λ=0.8μm is 220m using 62.5μm diameter fiber and 500m using 50μm diameter fiber. For wavelengths around 1.3μm, the specification is 550m at both fiber sizes. It is also interesting to note the standard specifies the minimum length for a copper 1.25 Gbit/s interconnect to be only 25m, which is in rough agreement with Figure 1-2.

The standard also makes other specifications about the laser characteristics. Besides an operating speed of 1.25Gbits/s within a specified eye-opening, the 0.8μm sources must be eye safe (i.e. power in the fiber <~400μW) and an extinction ratio of 9dB which means a low state of ~50μW in the fiber. This relatively low, low state means that the system design must be able to tolerate changes in threshold which can raise the low-state. In addition, the laser should launch light into the both the radial and azimuthal modes of the multimode fiber which means that one needs a laser beam to be more divergent than the numerical aperture of the fiber and laser should probably be off-centered from the fiber (or perhaps the laser should even launch a donut-shaped mode[8])

Typical power consumption for the whole transceiver unit is ~800mW[9], which means the laser power dissipation is of less concern than (as we will discuss) for free-space optical links. However, the operating voltages need to be under ~3volts for compatibility with 5V emitter coupled logic (ECL) and under 2 volt in the future for compatibility with 3.3V positive emitter coupled logic (PECL) drivers.[10] Depending on the packaging one may need to worry about impedance matching to the laser, and desire a dynamic resistance ~50Ω. The following table adapted from [10] summarizes the requirements:

Data Rate	1.25 Gbit/sec
Laser Electrical Power	<~20-30mW
Peak Optical Power	~7-10mW
Dynamic Resistance	<~50Ω
Drive Voltage at operating power	<2 volts (3.3V-PECL), <3V (5V-ECL)
Threshold	<6mA
Modal Characteristics	very multimode

Table 1-1: Desired Characteristics for VCSELs used in commercial single channel links [10]

The requirements are not too stringent for VCSELs in single-channel, Gbit/sec links and this tolerance has facilitated their manufacture, but is improved

device scaling useful in this case? Typically, the VCSELs in this application are 15-30µm diameter proton implanted structures, but moving to lower scattering loss oxide apertures allows slightly smaller multimode VCSELs that can still be fabricated in a planar geometry. Oxide apertures will allow better modal stability by providing optical confinement without needing thermal lensing. These improvements are not critical, but allow some tolerances to be relaxed - for example it is much easier to reach the threshold requirement with oxide apertures than with proton implantation.

VCSELs for HIPPIs
(1-D Arrays, ~1-100m interconnects)

Although the nineteen sixties counterculture showed little interest in vertical cavity lasers, today HIgh Performance Parallel Interconnects (HIPPIs) are demanding an optical solution. Looking back at Figure 1-2, we see such Parallel Optical Fiber interconnects (POFIs) fall in the about the same distance or less than Gigabit Ethernet, but have a smaller interconnect spacing. Instead of being used as a network backbone, these links are a backbone for processor to processor connections. It sounds similar, but in the second case, a parallel computing task is demanding bandwidth rather than a bunch of multiplexed end-users. The present HIPPI standard is for connections at 400 and 800Mbit/s implemented over copper. But the proposed optical HIPPI-6400 standard is 8Gbit/s[11].

Here we should also mention that telecom switching inside metropolitan area central offices sometimes need to operate over larger distances due to space considerations in the building. Here a bandwidth around 10Gbit/s over meters to tens of meters is likely to be needed.[11].

One can imagine satisfying these short-distance high bandwidth applications either with single or parallel channels (to avoid extra multiplexing circuitry). Electrical complexity and packaging considerations dictate some trade-off, and in either case one would like to keep a small form factor. The size of the package form factor determines the ability to conduct heat given that one has a maximum ΔT between the package and the room temperature in order that the

package is not too hot to touch. The thermal requirements for a single fiber channel still allow in-plane lasers to satisfy the requirements, but the thermal requirements for arrays and their circuitry are a factor N more stringent (N being the number of channels) and designers in the real world are forced to use devices which have higher wall-plug efficiency at lower output power: VCSELs[11].

For array applications, eye safety issues naturally force a lower operating power per laser - assuming one does not build in feedback to shut off the laser. For an array of ten 830nm VCSELs coupled into ten fibers this means an maximum power of ~100μW in each fiber. Note this number is *not* one tenth of the single channel eye safe power of ~400μW because an array of fibers cannot be focused to one spot. However, if one used an array of VCSELs operating at slightly different wavelengths coupled into one fiber then the maximum coupled power per laser is 40μW. [12]

Given the advantages of VCSELs at lower operating power, several companies are working on interconnects with arrays of VCSELs including Gore[11], Siemens[13], NTT[14], Honeywell[15],and Hewlett-Packard[16]. One example of a twelve channel link module is shown in Figure 1-3.

To satisfy the requirement of higher efficiency and lower current at lower output power, not only are VCSELs preferable to in-plane lasers, but oxide confined VCSELs are preferable to proton-implanted VCSELs. In fact, the HP PONI module uses oxide confined VCSELs with I_{TH}~2mA[16].

Module Housing

CMOS
Network
Interface
IC

MT
Connector

POSA with
VCSEL/PIN
Arrays

Tx or
Rx IC
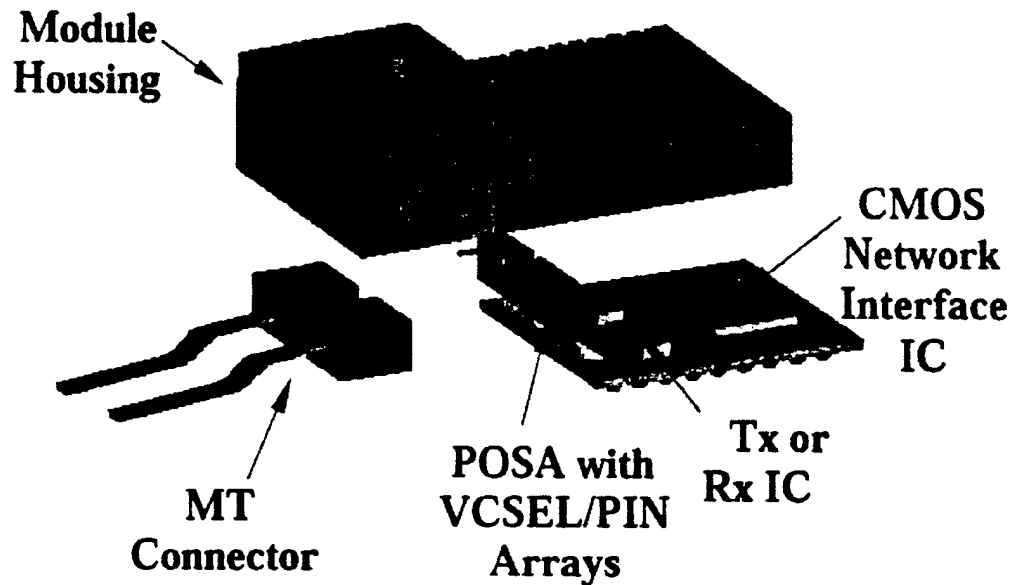
Figure 1-3: An example of a parallel link module made by Hewlett
        Packard using flexible transmission lines to connect the
        electronics with the VCSEL/PIN arrays (taken from [16])

Table 1-2 summarizes some estimate of the desired characteristics for arrays. Unfortunately, the variation in channel spacing, variations in VCSEL packaging and industry confidentiality make it difficult to predict the exact specifications needed. Probably, at this point module design is more driven by what an optimized multimode VCSEL can do rather than the other way around.

Presently, the market is very cost driven towards multimode fiber, but if cheaper connections to dense arrays of single-mode fiber or waveguides become available in the future, then this application may require single mode VCSELs. In which case, improvements to optical confinement in smaller VCSELs become more important. Nevertheless, improvements to the current confinement even for moderately sized 8-15μm VCSELs is desired and proper oxide aperture and doping design has a role in this area (as will be discussed in Chapter 2). Note again low dynamic resistance is important if transmission lines are used to transmit signals to the lasers. But this requirement could be relaxed as the VCSEL is brought closer to the circuit (for example using flip-chip bonding).

Lastly, for reduced package size it is desirable to use integrated arrays of detectors and lasers, if crosstalk requirements can be satisfied.

Data Rate	1-2 Gbit/sec
Laser Electrical Power/Channel	<10mW (?)
Peak Optical Power	~5mW (?)
Dynamic Resistance	<~50Ω (assuming no flip-chip bonding)
Drive Voltage at operating power	<2 volts
Threshold	<3mA
Modal Characteristics	very multimode (or possibly single mode)

Table 1-2: Desired Characteristics for VCSELs used in parallel optical fiber links

VCSELs within computers (2-D arrays, <1m Interconnects)

A more distant application area for VCSELs is interconnecting nodes on a chip or between chips within computers. Such high-speed connections are needed to talk to other co-processors or memory (though memory is a bit slower than another processor) or, more generally, to carry data within a dense electrical switching architecture. Here two major issues to address are (1) the extra power consumption and current distribution to drive bonding pads and high speed transmission lines and (2) packaging considerations necessary to achieve the desired interconnect density.

We will discuss both these issues for electrical interconnects and then discuss the optical interconnect alternatives which can be modulator based or source based. Finally, we will use the performance criteria to motivate improvements to smaller VCSELs.

Optical vs. Electronic links inside computers

From a power consumption point of view, there are two issues to deal with for an interconnect: the power lost during transmission and the switching power necessary even if no power is lost during transmission. The first issue we have discussed in the case of transmission lines in the previous section, but we will look briefly at this issue from a lumped element point of view. The analysis of the second issue (switching power) shows that is it very significant - using the 3-5V drive voltages of the '80s and '90s, but lower signal voltages in the twenty first century present tough competition for an optical interconnect solution based upon power considerations. The conclusion drawn is that within a computer the power consumption per interconnect (excluding drive circuitry) should be well under a 1 mW in order to compete with an electronic alternative from a power consumption perspective. The following discussion draws upon the rudiments of an older reference [17], some of my own contemplation, a brief, but enlightening discussion with Professor Mark Rodwell, and a very helpful reference [18]. Another good discussion is in [19].

Electrical transmission medium losses (small compared to switching power)

There are two ways to look at the loss of an electrical interconnect: as a lumped element on chip or as a transmission line between chips. When driving a metal line on a chip, one encounters the typical RC limit which at high enough frequency sets a maximum bit rate. For a simple parallel plate capacitor strip line, the time constant, τ, is *independent of the line width* (if fringing fields are ignored)

$$\tau = RC = \left(\frac{\rho}{t}\right)\left(\frac{\varepsilon}{d}\right)L^2 = (R_{SH}C_L)L^2 \qquad (1\text{-}4)$$

where ρ is the resistivity of the metal, t is the thickness of the metal, ε is the dielectric constant, d is the distance between the interconnect line and the ground plane, and L is the length of the interconnect. Based on some typical interconnect values in VLSI [20]: a 1.2μm thick Al (metal2) interconnect layer with 0.05 Ω-μm resistivity and even a somewhat pessimistic capacitance per area of 50 attofarad/μm² one obtains a 3dB-frequency roll off of

$$f_{3dB} \sim \frac{1}{2\pi\tau} = \frac{76\,\text{GHz} - \text{mm}^2}{L^2}. \qquad (1\text{-}5)$$

Such a parasitic limit becomes significant (<1GHz) only for on-chip interconnect lengths ~1cm. However, the analysis ignores any inductance which actually helps counteract the capacitive parasitic (since an inductor's impedance increases with frequency) and the true distributed rather than lumped element nature of the problem when L approaches λ. Ultimately, one has to consider a many inductors and capacitors in a row, namely, a transmission line which is the limit that we discussed in the previous section. In that case, the attenuation limit from skin effect losses is not significant at the interconnect density that an optical solution presently might provide.

Switching Power (in the absence of losses from the transmission medium)

Even with perfectly conducting interconnect lines, there is still power required to charge and power lost discharging them in order to send signals (due to the source and load resistance). For the case of a line with capacitance, C, the power dissipated is energy to charge plus discharge the capacitor times the frequency, f:

$$P = C(\Delta V)^2 f \qquad (1\text{-}6)$$

where ΔV is the voltage swing. For the example of the on-chip line with capacitance per area of 50 attofarad/μm^2 and f=1Ghz and a voltage swing of 2.5 volts, we obtain,

$$P_{\text{on chip interconnect}} = 0.3\,\text{mW}\,/\,\text{mm}\,/\,\mu\text{m} \quad (L\ w) \qquad (1\text{-}7)$$

where w is the linewidth in μm, and L is the line length in mm. This power is still pretty low in comparison to what a VCSEL might need to transmit at 1Gbit/sec (~0.5mW) unless the on chip length is several cm.

Switching power and density considerations from output pins

Probably a more important parasitic is the power requirement to drive the output pins on a chip. Even though CMOS dimensions may scale the bond pad sizes and packaging wires do not. At the periphery of a chip (see Figure 1-4), there are bond pads typically spaced by 200μm. To add even more pins

sometimes there are multiple rings of these bond pads.   In fact, another argument[21] for free-space interconnects is mainly from a density perspective that as chips get larger, the area available for interconnection from pads at the edge of the chip scales as the length, L, of a side of the chip. But the area available from the whole chip scales as, L^2. However, one should keep in mind that IBM's a flip-chip bonding process (called C4) would allow electrical interconnections over the whole area of the chip. In addition, a ball-grid array can be used allowing (as many as a thousand) connections (which scale with area) from the package to the board.[18]
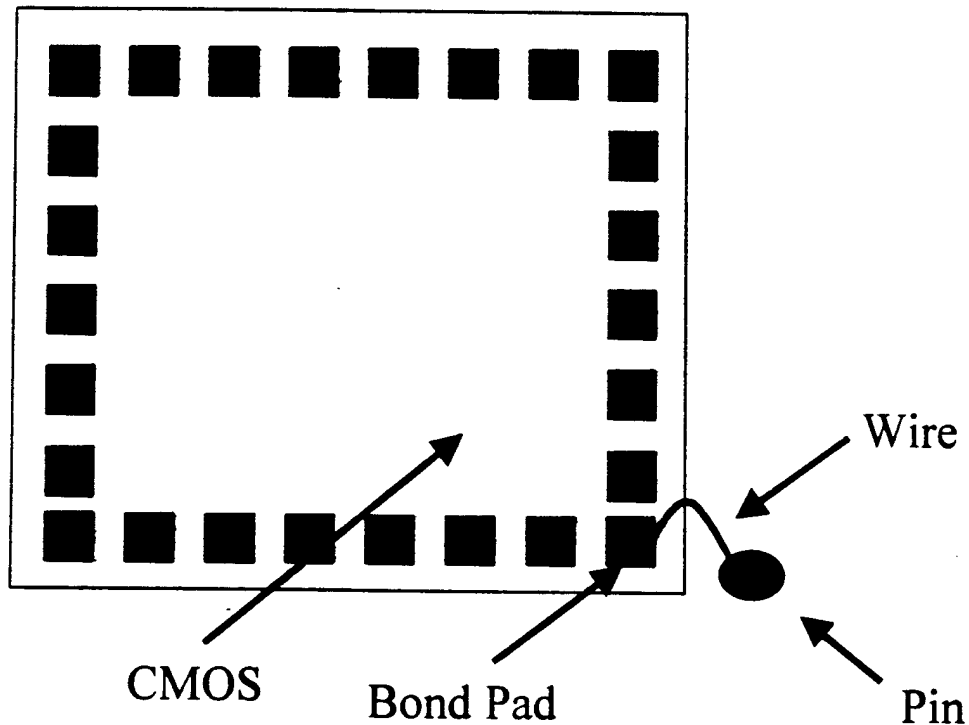
Figure 1-4: Schematic of a CMOS chip with the pads that get connected to the package pins and subsequently to lines on a printed circuit board. Driving these pads/pins/ and lines at high speed takes a significant amount of power and current in today's chips

But as far as switching power considerations, one must contend with a significant capacitance not only from the bond pad, but also the board trace. Typically, chips are tested with total capacitance of 50pF per pin[18]. (This

figure is high due to the typical length of board traces.) Again using $f=1\text{GHz}$ and a voltage swing of 2.5 volts, we obtain,

$$P_{\text{off chip interconnect}} = C\Delta V^2 f = 0.3 \text{ W/GHz} \qquad (1\text{-}8)$$

This power is huge! Especially if there are hundreds of pins to drive. However, one probably would not use traditional board traces for 1GHz signals. With better packaging one would drive an impedance matched transmission line instead of a pure capacitive load, then the power required essentially frequency independent (barring skin-effect losses). Under these assumptions, the transmission line will not draw any power, but a matched load (or a matched source sinking current) will. then the consumption is

$$P_{\text{transmissionLine}} = \frac{\Delta V^2}{Z} = 125 \text{ mW} \qquad (1\text{-}9)$$

for a swing of 2.5 volts and an impedance, $Z=50\Omega$. This power is still very high compared to the few mW of power for an optical link.

To reduce the electrical power required, one would like to use higher impedance lines, but impedances over 100Ω are difficult to achieve for microstrip lines (for coax cable it is possible, in theory, with really fat cable). But the other thing to do is simply to reduce the voltage swing. The limit encountered reducing the voltage swing is the stability of the threshold voltage. Design specifications for operating between 25 and 100°C, imply a 60meV uncertainty in V_{th}. And this uncertainty bounds an optimum threshold around 0.2 volts[22]. For a 0.4 rather than a 2.5 voltage swing, the power consumption is reduced by a factor of forty to

$$P_{\text{off chip interconnect}} = 8 \text{ mW/Ghz} \qquad (1\text{-}10)$$

$$P_{\text{transmissionLine}} = \frac{\Delta V^2}{Z} = 3.2 \text{ mW} \qquad (1\text{-}11)$$

In fact, a 2Gbit/sec/pin link has been demonstrated with 150mV signal amplitude[23, 24]. Depending on channel skew, one will need to lock to a clock for every nth channel. (This obviously depends whether one is using a bus or a star architecture.) To lock to the clock one needs a phase or delay lock loop and it should also be noted that for these circuits, the phase-lock-loop (which would be present in both optical and electrical links) consumes a much

larger power of 170mW[24]. However, for one central chip talking to many other chips, the phase lock loop can be taken off the central chip to reduce the power consumption by 75%[23, 24], then the power budget depends more upon the laser and driver on the central chip. In that case it is necessary to have low power laser drivers in CMOS to reduce total power consumption. As discussed in the LAN applications section, typical drivers with ECL inputs consume much more power than the laser. However, groups have demonstrated low power CMOS drivers which consume power comparable to the VCSEL[25, 26].

The numbers for lower voltage driving of metal interconnect lines suggest that for optics to be a competitive solution (as far as power consumption goes), the power consumed by the laser/modulator should be well under a 1mW per link.

Current distribution considerations:

As far as power consumption is concerned, future electrical solutions are very competitive with optical solutions, but what about current considerations? For the voltage swing of 2.5V into a 50Ω line, the peak AC current required is 50mA. So? If you have a hundred of these lines to drive then (in the worst case that all the outputs were swinging high or low) you need a whopping 5A of current from your supply and ground But even supposing 60% are all going high at once, then you have 0.5A, which is still a lot of current to be routing on a chip. Given these numbers, an optical solution looks very attractive. But using a lower future swing voltage of 0.4V, the current for ten lines going high at once drops to 80mA. If one uses low threshold VCSELs, the change in current for ten of them going high at once will be around 2mA (assuming they can be operated at ~100μW output power swing with 0.5W/A). This is a much lower AC current. However, with the DC bias, the power supply is guaranteed to have a load from all the lasers all the time of around 50mA (assuming above threshold bias). A laser based solution still has a slight edge, but it gets narrower as voltages are able to be lowered in future chips. Thus, reducing the bias point as much as possible is necessary for optics to have any hope of competing with metal interconnects inside future computers.

Optical Interconnect Architecture: VCSELs vs. SEEDs

If optical interconnections are to be used within a computer (or over short distances in general, such as for switching) one must decide whether to use a modulator based architecture or a laser-based architecture. The major issues for either system to address is the ease of integration both with semiconductor components and the external optics and the power consumption (mW/Gbaud). In addition, the usual issues of uniformity and stability much also be satisfied. Furthermore, one would also like have some magnification/de-magnification whereby one chip can talk to more than one other chip. (See Figure 1-5) Otherwise, one might as well just solder bond the chips to each other.

4 CMOS chips (2 shown from perspective)

(a)

Distributed processors

(b)

(c)
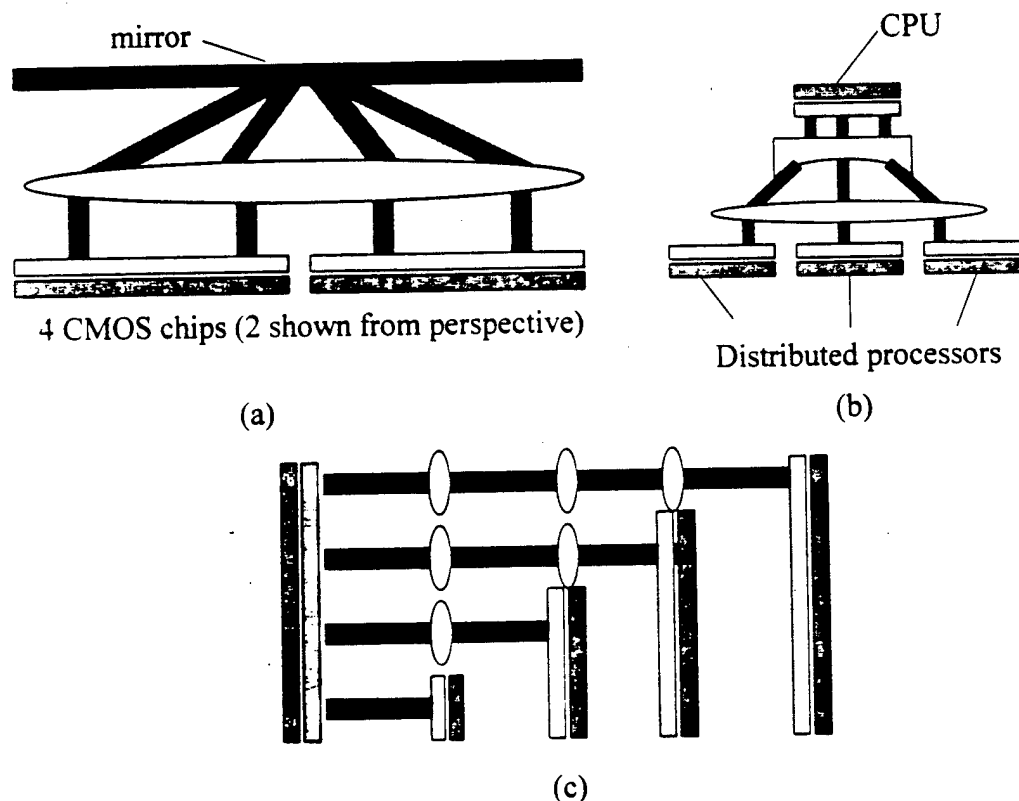
Figure 1-5: Examples of optical interconnect "magnification" so that one chip can talk to more than another chip of the same size. (a) A scheme used by Applied Photonics (b) A Focusing/De-focusing arrangement (c) A bus-like scheme with pass through that can be implemented optically (as shown) or electrically

The main difficulty with a modulator based interconnect system using Self Electro-Optic Devices (SEEDs) is that these need light incident normal to the surface. To bring the light in and send the modulated light to a detector array would require the use of beam splitters as shown in Figure 1-6. And connection to multiple chips can only be implemented in a bus like architecture.

But the main advantage of presently of SEEDs is that they are more mature. Arrays with 256 modulators integrated with 4096 detectors (for multiplexing purposes) have been demonstrated[27]. In addition, SEEDs presently have more "smartness" than source based interconnects. Specifically, FETs and SEEDs have been monolithically integrated to make circuits which can implement switching, neural networks, correlation etc[28]. This "smartness" is not inherent to SEEDs, because a source-detector based system can be made "smart" simply by flip-chip bonding it to CMOS circuitry. However, the same level of complexity has not yet been achieved with VCSELs and detectors.
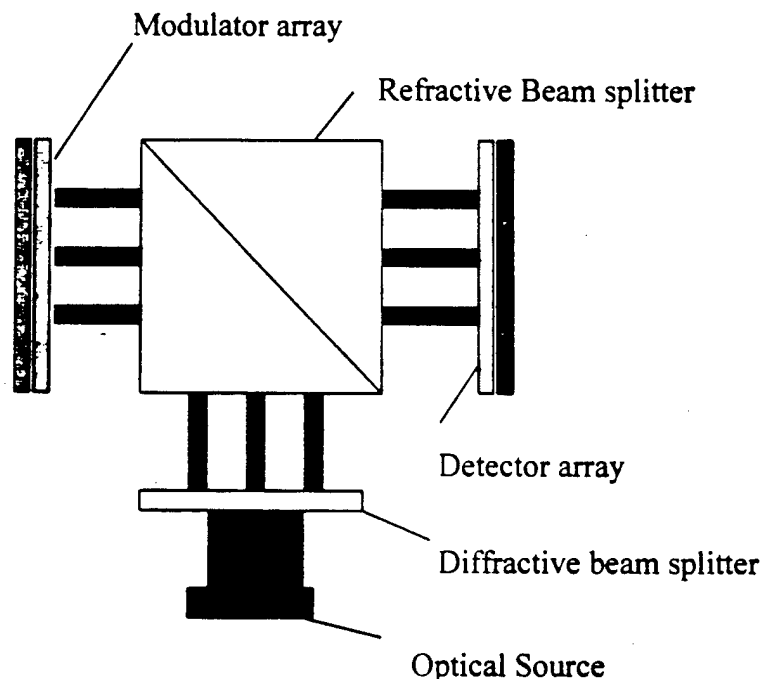
Figure 1-6: Packaging difficulty with a modulator based interconnect system. (It gets even worse for two-way communication)

The "on-chip" power consumption for a SEED/Detector based system is relatively low. For a 10x10μm modulator (with a 100fF capacitance) and $\Delta V=3$ volt, the drive power is[29]:

$$P_{SEED} \sim 1mW / (Gbit/\sec) \tag{1-12}$$

This consumption is lower (but not dramatically) than the electrical power consumption ($\sim 3mW$) described above for low-voltage interconnects. The total dissipated power will also include some optical power from the source which does not arrive at the detector array. If the optical elements are efficient at directing the optical power on the array and to the detector, then one needs only carry enough power for the receiver $\sim 0.1mW$/channel. Budgeting for some power absorbed by the SEED (say 50%) incident power, then SEED dissipated power is 1.1mW/Gbaud. However, if the optics are not efficient, one would need high power incident on the SEEDs and they could easily consume several mWs/Gbaud.

The SEED technology is relatively mature, but VCSEL technology is catching up with SEEDs in both the essential areas: device integration and device performance. A major issue being addressed at UCSB is the monotlithic integration of VCSELs and photodetectors in a manner compatible with flip-chip bonding to driver circuitry. A novel way to do this which Duane Louderback and I came up with is to use lateral oxidization of AlGaAs to create a high reflectivity bottom mirror while leaving un-oxidized an adjacent mirror to be used as part of a resonant cavity photodetector. (See Figure 1-7.) Although the oxidation dramatically changes the refractive index (from ~ 3 to ~ 1.6), it is possible to design the layers in such a manner that the resonant wavelength of both structures is the same.[2] The other "nice" features about this design are that it requires no regrowth, and it uses substrate coupled lasers/detectors so the devices can easily be flip-chip bonded. Many more details about the design and its successful measured performance will be described in Duane's thesis.

---

2 Note there is no way to make the optical thickness of a period $\lambda/2$ in both cases, but the out of phase reflections can be kept away from the cavity.
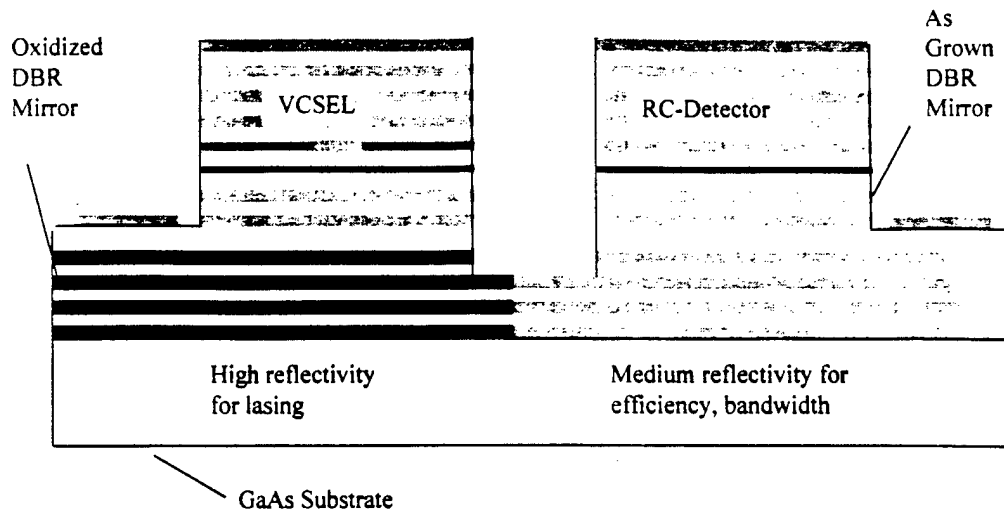
Figure 1-7: Technique for monolithic integration of Vertical Cavity
Lasers and photodetectors - a key step needed for creating a
VCSEL-based interconnect architecture

Aside from easy integration with other components, it is also necessary for a VCSEL/Detector based interconnect scheme to reduce the power consumption at a given data speed in order to be competitive with an electronic solution. This is a major issue being addressed in thesis. As we will describe in the next chapter, improved wall-plug efficiency at lower power and improved modulation current efficiency can be achieved by scaling the size of the device, provided one can remove prohibitive parasitics like optical scattering losses and current/carrier leakage. The major thrust of this work is to characterize and remove these parasitics through improved design of the oxide apertures in VCSELs. The drive power requirements for VCSELs in these systems obviously depends upon the receiver sensitivity and the what fraction of power is expected to be lost through the optical system. However, the results from this work imply that if the average output power of the laser is around 100-200μW (which is plenty, if the receiver can get it all), then the power consumption will be around 0.5-1mW which is comparable to the power consumed by SEEDs.

VCSEL Characteristics for free-space interconnects:

As discussed above, the wall-plug efficiency of a VCSEL at low powers (total consumption <1mW) is very important to be able to compete with an electrical solution and with alternative modulator based interconnects. Also it is necessary for the VCSEL to be able to operate a high-speed (~GHz) at these low powers. But with improvements to the design (namely, thin oxide apertures), that the work presented here helped motivate, the 3μm diameter VCSELs of Brian Thibeault demonstrated -3dB frequency of 4GHz with only 50μW output power[30]! Thus, properly scaled small devices should have no problem reaching Gbit/sec transmission at low power.

In addition to power and speed requirements, the VCSEL should be single mode not only to avoid mode competition noise but also to avoid optical crosstalk as the mode is sent through the collimating optics. Further one would like the operating voltage to be well under 3V so that it could be directly driven by lower voltage CMOS circuits. Smaller VCSELs have higher resistance, but the lower output power required helps reduce the drive voltage. In addition, if the VCSELs are flip-chip bonded directly to driver circuitry then matching issues with transmission lines forcing the need for ~50Ω dynamic resistance is not as critical. The threshold naturally needs to be low for higher wall-plug efficiency at lower output power, and low-threshold is definitely desired to reduce the quiescent current. As we will discuss in Chapter 6, the optimized single-mode VCSELs presented here with a wall-plug efficiency of 20% at only 150μW output power are presently the state of the art in terms of meeting these requirements, but even further progress is desired for this application.

Data Rate	1-2 Gbit/sec
Laser Electrical Input Power	As low as possible < 1mW
Peak Optical Power	1-2mW
Resistance	not critical (so long as V<2.5volts)
Drive Voltage at operating power	<2.5 volts
Threshold	optimized for min operating power

Modal Characteristics	single-mode

Table 1-1: Desired Characteristics for VCSELs used in free-space interconnects

VCSELs for Printing

Just as we have seen density considerations drive the need for improved smaller VCSELs in communication, we can see the a similar trend in laser printing. In desktop and some larger scale laser printers, the laser and mirrors for deflecting the beam essentially replace the flashlamp and focusing optics in a photocopy machine. (Note: There are other types of laser printers which require high power lasers for thermal dye ablation/transfer or for exposure of photographic silver halide materials[31]) For background, the xerographic process is shown in Figure 1-8. The key component in the process is photoconducting material which behaves as an insulator in the dark, but a conductor in the light. This photoconductor on the drum is first charged electrically, then laser light is used to selectively make the photoconductor conductive so that it will discharge to the lower potential drum. The remaining charged photoconductor on the drum then picks up toner which is subsequently fused to the paper. Further details of this process can be found in [32].

Let us now consider the fundamental power and speed issues. Suppose we have a given dot density on the photoconductive drum, which dictates the number N_D of dots per page and it takes an energy E_D to expose one dot to make it conductive. The time, t_P to expose a page is given by:

$$t_P = \frac{N_D E_D}{P_{TL}} = \frac{N_D E_D}{N_L A_L P_D} \qquad (1\text{-}13)$$

where P_{TL} is the total power from the laser or lasers which is not lost by focusing optics. N_L is the number of lasers, A_L the area of a laser beam and P_D the fraction of the power density from a laser which is not lost by focusing optics. This analysis assumes that the exposure process is not limited by the transit time of the charge to ground and no non-linear optical effects are taking place and should work for photoconductor exposure times $(t_P/N_D/N_L)$ from 3μsec to 1sec[32]. From the right side of Eq. (1-13) we see that we can

decrease the exposure time by increasing the total optical power which can be done either by adding more beams at the same power (to simultaneously expose different dots) or increasing the power from a single beam.

(5) Hot Fuser Rolls to stick toner to paper

(1) Electric field to charge photoconductor

New Paper

(2) Laser Beam Selectively Illuminates Photoconductor to discharge it

(4) Electric field to transfer charged toner to paper

Rotating drum with photoconductor

(3) Toner in carrier deposited on charged photoconductor
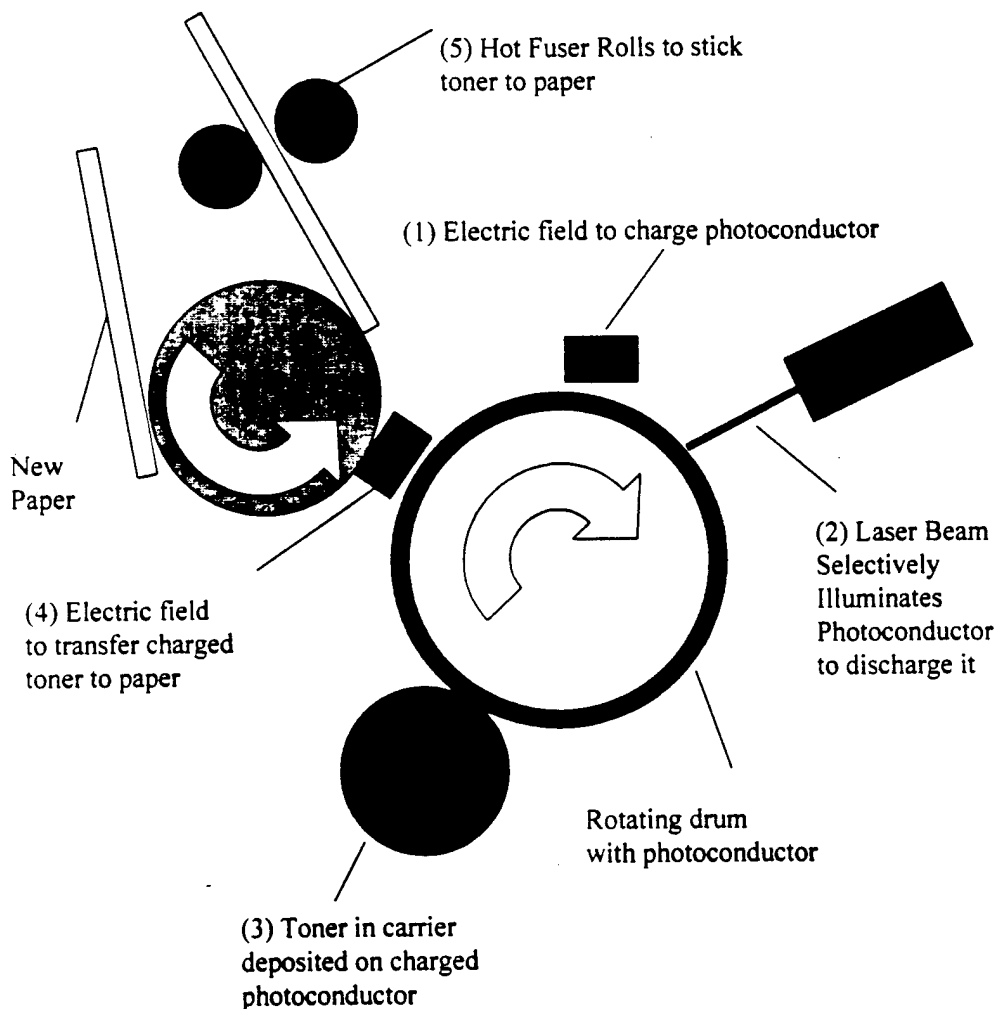
Figure 1-8: Schematic of the laser printing process (adapted from [32])

If one increases the power from a single beam the scan speed of the beam across the page must be increased. The beam is typically scanned across the page using a rotating mirror (or actually several mirrors on the outside of a polygon - See Figure 1-9). Higher scanning speeds require higher priced motors. Consequently, even being able to use two or four lasers is a major cost savings. (Two element arrays are already in manufactured printers.) The

extreme approach that Xerox hopes to take is to use an array of ~14,000 lasers with one for every dot across the width of a page. In that case no motorized scanning mirror is required.[33] One advantage that we will discuss in the next chapter is that properly scaled smaller lasers can reach a higher power density than larger ones. So if one can increase the number of lasers to compensate for the reduction in area, then one will have more total power (which is an equivalent measure of print speed).

Laser(s)+Optics

More optics

Rotating
Polygon mirror

Rotating drum with photoconductor
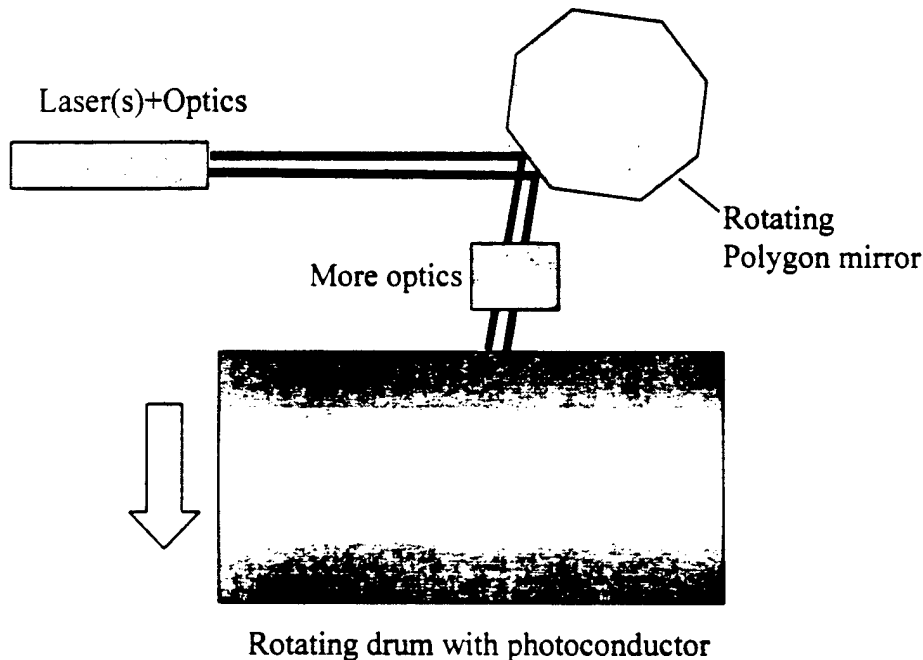
Figure 1-9: Scanning mechanism in a laser printer - a side view of Figure 1-8. (Adapted from [33])

The actual amount of power necessary also depends upon wavelength and the photoconductor used, and generally the materials are more sensitive to visible rather than infrared light (wavelengths <800nm are required), but using an energy density typical in the red of $10mJ/m^2$[32], then to print one 8.5"x11" page in one second would require 0.6mW. Of course, this power can be an order of magnitude higher depending upon the throughput of the optics. But if an array of lasers is used then one can easily get that order of magnitude back.

The laser beam in these systems needs to be pretty clean which normally means using a single mode laser (or at least single-mode looking), but possibly

one could also use a heavily moded large VCSEL which would still look okay. Thus, to put VCSELs to use in this application means moving towards arrays of many VCSELs with relatively low power. As array size increases improvements in scaling to increase the power density and decrease the thermal load become important.

Final Comments and Summary:

A system perspective provides an understanding of where VCSELs may be employed in the future and what issues need to be addressed. But it is not always the best perspective because often times technology is more of a chicken and egg problem (i.e. which should come first) and people working on one technology (e.g. high performance optical interconnects) may have no application until another technology (e.g. packaging) improves. So sometimes it is necessary to improve a technology without an existing application, but existing needs are not a bad starting place.

In this chapter, we examined applications for both data communication and laser printing. In both cases we have seen that the scaling of VCSELs becomes important as the array size increases. Scaling the VCSEL is not so much needed to allow more VCSELs to fit in a given space as it is to minimize the thermal and electrical load of the whole array. Perhaps in the future scaling will also be needed for higher speed per channel. Figure 1-10 pictorially summarizes the different VCSEL structures to meet the different requirements.

Already proton implanted VCSELs are being employed in single channel data links to meet Gigabit Ethernet and Fibre channel standards. And soon VCSEL arrays will be available for *multichannel* higher speed links using multimode fiber over shorter distances in parallel computing applications and in phone switching centers. And moderate improvements in optical and electrical confinement through the use of oxide apertures are needed to help satisfy the requirements for these ~10 channel arrays.

Perhaps future requirements for multichannel fiber links will force further improvements in confinement for higher speed, but the most demanding

application for VCSELs is free-space optical interconnections within computers.
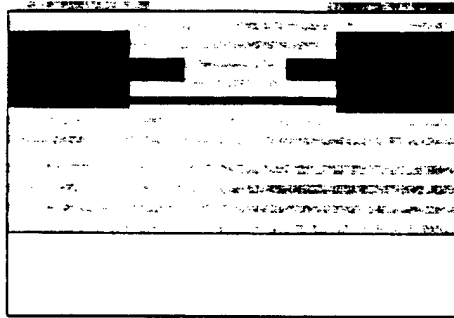
Type: Proton Implanted
Size: ~15-30μm
Modedness: Multimode
Application: Single
    channel, 1.3 Gbaud
    data links, ~10-200m

(a)
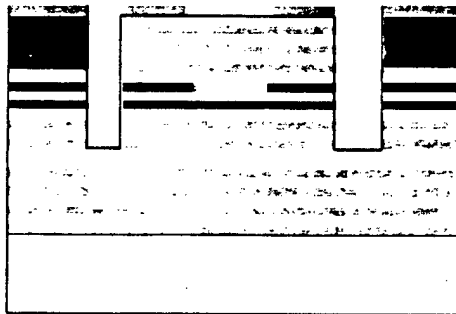
Type: Oxide Confined
Size: ~10-20μm
Modeness: Multimode
Application: Multi
    channel, 1-2 Gbaud
    data links, ~1-100m

(b)
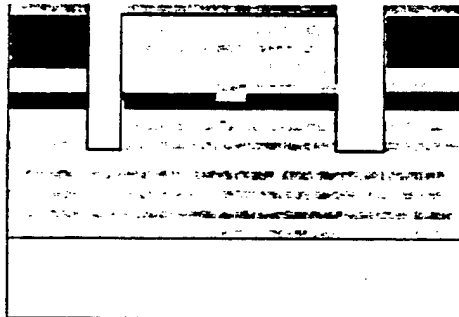
Type: High Performance
        Oxide Confined
Size: <6μm
Modedness: Single
Applications: Multi
    channel, Multi-Gbaud
    data links, <10m
    and laser printing

(c)

Figure 1-10: Summary of various VCSEL applications and an
        applicable structure. The necessary VCSEL size (and design)
        scales with application requirements. (We have ignored
        etched pillar devices since industry is already leapfrogging this
        structure in favor of planar oxide confined structures.)

The analysis of electrical interconnection vs. optical interconnection within computers suggest that with present day drive voltages for pins and board traces that an optical interconnect solution has almost a hundred-fold advantage in terms of power consumption at gigabit speeds (in terms of the power to send the actual signal), but if drive voltages are reduced to the values present in research interconnects, then electrical interconnect power consumption is on the same order as optical interconnect power consumption.

If free-space optical interconnects are to be used, then one would like to use a convenient, low-power architecture. Previously VCSELs seemed only more attractive due to packaging considerations, and SEEDs seem more attractive in terms of power consumption and the ability to integrate easily with detectors and transistors (though unattractive in terms of other packaging considerations). However, my work and my colleagues work at UCSB has helped both to improve the efficiency of VCSELs at low power (and smaller sizes as desired for single-mode operation) and to ease the integration of VCSELs and detectors making VCSELs more competitive with a modulator based interconnect solution.

Lastly, laser printing may become another application for VCSEL arrays. The power requirements per laser fall as the number is increased, driving improvements in the efficiency in single mode smaller VCSELs.

References:

[1]   E. A. Wolff and R. Kaul, Chapter 8 in *Microwave Engineering and System Applications*. New York: Wiley, 1988.

[2]   P. Bhartia, Chapter 6 Transmission Lines II in *Millimeter wave Engineering and Applications*. New York: Wiley, 1984.

[3]   R. A. Pucel, "Design Considerations for Monolithic Microwave Circuits," *IEEE Trans. Microwave Theory and Techniques*, vol. MTT-29, pp. 513-534, 1981.

[4]   D. Kuchta and C. J. Mahon, "Mode Selective Loss Penalties in VCSELs Optical Fiber Transmission," *IEEE Photon. Technol. Lett.*, vol. 6, pp. 288-290, 1994.

[5]   R. Soderstrom and K. Jackson, "New 850nm VCSELs and CD-Type Lasers Provide Interoperable Low Cost Data Links," in *Proc. LEOS '95*, Vol. 1, paper no. OPMR2.4 p. 236-7, 1995.

[6]   IEEE-LAN-MAN-Standards-Committee, "IEEE Approved Draft P802.3z," : IEEE, 1998.

[7]   S. Joiner, "Vertical Cavity Lasers for datalinks," in *Proc. LEOS Summer Topical Meeting*, paper no. WA3, p. 57,58, 1997.

[8]   J. W. Scott, "Presentation about Ciello Gigabit ethernet products," . Santa Barbara, CA, 1998.

[9]   "Cielo   Gigabit   Products,"   .   Broomfield,   CO: http://www.cieloinc.com/English/Products/Gbit_Ethernet/Gbit_Etherne t_Top.html, 1998.

[10]   R. A. Morgan, "Vertical Cavity Surface Emitting Lasers: Present and Future," in *Proc. Photonics West*, Vol. 3003, p. 14-26, 1997.

[11]   C. R. Theorin, S. P. Kilcoyne, F. H. Peters, R. D. Martin, and M. N. Donhowe, "A "Seamless Migration" to VCSEL based Optical Data Links," in *Proc. Photonics West '97*, Vol. 3003, p. 120-129, 1997.

[12]   K. Hahn and K. Giboney, "VCSEL-Based Fiber-Optic Data Communications," in *Vertical Cavity Surface Emitting Lasers*, T. Wilmsen, Coldren, Ed.: to be published, 1999.

[13]   H. Karstensen, "Parallel Optical Link - PAROLI, A Low-Cost 12-Channel Optical Interconnection," in *Proc. LEOS 95*, pp. 226-227, 1995.

[14]   M. Usun, N. Matsuura, N. Sato, M. Nakamura, N. Tanaka, A. Ohki, M. Hikita, R. Yoshimura, K. Tateno, K. Katsura, and Y. Ando, "700Mb/s x40 Channel Parallel Optical Interconnection Module using VCSEL Arrays and Bare Fiber Connectors (ParaBIT: Parallel Inter-Board Optical Interconnection Technology)," in *Proc. LEOS '97*, Vol. 1, paper no. MG2, p. 51, 1997.

[15]   Y. M. Wong and t. o. people, "Technology Development of a High-Density 32-Channel 16-Gb/s Optical Data Link For Optical Interconnection Applications for the Optoelectronic Technology

Consortium (OETC)," *J. Lightwave Technol.*, vol. 13, pp. 995-1016, 1995.

[16] L. Buckman, A. Yuen, K. Giboney, P. Rosenberg, J. Straznicky, K. Wu, and D. Dolfi, "Parallel Optical Interconnects," in *Proc. HOT Interconnects 6*, 1998.

[17] M. R. Feldman, S. C. Esener, C. C. Guest, and S. H. Lee, "Comparison between optical and electrical interconnects based upon power and speed considerations," *Applied Optics*, vol. 27, pp. 1742-1751, 1988.

[18] Horowitz, "EE271 Lecture 17: Input Output Issues ESD, Inductance, and Sychronization," . Palo Alto: http://www-leland.stanford.edu/class/ee271/, 1998.

[19] R. A. Nordin, A. F. J. Levi, R. N. Nottenburg, J. O'Gorman, T.Tanbun-Ek, and R. A. Logan, "A system perspective on Digital Interconnection Technology," *J. Lightwave. Technol.*, vol. 10, pp. 811-827, 1992.

[20] N. H. E. Weste and K. Eshraghian, Chapter 4 in *Principles of CMOS VLSI Design*. Reading, MA: Addison-Wesley, 1993.

[21] M. W. Haney and M. P. Christensen, "Performance scaling comparison for free-space optical and electrical interconnection approaches," *Applied Optics*, vol. 37, pp. 2886-2894, 1998.

[22] R. Gonzalez, B. Gordon, and M. Horowitz, "Supply and Threshold Voltage Scaling for Low Power CMOS," *IEEE J. Solid State Circuits*, vol. 32, 1997.

[23] K.-Y. K. Chang, W. Ellersick, S.-T. Chuang, S. Sidiropoulos, and M. Horowitz, "A 2Gb/s/pin CMOS Asymmetric Serial Link for High-Bandwidth Packet Switches," in *Proc. Hot Interconnects*, 171-179, 1997.

[24] K.-Y. K. Chang, W. Ellersick, S.-T. Chuang, S. Sidiropoulos, M. Horowitz, and N. McKeown, "A 2Gb/s/pin CMOS asymmetric serial link," *VLSI Circuits Symposium*, pp. 216-217, 1998.

[25] L. P. Chen, M. Y. Li, C. J. Chang-Hasnain, and K. Y. Lau, "A Low-Power 1-Gb/s CMOS Laser Driver for a Zero-Bias Modulated Optical Transmitter," *Photon. Technol. Lett.*, vol. 9, pp. 997-999, 1997.

[26] B. Madhavan and A. F. J. Levi, "Low-Power 2.5Gbit/s VCSEL driver in 0.5um CMOS technology," *Electronic Lett.*, vol. 34, pp. 178-9, 1997.

[27] A. L. Lentine, K. W. Goossen, J. A. Walker, L. M. F. Chirovsky, L. A. D'Asaro, S. P. Hui, B. J. Tseng, R. E. Leibenguth, J. E. Cunningham, W. Y. Jan, J.-M. Kuo, D. W. Dahringer, D. P. Kossives, D. D. Bacon, G. Livescu, R. L. Morrison, R. A. Novotny, and D. B. Buchholz, "High-Speed Optoelectronic VLSI Switching Chip with >4000 Optical I/O Based on Flip-Chip Bonding of MQW Modulators and Detectors to Silicon CMOS," *IEEE J. Selected Topics in Quantum. Electronics*, vol. 4, pp. 77-83, 1996.

[28] H. S. Hinton, "Progress in the Smart Pixel Technologies," *IEEE J. Selected Topics in Quantum Electronics*, vol. 2, pp. 14-23, 1996.

[29] F. A. P. Tooley, "Challenges in Optically Interconnecting Electronics," *IEEE J. of Selected Topics in Quantum Electronics*, vol. 2, pp. 3-13, 1996.

[30] B. J. Thibeault, "High Efficiency Vertical Cavity Lasers Using Low-Optical Loss Intra-Cavity Dielectric Apertures", Ph.D. Dissertation, Electrical and Computer Engineering, University of California, 1997

[31] D. Kessler, "Applications of lasers for printing," in *Proc. LEOS Summer Topicals*, paper no. FC2, p. 70, 1997.

[32] E. M. Williams, *The Physics and Technology of Xerographic Processes*. New York: Wiley, 1984.

[33] R. L. Thornton, "Vertical Cavity Lasers and their application to Laser Printing," in *Proc. Photonics West '97*, Vol. 3003, p. 112-119, 1997.

Chapter 2 :
Scaling of VCSEL Parameters

Introduction:

The major success of semiconductor lasers has much to do with the ability to scale the device size. Not only are semiconductor lasers more convenient to handle and package than much larger gas lasers, but also their smaller volume makes possible much higher direct modulation speeds and higher efficiency at lower output power. Consider that gas lasers like the CO_2 laser can have high power conversion efficiencies of 20-30%, but at output powers around several kilowatts. Typical in-plane lasers can reach such efficiencies at powers around of tens of milliwatts and the VCSELs presented in this work can reach those efficiencies at powers around hundreds of microwatts. Scaling down from a gas laser to an in-plane semiconductor laser involves both (1) shrinking the cavity length with similar reflectivity mirrors (which is possible because the increased density of atoms in a solid relative to a gas creates a much higher gain per length) and (2) shrinking the cross-sectional area (which is possible because of fabrication techniques which circumvent otherwise significant parasitics.) Similarly, fabrication of vertical cavity lasers can be viewed as another step in the continuation of scaling of the laser size. The scaling from in-plane lasers to vertical cavity lasers is again involves both (1) shrinking the cavity length (by about a factor of a hundred) which is permitted by using higher reflectivity mirrors, and likewise, shrinking the cross-section area which

is possible with improved fabrication techniques to avoid parasitics. This second step is key to improved performance, and a central topic of this thesis. In this section, we will examine the both the advantages that scaling the area has to offer and the limitations to doing so.

Ideal Scaling

In this section, we start with some very simple assumptions about laser characteristics and examine the consequences for scaling of various VCSEL parameters in order to present the benefits of ideal scaling. In a later section, we will discuss what happens to this picture when the parasitics come into play.

Slope Efficiency, Threshold current density, Diode voltage drop

Under ideal scaling, the slope efficiency (photons per electron or hole injected), η_{EX}, of a VCSEL would remain the same at all sizes and the broad area threshold current density, J_{TH} and voltage drop across the active region, V_D, would also be constant for all sizes. Thus, the threshold current, I_{TH}, would drop with R^2. These assumptions imply that there are no excess optical losses at any size, that the injection efficiency is also constant, and that there is no lateral current or carrier leakage. However, we're not assuming everything else is so perfect.

Electrical Resistance

Ideal scaling (at least in this description) still implies varying electrical resistance, R_E. For an etched pillar of radius, R_P, (as shown in Figure 2-1 for the case of $R=R_P$) the resistance will be dominated by the current transport through the pillar and vary approximately as $1/R^2$. This scaling is very detrimental to device performance even though the pillar is sometimes a convenient geometry for exotic microcavity VCSELs or those using impurity induced disordering. What is even worse is that the current must all move vertically through the structure, and as we will discuss in the next chapter, the vertical conductivity is several times higher than the lateral conductivity. For

the case of an apertured device, there is not an exact analytical form for the resistance, but for the case the aperture is flowing current into a semi-infinite region of uniform, isotropic conductivity (i.e. the pillar radius is much larger and further away), then the resistance varies as $1/R$. This scaling is not only observed experimentally for top contacted apertured VCSELs as will be described in the device results section, and but also this $1/R$ scaling is observed for intracavity contacted devices[1].

It is useful to do a bit more analysis to determine how big to make R_P-R in order to be in this $1/R$ scaling regime. Even with differing lateral, ρ_L, and vertical resistivities, ρ_V, one can determine an approximate analytic expression valid when the aperture radius is large compared to the pillar height by adding a pure vertical resistance, R_V, within $r<R$ in parallel with a lateral-vertical resistance, R_{LV}, for $r>R$. The lateral-vertical resistance is determined by assuming the radial current flow looks like flow into a bar of width $2\pi r$ and using the resistance for such flow as also determined for flow under finite length contacts for contact resistance measurements[2].

$$\frac{1}{R_E} = \frac{1}{R_V} + \frac{1}{R_{LV}} = \frac{\pi R^2}{h\rho_V} + \frac{2\pi R}{\sqrt{\rho_V \rho_L}} \tanh(\Delta R / L_{SM}) \qquad (2\text{-}1)$$

where $\Delta R = R_P - R$ and the characteristic length, $L_{SM} = h\sqrt{\rho_V / \rho_L}$. More interesting to look at is the ratio of the total resistance, R_E, to the vertical electrical resistance, R_V, through a pillar of radius R_A:

$$\frac{R_E}{R_V} = \frac{1}{1 + (2L_{SM} / R)\tanh(\Delta R / L_{SM})}$$

$$\approx \frac{1}{1 + (2\Delta R / R)} \text{ (for short oxidation)} \qquad (2\text{-}2)$$

$$\approx \frac{1}{1 + (2L_{SM} / R)} \text{ (for long oxidation)}$$

Because of assumptions we cannot expect this ratio to be that accurate, but we can use it to get a good enough idea how big to make ΔR. We see there are two length scales involved: For short oxidation, $\Delta R<L_{SM}/2$, (which is 2-4 times the pillar height), then improvement depends roughly on the oxidation depth in comparison to the aperture radius. For, say a factor of ten reduction in

resistance relative to the etched pillar, $\Delta R > 5R$. For a 3μm diameter aperture, we would need to oxidize 8μm which is still in the "short-oxidation" regime. Of course for long oxidation the improvement reaches a maximum indicated in Eq. (2-2). One must find some compromise because too long an oxidation will increase the parasitic capacitance and limit the speed of the device even though the DC resistance is lower.

For the case of 7μm high mirrors for λ=1.55μm, full three-dimensional current flow analysis of this problem has been performed by Near Margalit[3] using the ATLAS program. The results show that the rule of thumb I derived above works fine in the "short oxidation" regime, though the improvement levels out more quickly. There was little (<5%) improvement once the oxidation/etching depth ΔR was over ~15μm.
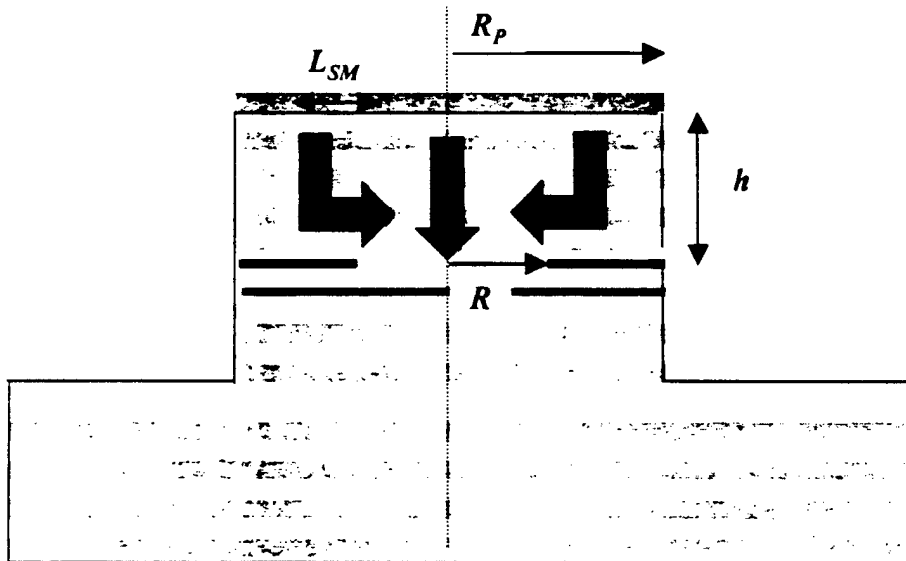
Figure 2-1: Current flow in the mirror of an apertured VCSEL.

Wall-Plug Efficiency

Given the size dependence to the resistance let us next examine the size dependent of the wall-plug efficiency under ideal scaling. Typically the peak wall-plug efficiency occurs well before thermal roll-over (because of the I^2R

term)[1] so we will put off thermal effects until the next section. The two important cases to consider are when the resistance scales as $1/R$ and as $1/R^2$. We begin by assuming a simple dependence for the voltage so the wall-plug efficiency is given by

$$\eta_{WP} = \frac{P_{OUT}}{P_{IN}} = \frac{P_{OUT}}{VI} = \frac{P_{OUT}}{(V_D + IR_E)I} \qquad (2\text{-}3)$$

We also assume a linear L-I curve so that

$$I = P_{OUT}/(\eta_{EX}V_P) + I_{TH} \qquad (2\text{-}4)$$

$V_P = h\nu/q$ is the photon voltage, P_{OUT} is the power out, and I_{TH} is the threshold current.

Let's now take a look at scaling. If one kept the output power constant, then one always must provide a minimum current even if $I_{TH}=0$. Consequently, the increasing resistance at smaller sizes (as $1/R$ or $1/R^2$) will eventually bring down the wall-plug efficiency (at a constant power). However, this simply means that peak efficiency occurs at lower powers for smaller size devices. But the scaling of this optimum operating point depends on the scaling of the resistance. In general, we can find the output power, P_{OPT} at which the wall-plug efficiency is a maximum ($d\eta_{WP}/d_{POUT}=0$). This occurs at a power of

$$P_{OPT} = \eta_{EX}V_P I_{TH}\sqrt{1 + V_D/(I_{TH}R_E)} \quad \text{(at max } \eta_{WP}) \qquad (2\text{-}5)$$

and the factor under the radical is the number of times threshold where the maximum occurs.

Case I: $R_E \sim 1/R^2$

For the case of an etched pillar without an aperture or a very short oxidation, $R_E = B/R^2$, where B is a constant independent of radius. The threshold $I_{TH} = \pi J_{BA} R^2$ scales inversely of the resistance. Then (using Eq. (2-5))the output power, P_{OPT}, where the wall-plug efficiency is a maximum also scales with R^2:

$$P_{OPT} = \eta_{EX}V_P \pi J_{BA} R^2 \sqrt{1 + V_D/(J_{BA}B\pi)} = P_{D0}R^2 \qquad (2\text{-}6)$$

---

[1] This is not true for very large devices as we see in the next section.

This implies that the peak wall-plug efficiency always occurs at a particular power density, P_{D0}, which further implies that the peak wall-plug always occurs at a particular current density, J_{D0}. This leads to the conclusion that (under this scaling of the resistance) the maximum wall-plug efficiency is constant with size! (although the power at which this maximum occurs gets smaller with size)

$$\eta_{WP}\big|_{PEAK} = \frac{P_{D0}}{\left(V_D + J_{D0}\pi B\right)J_{D0}} = \text{Indepedent of R!} \qquad (2\text{-}7)$$

Although scaling will not improve the peak wall-plug efficiency, it will improve the efficiency at lower powers.
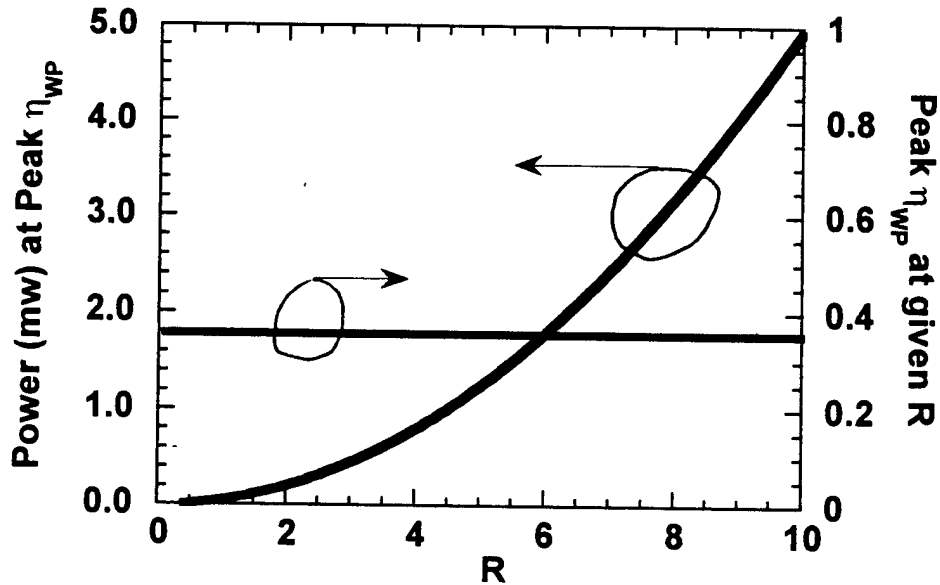
Figure 2-2: Ideal scaling (constant J_{TH}, η_{EX}) of power for peak η_{wp} and value of peak η_{wp} for the case that $R_E \sim 1/R^2$. This graph also applies conversely to give the optimum device radius for a given output power.

Another related problem to solve is to start with a given output power P_{OUT0}, and ask what is the optimum radius device, R_{OPT}, for the highest wall-plug efficiency at that output power. Here we set $d\eta_{wp}/dR=0$ and solve for R.

However, it turns out that the optimum radius is just given by inverting Eq (2-6). So the optimum radius $R_{OPT} \sim (P_{OUT0})^{1/2}$. This may seem obvious, but these problems give different answers in the next section. Figure 2-2 graphs of the scaling using some optimistic typical values: $\eta_{EX}=0.6$, $.Vp=1.26$, $V_D=1.3$, $B=5.04\text{k}\Omega\text{-}\mu\text{m}^2$, $J_{BA}=500\text{A/cm}^2$.

Case II: $R_E \sim 1/R$

When the depth of the oxidation or etching is sufficiently large, then for intracavity contacted or p-mirror contacted devices the resistance approximately follows $R_E = C/R$, where C is a constant independent of radius. We can again use Eq. (2-5) to determine the output power where the wall-plug efficiency is a maximum,

$$P_{OPT} = \eta_{EX} V_P \pi J_{BA} R^2 \sqrt{1 + V_D/(J_{BA} C \pi R)} \quad (\text{at max } \eta_{WP}) \quad (2\text{-}8)$$

At large sizes $P_{OPT} \sim R^2$ which implies the peak wall-plug efficiency occurs at some constant power density and constant current density as $R \rightarrow \infty$. But when $R_E \sim 1/R$, then a constant power and current density implies that the peak wall-plug efficiency falls off as $\eta_{WP\text{-}PEAK} \sim 1/R$ for large R.

The other extreme is $R \rightarrow 0$, and we see that $P_{OPT} \sim R^{3/2}$. Turning the crank further, we find that

$$\eta_{WP}\big|_{PEAK,R\rightarrow 0} = \frac{\eta_{EX} V_P}{V_D + \sqrt{V_D C J_{BA} \pi R}} \quad (2\text{-}9)$$

Unlike the case for $R_E \sim 1/R^2$, the peak wall-plug efficiency actually increases at smaller sizes and eventually reaches its maximum value of $\eta_{EX} V_P/V_D$ for $R=0$.

The other problem to solve is the determine the optimum radius, R_{OPT}, for a given output power, P_{OUT0}. Because the peak wall-plug efficiency improves with smaller device radii, it actually is advantageous to choose a device of slightly smaller size such that $P_{OUT0} > P_{OPT}$ rather than use the larger size device at which $P_{OUT0} = P_{OPT}$. This is a subtle distinction, but it does make some difference. To find the operating point, we compute the combination of $R = R_{OPT}$ and P_{OUT0} which satisfies $d\eta_{WP}/dR = 0$. The scaling is indicated graphically in Figure 2-3. (As $R \rightarrow 0$, $R_{OPT} \sim (P_{OUT0})^{2/3}$.)

Regardless of the differences between these two problems, the main trends are clear. When the resistance scales as $1/R$ not only do smaller devices provide higher wall-plug efficiency at lower power, but also the peak efficiency is higher in general at lower output powers.
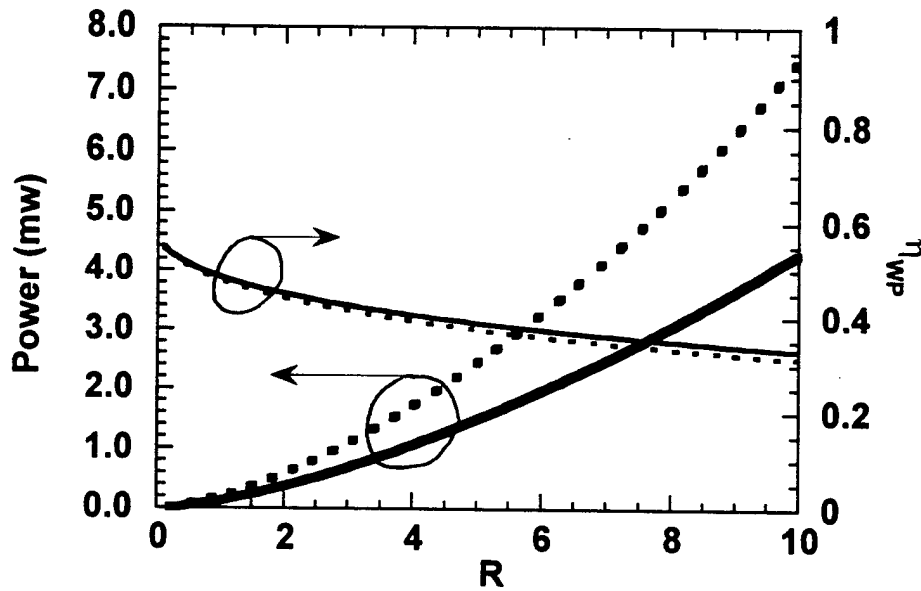
Figure 2-3: Ideal scaling (constant J_{TH}, η_{EX}) of power conversion efficiency for the case that $R_E \sim 1/R$. The solid lines indicate the power, P_{OPT}, where the peak η_{wp} occurs and its value at a given radius. The dashed lines are for the converse problem. For a given power, the dashed lines indicate the optimum radius, R_{OPT} to choose and the η_{wp} at that radius and output power (Parameters: $\eta_{EX}=0.6$, $.Vp=1.26$, $V_D=1.3$, $C=684\Omega$-μm, $J_{BA}=500$A/cm^2)

Operating Voltage

Maintaining low operating voltage is extremely important given that voltage supplies running around on circuits keep going down. Already 2.5 volts is a maximum for many applications. We know if we keep the same operating

current, as we reduce the size that that the resistance will skyrocket and so will the voltage, but if (as in the case that $R_E \sim 1/R^2$) the power density is held constant in order to keep the operating point at peak wall-plug efficiency, then the operating voltage will remain constant with size. In the case that the resistance scales with as $R_E \sim 1/R$, then the operating voltage will go down approximately as $V_D + \sqrt{V_D C J_{BA} \pi R}$ (for small R) when the power or size is set for peak efficiency. So scaling may not be so bad for the operating voltage.

Heating

So far we have ignored heating effects, but now let's examine the scaling of the temperature rise. For an etched pillar or an apertured device of radius, R, the thermal resistance will vary approximately as $1/R$ in theory and in experiment as confirmed by many others measurements of VCSELs. And the temperature rise is given by

$$\Delta T = R_{TH} P_D$$
$$= \frac{\rho_{TH}}{4R} P_{OUT} \left(\frac{1}{\eta_{WP}} - 1 \right) \tag{2-10}$$

If we keep the same output power, eventually the increasing thermal resistance will be a show stopper as size decreases, but we can ask again what happens if instead we try keep the same power density, P_D, as we would like to in order for maximum wall-plug efficiency (for the case that $R_E \sim 1/R^2$). Then, as discussed above, η_{WP} is constant with size and the temperature rise will vary as

$$\Delta T = \frac{\rho_{TH}}{4R} \pi R^2 P_D^2 \left(\frac{1}{\eta_{WP}} - 1 \right) \sim R \tag{2-11}$$

Thus, the temperature rise actually gets lower with size. This implies that if we were to include thermal roll over in the previous analysis of the wall-plug efficiency (still under the other assumptions of ideal scaling, namely, constant J_{TH}, η_{EX}), that the peak efficiency (rather than being constant for all sizes as in Figure 2-2) would drop at larger sizes.

For the other case that the resistance scales as $R_E \sim 1/R$, the math is uglier, but as R->0, then $P_{OUT} \sim R^{3/2}$ for the optimum wall-plug efficiency. Then, $\Delta T \sim R^{1/2}$. This is slightly worse scaling of the thermal drop, but it still is lower at smaller

sizes. Both cases, imply another important point: the peak power density before thermal roll-over should be higher in ideally scaled smaller devices

Modulation Speed:

The modulation bandwidth of VCSELs can be found from the relaxation resonance. For bias currents sufficiently far above threshold to insure effective carrier clamping, the frequency of this resonance is given by[4]

$$f_R = \frac{1}{2\pi}\left[\eta_i \frac{\Gamma v_g}{qV}\frac{\partial g}{\partial N}(I - I_{th})\right]^{1/2} = MCEF(I - I_{TH})^{1/2}$$

$$= \frac{1}{2\pi}\left[\eta_i \frac{\Gamma_{xy}\Gamma_{enh}v_g}{qL}\frac{\partial g}{\partial N}(J - J_{th})\right]^{1/2} \tag{2-12}$$

Provided the damping and parasitics are not too large, the 3 dB modulation bandwidth is about $1.55 f_R$. Here $V = \pi R^2 L$ is the cavity volume and Γ_{enh} is the enhancement factor, and dg/dN is the differential gain. Under ideal scaling the threshold gain does not increase at smaller sizes so the differential gain also remains constant with size. Then the modulation current efficiency factor (MCEF) increases as $1/R^2$. Essentially, this means that smaller VCSELs can reach a given bandwidth with much lower current and powers. From Eq. (2-12) it appears that scaling would have no advantage for the maximum -3dB bandwidth. However, the lower heating at given power or current density from in smaller devices means that they will be able to reach a higher J-J_{TH} before the gain increases the differential gain drops due to heating.

Eventually, we might have to worry about scaling to smaller size and lower power because of the shot-noise limit since the noise floor RIN~$1/P_{OUT}$. However, around 100μW, this is typically not a concern.

Yield

Device yield is limited by many different process parameters, but for VCSELs, much of the engineering is done in the growth and laser performance is less related to process control than say for DFB lasers in which the mirrors are formed lithographically. At smaller sizes precise control over the area of the

device becomes much more important, but let us assume for the moment that it is possible to have precise control over the area of the device, then the yield for an array of VCSELs is limited more by the defect density, ρ_D, on the wafer. In that case the probability of a given number of failures is a Poisson random variable[5], and the yield, Y, for an array of N devices is found from $Y = 1-$ {probability that at least one device has defects in the active region} and is given by:

$$Y = \exp\{-\rho_D \pi R^2 N\} \qquad (2\text{-}13)$$

So we see that as the array size increases it is better to be using smaller devices for similar yield. This principle may also apply even without ideal scaling, but if the operating current density or temperature in the active region is significantly higher in smaller devices they will be apt to degrade more readily.

Summary of benefits of ideal scaling:

The analysis in this section has shown that despite increasing thermal and electrical resistance at smaller sizes, the device properties can improve at smaller sizes for lower operating powers if the broad area threshold current density and slope efficiency can be kept constant with size. The following table summarizes the different trends:

Parameter	Size Dependence Long Aperture	Short/No Aperture
J_{TH}	constant	constant
η_{EX}	constant	constant
R_E	~1/R	~1/R^2
P_{OPT} = Power for peak η_{WP}	~R$^{3/2}$ (as R→0)	~R^2
η_{WP} at P_{OPT}	↑ as R ↓	constant
Voltage (at P_{OPT})	↓ as R ↓	constant
R_{TH}	~1/R	~1/R
ΔT at P_{OPT}	~R$^{1/2}$ (as R→0)	~R
MCEF	~1/R	~1/R
MAX f_{3dB}	↑ as R ↓	↑ as R ↓
Yield (limited by defects)	$\exp\{-\rho_D N\pi R^2\}$	$\exp\{-\rho_D N\pi R^2\}$

Table 2-1: Scaling of VCSEL Parameters under ideal conditions of no optical, current or carrier losses

Barriers to Ideal Scaling

Although it is useful to know what improvements can and cannot be expected under conditions of constant threshold current density and slope efficiency since such potential improvements motivate the work here, in reality one must contend with parasitic optical, current and carrier losses which prevent ideal scaling. We will briefly cover each of these here before expanded coverage in later chapters.

Size Dependent Optical Scattering Losses

Perfect scaling of the external efficiency implies constant injection efficiency and constant optical efficiency, $\eta_{opt} = T_{OUT}/(T_{OUT} + L_{RT})$ where T_{OUT} is the output mirror power transmission and L_{RT} is the round-trip losses. In reality these round-trip losses are a combination of size-independent losses, L_{BA}, (due mainly to free-carrier absorption) and size-dependent excess losses, L_S (which are absent in large devices).

$$L_{RT} = L_{BA} + L_S \tag{2-14}$$

The parasitic losses can come from scattering due to imperfect sidewalls and from scattering due to modal mismatches (which happen in an otherwise optically smooth structure). See Figure 2-4. VCSELs confined by ion implantation do not have the problem of excess optical losses, but they provide essentially no optical guiding. So one cannot even confine small modes to begin with. As a result the gain required increases significantly in devices with a small implant radius. For etched pillar and index apertured devices, the modal mismatch occurs when a radially abrupt waveguide (with Bessel functions for modes) is connected with an unguided region (with Hermite Gaussian modes). The scattering loss from modal mismatch in the etched pillar structures (also called diffraction loss in this case) has been investigated theoretically by Babic[6]. Experimentally, the scattering from modal mismatch is not as severe compared to scattering from roughness at pillar sidewalls as confirmed by Thibeault's measurements on VCSELs etched to

different depths[1]. And an extensive discussion of scattering losses due to modal mismatch apertured VCSELs and experimental measurement of losses will be given in the Chapters 4 and 6. For now, let's just look at the consequences of excess losses.

(a)   (b)
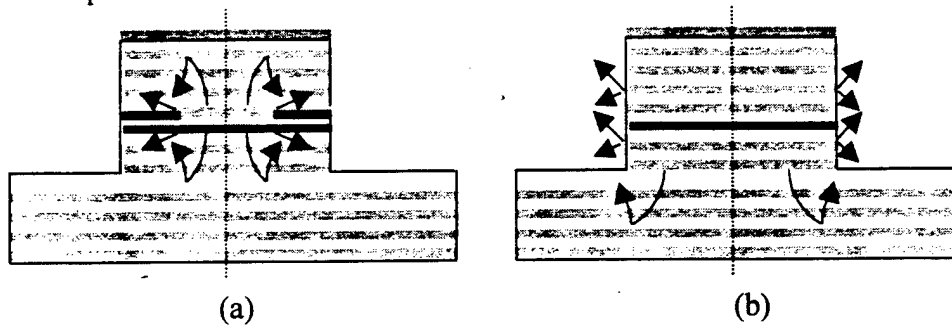
Figure 2-4: Optical scattering loss mechanisms from roughness (straight arrows) and from modal mismatch (curved arrows) for (a) an index apertured structure and for (b) an etched pillar structure. Chapter 4 provides further discussion of (a).

The excess optical losses which are a combination of these scale approximately as

$$L_S = \left(\frac{R}{R_S}\right)^{-2.7} \tag{2-15}$$

In etched pillar devices, this size dependence is measured experimentally and expected theoretically from both modal mismatch [6] and roughness [7] in etched pillars devices. (Babic estimates the size-dependence of sidewall scattering losses by examining a corrugated waveguide in [7]). For index apertured devices, the scaling law is less accurate, but still roughly true in both theory and experiment (as discussed in Chapters 4 and 6).

The key point for now is that these scattering losses increase rapidly below a characteristic radius. Once the losses turn up, other device characteristics quickly degrade. Increased losses not only mean a lower slope efficiency, but also an exponentially higher threshold ($J_{TH} \sim \exp(L_S)$). This higher current in the active region in turn leads to increased lateral leakage current and further increase in threshold.

For etched pillars the losses become comparable to the background losses, L_{BA}, below a radius around 5μm and for "traditional" index apertured devices this radius is around 2μm, but with the improvements from Brian Thibeault's and my own work the characteristic radius is now around 1μm. Figure 2-5 shows a plot modified slightly from the work of Brian Thibeault includes his devices (etched pillar and thin aperture), device from this work (tapered) and those of Phil Floyd (air-gap apertures).
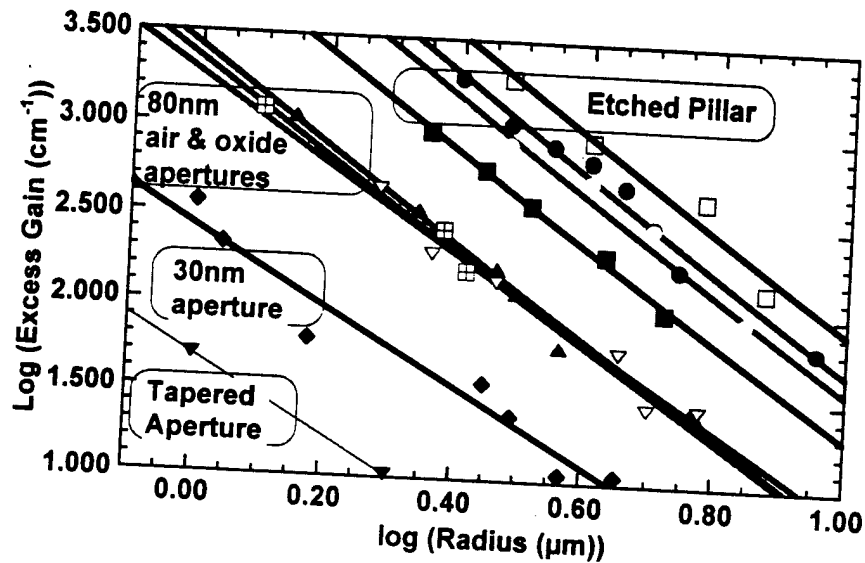
Figure 2-5: Scaling of excess optical losses (equivalently excess gain) in etched pillar and air and oxide apertured VCSELs

Lateral Current and Carrier Leakage

Even if the optical scattering losses can be removed, one still needs to confine the carriers and current going into the active region of the device. Figure 2-6 shows a cartoon of these leakage mechanisms. Typically, the leakage becomes important for devices before scattering loss does. However, the lateral current and carrier leakage has almost no effect on the gain, or the slope efficiency. So these parasitics (unlike scattering loss) do not amplify as many other parasitics.

We will discuss current spreading further in Chapter 5, but for now note that the current spreading results in an increase in threshold current that scales like

$$\Delta I_{TH} = \frac{I_o}{2} + R\sqrt{\pi J_{BA}I_o} = \text{some constant} + R(\text{some other stuff}) \qquad (2\text{-}16)$$

This scaling is very similar to the scaling of the leakage due to diffusion under the assumption of no current spreading. Since both mechanisms involve flow out the edge of the device one expects some scaling with device perimeter. Thus, it is hard to separate their effects when fitting the size dependence of the threshold current. On the other hand, this means it's easy to fit any kind of leakage current with a single size-dependence.
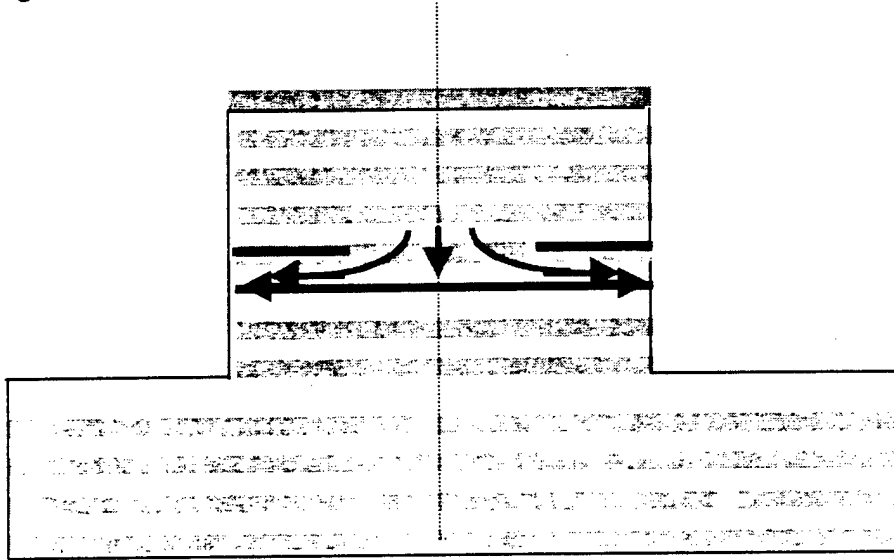
Figure 2-6: Lateral leakage from spreading of the current between the active region and the aperture and diffusion of carriers in the active region

It may appear as though current spreading above the active region would mean that above threshold one is also wasting current laterally and the injection efficiency should go down. However, the analysis in Chapter 5 and experimental evidence in Chapter 6 will show that because the diodes in the active region clamp, this is not the case. Only a small decrease in the injection efficiency is expected.

In the case that current spreading is significant then the carrier density injected into the active region already has a much smaller gradient than would exist if

current spreading were absent. Consequently, lateral carrier diffusion should be low. However, if current spreading above the active region can be eliminated then the gradient in the injected carriers is much larger so the scaling of the threshold (forgetting about optical scattering losses) is limited by the diffusion of carriers in the active region.

The scaling of the diffusion current can be found approximately from solving the equations for diffusion and recombination in the region $r>R$ which does not have any injected current:

$$I_r = -qDt(2\pi r)\frac{dn}{dr}$$

$$\frac{dI_r}{dr} = -qt\frac{n}{\tau}(2\pi r) \tag{2-17}$$

where I_r is the radial current, t is the thickness of the layer with the carrier diffusion (the quantum well or SCH thickness), D is the diffusion constant and τ is the recombination time (assumed independent of n). The equations can be rewritten in a normalized coordinate $r_N = r/L_D$, where $L_D = (D\tau)^{1/2}$. One then obtains:

$$\Delta I_{TH} = I_r(R) = qtDn(R)2\pi R_N \frac{K_1(R_N)}{K_0(R_N)} \approx qtDn(R)2\pi\left(R_N + \tfrac{1}{2}\right) \tag{2-18}$$

where $R_N = R/L_D$ and K_0 and K_1 are the modified Bessel functions of the 2nd kind. For $R_N > 1/2$, the approximate expression on the right holds although as $R \to 0$, $R_N K_1(R_N)/K_0(R_N) \to 0$. To really be accurate, one must use the correct carrier concentration at R which at small size $R \sim L_D$ may differ a fair amount from the carrier concentration in the center. However, the approximations of the recombination rate and diffusion constant being independent of n are probably bad enough that pursuing greater accuracy within this model is a moot point. The main message here is that the excess current at threshold scales roughly with R + (some constant), which is similar to the scaling of the current spreading. The other point to consider is that when reasonable diffusion constants are chosen 5-20cm^2/sec, then the diffusion current is typically much less than the current spreading assuming some average parameters. Further discussion and examples of the spreading will be given in Chapters 5 and 6.

Removing lateral carrier diffusion is a difficult problem for VCSELs which will not be addressed in this thesis. Already millions of dollars have been spent at UCSB trying to remove lateral carrier diffusion in VCSELs without major success but perhaps regrowth is the most likely candidate for solving this problem.

Impact of Optical Scattering loss and Current/Carrier leakage:

Figure 2-7 compares how the various optical and electrical loss parasitics will effect the scaling of the threshold current. Realistic numbers were chosen as detailed in Table 2-2 (e.g. the scattering loss is approximately that from an 80nm thick oxide aperture in the first mirror period), but the curves are presented mainly to show how they change qualitatively.
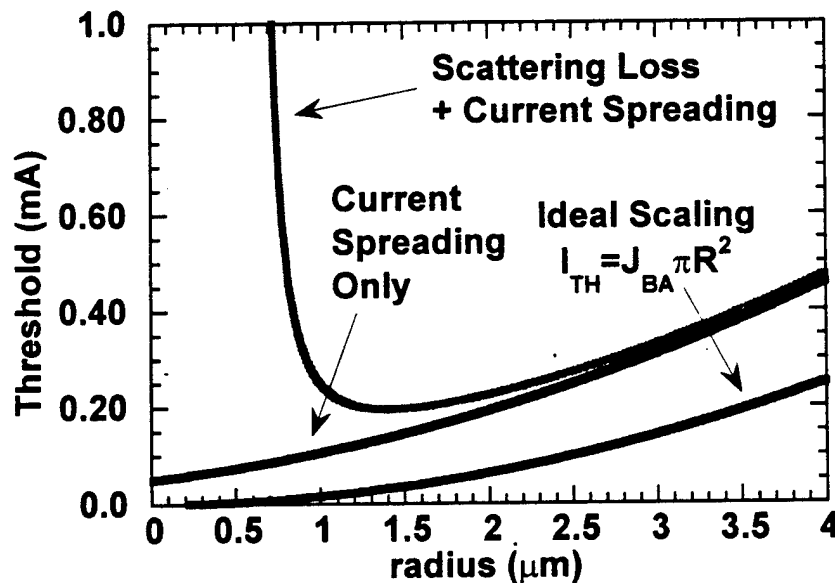
Figure 2-7: Scaling of threshold with various parasitics

For example, only excess optical losses can cause the curves to turn up at small sizes (This fact does not imply that if a measured I_{TH} vs R curve does not turn up that there are no excess optical losses, but the converse is true.)

For the wall-plug efficiency, we expect under ideal scaling that smaller devices will be better for at lower powers and that the wall-plug efficiency should be higher at lower powers (using the optimum device size) provided the resistance, $R_E \sim 1/R$. Figure 2-8 shows what happens when we have parasitics. To generate the curves, the wall-plug efficiency vs. size was calculated for a given output power, then the optimum size for a given output power and the corresponding wall-plug efficiency was found. The parameters and equations of model are pretty simple and shown in Table 2-2. The scaling of resistance is better than in the devices measured in this thesis and represents what might be characteristic if optimized carbon doping was used. The current spreading parameter was chosen to be characteristic of the best performing devices in this work. But again, let's first explain the plot qualitatively.

In general, the optimum radius is smaller as the output power is lower. But when scattering losses occur, the slope efficiency drops rapidly below a particular radius (in this case 2μm), this forces the optimum device sizes to be larger than this radius. When scattering losses are eliminated, but current spreading remains, then the optimum radius is slightly lower than the ideal case because it is still advantageous to shrink the size for lower threshold (Though resistance increases slightly over the ideal case this is less of an issue at larger sizes).

The main point to take from Figure 2-8 is that the optimum radius is <~3μm, for output powers below 1mW and that at these small sizes eliminating parasitics has a large effect on the wall-plug efficiency obtained. Essentially removing excess optical losses and reducing current spreading is important for improved efficiency at output powers <1mW. We only showed the case of $R_E \sim 1/R$; so we should remember that the ideal scaling curve in Figure 2-8b would be flat if $R_E \sim 1/R^2$.
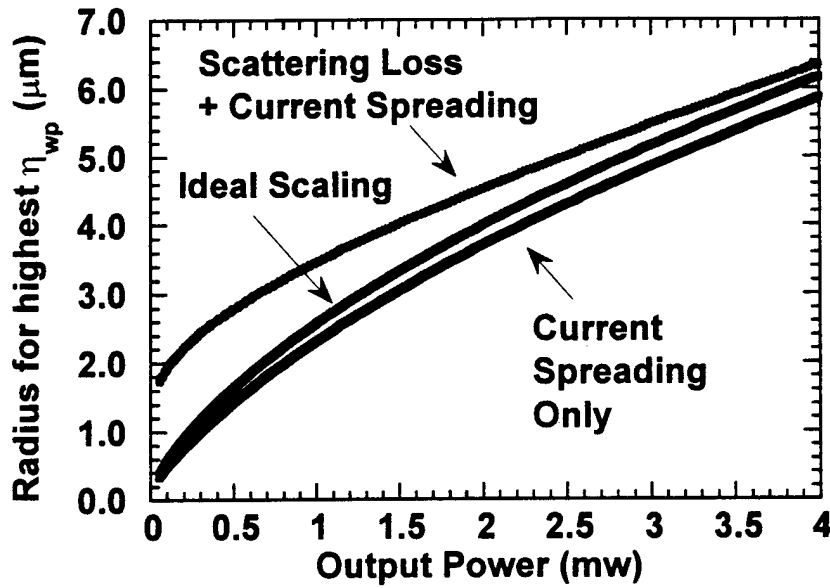
(a)
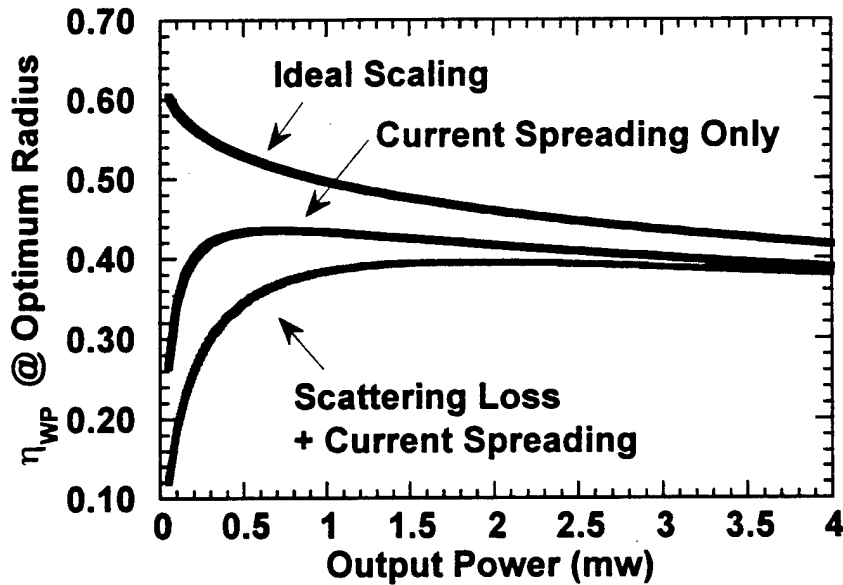
(b)

Figure 2-8: Effect of current spreading and scattering losses on the
optimum size for the highest ηwp and its value vs. power

$L_S = 0.3(\%\text{RT})\left(R/R_o\right)^{-2.7}$	$R_o = 2\,\mu m$
$J_{ACT} = J_{BA}\exp(L_S/G_o)$ $I_{ACT} = J_{ACT}\pi R^2$	$G_o = 1.06\%RT$ (for 3 - 8nm InGaAs wells) $J_{BA} = 500\text{A/cm}^2$
$I_{TH} = I_{ACT} + I_o/2 + \sqrt{I_{ACT}I_o}$	$I_o = 100\,\mu A$
$\eta_{EX} = \eta_i\dfrac{T}{T + L_{BA} + L_S}$	$T = 0.7\%\text{RT}, L_{BA} = 0.2\%\text{RT}$ $\eta_i = 0.9$
$I = P_{OUT}/\left(\eta_{EX}V_P\right) + I_{TH}$	$V_p = 1.26$
$R_E = C/R$ $V = V_D + IR_E, \eta_{WP} = P_{OUT}/\left(VI\right)$	$C = 684\Omega - \mu m$ $V_D = 1.3\text{volts}$

Table 2-2: Relations and parameters for calculations in Figure 2-7 and Figure 2-8

Resistance-Capacitance Speed Limit

A barrier to the higher modulation bandwidth expected in smaller VCSELs is their higher resistance in combination with the capacitance. However, we should note that one must consider the dynamic resistance which is affected by the amount of capacitance. Figure 2-9 shows why. Either in intracavity contacted or mirror contacted devices, the RC limit is given by the source resistance, R_S, in series with the dynamic resistance, R_D, times the dynamic capacitance, C_D .i.e. $\tau=(R_{TD}C_D)=(R_D+R_S)C_D$. If the frequency is high enough then the resistance, R_D, one encounters is pretty low, since the current will be flowing straight down to the aperture. In an intracavity contacted device there are no mirror periods to go through so the R_D at high frequency is even lower. In this case the total dynamic resistance at high frequency is $R_{TD}\sim R_S=50-$ no matter how small the aperture is. For the case of a mirror contacted pillar of radius, R_P, at high frequency the time constant τ becomes frequency independent because $(C_D\sim R_P^2)(R_D\sim 1/R_P^2 + R_S)\sim(\text{constant} + R_P^2)$. In both cases, the high frequency limit still depends on the pillar radius because of the capacitance in combination with the source resistance. Thus, reduced capacitance with thicker layers or less area is somewhat more important than reduced resistance (as far as the maximum 3dB bandwidth). Of course for

impedance matching to avoid reflections over long transmission lines, the dynamic resistance is very important.
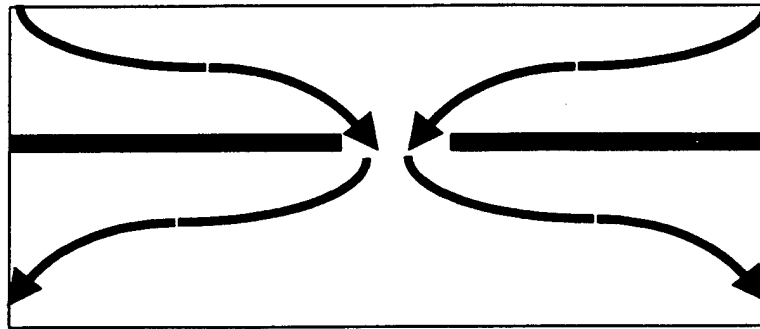
(a)
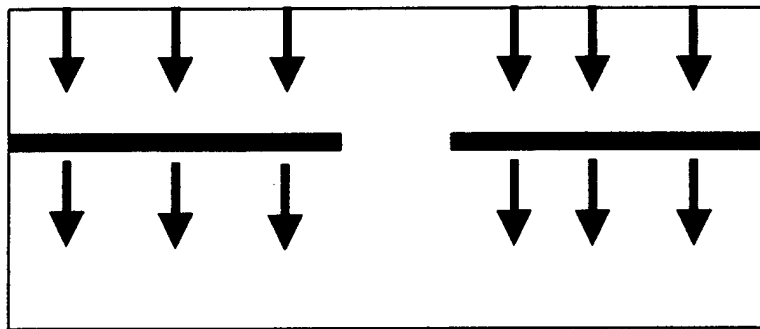
(b)

Figure 2-9: Contours of (a) DC and (b) AC current flow in an apertured structure

Conclusion:

In this chapter, we first examined what benefits one obtains by ideal scaling i.e. being able to maintain a constant J_{TH} and η_{EX} as device size shrinks. Not only is the threshold lower as size is reduced, but also the wall-plug efficiency is higher at lower powers, and even the operating voltage and operating temperature (at the optimum operating power) can be lower despite increased electrical and thermal resistance that comes with smaller sizes. Furthermore the peak power density, the MCEF and the maximum -3dB bandwidth are also

higher in smaller, properly scaled devices. Finally, when array yield depends on wafer defect density, smaller devices are advantageous.

Unfortunately, all these benefits are not realized in actual devices due to optical scattering losses, current and carrier leakage. Removing these parasitics is especially important for improved wall-plug efficiency at powers <1mW, which is needed for denser arrays for free-space interconnect schemes as described in Chapter 1.

This chapter already outlined some of the parasitics including their magnitude and their impact on device performance. However, the understanding of the effects rest upon the analysis of actual devices and the theoretical models that confirmed those hypotheses . Essentially, many of the comments made in this chapter about parasitics in apertured VCSELs would not have been possible without the theoretical and experimental analysis of the size dependence of device parameters that is to be described in the following chapters, and others analysis of their own devices using the models which have yet to be presented fully within this work.

References:

[1]   B. J. Thibeault, "High Efficiency Vertical Cavity Lasers Using Low-Optical Loss Intra-Cavity Dielectric Apertures", Ph.D. Dissertation, Electrical and Computer Engineering, University of California, 1997

[2]   R. Williams, Chapter 11: Ohmic Contacts in *Modern GaAs Processing Methods*. Boston: Artech House, 1990.

[3]   N. M. Margalit, "High-Temperature Long-Wavelength Vertical Cavity Lasers", Ph. D. Dissertation, ECE Technical Report #98-15, University of California, 1998

[4]   L. A. Coldren and S. W. Corzine, Chapter 5 in *Diode Lasers and Photonic Integrated Circuits*. New York: Wiley, 1995.

[5]   S. Ross, *A First Course in Probability*. New York: Macmillan, 1988.

[6]   D. I. Babic, Y. Chung, N. Dagli, and J. E. Bowers, "Modal Reflection of Quarter-Wave Mirrors in Vertical-Cavity Lasers," *IEEE J. Quantum Electron.*, vol. 29, pp. 1950-1955, 1993.

[7]   D. I. Babic, "Double-fused long-wavelength vertical cavity lasers", Ph. D. Dissertation, UCSB, 1995

Chapter 3 :
Vertical Design Issues

Probably the most important part of VCSEL design is not the lateral current and optical confinement method, but the design of the layer structure (in terms of the doping, layer composition, number of wells, and number of mirror periods) for improved performance of all sizes of devices. Most of the basics (i.e. figuring out mirror transmission, and the quantum-well gain model) have been covered very well elsewhere, so here we will just summarize some issues and focus on a few points not emphasized by other descriptions.

Loss and Gain

The biggest constraint in the VCSEL vertical design is the background absorption due to the doping. Typically, this value is 0.2-0.3%[1] round-trip at ~1000nm in AlGaAs mirrors with reasonable doping whether you use intracavity contacts or not. And it is difficult to change this value by any

---

[1] Dapkus's group has done a careful loss measurement in low-doped devices and obtained 0.14% round-trip loss[1], and this is also the value estimated for the best devices presented in this thesis.

significant factor. This amount of loss dictates the output mirror transmission should be 0.5-1.0% for reasonable slope efficiency, which in turn dictates the number of InGaAs quantum wells should be three in order to have enough gain (unless the device is operating at 77K, in which case, just one well is enough to provide 1% round-trip gain[2]!). For four wells the enhancement factor goes down so each well is still operating at almost the same gain per well as for three wells. These basic design issues are described well in Chapter 5 of Scott Corzine's thesis[3], Section 2.7 of Randy Geel's thesis[4], Appendix D of Jeff Scott's thesis[5], and Section 2.1 of Brian Thibeault's thesis[6].

Comment on value of absorptive loss

The absorption for GaAs at 980nm we have commonly quoted over the years at UCSB has been $11cm^{-1}$ per $10^{18}cm^{-3}$ for p-type material and $5cm^{-1}$ per $10^{18}cm^{-3}$ for n-type material for $\lambda\sim 1\mu m$[5, 7-10]. However, the p-type value is not strongly based on measurement, and I will summarize others discussion in order to question the folklore. In Chapter 5 of his thesis[3], Corzine has a scatter plot of various measured values for absorption at various doping levels. Although the values measured for n-type material suggest that an approximate linear relationship between concentration and absorption is valid and the commonly quoted constant $5\ cm^{-1}$ per $10^{18}cm^{-3}$ fits others results (including the measurements presented below of transmission through n-substrates), the absorption data for p-type material is scattered. In fact the single measured value near a hole concentration of $1\ 10^{18}cm^{-3}$ (and $\lambda=950nm$) is $17\ cm^{-1}$[11]. But this value is higher than that measured at $1.3\mu m$ which is contrary to the trend of higher intervalence band absorption at longer wavelengths (See section 4.4.1 of Babic's thesis[10]). So while the folklore value of $11cm^{-1}/10^{18}cm^{-3}$ may not have been directly measured, it isn't necessarily wrong. And at $1.55\mu m$, Babic's compilation of data does show a "clean" approximately linear trend of absorption with hole concentration at $1.55\mu m$. In any case, these values need some error bars.

Growth Tolerances

By growing a wavelength calibration sample before the laser, most MBE growths at UCSB are within ±1% of the design wavelength. (The use of

calibration samples before MOCVD growth have provided ±0.6% thickness control[12]). But occasionally due to redistribution of recently loaded source material (which seems to be more trouble in smaller hot-lipped effusion cells) or simply due to lack of source material shifts of -7% to +2% from the design wavelength can occur, if you're unlucky. Structures with shorter oxide mirrors more likely to come closer the design thicknesses (hitting the design wavelength of course depends upon oxidation conditions which are beyond the grower's control) because the cavity is grown closer in time to the calibration sample. With proper[2] white light in-situ monitoring ±0.5% thickness control is possible[6]. The control of the thickness is not only important for the lasing wavelength, but can be intolerably important for the thickness of the DBR periods away from the active region when the index step is small. Consequently, increasing the Al fraction from 70% to 90% in the top DBR helps reduce the problem of the parasitic transmission in bottom emitting structures. (And colder growth has allowed Be doping of the 90% Al layers and discussed in Chapter 6.)

The other constraint in VCSEL growth is control over the wavelength of the gain peak of InGaAs quantum wells. Typically, reproducing the desired wavelength photoluminescence is relatively easy compared to the wavelength because the same In cell temperature gives nearly the same growth rate (at least it is more trustable sometimes than InGaAs RHEED on GaAs).

Substrate loss:

While bottom emitting (through the substrate) configurations are convenient for flip-chip bonding, substrate losses can drain some of the output power in an otherwise efficient device. P-substrates are generally lossy enough[3] that they

---

[2] For the in-situ monitor to work, the light should be centered on the sample and the sample temperature must be known. Sometimes centering is difficult to achieve during the growth interruption, depending upon the angle of the substrate holder, because monitoring is normal to the surface. A more robust design would have the monitor permanently fixed outside the chamber (perhaps through ellipsometry ports) so the measurement angle and position on the substrate is fixed and only the substrate angle is adjusted.

[3] P substrates with moderate doping are difficult to obtain and those with high doping ($\sim$5e18 /cm^{-3}) transmit only 10% at λ=1μm [10].

are not even considered for substrate emitting devices, but even n-substrates have enough loss that it is desirable to avoid them and make an n-intracavity (or p-intracavity, if you grow your device p-side-down) contact. To measure the loss, one can take different wafers and examine the reflection from the bottom using a spectraphotometer. We can even examine the wafers post-VCSEL-growth (by looking at the reflection within the stop-band of the DBR) in order to characterize the material instead of contaminating good epi-ready wafers. For VCSEL epi, the reflection can be normalized to the reflection from the top of the structure. Because of the substrates' thickness and the linewidth of the spectraphotometer, the internal reflections add incoherently i.e.

$$R_T = R_1 + (1 - R_1)^2 T_S^2 R_2 \left[1 + R_1 R_2 T_s^2 + \left(R_1 R_2 T_s^2\right)^2 + \cdots \right] \qquad (3\text{-}1)$$

Adding these up, you get the following formula:

$$T_S = \left(\frac{R_T - R_1}{(1 - R_1)^2 R_2 + R_1 R_2 (R_T - R_1)} \right)^{1/2} \qquad (3\text{-}2)$$

where R_T is the total reflection from the bottom of the substrate, R_2 is the reflection from the top surface (~1 in the stopband of a VCSEL), R_1 is the reflection from the substrate/air interface and T_S is the substrate transmission (All values are power reflection/transmission coefficients.) Figure 3-1 shows what the symbols mean, and Figure 3-2 plots the relationship between R_T and T_S for the case of a R_1=0.31 and R_2=1.

The bottom line is that n-substrates only transmit 65-80% of the light depending on the doping which varies even among wafers cut from the same crystal (lower wafer numbers for wafers from MCP usually have lower doping). This transmission corresponds to an absorption of 5.6 cm^{-1} to 11cm^{-1} and this is consistent with the usual estimates for loss in n-type material given that the wafers were specified to be Si doped between 1 and 2x10^{18}cm^{-3}. On the other hand, SI wafers transmit 87%. *So you can get a improvement in slope and wall-plug efficiency of as much as 30% by using the SI substrates for bottom-emitting devices.*

$$R_T \quad\quad R_1 \quad T_S \quad\quad R_2$$

Bottom of
substrate

Top of
substrate
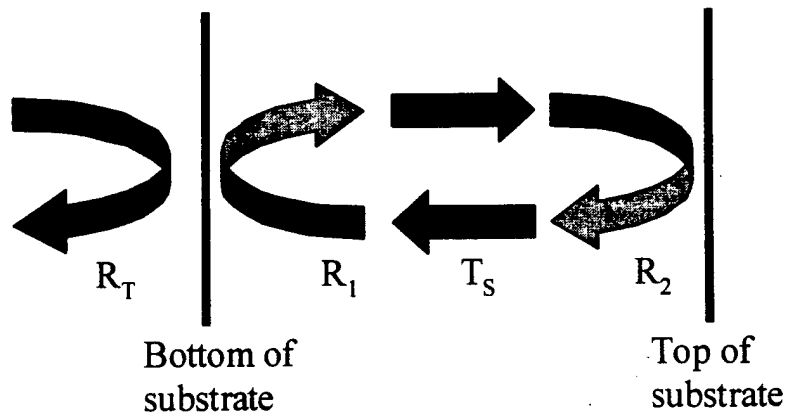
Figure 3-1: Schematic of reflections within the substrate

Contacting Scheme

Simply from the point of view of substrate loss, n-intracavity (or more generally, bottom-intracavity) contacts look attractive for bottom emitting devices. Although intracavity contacts allow one to bypass the mirrors typically one needs highly doped thick $3\lambda/4$-$5\lambda/4$ layers and these layers, if placed near the active region, add a considerable amount of loss (in addition to increasing cavity length). One can bring these layers a few periods back to avoid the loss (and avoid a longer cavity) or one can devise an intracavity contacting scheme to avoid these thick layers[4] or one can pump through the mirror. For the p-mirror (or top mirror, in general) this has the advantage that you have a big. area to contact before the current gets funneled into the aperture. Chapter 2 of Brian Thibeault's thesis has a good discussion of the trade-offs in loss and voltage for single, double, and no intracavity contacts. The analysis leads to the general conclusion that a p-top contact and n-intracavity contact will provide the optimum configuration, and in practice, devices with large area (20-50μm diameter) p-top contacts have yielded the

---

[4] Instead of only using reactive-ion etching to reach the p-intracavity contact, one could use a combination of both RIE and selective wet etching with citric/peroxide to reach the p-contact. Then a thick undoped layer can be placed above the contact layer to stop on using RIE and then the wet etch used to stop right at the top of the p-GaAs allowing use of a much thinner, highly doped layer (placed ideally at the null, if you shift the usual AlGaAs/GaAs interface)

highest wall-plug efficiencies. Although fewer have been made, p-side down VCSELs are showing comparable to better performance than n-side down[13].
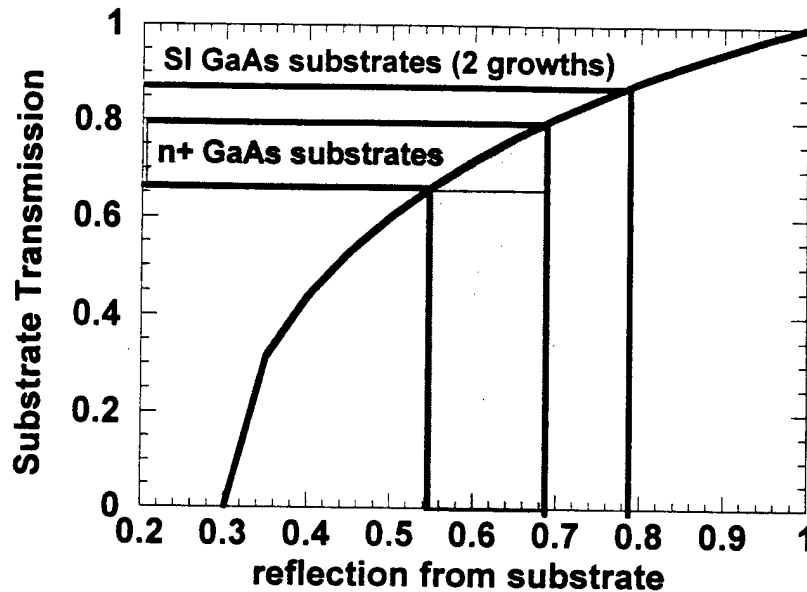
Figure 3-2: Relationship between substrate transmission and reflection from the bottom for a GaAs substrate with a top mirror of reflectivity ~1.

Because of the easier processing of p-top contacted devices, p-intracavity contacts are typically not worth the effort except in two cases: devices operating at low temperature (77K)[2] where the thermionic emission is low and WDM VCSEL arrays employing dielectric mirrors to widen the mirror stop-band (and hence) the tuning range[14]. Initial designs used in this work did not employ any intracavity contacts, simply for easier processing. But optimized designs used an n-intracavity contact which was placed a few mirror periods into the bottom DBR. (We will discuss the designs in more detail in Chapter 6.)

Mirror Doping/Grading Scheme

Lower Resistance vs. Higher Loss

A major trade-off in VCSEL design is the device resistance vs. the optical absorption. The resistance of the DBR is roughly inversely proportional to the doping (assuming you can properly engineer the interfaces to remove the voltage drop), and the loss is roughly proportional to the doping (or more precisely, to the free carrier density). So a nice figure of merit for a design might be the resistance-loss product. And it turns out to be a good one (if you can be a little generous with approximations).

Consider the wall-plug efficiency which varies with device resistance, output coupling, drive current, etc. Aside from the injection efficiency, diode turn-on voltage and photon energy, it can be shown that the rest of parameters controlling the maximum wall-plug efficiency can be wrapped up into a single parameter called the loss-voltage, V_L.[15] V_L is the excess voltage drop due to optical losses alone, and the wall-plug efficiency always increases for smaller V_L. This voltage drop is proportional to the resistance of the device and the change in threshold due to losses. But the change in threshold due to loss is linear with loss[5]. So V_L is proportional to the resistance-loss product. *Consequently, to maximize wall-plug efficiency one needs to minimize the resistance-loss product.*

Minimizing resistance and loss for the whole mirror

Assuming pumping through the mirror is employed, one needs to choose an average level of doping between the mirror interfaces and try to reduce the mirror interface resistance. The field intensity is stronger closer to the active region; so intuitively it would be better to lower the doping in this region and increase the doping for the upper mirror periods. (See Figure 3-3)

---

[5] To a first order approximation. Of course everything varies linearly to first order, but the point is that the first order term is significant.

Suppose the first five mirror periods (about equal to one mirror penetration depth, L_m) are doped (on average) at a low level and the upper periods are doped (on average) at a higher level. *What's the optimum ratio between the doping in the high doped vs. the low doped region? The answer is about a factor of three.*
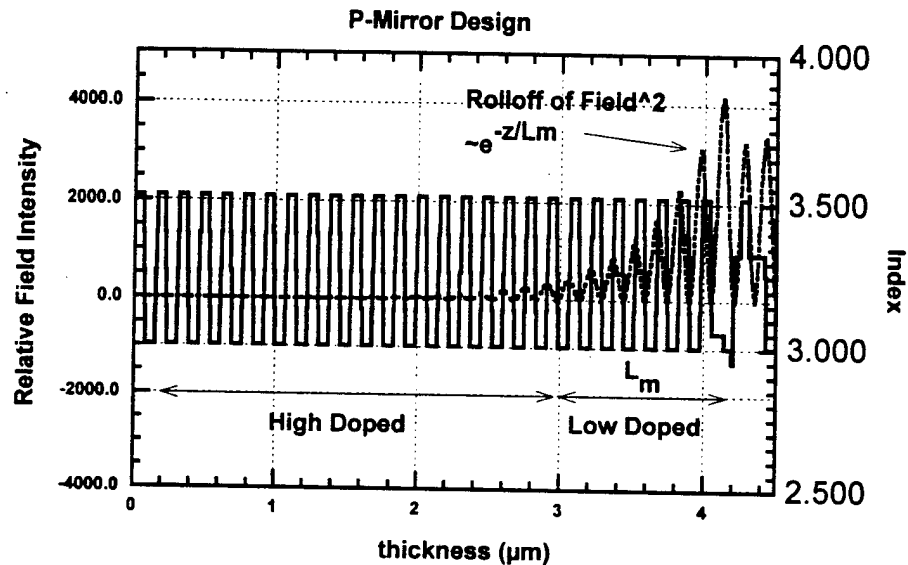
Figure 3-3: Relative field intensity in the top mirror of a VCSEL.

To deduce this factor, we will assume that we have two doping schemes for a mirror period. One design with a factor f lower resistance than the other, and we will assume the doping designs are optimized so that they have the same loss-resistance product averaged over one mirror period (This isn't a bad assumption as we'll see in the next section.)

Low Doped Region	Loss $= f^1 L_H$	Resistance$= f R_H$
High Doped Region	Loss $= L_H$	Resistance$= R_H$

Because ~2/3 of the optical power is the first fifth of the mirror, the loss-resistance product for the whole mirror is given by:

$$LR = \left[\tfrac{2}{3}(L_H / f) + \tfrac{1}{3} L_H \right]\left[\tfrac{4}{5} R_H + \tfrac{1}{5}(f R_H) \right]$$
$$= L_H R_H \left[2/(3f) + \tfrac{1}{3} \right]\left[\tfrac{4}{5} + f/5 \right] \tag{3-3}$$

The factors on the right reaches a maximum for f=3.

We can take this analysis a step further and assume we have an *arbitrary* field^2 distribution, $\Phi(z)$, and ask, if the loss-resistance product were always a constant, Ω_0, at a particular location, but you could vary the loss (or the resistance) profile what should the *relative* distribution of loss $\alpha(z)$ look like? We would want to minimize the loss-resistance-product over the whole length of the device:

$$\Omega_L = \left(\int_0^L \alpha(z)\Phi(z)dz \right)\left(\int_0^L \frac{\Omega_0}{\alpha(z)} dz \right) \tag{3-4}$$

To solve for the function $\alpha(z)$ such that Ω_L is minimized, we can use symmetry arguments to make a good guess and then use the calculus of variations to prove it. The answer is:

$$\alpha(z) = \Omega_0 / \left[+ \sqrt{\Phi(z)} \right] \tag{3-5}$$
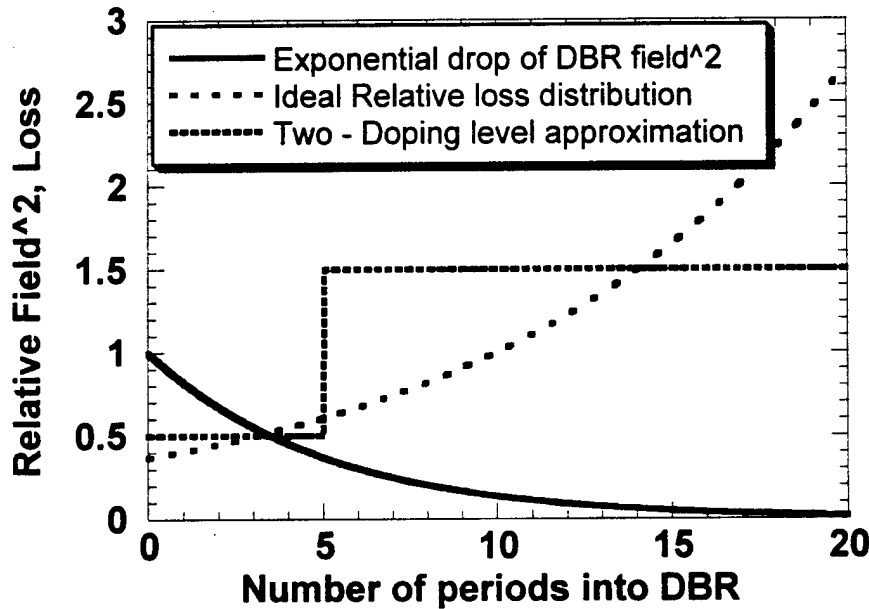
Figure 3-4: Relative Field^2 (ignoring standing-wave effects) in a DBR along with the ideal relative loss distribution for the minimum loss resistance product and a two-step approximation

For the case of a field decaying exponentially, then the relative loss should be increasing exponentially at half the decay rate or doubling about every seven to eight periods (for an AlGaAs/GaAs DBR). Figure 3-4 compares this result with the earlier two-step approximation. (Perhaps three steps would be worth the effort.) And Table 3-1 compares the relative improvement in the loss-resistance product for a mirror six penetration depths long.

Doping/Period over length of DBR	Entire Mirror Loss Resistance
Uniform	Ω_{LU}
Two-Step (Low then high)	0.78 Ω_{LU}
"Ideal" ~ exp(z/(2L$_m$))	0.66 Ω_{LU}

Table 3-1: Comparison of relative doping for the whole mirror

Another doping (or carrier) profile to calculate is for a thick section of material with uniform index (like a contact layer) with an intensity distribution, $\sin^2(kz)$. Here the doping should vary proportional to $1/|\sin(kz)|$. Of course, all our assumptions about loss vs. doping and resistance vs. doping fail at the zeros of the sine function, but we can ignore values above, say 20, and then have a useable distribution.

Aside from problems of Be dopant diffusion, the time to change dopant cell or carbon filament temperature (order of ~1 minute) makes such precise continuous variations impractical (though step variations over longer distances of ~0.1μm as in the first example are realistic). However, by using "digital" doping or by using a quickly tunable gas source for carbon doping, more fast and precise changes in doping level may be possible.

Traditional design: Minimizing resistance within a p-mirror period (Valence band engineering)

Much previous work at UCSB[7, 16] has focused on engineering a *flat* valence band around the mirror heterointerfaces with more regard for minimizing voltage than loss. Here one designs the junction with the philosophy that the potential created by the change in the doping profile should cancel the potential barrier created by the bandgap change. For a uniformly p-doped heterjunction

between GaAs and AlGaAs a depletion of holes occurs on the AlGaAs side and an accumulation of holes occurs on the GaAs side. To fix this problem, the junction is graded, extra doping is added to the AlGaAs side, and doping is lowered (or even made n-type) on the GaAs side. If the valence band were flat, the free carrier distribution would be uniform. So one designs the distribution of excess ionized dopants (The excess being the difference between the doping level and the carrier concentration - which should be uniform and equal the average concentration.) so that the potential created by these charges exactly cancels the potential change in the bands.

A now common scheme (investigated experimentally by Peters[7]) is to bi-parabolically grade the junction and use square doping profile (as we will see later in this section). One may also linearly grade the junction and use delta-doping. However, in a mirror with many periods, the use of delta-doping may create a significant disturbance to the lattice and is suspected of damaging material during high temperature anneals[9]. Straining of the lattice is worse for carbon than for beryllium[17], and is suspected of exacerbating roughness in DBR mirrors doped using a carbon-filament[7]. Thus, designs in this work did not use delta-doping.

The schemes for creating a flat-valence band generally produce a uniform carrier density. However, we know the standing-wave pattern, that this is not what we want! In addition, from the point of view of lateral conductivity, accumulations in the hole concentration are good. Intuitively we expect improvements by higher doping where the standing-wave is weakest. In the following sections, we aim to quantify what doping profiles are necessary and what improvements they make.

Loss and Resistance within a p mirror period

To compare different designs, it would be handy to use the loss-resistance product across a mirror period. However, an accurate model of the resistance is rather complicated. Programs like, SimWindows, provide one though the

assumptions are not clear and the results are sometimes suspicious[6]. On the other hand, solving Poisson's equation for the steady-state carrier, field and potential distribution is a problem more clearly defined and relatively straightforward (and can be verified by several programs). Perhaps the most simplistic model for the resistance of a mirror period, R_m, is to simply integrate the resistivity:

$$R_m = \int_0^{L_p} \frac{1}{q\mu(x)p(x)} dx \qquad (3\text{-}6)$$

where $p(z)$ is the hole concentration from the solution of Poisson's equation, $\mu(z)$ is the mobility and L_p is the length of a mirror period. At a first glance, this model appears distastefully simple. We have ignored diffusion current and the heterobarriers. But the latter claim is not quite true. The heterobarriers will cause depletion of charge (accounted for by the Poisson solver) which will appear as increased resistance. In fact, if the integral of the free carrier density is fixed, then the carrier distribution to minimize R_m (ignore mobility changes for now) is a flat carrier distribution which is created by a flat band. And if the carrier distribution is flat, then diffusion currents should be small. For the case of significant depletion (as in a p-n junction), Eq. (3-6) overestimates resistance. In fact, a p-n junction diode would have nearly infinite resistance (which is still correct to zeroth order at V=0) since the depletion region removes all the free carriers. This inaccuracy is a result of ignoring the redistribution of carriers with bias and subsequent diffusion currents.

---

[6] If one simulates a bi-parabolic grade with a doping of $p_0+\delta p$ along the parabola on the AlGaAs side and with a doping of $p_0-\delta p$ along the parabola on the GaAs side (and a doping level, p_0, everywhere else), then one can find a value for δp (call it δpF) such that the band and the carrier concentration is the flattest. One can also find the value of δp to minimize the current density SIMWINDOWs calculates at a small bias voltage across the mirror period (0.01 volts). (Call this value δpR.) When the mobility is independent of composition, then $\delta pF=\delta pR$ as expected. However, when the mobility varies with composition (but is still independent of carrier density) $\delta pR<\delta pF$. For a grade from x=0 to x=90% over 28nm with p_0=1e18cm-3, δpF = 1.5e18cm-3 and δpR=0.6e18cm-3. This might make sense if the lower mobility region is on the GaAs side (as discussed below), but the lower mobility region is in the AlGaAs. Continued on next page. And the result is not related to the direction of current flow since both up and down gradings are within one mirror period. A free drink awaits the first person who can explain this result satisfactorily.

Although Eq. (3-6) doesn't accurately model the resistance in all cases, at least, if we minimize, R_m, then the true resistance should be correlated with it.

By using the integral of the free carrier density times the standing wave,

$$\alpha_m = \left(11cm^{-1}/10^{18}cm^{-3}\right)\frac{1}{L_m}\int_0^{L_m}\left[\sin(2\pi/L_m z)+1\right]p(z)dz \qquad (3\text{-}7)$$

along with an estimate for the mirror resistance, R_m, we now have metric, the loss-resistance product, $\alpha_m R_m$, which we can use for comparison of various designs.

P-Mirror Period Designs: a comparison

In this section, we'll examine various doping/grading schemes for mirror periods and compare their loss and resistance. The simplest mirror period design is to use a linear grade and spike the doping along the grade (See Figure 3-5). For a doping step large enough for low resistance, the design suffers excess loss, and for lower doping the design has a depletion region on the AlGaAs side and excess resistance. Figure 3-6 shows the next generation of design which is to bi- parabolically grade the interfaces and use step up and down doping which coincide with the changes of the curvature of the grade. To determine the optimum step, it is important to accurately know the valence band offset. Here we used $\Delta E_v = 0.4\ E_{G\Gamma}$ [18], where $E_{G\Gamma}$ is the *direct* band-gap (between the valence and the Γ valley) not the minimum band-gap. This offset is larger than that used by Peters[7] which was based upon the minimum band-gap.

We can make a couple more improvements to the designs: adjust the doping to account for differences in mobility and increase the doping at the standing-wave nulls. *First, consider that AlAs has about a factor of three lower hole mobility than GaAs and for electrons this factor is ten!*[19]. If one has a constant total doping to distribute between two regions of equal thickness but the second region has factor of $r_2 = \mu_2/\mu_1 > 1$, higher mobility, then for minimum resistance, the low mobility region should be doped higher than the average hole concentration, $\bar{p}$, by a an amount Δp, and high mobility region should be doped lower than average, by an amount Δp, where $\Delta p = \bar{p}\left(\sqrt{r_2}-1\right)/\left(\sqrt{r_2}+1\right)$.

(a)

(b)

Figure 3-5: Plots of (a) the composition and doping profile and (b) the relative field^2 (dashed curve), and the ideal (dotted curve) and predicted (solid curve) hole concentration for a linear grade with pulse doping.

Figure 3-6: Plots of (a) the composition and doping profile and (b) the relative field² (dashed curve), and the ideal (dotted curve) and predicted (solid curve) hole concentration for a bi-parabolic grade with step doping.

Because of the root dependence, $\Delta p / \bar{p}$ does not vary rapidly. For a factor of two difference in mobility $\Delta p / \bar{p} = 17\%$, for a factor of three, $\Delta p / \bar{p} = 26\%$, and for a factor of ten, $\Delta n / \bar{n} = 52\%$ *For an arbitrary change in mobility with position, the carrier density should vary proportional to* $1/\sqrt{\mu(z)}$ *for the minimum resistance with a constant total number of carriers.* (The mathematics of the problem is very similar to the solution of Eq. (3-4).)

Second we can lower the resistance with only a small increase in loss by increased doping at the nulls. In the previous section we showed the relative loss should vary as $1/|\sin(k_0\ n\ x)|$ for when the spatial variation of the resistance is inversely proportional is the spatial variation in the carrier concentration. As discussed, this distribution blows up the nulls, but we can still use it to give us some idea of the width of the region with higher than average losses. Consider that $1/|\sin(k_0\ n\ x)| > 2$ over a region $\lambda/6$ wide and, if our dreams came true, the resistance could be made effectively zero in this region and we would expect the loss-resistance product to be cut by 33%. Figure 3-7 shows a specific design using two bi-parabolic grades with extra doping at the null. (The values for N_d and N_a assume all the dopants are active.) As seen in Table 3-2, the simulated designs with extra null doping show about a 20% reduction in $\alpha_m R_m$ over the "traditional" bi-parabolic design. As part of the optimization process, one needs to slightly adjust the AlGaAs and GaAs thickness so the grading region lies at a null. The adjustment made here was for a standing-wave with a period based on the average index. In reality, the wave period changes in the different regions. So, the thickness adjustment would have to be made based upon transmission matrix calculations of the standing-wave taking into account the other layers in the device.
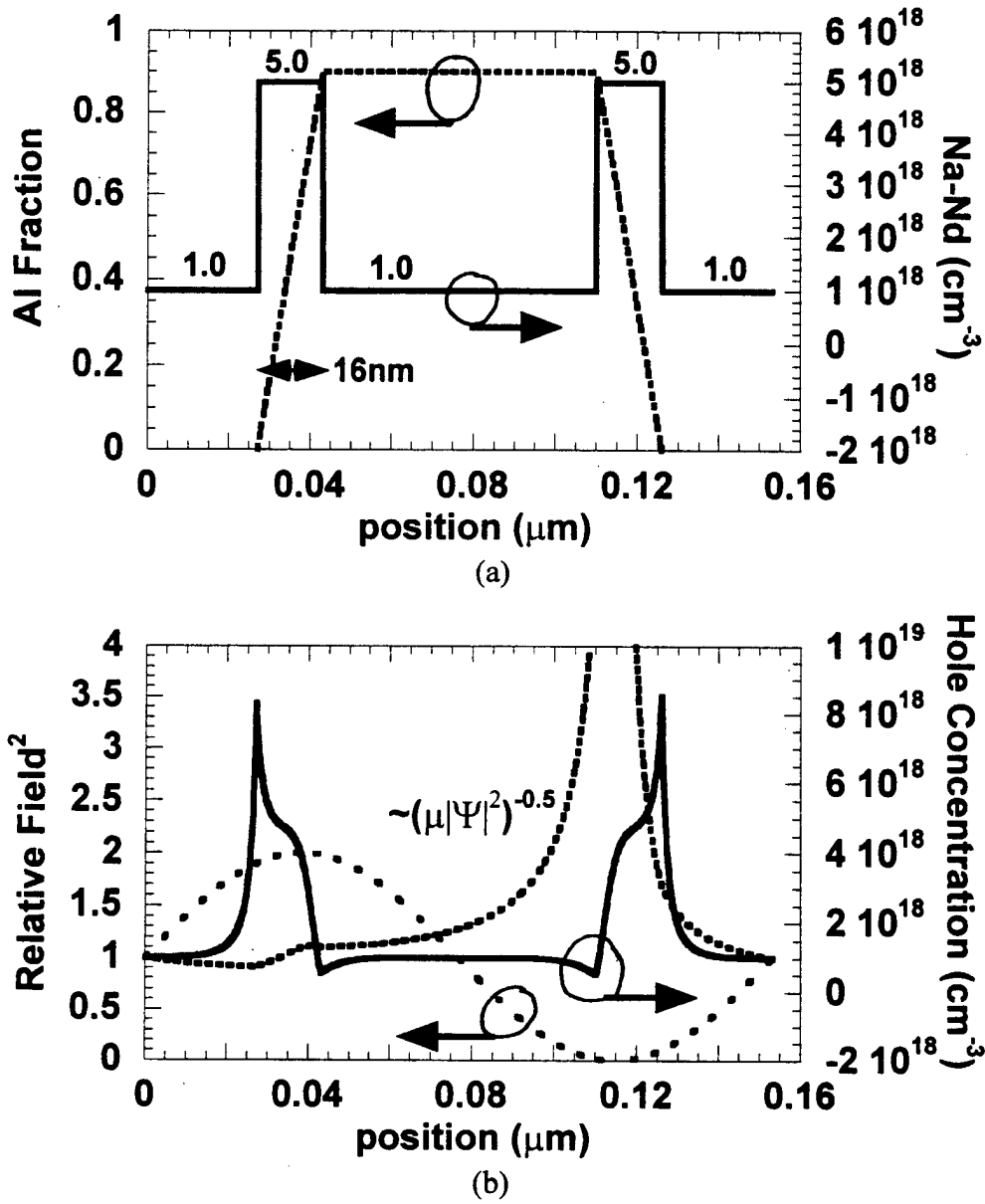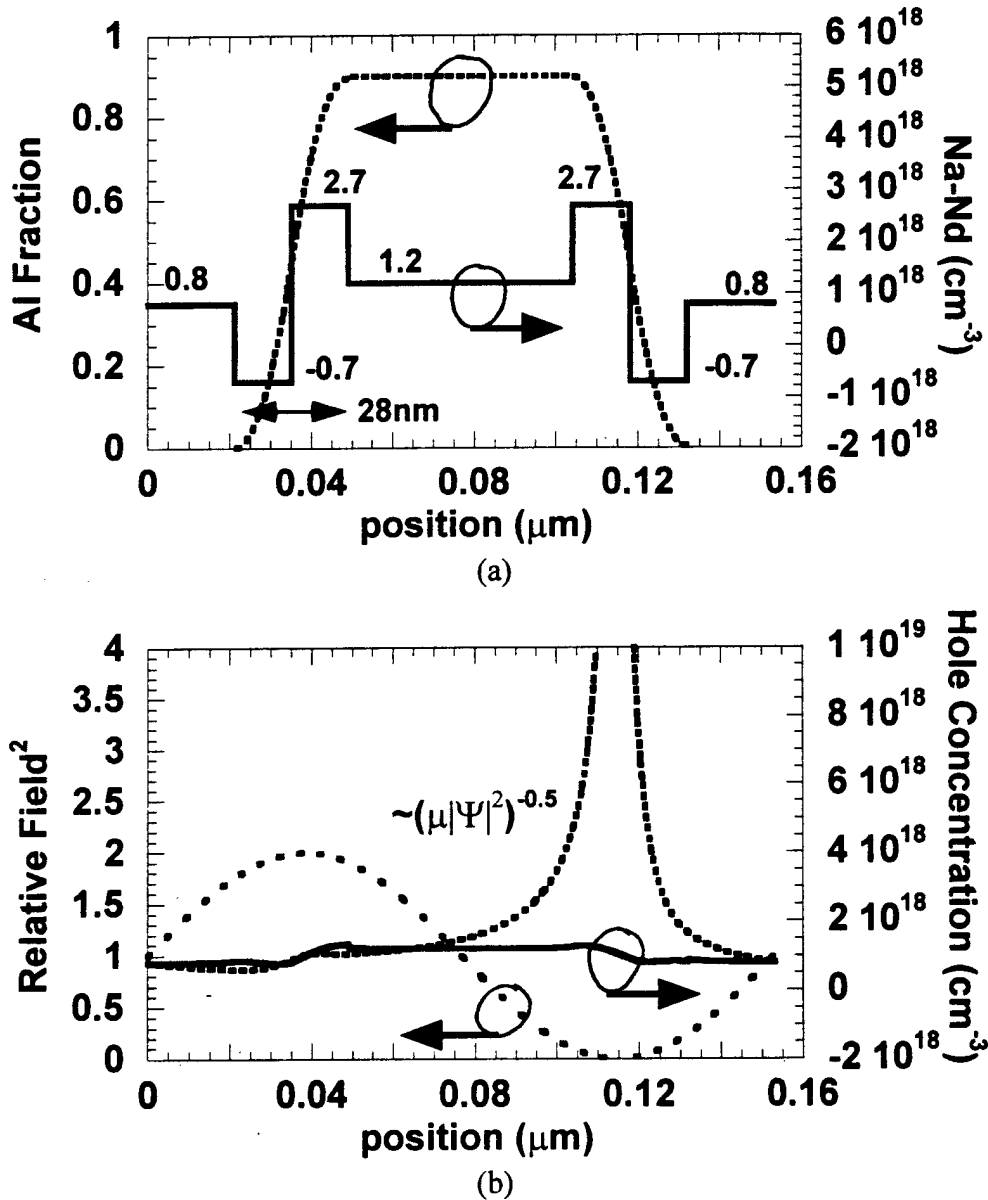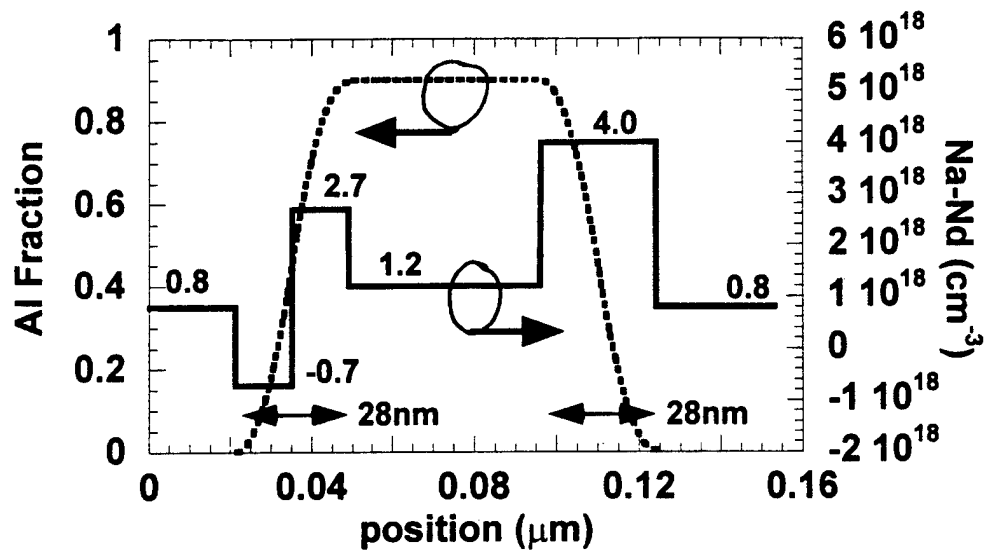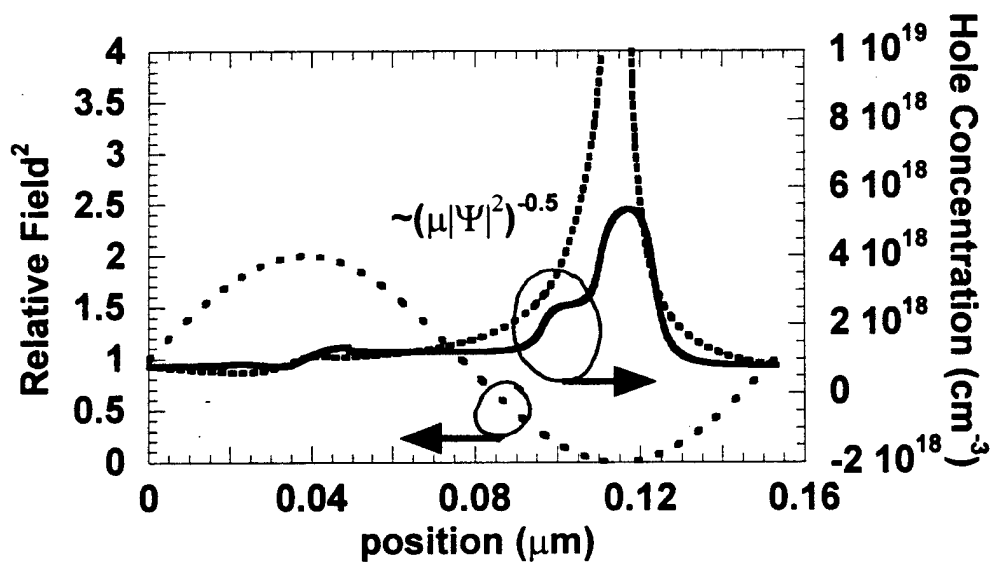
Figure 3-7: Plots of (a) the composition and doping profile and (b) the relative field^2 (dashed curve), and the ideal (dotted curve) and predicted (solid curve) hole concentration for a bi-parabolic grade with step doping *and extra doping at the null*.

Because of growth variations, the standing wave null, made not be exactly where you would like it, but fortunately, one has a fairly wide region which can still be highly doped.

The "optimal" carrier distribution given in Eq. (3-5) we have been working with was derived assuming a constant mobility, but one can also account for position dependent mobility variations, then we find the loss (or carrier density) should vary proportional to:

$$\frac{1}{\left[+ \sqrt{\Phi(z)\mu(z)} \right]} \tag{3-8}$$

(Again, $\Phi(z)$ is the field[2]). As before we have not accounted for carrier dependent mobility variations so the distribution still blows up at standing-wave nulls. But we just need to keep the doping below $\sim 10^{19}$ cm^{-3} where the higher doping generally stops buying you lower resistivity. This distribution is plotted along with the calculated carrier density for the various designs in the figures. If carriers did actually follow this distribution, then loss resistance product would be 0.95e3 Ω-cm, and this gives a benchmark to shoot for. Unfortunately, the lateral resistance is (unrealistically) zero because of the singularity.

Another popular type of grading is the uni-parabolic grade[20]. Here the idea is to grade and increase doping on the AlGaAs side of the interface where the depletion of holes usually occurs (for a uniformly doped heterojunction), but not to grade the interface on the GaAs side where the accumulation of holes would normally occur. The high accumulation of holes can also be designed in a region with no impurities to increase the lateral conductivity as in a MODFET. Figure 3-8 and Figure 3-9 show two variations on the purely bi-parabolic designs. One design has the uni-parabolic grading at the null and the other has uni-parabolic grading at both the peak and the null. The uni-parabolic grades are actually a parabolic grade over 14nm (from 90% to 45% Al) followed by a 7nm linear grade.

"High-Doped" Mirror Designs	Extra Doping @Null?	Average loss, α_m (cm^{-1})	Resistance		Loss Resistance $\alpha_m R_m$
			R_m (Ω-μm^2)	R_L (kΩ/)	
2 Linear-Grades/ Spike doping	No	20.2	103	1.8	2.08e3
2-Bi-Parabolic	No	11.2	108	4.0	1.21e3
2-Bi-Parabolic	Yes	11.5	88	2.3	1.01e3
Bi+Uni Parabolic	Yes	10.0	101	2.1	1.01e3
2-Uni Parabolic	Yes	10.0	101	2.1	1.01e3
"Ideal" Carrier	Yes	0.9e3/R_m	R_m	Zero	0.95e3

Table 3-2: Comparison of loss and resistance for various mirror period designs with approximately the same doping level (1e18 cm^{-3}). The structures doped highly at the null have nearly the same loss resistance product, but the structures with uni-parabolic grades have slightly lower lateral resistance, R_L

As with the purely bi-parabolic design, the position of the second interface is adjusted so the peak in the carrier concentration is lined up with the null. Even so, as Table 3-2 shows, the uni-parabolic designs show similar loss-resistance products to the optimized bi-parabolic design. This is essentially because the spike in the hole concentration created by the grading is relatively narrow compared to the width of the distribution that can be highly doped at the nulls.

Although the estimation of resistance per period, R_m, is meant mainly for relative comparison of different designs, the measured resistance/period[7] for the AlAs/GaAs mirrors doped on average at concentration of 1e18 cm^{-3} (and grown at a substrate temperature of 480°C for complete Be incorporation) is about a factor of three higher. Nevertheless, it should be noted that these same measurements show an almost identical resistance for a band-gap engineered structure (with average 1e18 doping) as for a pulse-doped structure (w/5e18 pulses), and this match also is calculated for the resistances of these structures in Table 3-2.

(a)

(b)
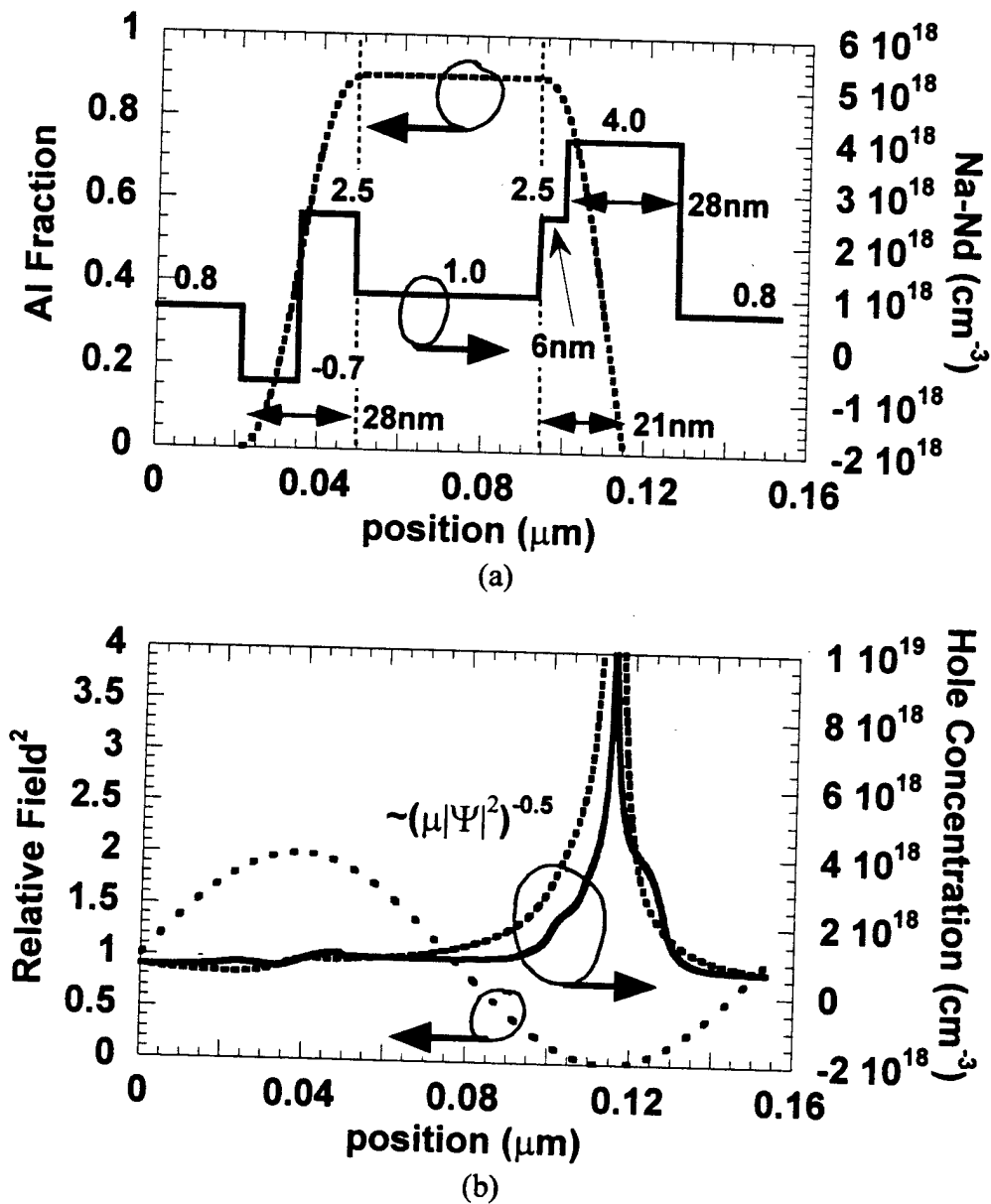
Figure 3-8: Plots of (a) the composition and doping profile and (b) the relative field[2] (dashed curve), and the ideal (dotted curve) and predicted (solid curve) hole concentration for a bi+uni parabolic grades with step doping *and higher null doping*
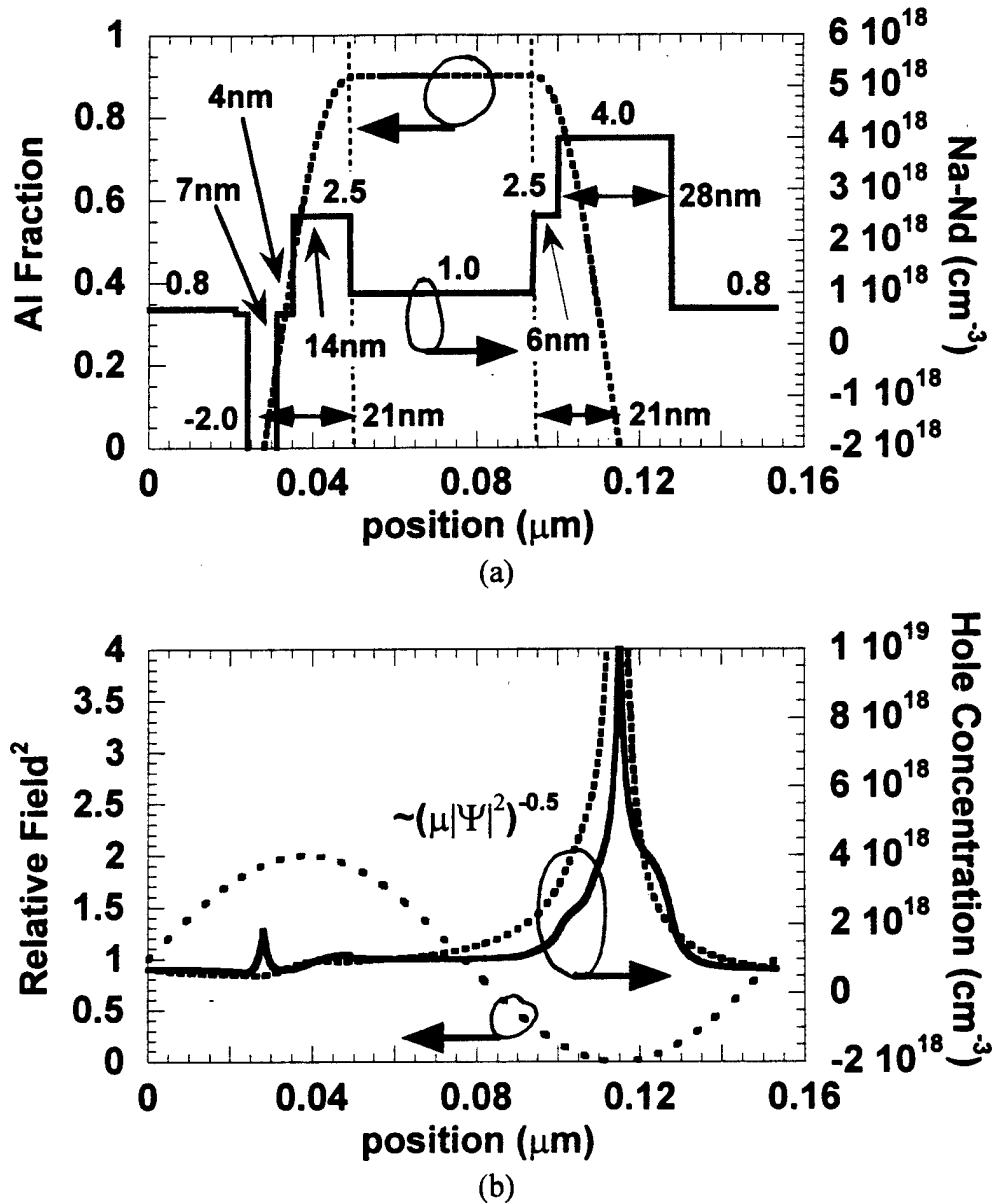
Figure 3-9: Plots of (a) the composition and doping profile and (b) the relative field² (dashed curve), and the ideal (dotted curve) and predicted (solid curve) hole concentration for two uni parabolic grades with step doping *and higher null doping*

Another issue to consider is the lateral conductivity of the various designs. (We are beginning to get into some lateral design issues, but it's unavoidable) These lateral resistances, R_L, are also shown in Table 3-2. As can been seen the better lateral resistance gives a slight advantage to the bi/uni-parabolic and uni/uni parabolic grading schemes which otherwise show about the same loss-(vertical) resistance product as for the optimized purely bi-parabolic design.

Tuning mirror period designs for different locations in the mirror

As discussed earlier in this chapter, we would like to use reduce the average doping level as the intensity in the DBR increases near the active region and increase the average doping level as the field decays towards the top of the mirror. And we can "tune" an optimized design to a new doping level simply by changing the doping in the regions of uniform composition by a scaling factor, but shifting the doping across the interfaces by a constant doping level in order to keep the doping step the same. (For example, the interface is doped at $N_A=2.7e18$ cm^{-3} on one side and $N_D=0.7e18$ cm^{-3} on the other, then this is changed to $N_A=2.3e18$ cm^{-3} and $N_D=1.2e18$ cm^{-3} to move the average doping level from 1e18 to 0.5e17). Such tuning will typically keep the loss-resistance product almost the same even with a change of loss and resistance. This is the assumption used earlier in deriving the optimized average doping profile in the DBR mirror. Table 3-3 gives two examples of a "high" doped and a "low" doped design along with the "medium" doped bi+uni parabolic design previously listed in Table 3-2. The doping and composition of the "high" doped and the "low" doped designs are shown in Figure 3-10.
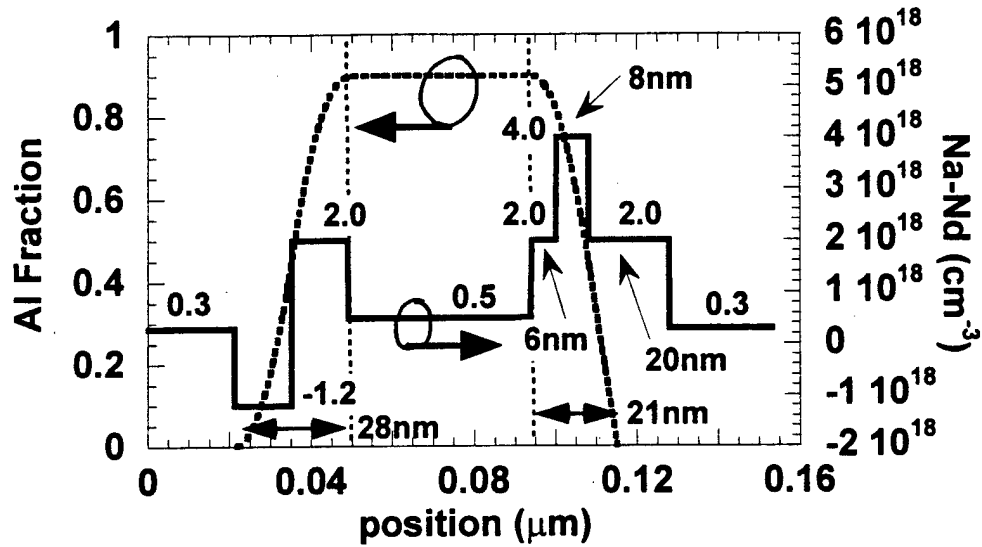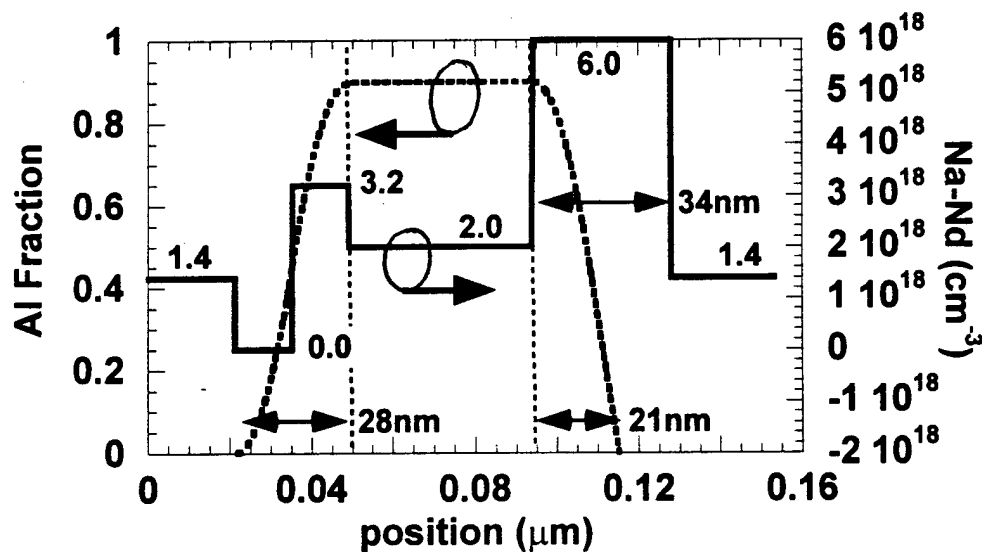
Figure 3-10: Plots of the composition and doping profile bi+uni
    parabolic grades with step doping for (a) low doped design
    and (b) a high doped design

Bi+Uni Parabolic Mirror Designs	Extra Doping @Null?	Average loss, α_m (cm^{-1})	Resistance		Loss Resistance $\alpha_m R_m$
			R_m (Ω-μm^2)	R_L (kΩ/)	
"Low Doped"	Yes	4.79	204	3.7	0.98e3
"High Doped"	Yes	19.3	52	1.25	1.00e3
"Medium doped"	Yes	10.0	101	2.1	1.01e3

Table 3-3: A potpourri of Bi+Uni Parabolic mirror period designs all with nearly identical loss-resistance products

N-mirror doping

Not as much design effort has been put into the n-mirror as the p-mirror for three main reasons (besides our own foolish consistency): (1) Electron mobility is almost twenty times higher than hole mobility (2) Typically the n-mirror is on the bottom so current can spread better than in the p (though apertures have somewhat mooted this issue), (3) The donor level in AlGaAs decreases around the direct to indirect gap transition[19] and so bandgap engineering is difficult. Consequently, we have typically employed a linear-grade with spike doping. However, the design can be improved and for n-up structures improvements are important. As mentioned, the factor of ten difference in mobility between AlGaAs and GaAs suggests the GaAs can be doped three times less. In addition, we can increase doping for periods away from the active region. Finally, we can attempt some band-gap engineering by parabolically grading on the AlGaAs side and then dropping the Al fraction directly from 60% to 20% in order to avoid any low carrier concentrations due to the DX center as successfully carried out in MOCVD grown devices[21].

Lower Loss-Resistance and Wall-Plug Efficiency

We have shown here how various improvements in design can lower the loss-resistance product. Changing the average doping of each of the mirror periods

can reduce the loss-resistance product by 22% (two-step profile) to 34% (ideal case). Adding extra doping at the nulls lowers the loss-resistance product by 20%. Making both improvements can lower the loss-resistance product by about 40-50%. Of course, lack of proper band-gap engineering of the interfaces can easily make a factor of two change in the loss-resistance product as seen back on Table 3-2. Consequently, if the dopants can be positioned correctly (via cold growth for Be or the use of carbon doping), one will see the most dramatic effect on the loss-resistance product.

But what does improving the loss resistance product mean for the wall-plug efficiency? Obviously, this depends on the power where the peak efficiency occurs and all kinds of other things. But we can assume some values and see the results. Figure 3-11 shows an example. When the loss-resistance product is reduced by 40%, the wall-plug efficiency improves by about 25% using the parameters given below. This reduction can be done either by lowering the loss, the resistance or a combination thereof, but the choice does not strongly effect the outcome. For larger changes in the loss-resistance product (factor of five), the changing of the loss or resistance does not strongly effect the peak value, but it does effect how the wall-plug vs. power behaves. For large changes, lowering resistance instead of loss will prevent the wall-plug efficiency (vs. output power) from dropping dramatically after the peak, whereas lowering loss instead of resistance will raise the efficiency for output powers before the peak.
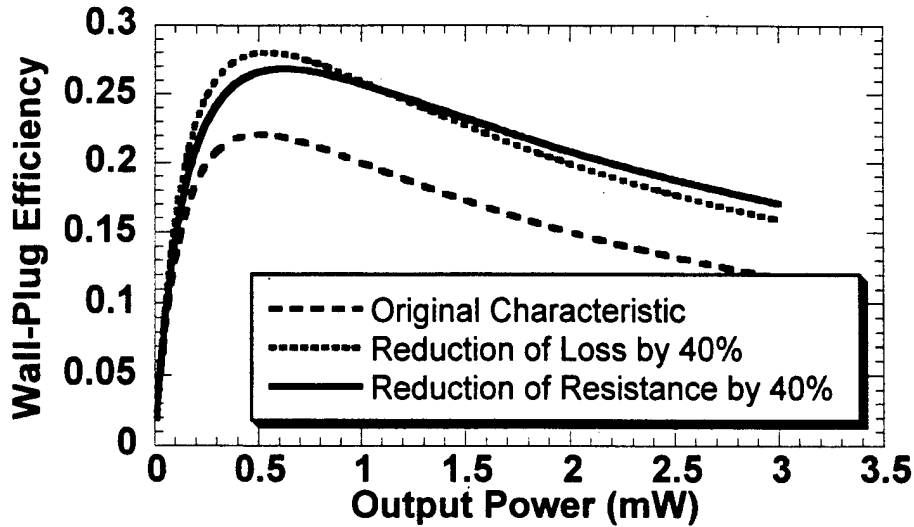
Figure 3-11: Improvement in wall-plug efficiency as the loss is lowered
or the resistance is lowered by 40%

For the curves in Figure 3-11, we assumed a 980nm VCSEL with I_{th}=0.3mA, η_{ex}= 55%, a mirror transmission, T_m=0.7%, η_i=0.9 and assumed η_{wp}=20%@1.0 mW output power and that the voltage varies linearly with current above 1.3 volts. These numbers are not too far from those for Brian Thibeault's devices[6]. We also assumed the threshold current varies exponentially with loss $I_{TH} \sim \exp(L/G_0)$ where L is the loss/round trip and G_0=1.05% for a three InGaAs quantum well active region centered on a standing-wave peak. Although we assumed a threshold, we are not accurately accounting for changes in lateral leakage current here (since we are not assuming any device radius). We are assuming that whatever leakage there is that it scales linearly with the broad-area threshold current density. As discussed in Chapter 2, lateral leakage can hinder higher wall-plug efficiency, and, in this regime, increasing the device size can quickly buy lower resistance at the same loss level without a significant change in threshold.

Doping around the aperture and active region

Lateral conductivity is very important just above (in p-up designs) the aperture and it is important to dope this region highly but one does not want significant doping between the aperture to avoid current spreading. This suggests an abrupt end to doping at the aperture. However, oxide apertures are in regions of high aluminum content and the composition will need to be graded to lower aluminum content before reaching the active region. One key issue here is doping of the grade just below the aperture. For a long growth, Be doping will usually diffuse far enough that doping the graded region will happen automatically. However, for a short growth (or when carbon is used), the graded region will not be doped. And this can create a several voltage penalty as will be further discussed in Appendix A. (See also Section 3.2.2 of Peter's thesis[7].)

Summary

The main focus of the chapter has been on improvements in the VCSEL design for higher efficiency devices at all sizes. The key points are:

- Use of SI substrates for bottom-emitting devices for a 10-30% improvement in efficiency
- Using a broad area p-contact and an n-intracavity contact for p-up devices
- Optimization of the doping in the DBRs:
- A good figure of merit that is tied to the peak wall-plug efficiency is the loss-resistance product. To minimize this product the carrier distribution should follow: $1 \Big/ \left[1 + \sqrt{\Phi(z)\mu(z)} \right]$ where $\Phi(z)$ is the field[2] and $\mu(z)$ is the position dependent mobility
- Decreased doping in the first few mirror periods for a 22-34% lower loss-resistance product
- Additional doping at the standing-wave nulls for another 20% reduction of the loss-resistance product.

- The use of a uni-parabolic grade around the nulls to improve the lateral conductivity
- An expected improvement of ~25% in the wall-plug efficiency for a 40% reduction in the loss-resistance product
- Doping above the aperture and of the grade-down from the high Al content layers of the aperture

References:

[1]   G. M. Yang, M. H. MacDougal, V. Pudikov, and P. D. Dapkus, "Influence of Mirror Reflectivity on Laser Performance of Very-Low-Threshold Vertical-Cavity Surface-Emitting Lasers," *IEEE Photon. Technol. Lett.*, vol. 7, pp. 1228-1230, 1995.

[2]   Y. A. Akulova, "Vertical Cavity Lasers for Cryogenic Optical Interconnects", Ph. D. Dissertation, ECE Technical Report #98-13, University of California, 1998

[3]   S. W. Corzine, "Design of Vertical-Cavity Surface-Emitting Lasers with Strained and Unstrained Quantum Well Active Regions", Ph. D. Dissertation, ECE Technical Report #93-09, University of California, 1993

[4]   R. S. Geels, "Vertical Cavity Surface Emitting Lasers: Design, Fabrication and Characterization", Ph. D. Dissertation, ECE, University of California, 1991

[5]   J. W. Scott, "Design, Fabrication and Characterization of High-Speed Intra-Cavity Contacted Vertical Cavity Lasers", Ph.D. dissertation, ECE Technical Report #95-06, University of California, 1995

[6]   B. J. Thibeault, "High Efficiency Vertical Cavity Lasers Using Low-Optical Loss Intra-Cavity Dielectric Apertures", Ph.D. Dissertation, Electrical and Computer Engineering, University of California, 1997

[7]   M. G. Peters, "Molecular Beam Epitaxy Growth of Vertical Cavity Lasers for Optical Communication", Ph. D. Dissertaion, UCSB, 1995

[8]   N. M. Margalit, "High-Temperature Long-Wavelength Vertical Cavity Lasers", Ph. D. Dissertation, ECE Technical Report #98-15, University of California, 1998

[9] D. B. Young, "Molecular Beam Epitaxy and Fabrication Techniques for Advanced Vertical Cavity Lasers", Ph. D. Dissertation, ECE Technical Report #96-17, University of California, 1996

[10] D. I. Babic, "Double-fused long-wavelength vertical cavity lasers", Ph. D. Dissertation, UCSB, 1995

[11] H. C. Casey, D. D. Sell, and K. W. Wecht, "Concentration dependence of the absorption coefficient for n- and p-type GaAs between 1.3 and 1.6eV," *J. Appl. Phys.*, vol. 46, pp. 250-257, 1975.

[12] H. Q. Hou, H. C. Chui, K. D. Choquette, B. E. Hammons, W. G. Breiland, and K. M. Geib, "Highly Uniform and Reproducible Vertical Cavity Surface-Emitting Lasers Grown by Metalorganic Vapor Phase Epitaxy with In-Situ Reflectometry," *Photon. Tech. Lett.*, vol. 8, pp. 1285-1287, 1996.

[13] K. L. Lear, H. Q. Hou, J. J. Banas, B. E. Hammons, J. Furioli, and M. Osinski, "Vertical Cavity Lasers on p-doped substrates," *Electron. Lett.*, vol. 33, pp. 783-784, 1997.

[14] A. Fiore, Y. A. Akulova, J. Ko, E. R. Hegblom, and L. A. Coldren, "Postgrowth tuning of semiconductor vertical cavities for multiple-wavelength laser arrays," *J. Quantum Electron.*, 1999.

[15] K. L. Lear, "Limits to the power conversion efficiency of vertical cavity surface emitting lasers," in *Proc. CLEO '96*, paper no. CThK35, p. 418-419, 1996.

[16] D. I. Babic, G. H. Dohler, J. E. Bowers, and E. L. Hu, "Isotype heterojunctions with flat valence or conduction band," *IEEE J. Quantum Electron.*, vol. 33, pp. 2195-2198, 1997.

[17] W. E. Hoke, P. J. Lemonias, P. S. Lyman, H. T. Hendriks, D. Weir, and P. Colombo, "Carbon doping of MBE GaAs and Ga0.7Al0.3As films using a graphite filament," *J. Crystal Growth*, vol. 111, pp. 269-273, 1991.

[18] W. I. Wang and F. Stern, "Valence band offset in AlAs/GaAs heterojunctions and the empircal relation for band allignment," *J. Vac. Sci. Technol. B*, vol. 3, pp. 1280-1283, 1985.

[19] S. Adachi, *Properties of Aluminium Gallium Arsenide*. London: INSPEC, the Institution of Electrical Engineers, 1993.

[20]   K. L. Lear and R. P. Schneider, "Uniparabolic mirror grading for vertical cavity surface emitting lasers," *Appl. Phys. Lett.*, vol. 68, pp. 605-607, 1996.

[21]   H. Q. Hou, R. P. Schneider, S. W. Corzine, B. E. Hammons, and S. Steward, "n-up 850nm VCSEL arrays with very low and uniform operation voltage for multimode fiber communications," in *Proc. CLEO '98*, paper no. CThK5, pp. 369-370, 1998.

Chapter 4 : Analysis of Index Aperture Optical Confinement

Introduction:

As described in Chapter 2, removing parasitic optical losses is critical for improved device properties at small sizes and low output powers. But do we expect such losses to be significant in devices with oxide or air apertures? And how much can we effect the parasitic loss by cavity design changes? How do apertures effect the mode in comparison to other guiding mechanisms that we understand namely, step-index uniform waveguides with Bessel functions for modes or lensed resonators with Gaussian modes?

The answers to these questions have already changed the typical aperture design in VCSELs, in part due to the analysis that follows and in conjunction with the initial experimental work of Thibeault[1, 2] and my own device results described in Chapter 6 as well as supporting experimental results of other research groups[3, 4]. Although the use of such loss models has not widely spread (except at UCSB), intuition about the aperture design has, and other research groups have converged on the same conclusions.

In this chapter, we discuss the optical guiding mechanism of index apertures which not only can be created by lateral oxidation or etching, but also by physical changes in cavity thickness. We then examine the optical losses that result from aperture not compensating for the diffraction in the laterally unguided regions of the VCSEL. We determine a semi-analytic formula for the optical losses of single, abrupt apertures in VCSELs in terms of two parameters: the effective phase shift of the aperture and the Fresnel number of the cavity. Using this formula, we estimate the losses for various VCSEL designs and use it to explain the drop or lack thereof in efficiency as the aperture closes in actual devices. We then examine losses using a more accurate iterative model that verifies the simpler estimate and allows us to examine the losses from tapered apertures and the limit on the mode size due to the drop-off in DBR reflectivity at large angles. We also present a method for estimating losses with multiple apertures and estimate the losses due to absorption.

Index Aperture Guiding

An index aperture in a cavity affects not only the mode shape, but also the gain and resonant wavelength. The refractive index of the aperture (typically air or oxide with n~1.6) is much lower than that of the semiconductor n~3. Consequently the optical path length is longer in the center of the cavity than in the region with the aperture. This longer optical path length in the center means that the aperture has a "lens-like" action that will tend to confine the mode. In principle, the lateral variation in the optical path length could be tailored parabolically creating a lens that would almost perfectly "undo" the diffraction in the unapertured regions of the laser. But even with imperfect lensing, the shortness of the cavity means the modes in an apertured structure are very similar to the modes expected from a vertically uniform waveguide. However, the small difference between the modes of a uniform waveguide and actual apertured VCSEL is mostly accommodated by lateral radiation modes even assuming no optical imperfections in the aperture. And for highly resonant structures like VCSELs a small amount of excess loss (0.1%/pass) implies a huge (~20%) fractional change in gain.

The shorter optical path length in the apertured regions of the VCSEL will mean the resonant wavelength (for a vertically travelling plane wave) is shorter in those regions. And as with any lateral optical confinement, the lasing wavelength (for a mode composed of both vertical and off-axis plane waves) will be slightly shorter than for a purely planar structure. The resonant wavelength for vertically travelling waves and for the lasing mode can be related to the effective optical path length across the aperture and the aperture diameter. The effective optical path length depends not only on the aperture thickness, but also its placement in the standing-wave inside the cavity. Let us now address all of these issues more quantitatively. In this section, we "focus" on the guiding mechanism.
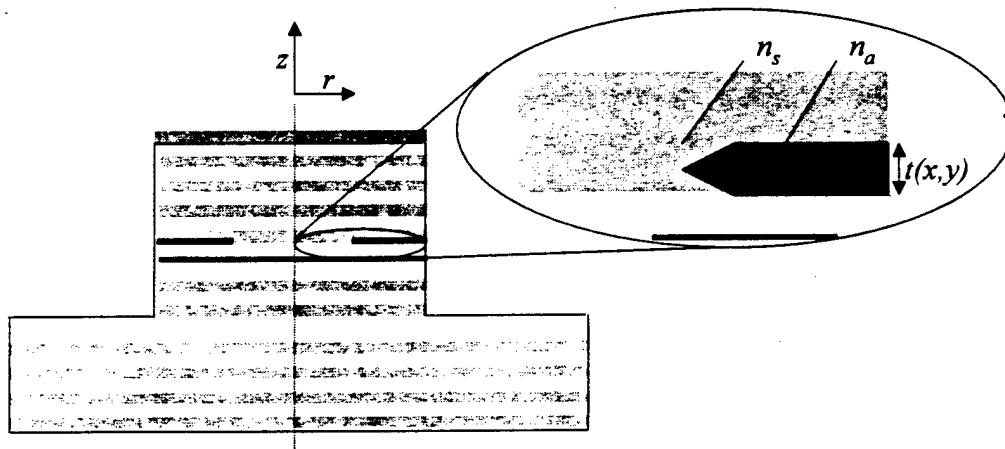
Figure 4-1: Index aperture inside a VCSEL cavity

Aperture phase shift

Shown in Figure 4-1 is a close up of an index aperture inside a VCSEL. If this aperture were not inside the VCSEL cavity (i.e. the other mirror layers were absent), we could simply say the difference in the phase shift between the apertured and unapertured regions of the VCSEL, is given by:

$$\phi(x,y) = k_0 \Delta n [t_{max} - t(x,y)] \qquad \text{(no reflections)} \qquad (4\text{-}1)$$

where k_0 is the free-space wavenumber, $\Delta n = n_s - n_a$ is the difference between the semiconductor index and the index of the aperture, $t(x,y)$ is the position dependent thickness of the aperture, and t_{max} is the maximum thickness of the

aperture. We have chosen to consider the phase shift nonzero in the unapertured region although it would be completely equivalent to add a constant phase shift and create a negative phase shift in the apertured region.

The aperture, however, is contained within a highly resonant structure with nearly equally strong forward and backward waves making a standing-wave. For the active region in a vertical cavity laser, correcting for standing wave effects is done by multiplying the gain by the standing-wave enhancement factor, Γ_{enh}. This correction to the optical path length or phase shift is also valid for small index differences Δn[5]. Adjusting the relative phase we have,

$$\phi(x,y) = \Gamma_{enh} k_0 \Delta n \left[t_{max} - t(x,y) \right]$$
(4-2)

(only accurate for small Δn)

where (as we will describe more rigorously) the enhancement factor for a thin aperture located in the jth layer of a VCSEL is given by,

$$\Gamma_{enh} = 2\cos^2(k_0 n_j z_{pja}) \exp(-z_{ma}/L_E).$$
(4-3)

z_{pja} is the distance between the aperture and the standing-wave-peak in the jth layer, and $z_{ma} > 0$ is the distance the aperture is positioned from the first mirror interface. (For an aperture in the spacer region, $j=0$ and $z_{ma}=0$.) See Figure 4-2 which shows standing-wave pattern.

Because the active region is usually between the DBRs, the enhancement usually only has the cosine term, but when writing the phase enhancement factor for index apertures, the exponential term is added to account the decreasing field strength in the mirrors. The length L_E is the DBR energy penetration depth[6].

Note that there are several different mirror penetration depths[6, 7]: the energy penetration depth, L_E, (which is based on the decay of the field-squared), the phase penetration depth, L_τ, (which is based upon the time delay for a pulse being reflected) and the diffraction equivalent distance, L_D, (based upon the spatial divergence of a mode compared with reflection from a hard mirror)[7]. Later on we will introduce a fourth penetration depth to define the DBR angular stop-band.

For high reflectivity mirrors, L_E is nearly identical to $L_r = \dfrac{\lambda}{4n_o}\left(\dfrac{q}{1-p}\right)$, where

q is the ratio (chosen to be less than unity) between the index of the incident medium (n_0) and the index of the first DBR layer (either n_L or n_H), and $p=n_L/n_H$ is the ratio between the low and high index of the DBR layers. (For the arrangement in Figure 4-2, $q=n_L/n_0$.)
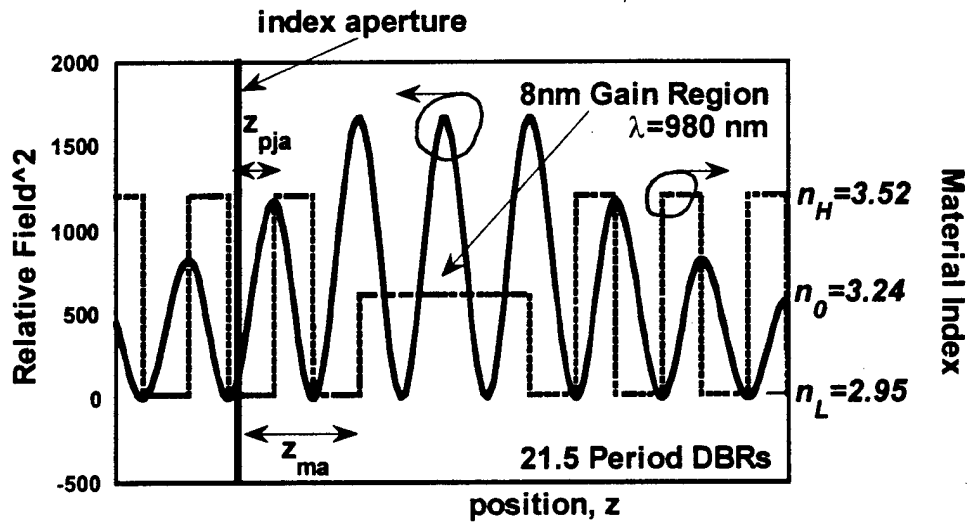
Figure 4-2: An aperture in the central portion of a typical VCSEL standing wave along with the index profile

Actual mirrors often have graded interfaces and sometimes extra spacer layers of multiples of half a wavelength. In Appendix B: Theoretical Odds and Ends, we discuss how the expressions for the various mirror lengths are modified.

Multiplying the phase by the standing-wave enhancement factor is the intuitive thing to do for those who already play with the position of quantum wells. However, the large index step $\Delta n_a \sim 2$ between the aperture and semiconductor, makes the correction fairly inaccurate. The more precise way to handle the problem is to begin by going back to the origin of the enhancement factor[5] and to calculate the intensity weighted average of the dielectric constant over all z as also done by Hadley[8]. This procedure yields the index step which would occur if the aperture index step were spread out uniformly in z. We will

discuss those standing-wave details in the section after next, but let us first compare the two situations of uniform or continuous vs. periodic waveguiding.

Unfolding the Cavity

Let us suppose for the moment that we can find the correct "effective" phase shift, $\phi(x,y)$, an aperture has for plane waves travelling along the axis of the cavity. As is commonly done when treating "thin" lenses, we can approximate the phase shift as the same both for on-axis and slightly off-axis waves. (Note: Although using the correct "effective" phase can account partially for reflections off of the aperture, it does not account for large reflections and we will discuss some consequences of this in a subsequent section). Next we need to consider the effect of the DBR mirrors for both on axis and slightly off-axis waves. Fortunately, Babic found that the variation in the phase shift for slightly off-axis waves hitting the DBR mirrors is just like they were passing through a region of uniform index, n_0, and hitting a hard mirror at a diffraction equivalent distance, L_D. For an infinite stack of quarter-wave thick layers that alternate between a high index of n_H and a low index n_L, the diffraction equivalent distance, L_D is given by [7],

$$L_D = \xi L_\tau \tag{4-4}$$

where $\xi = \dfrac{n_o^2}{2}\left(\dfrac{1}{n_L^2} + \dfrac{1}{n_H^2}\right)$ and L_τ is the phase penetration depth as given before. (Refer to Figure 4-2 again for definitions of n_0, n_L and n_H.) Because of the prefactor, ξ, the energy, phase, and diffraction depths are not exactly equal. However, when the index of the spacer region (the incident medium for the mirrors), n_0, is near the average of the high and low indexes, then they are not too different - For n_L=2.95, n_H=3.52 and n_0=3.24, ξ=1.02.

For a cavity with a central spacer region of index n_0, and thickness, L_0 the total diffraction equivalent cavity length is [9]

$$L_C = L_{D_1} + L_{D_2} + L_0 \tag{4-5}$$

where L_{D_1} and L_{D_2} are the diffraction equivalent distances for the first and second DBRs, respectively. Using this total cavity length, we can represent an apertured VCSEL as an aperture between two hard mirrors. (See Figure 4-3.) Here we have centered the aperture between the mirrors for simplicity.
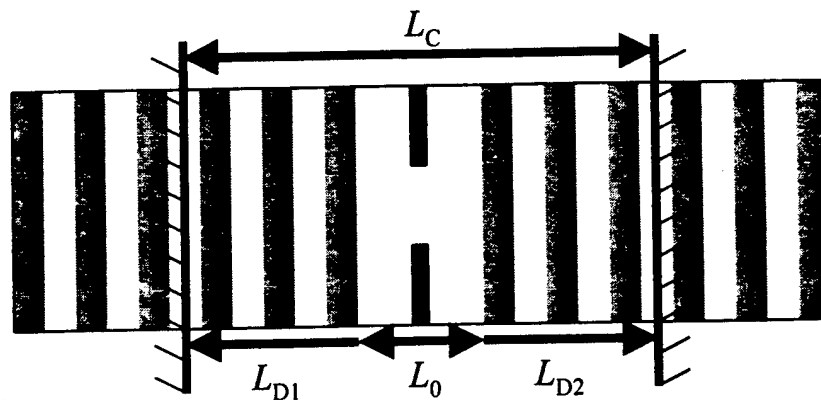
Figure 4-3: Schematic of an aperture centered in an effective cavity of length, L_C.

Next we imagine a mode moving back and forth between the mirrors, and as commonly done[10], we draw an unfolded cavity as shown in Figure 4-4. It is simplest to see the effect of the aperture, if we consider an ideal case, when the aperture is a perfect lens; so it has a parabolic phase profile. Then for a stable resonator, the fundamental mode of the system is a Gaussian with planar phase fronts occurring half a cavity length from each aperture[10]. (See Figure 4-4b.) Because the lens can exactly compensate for the diffraction of the mode there is no scattering loss.

In the case of abrupt apertures (in Figure 4-4a), the mode cannot be perfectly focused and so there are scattering losses. However for short cavities, or large apertures, the phase front will stay relatively flat between apertures, and this periodic waveguiding can be well approximated by a uniform waveguide[8, 11]. In fact, in the simplest form of the Beam Propagation Method (BPM) [12], a waveguide (uniform in z) is numerically modeled by a repetitive application of a spatial dependent phase shift followed by diffraction through free-space. In this case, the model and reality are reversed since we are considering a continuous waveguide as an approximation to a periodic one. The waveguide shown in Figure 4-4c, has a index profile $\Delta n_d(x,y) + n_{d\text{-min}}$.

L_C

$\phi(x,y)$ (a)

(b)

$n_{d\text{-min}}$

$n_{d\text{-min}} + \Delta n_d(x,y)$

(c)
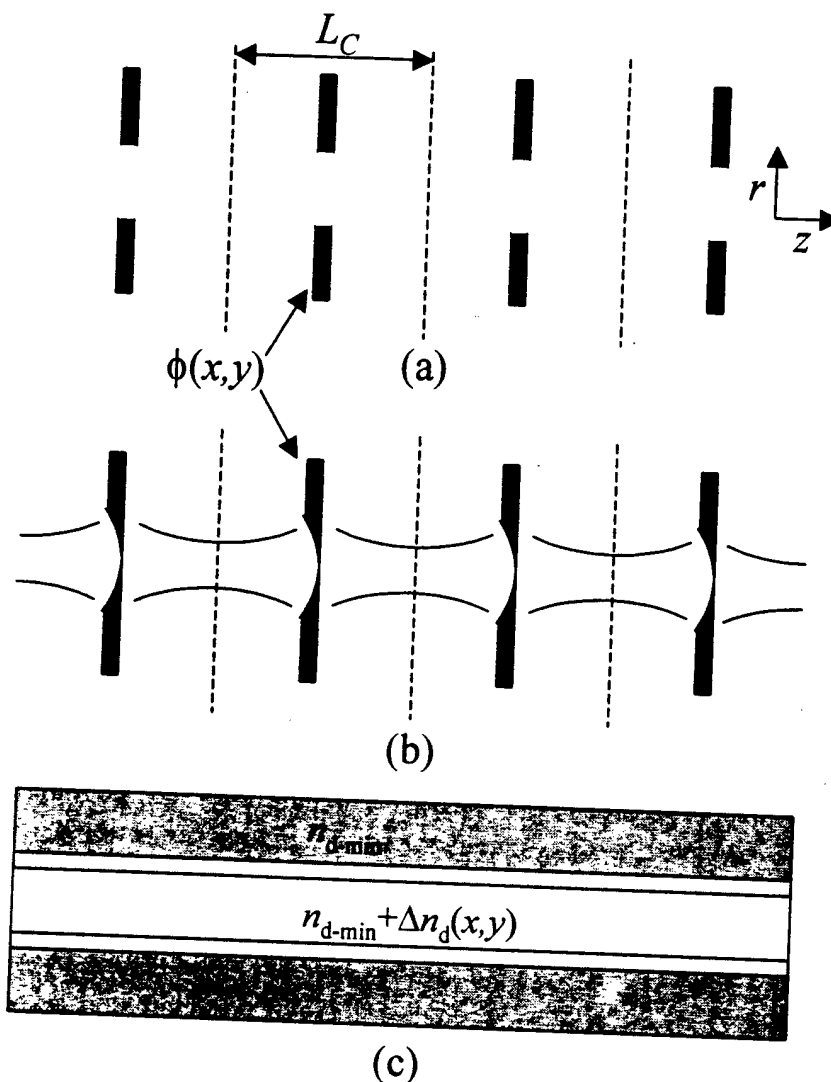
Figure 4-4: (a) The unfolded cavity for the simplified apertured-cavity shown in Figure 4-3. The medium between apertures has a uniform index n_0. The aperture is modeled by a spatially dependent phase shift $\phi(x,y)$. In general, $\phi(x,y)$, may be any shape, but this case shows an abrupt aperture which at smaller sizes and longer cavity lengths is unable to completely refocus the mode instead scattering energy into free-space.

(b)   The unfolded cavity with a parabolic phase shift, $\phi(x,y)$, i.e. an ideal thin lens.   For a Gaussian mode undergoing Fresnel diffraction between the apertures, the phase shift is able to exactly correct for the diffraction, eliminating scattering losses.   Given the symmetry chosen, the mode has planar phase fronts half-way between the apertures as indicated by the dashed lines. (c)   A uniform waveguide which, in the limit of vanishing cavity length, corresponds to the unfolded cavity with $\phi(x,y)=k_0\Delta n_d(x,y)L_C$

Thinking of the BPM method allows us to see that if we wish to obtain the same mode using both approaches (in the limit of vanishing cavity length), then the phase shift of aperture should be[12]

$$\phi(x,y) = k_0\Delta n_d(x,y)L_C \qquad (4\text{-}6)$$

In Appendix B: Theoretical odds and ends, we will show the periodic waveguiding in the Fresnel limit matches the wave equation to second-order in L_C.

Knowing the correspondence between the uniform waveguide index distribution and the phase shift will allow us to work backwards to find the appropriate effective phase shift for the aperture.   And, in the case of an abrupt aperture of radius, a, corresponding to a step-index waveguide, we can now use the $V = k_0 a\sqrt{2n_0\Delta n_d}$ number[13] to determine the dispersion curves, modes, confinement factors, etc.   (The confinement factor vs. V number is given in Appendix B: Theoretical Odds and Ends.)   Interestingly, the phase shift of an abrupt aperture, ϕ_0, and the Fresnel number for the cavity, $F=a^2n_0/(\lambda L_C)$ are related to the V number by, $V = \sqrt{4\pi\phi_0 F}$.

The distributed index step:

Using the analysis so far, one would determine the effective index step of an equivalent uniform waveguide from the phase shift given in Eq. (4-2) and Eq. (4-6) to be,

$$\Delta n_d(x,y) = \Gamma_{enh}\Delta n[t_{max} - t(x,y)]/L_C \qquad (4\text{-}7)$$

However, this relation is only accurate for small index differences between the aperture and the semiconductor.   A better approach to use the dielectric

constant, which is the fundamental parameter in the wave equation. As done so by Hadley[8], a distributed dielectric constant ε_d is defined by,

$$\varepsilon_d(x,y) = \int \varepsilon(x,y,z) |\Psi(z)|^2 dz \bigg/ \int |\Psi(z)|^2 dz \qquad (4\text{-}8)$$

where $\Psi(z)$ is the longitudinal electric field in the unapertured VCSEL structure (as can be calculated using a 1-D transmission matrix technique with $\varepsilon(0,0,z)$). Then the distributed index difference is given by:

$$\Delta n_d = \sqrt{\varepsilon_d(x,y)} - \sqrt{\varepsilon_{d\text{-min}}} \qquad (4\text{-}9)$$

where $\varepsilon_{d\text{-min}}$ is the value of ε_d where the aperture is the thickest. This distributed index difference can now be used to estimate mode etc. and also used in Eq. (4-6) to determine the effective phase shift of the aperture.

If one approximates the VCSEL field[2] as $|\Psi_0|^2 \cos^2(k_0 n_j z_{pj}) e^{-z_m/L_E}$ in the DBRs and $|\Psi_0|^2 \cos^2(k_0 n_0 z_{p0})$ between the DBRs plugs that into Eq. (4-8) and takes the limit of small index steps, thin apertures, a penetration depth long compared to the period of oscillation, then we obtain a similar but more accurate version of Eq. (4-7):

$$\Delta n_d(x,y) = \left(\frac{n_j^2 - n_A^2}{2n_0} \right) \frac{[t_{max} - t(x,y)]}{L_{CE}} \Gamma_{enh} \qquad (4\text{-}10)$$

where $L_{CE} = L_0 + L_{E1} + L_{E2}$, which is almost the same as L_C, when the index of the spacer is near the average index of the cavity.

The variation in the distributed index step as an aperture is moved from peak to null through the VCSEL cavity is illustrated graphically in Figure 4-5. The solid line shows the distributed index difference vs. the aperture position. The index step was calculated for a 20nm thick aperture with $n_A = 1.55$. The dashed line indicates the index of the unapertured cavity. (For the purpose of showing a continuous curve, we have allowed the aperture to move into the GaAs regions. Consequently, kinks occur at the interfaces as the index step between the aperture and the background index changes.) The variation looks very similar to the standing-wave intensity, and in the limit of thin apertures, and small Δn, the distributed index difference will be directly proportional to it. The curves in Figure 4-5 were calculated from Eqs. (4-8) and (4-9), but they

agree with Eq. (4-10) to within 10%. (Using Eq. (4-7) causes errors three times larger.)
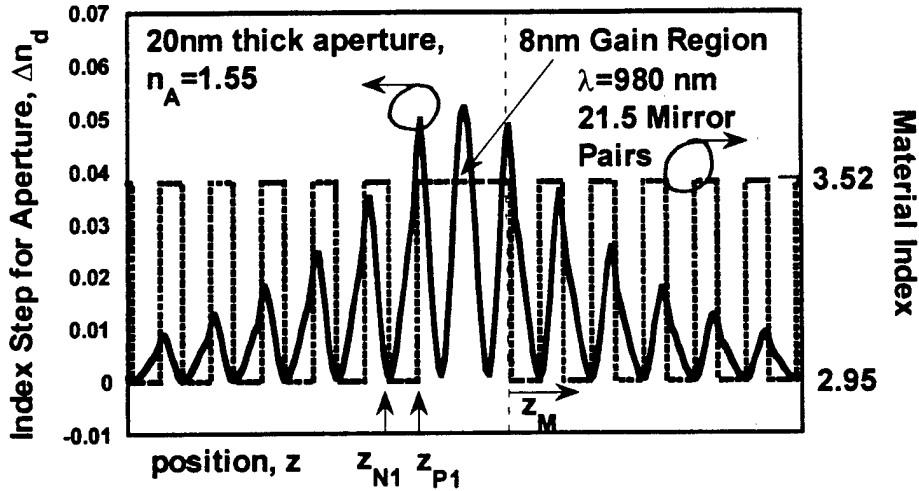
Figure 4-5:   Plot of the distributed index step, Δn_d, calculated for a 20nm thick oxide (n=1.55) aperture vs. position in the cavity. The refractive index distribution in the unapertured cavity is indicated by the dashed line.

Eq. (4-10) may look nice on the back of an envelope, but in practice one usually has a transmission matrix program handy and can either use Eqs. (4-8) and (4-9) directly or look instead at the change in cavity resonance to obtain the distributed index step.

As we know the change in optical path length from the unapertured to the apertured regions of the cavity will change the resonant wavelength. Consider the cases shown in Figure 4-6 for a cavity of nominally of length $L_C=m\lambda_0/(2n_0)$, (where m is an integer). It is resonant at a wavelength, λ_0 when filled with a medium of index n_0. When the index is reduced by Δn_d, the wavelength shifts to:

$$\lambda_1 = \left(L_C \, 2(n_0 - \Delta n_d)\right)/m = \lambda_0\left(1 - \Delta n_d/n_0\right) \qquad (4\text{-}11)$$

And so,

$$\Delta\lambda/\lambda_0 = \Delta n_d/n_0 \qquad (4\text{-}12)$$

$$L_C = m\lambda_0/(2n_0)$$

$$n_0$$

(a)

$$n_0 - \Delta n_d$$

(b)

$$L_C + \Delta L$$

$$n_0$$

(c)
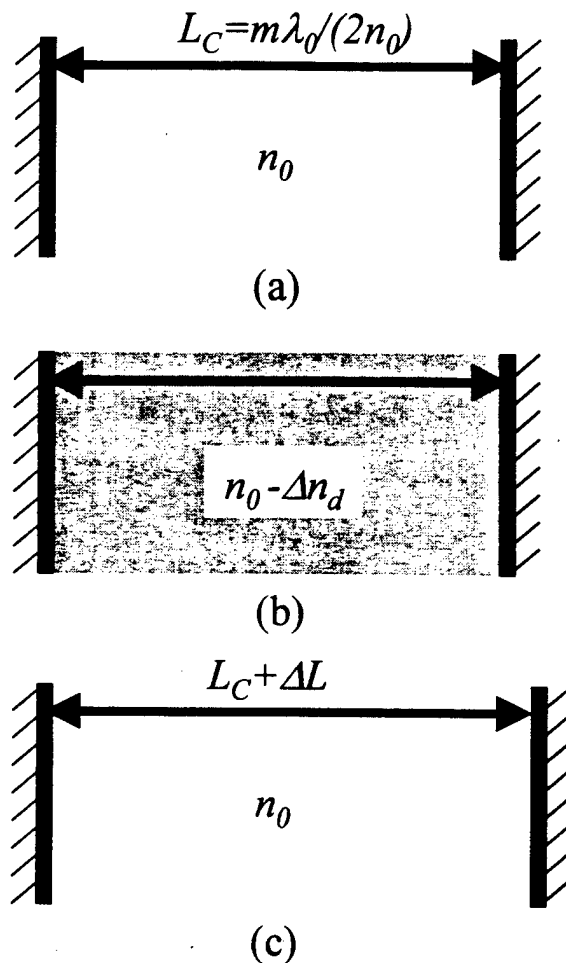
Figure 4-6: Cavities with two hard mirrors (a) filled by an index n_0, (b) filled by an index of $n_0-\Delta n_d$, (c) filled again by index n_0, but of slightly longer length

For VCSELs, the situation is very similar except that the effective cavity length of a VCSEL (the sum of the spacer length and the mirror penetration depths) is not normally a multiple of half the resonant wavelength because the effective phase penetration depth of the mirrors comes only from the *change* in phase from the center wavelength. However, if you just look at the *change* in the resonant wavelength, the second relationship, (4-12), as derived by Hadley[8] for index apertured VCSELs, still holds. Knowing this relation, one can then turn the problem around and calculate with a 1-D transmission matrix method or measure experimentally the shift in the 1-D cavity wavelength in the

apertured vs. the unapertured regions to determine the distributed index difference that is created by the index change of the aperture or apertures. In passing, we should mention that the change can also come from variations in layer thickness as shown in Figure 4-6c which might be created by etching and regrowth. If the change in thickness occurs in the spacer region of a VCSEL, then we can write,

$$\Delta\lambda/\lambda_0 = \Delta L/L_{C\tau} \tag{4-13}$$

where $L_{C\tau}=L_0+L_{\tau 1}+L_{\tau 2}$, is the effective cavity length based upon the mirror phase penetration depths and is almost identical to L_E, (the length based upon the DBR energy penetration depths) and is within a few percent of L_C when the index of the spacer region is near the average index. The fractional change above can again be thought of as an equivalent fractional change in the effective index using (4-12). One can then apply the subsequent scattering loss modeling for apertures also to guiding based on changes in physical thickness.

There are a couple of caveats when using changes in the resonant wavelength. If the aperture is thick enough and the DBR stop band large enough, the center mode may be shifted so far to shorter wavelengths, that a second mode at longer wavelengths will appear and one might incorrectly conclude the index change is of the opposite sign. A related problem is shifting the mode in the apertured region beyond the mirror stop-band in which case the approximations used to derive Eq. (4-12) do not really hold. In these cases, it may be more accurate to use the integral approach Eq. (4-9). Although reference [8] suggests significant discrepancy between the methods, they agree (as we show next) for thin apertures provided one uses the same standing-wave intensity profile for all values of x and y (in accordance with perturbation theory).

In Figure 4-7, we plot the distributed index difference vs. the aperture thickness for an aperture positioned in the first quarter-wave layer of the DBR (as shown in Figure 4-5). The three sets of curves show Δn_d vs. the thickness of the aperture in the cases that the thickness is increased from the standing-wave null, from the standing-wave peak and from the center of those positions. The dashed lines correspond to the result of Eqs. (4-8) and (4-9) while the solid lines are the result of Eq. (4-12). For the aperture starting from the null, the

increase in Δn_d is much slower initially than for the aperture starting from the peak. Initially, the increase is quadratic with thickness. Thus, if an aperture is tapered in a linear fashion from the null, then the effective phase profile will be parabolic.
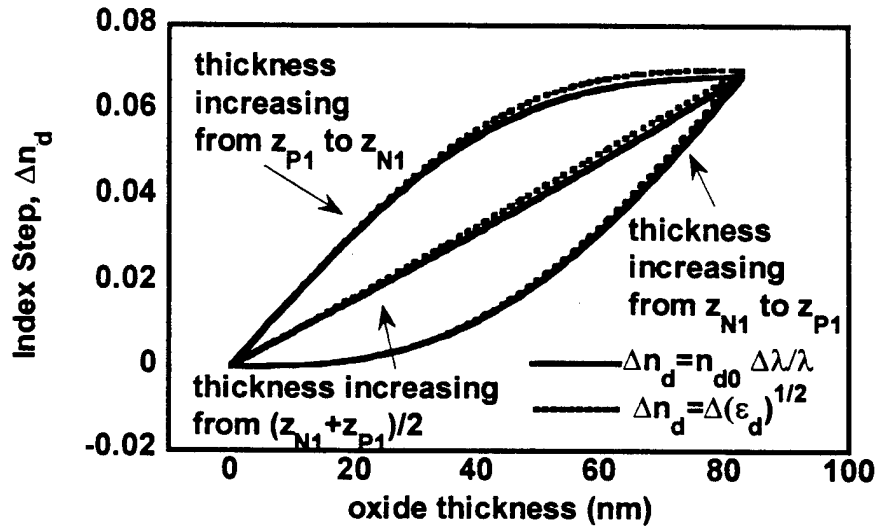
Figure 4-7: The distributed index difference, Δn_d, calculated for the same unapertured cavity as labeled in Figure 4-5 now plotted vs. the thickness of the oxide aperture extending from the peak of the standing-wave, from the null, and from the center of these positions. The solid lines indicate the result of Eq. (4-12)and the dashed lines indicate the result of Eqs. (4-8) and (4-9).

Lasing Wavelength(s)

We have described how the aperture shifts the distributed index from the core to the "cladding" or apertured regions of the VCSEL. And we know that the actual mode will have some effective modal index, n_m between n_0 and $n_{d\text{-min}}$. For the case of circular step-index waveguides, we can determine that effective modal index from the V number, which we can use to get the normalized propagation constant, b[13] that we can read from dispersion charts or

calculate ourselves. The index difference, $\Delta n_m = n_0 - n_m$, between the "core" index, n_0, and the mode index is approximately given by:

$$\Delta n_m = (1-b)\Delta n_d \qquad (4\text{-}14)$$

when the distributed index steps are reasonably small. (And they typically are in comparison with the average index!) When the mode is in a fiber, we know the wavelength is constant, but the propagation constant, $\beta=(2\pi/\lambda)n_m$ changes for different modes. In our subsequent analysis of diffraction/scattering losses, we will be examining "unfolded" cavities and these will appear similar to continuous fibers in the sense that we will hold the wavelength fixed and β will change. However, for determining the amount of diffraction it is not very critical to account for the change in wavelength because the percentage change is very small. Of course, we know that in the actual cavity, we have resonance which will force the wavelength to change so that β is the same for all modes. (More precisely, we should say $\beta=m2\pi n_0/\lambda_0$ for all the modes, where λ_0 is the resonant wavelength of an unapertured cavity - the longest wavelength that a mode can have, and m is an integer not necessarily the same for all modes.) For the case of abrupt apertures, we can satisfy this condition using the circular step-index waveguide analysis. We can determine the difference, $\Delta\lambda_m = \lambda_0 - \lambda_m$, between this "core" wavelength and the lasing wavelength, to first order, using:

$$\frac{\Delta\lambda_m}{\lambda_0} = \frac{\Delta n_m}{n_0} = \frac{(1-b)\Delta n_d}{n_0} \qquad (4\text{-}15)$$

which one can verify will cancel any first-order changes in β from the change in n_m.

Using the different b's for different modes, one can find their wavelength separation. And this separation of modes predicted from a uniform waveguide model has been shown to match the wavelength separation measured in VCSELs[14]. Consequently, measuring the changes in resonant wavelength for the first-order and higher order modes allows one to work backwards and find the VCSEL aperture size which will produce such a wavelength separation as done by Thibeault[15], Floyd[16] and others.

Gain and Thermal Guiding

When the index confinement is very weak, we will eventually need to consider the effect the gain has confining the mode. The "gain" confinement in the case of no lateral variation in the real part of the refractive index has been analyzed previously in ref. [9]. The confinement due to the gain is typically much weaker than any index confinement. If the change in the imaginary part of the index is distributed through the cavity then the index step is $Im\{\Delta n_d\} = G/(k_0 L_C)$, where G is the gain per pass. For typical VCLs, G=0.005, L_C=1.2μm and λ=1μm, $Im\{\Delta n_d\} = 0.0007$, which is generally much lower than the real part of the index step. The gain also induces a similar size change in the real part of the index (through the Kramers-Kronig relation). Either change, however, will affect the mode shape only for very weak index guiding.

A more important limit to consider is that of thermal lensing. Guiding may be dominated by thermal lensing when a large temperature gradient exists within the radius of the aperture. For typical AlGaAs/GaAs VCLs the mode moves ~0.06nm/°C [17]. For a 20°C gradient, λ=1μm, and n=3.2, then $\Delta n_d = n \Delta \lambda / \lambda = 0.004$. Even apertures with relatively small distributed index steps (five to ten times this value) will still dominate the waveguiding in a device.

Overview of Index aperture optical losses

The periodic nature of the guiding revealed by an unfolded cavity, like that in Figure 4-4a shows that an abrupt aperture cannot perfectly focus the mode and so there will be some power radiated laterally. There can be other size-dependent optical losses as well such as absorption by the aperture or scattering due to the roughness of the aperture. However, the loss we will be considering in the next sections is due to the imperfect lensing of the aperture. By imperfect lensing we mean there is a modal mismatch between the aperture/lens region (which, in the case of abrupt apertures, has Bessel functions for modes) and the unguided region with free-space or Hermite Gaussian modes. This mismatch must be accommodated by a superposition of higher-order guided and radiation modes. Technically speaking, the whole

mode of a laser is a radiation mode, but one often considers it in several parts by expanding it in the basis set, say of modes of a waveguide which is uniform along the z-axis. From this perspective, we can estimate how much power is radiated away uselessly (i.e. power which cannot be captured by a reasonable numerical aperture just beyond the output facet).

In the next sections, we will present calculations of the scattering loss based on coupling losses and based on a more complicated iterative model. These calculations have confirmed the hypothesis that optical scattering losses are responsible for the increased gain and lower slope efficiencies of small <4μm diameter VCSELs with abrupt, 80nm thick apertures. And the calculations directed subsequent VCSEL designs towards optically weaker (thinner or positioned at nulls) or tapered apertures for lower scattering losses at small diameters.

Effect on threshold gain:

The scattering losses we will calculate in terms of the excess loss *per pass*, α_S. Since the gain will need to rise to match these losses, the threshold condition now reads:

$$\Gamma_{xy}\Gamma_{enh}gL_a = \frac{1}{2}(T_1 + T_2) + \alpha_{BA} + \alpha_S$$

$$G = \alpha_0 + \alpha_{BA} + \alpha_S$$

(4-16)

where T_1 and T_2 are the power transmissions for a plane-wave at normal incidence upon the top and bottom mirrors, Γ_{enh} is the enhancement factor for the gain region (between 0 and 2), g is the material gain per well (in units of inverse length) - assumed here to be laterally uniform, L_a is the total length of the active region(s), and α_{BA} is the size independent loss *per pass* due to absorption from dopants, etc. ($\alpha_{BA}=\alpha_m L_C$ may be thought of as an average material absorption, α_m, in units of inverse length times the cavity length.). We have also expressed the equation in terms of the modal gain per pass, G, and the transmission loss per pass, α_0. Later, we will use the change in the modal gain relative to that for a planar structure, $\Delta G = \alpha_S$ to determine the excess loss. We also note that if the injection of carriers can be kept within the aperture then the lateral confinement factor Γ_{xy} will decrease as the aperture closes, and

this will cause the gain to increase, but will not change the modal gain which is what we use to define the scattering losses. (If one just examines material gain, g, sometimes it appears as though thicker apertures will be "better" because of a larger lateral confinement factor.)

Effect on slope efficiency:

Scattered light has to go somewhere, and if we could collect all of it, then in theory we would not observe any change in the slope efficiency. However, as we found from calculation, most of the "scattered" light travels at angles so far off-axis it is totally internally reflected at a planar air/semiconductor interface. This light is hard (impossible) to capture with any reasonable numerical aperture just outside the cavity. And so one may write the modified slope efficiency as:

$$\eta_{EX} = \eta_i \frac{T_1/2}{\left(a_0 + a_{BA} + a_S\right)} \tag{4-17}$$

where T_1 is the output mirror power transmission. We will discuss the path of scattered light further after describing the iterative model to calculate the scattering losses.

Single-Pass Coupling Loss Estimate of Scattering Losses

To estimate the scattering loss per pass, we can calculate the coupling losses after passing an appropriate mode through one unit cell of the periodic structure shown in Figure 4-4. Unfortunately, guided modes for the periodic structure only can be found in the cases of a parabolic aperture (ideal lens) or vanishing cavity length (uniform waveguide). In other cases, the periodic waveguide radiates energy to free space. In order to estimate the loss in these cases, we will take a perturbation approach and consider the periodic waveguide as a perturbation of a uniform waveguide. The mode of the uniform waveguide has planar phase fronts. And so it should match the mode of the periodic waveguide best when that mode of the periodic waveguide also has planar phase fronts. As shown in Figure 4-4b (in the case of an ideal lens), planar phase fronts occur exactly half way between each of the apertures (given

the symmetry we have chosen). Thus, we have chosen to begin the cell at this position. As we describe in Appendix B, the uniform waveguide equation matches the periodic waveguide eigenmode equation to second order in L_c when the cell begins midway between the apertures (or in the middle of the aperture), but the equations match only to first order in L_C when the cell begins elsewhere.

Although the periodic structure will perturb the uniform waveguide mode, an important result of perturbation theory is that a first order change in the mode provides only a second order change in the propagation constant [18, 19]. Thus, the technique should be somewhat tolerant to error in the choice of the mode.

The procedure for estimating losses is outlined in Figure 4-8. We pass a uniform waveguide mode once through the cavity and compute the overlap with the original mode. The scattering loss is taken to be one minus this overlap. Essentially, what is being assumed is that the power not coupled back to the original mode is lost to radiation. Obviously, some power could be coupled to higher order even modes. And perhaps it would be more accurate to also compute the power coupled to the third order uniform waveguide mode and subtract that from the scattering loss. Nevertheless, as we will describe, the procedure shows good agreement with a more accurate iterative model that solves for the actual mode.
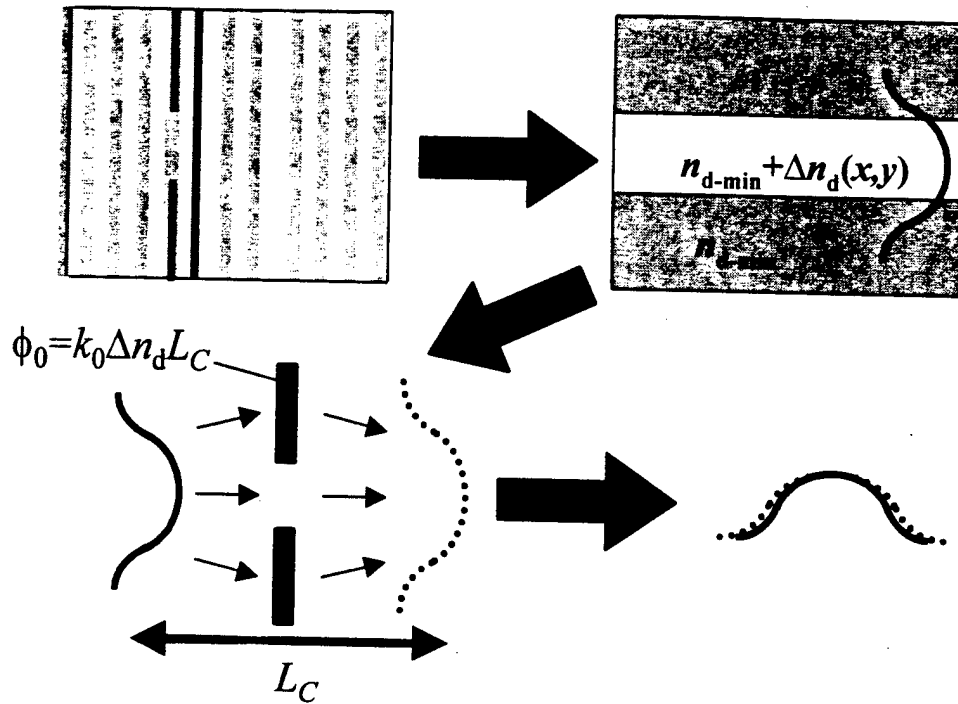
Figure 4-8: Flowchart of the single-pass coupling loss estimate of scattering losses. First, the effective index is found for an equivalent uniform waveguide and the scalar mode is for that waveguide is calculated. Next the uniform waveguide mode is propagated through half a cavity length, phase shifted by the aperture (using a phase shift corresponding to the uniform waveguide index step), and propagated through another half cavity length. The scattering loss is taken to be difference between unity and the overlap of modes. For apertures without tapering, a fitting formula was found for the results of this procedure which allows one determine the scattering loss by simply "plugging in" the Fresnel number and the effective phase shift of the aperture.

We will also show the results of this procedure for apertures without tapered tips can be summarized by a fitting formula (Eq. (4-25)) for the scattering loss in terms of the effective phase shift of the aperture and either the Fresnel number, F, (of the cavity) or the V number of the uniform step-index waveguide. Now we show the details.

Formalism

Mathematically, passing a scalar mode, Ψ, through a cell of the periodic waveguide can be represented as the operator, $\hat{P}$.

$$\hat{P}\Psi = \hat{D}\exp\{j\phi(x_N, y_N)\}\hat{D}\Psi \tag{4-18}$$

The middle factor expresses the position-dependent phase shift of the aperture defined by Eqs. (4-6) and (4-9) or (4-12), and $\hat{D}$ is the free-space propagator for the wavefunction diffracting through half a cavity length. The operators are in terms of normalized coordinates: $x_N = x/a$, $y_N = y/a$, where a is the characteristic size of the aperture. For abrupt apertures, a is defined simply as the radius of the aperture. The $\hat{D}$ operator is defined (in the Fresnel limit) by [13]

$$\hat{D} = \hat{F}^{-1}\exp\left\{-jk_{rN}^2 L_C\big/\left(4k_0 n_0 a^2\right)\right\}\hat{F} = \hat{F}^{-1}\exp\left\{-jk_{rN}^2\big/(8\pi F)\right\}\hat{F} \tag{4-19}$$

where the operator $\hat{F}$ is the Fourier transform defined by

$$\hat{F} = \iint dk_{xN}dk_{yN}\exp\left\{jk_{xN}x_N + jk_{yN}y_N\right\} \tag{4-20}$$

Again, we are using the normalized variables, $k_{xN} = k_x a$, $k_{yN} = k_y a$ and $k_{rN}^2 = k_{xN}^2 + k_{yN}^2$. $F = \dfrac{a^2 n_0}{\lambda L_C}$ is the Fresnel number [13].

The scattering (coupling) loss per pass, α_s is now written as

$$\alpha_S = 1 - \left|\iint dx_N dy_N \Psi^*\hat{P}\Psi\right|^2 \bigg/ \left(\iint dx_N dy_N |\Psi|^2\right)^2 \tag{4-21}$$

What is important to observe from these equations is that for a given aperture shape the scattering loss only depends on two parameters. As we have expressed on the right-hand side of Eq. (4-19), the diffraction only depends on the Fresnel number. Let us next write the phase shift as $\phi(x_N, y_N) = \phi_0 s(x_N, y_N)$, a product of a characteristic phase shift of the aperture, ϕ_0, and, $s(x_N, y_N)$, a function which only depends on the aperture shape. Modes of the uniform waveguide (for a given index profile) are the eigenmodes of $\hat{P}$ in the limit that $\Delta n_d(x,y)$ is held constant and L_C approaches zero (as shown in Appendix B.) So these will also only depend ϕ_0 and F. Therefore, once the shape of the aperture $s(x_N, y_N)$ is defined, the scattering loss, L_S is only a function of ϕ_0 and F.

Analysis of Parabolically Tapered Aperture (Ideal Lens)

For the case in which the phase shift is parabolic, i.e., $\phi(r) = -k_0 n_0 r^2 / (2f)$, corresponding to a lens of focal length, f, then so long as $f > L_C / 4$ (for the symmetric cavity) the eigenmodes of the periodic waveguide, $\hat{P}$ will be all guided, Hermite-Gaussian modes [10]. This can be seen easily by operating on a Gaussian mode with $\hat{P}$. The Fourier transform will yield a Gaussian which when multiplied by a quadratic phase will still be Gaussian. One can solve for the Gaussian beam-waist such that $\hat{P}\Psi = e^{j\theta}\Psi$ (where θ is a real constant). Plugging this condition into (4-21) gives identically zero scattering loss.

Analysis of Abrupt Apertures

For an abrupt aperture,

$$\phi(r_N) = \begin{cases} \phi_0 = k_0 \Delta n_d L & r_N < 1 \\ 0 & r_N \geq 1 \end{cases} \tag{4-22}$$

In this case there is scattering loss to radiation, so as described before, we will use the guided mode that best approximates the mode of the periodic waveguide to calculate the scattering loss. The mode of the uniform, circular, step-index waveguide is determined simply from the V number [13], and in the limit of small index steps,

$$V = k_0 a \sqrt{2 n_0 \Delta n_d} = \sqrt{4\pi\phi_0 F} \tag{4-23}$$

is only a function of ϕ_0 and F as asserted above. As commonly done, the V number is used to find the normalized propagation constant, b, and then the lowest order mode which is given by[13]:

$$\Psi(r_N) = \begin{cases} J_0(\kappa_N r_N) / J_0(\kappa_N) & r_N < 1 \\ K_0(\gamma_N r_N) / K_0(\gamma_N) & r_N \geq 1 \end{cases} \tag{4-24}$$

where J_0 and K_0 are Bessel functions, $\kappa_N = V\sqrt{1-b}$, and $\gamma_N = V\sqrt{b}$. Knowing the mode shape, we can then use Eq. (4-21) to find the scattering loss, α_s.

In Figure 4-9, we plot using solid lines the scattering loss (for abrupt, circular apertures) vs. the Fresnel number, F for different values of the phase shift per pass, ϕ_0.

$\lambda=0.98\mu m, L_C=1.15\ \mu m, n_0=3.52$

Radius, a (µm)
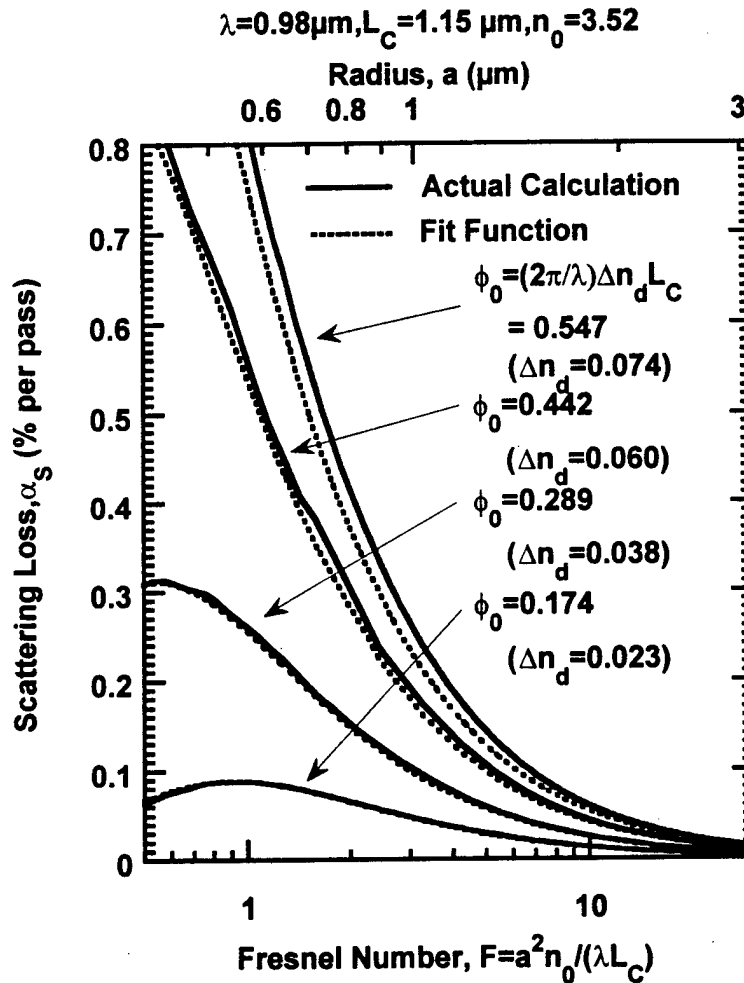
Figure 4-9: Results of the single-pass coupling-loss estimate for scattering loss for laterally abrupt apertures. The estimate only depends on two parameters: the Fresnel number of the cavity (plotted along the x-axis) and the effective single pass phase shift of the aperture, ϕ_0. For reference, the radius, a, of the abrupt aperture is specified along the upper axis for the parameters given. Using those same parameters we have also given the index step, Δn_d shown in parenthesis. The solid lines show the result of Eq. (4-21) and the dashed lines are calculated from an approximate fitting function, Eq. (4-25).

To get a feel for the Fresnel number, we have included a scale of the aperture radius along the upper axis (for the particular set of parameters given at the top of the graph). These same parameters yield $\phi_0=0.442$ when $\Delta n_a=0.06$. For a large Fresnel number, we see the scattering losses decrease. The larger Fresnel number can be obtained from a shorter cavity length, an increased aperture size, or a shorter wavelength. In either case the mode diffracts less, and the losses are lowered. Alternatively, as the optical strength of the aperture is decreased (i.e. ϕ_0 is lowered), then the scattering losses also decrease. A less intuitive feature of the plot is that for small ϕ_0 and small F, the scattering loss tends to zero. In this region, the waveguide becomes so weak that further shrinking of the aperture size widens the mode, decreasing the amount of diffraction.

We can add curves in Figure 4-9, to cover many more values of ϕ_0, and subsequently fit those curves to a functional form. We can then obtain a formula for the scattering loss of the lowest order mode of abrupt, circular apertures:

$$\alpha_S \text{ (\% per pass)} = 2.28 \frac{\phi_0^{1.19}}{F^{1.3}} \exp\left\{-\frac{0.206}{\phi_0 F}\right\} \tag{4-25}$$

The dashed lines in Figure 4-9 show the results of Eq. (4-25). This formula matches the results of Eq. (4-21) extremely well for the smaller values of ϕ_0, although at higher values the formula begins to deviate from Eq. (4-21). Given the correspondence between the step-index uniform waveguide and the periodic waveguide with an abrupt aperture, we can also express Eq. (4-25) in terms of the V number using the relation in Eq. (4-23):

$$\alpha_S \text{ (\% per pass)} = 61.2 \frac{\phi_0^{1.49}}{V^{2.6}} \exp\left\{-\frac{2.59}{V^2}\right\} \tag{4-26}$$

This analysis can also be extended to higher order modes to determine the mode suppression ratio created by scattering losses as done by Dan Lofgreen (unpublished). The main conclusion of such analysis is that to obtain a significant mode suppression ratio (~30dB), the lowest order mode also must suffer severe scattering losses.

Analysis of Tapered Apertures

To estimate losses for cavities with tapered apertures, we would like to find the mode of an axially uniform waveguide with a tapered index profile and then use Eq. (4-21) to estimate the loss. Unfortunately, performing such a calculation may not be much easier than directly using the iterative method described in the next section. One can instead use a cruder estimate for the mode to calculate the loss. As mentioned before, the first order error in the mode will lead to only a second order error in the losses. Although using a Bessel function (the mode of a step-index uniform circular waveguide) in combination with a linearly tapered aperture yields lower losses than for an abrupt aperture, the loss is significantly higher than found using the iterative model (as we will discuss). Because the loss is so low the second order errors for this "cruder" estimate are significant, and to obtain greater accuracy one is forced to use the iterative method or to find the uniform waveguide mode.

Comparison with measured losses for VCSELs with abrupt apertures

Given the ease of determining the scattering loss for abrupt apertures in different structures, we can use the model to explain experimental results. In Figure 4-10, we compare the theoretical predictions to experiment for a variety of designs with abrupt apertures. We consider three different 980nm oxide-apertured VCSELs. (In Chapter 6, we will analyze experimental results for VCSELs with tapered apertures.) The experimental data for the scattering loss are extracted from the dependence of the differential efficiency on the aperture size [15, 20]. One uses an inverted form of Eq. (4-17)

$$\alpha_S = \frac{\eta_i}{\eta_{EX}} \frac{T_1}{2} - \alpha_0 - \alpha_{BA} \approx \frac{T_1}{2}\left(\frac{\eta_i}{\eta_{EX}} - 1\right) - \alpha_{BA} \qquad (4\text{-}27)$$

To use the above relation, one calculates a value for the output mirror transmission, T_1, and determines α_{BA} by assuming that $\alpha_S=0$ for large area devices. One must also estimate η_i by some means (such as from in-plane laser measurements) and assume it does not vary with device size. We will discuss this issue further in the next chapter, but what is expected in theory and supported by experimental evidence is that the injection efficiency is

essentially constant with size (at least when the excesses loss is low) even with lateral current and carrier leakage increasing the threshold current. In some ways, the arguments are self-supporting because we will assume that the injection efficiency does not vary with size and see if we can explain the experimentally observed drop in slope efficiency from our estimate of the scattering losses.

The size of the devices (presented in Ref. [16] and Ref. [15]) were first estimated from an optical microscope image of test patterns on the sample. Then to obtain more precise results the spacing (in wavelength) of the lateral modes was measured for the particular device under test. The uniform waveguide approximation [14] was then used to determine the device radius which would produce that same wavelength spacing. The method is accurate to within 5-10% and works better for smaller size devices in which the wavelength separation is larger.

The first VCL has AlGaAs/GaAs mirrors and a 80nm oxide aperture. A full description of the structure can be found in [16]. Assuming a spacer completely of index of n_0=3.21, we calculate a cavity length of L_C/n_0=0.483µm (F=4.8 at a=1.5µm) taking into account the extra $\lambda/2$ spacer and grading using the method specified in Appendix B. We show the calculated loss for the case of an oxide aperture in the structure, which has a Δn_d=0.055 and, consequently, ϕ_0=0.547. And we show the case in which air is used instead of the oxide, yielding, Δn_d=0.068, and consequently, ϕ_0=0.676. Even if the aperture were air instead of oxide, the predicted losses are not significantly higher despite the larger index step.

The second VCL also has AlGaAs/GaAs DBR mirrors, but with a thinner 30nm oxide aperture [15]. The thinner oxide leads to a lower Δn_d=0.02 and ϕ_0=0.174. The shorter cavity length of L_C/n_0=0.423µm (F=5.4 at a=1.5µm) is due to using a higher aluminum mole fraction in the top DBR.

The third set of data corresponds to a 47nm thick oxide layer in a $\lambda/2$ spacer region with a MgF/ZnSe top mirror. The loss was extracted from differential efficiencies in Ref. [21] assuming η_i=0.8. Despite the variation in the data at

the smaller size, the losses are still significantly lower than those predicted for the device with the 80nm thick oxide, and in the neighborhood of the theoretical prediction. The high contrast mirrors and short spacer, lead to a very short cavity length of $LC/n_0=0.30\mu m$ ($F=7.7$ at $a=1.5\mu m$). The aperture position (near a standing-wave null) keeps the index step $\Delta n_d=0.023$ roughly the same as the device with the 30nm thick oxide.

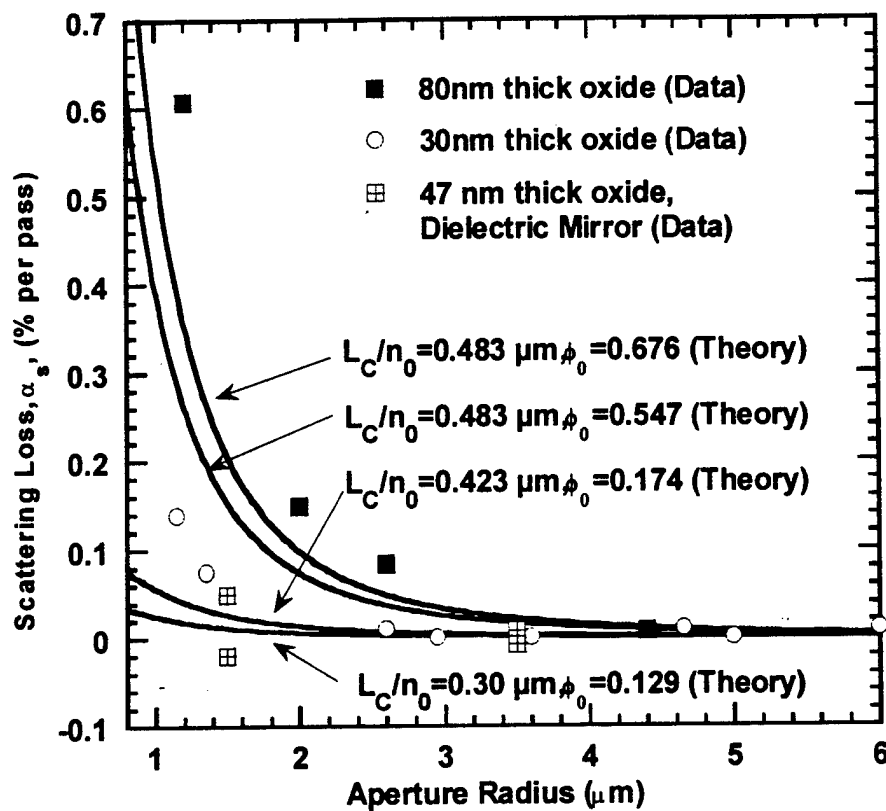Figure 4-10: Comparison of the single pass estimate with experimental results with 980nm oxide-apertured vertical-cavity lasers. The data indicated by solid black squares is from Ref. [16]. The device has an 80nm thick oxide aperture and AlGaAs/GaAs mirrors. The two upper theoretical curves with $\phi_0=0.676$ and $\phi_0=0.547$, respectively correspond to 80nm thick air and oxide apertures in that device.

The curve with ϕ_0=0.174 and a slightly shorter cavity length corresponds to the data (indicated by the circles) for a device with a 30nm oxide aperture and AlGaAs/GaAs mirrors from Ref. [15]. The lowest curve using the shortest cavity length, L_C/n_0=0.3μm and ϕ_0=0.129, corresponds to data (indicated by the four-square pattern) from Ref. [21] That device has a MgF/ZnSe top DBR and a $\lambda/2$ cavity. The variation in cavity length in the different devices is inversely proportional to the Fresnel number which at radius a=1.5 μm, varies from F=4.8 for the upper two curves to F=5.4 and F=7.7 for the lower two curves.

The data show scattering losses close to, but generally higher than that predicted theoretically. Although we have not compared directly to the more accurate iterative model, the single pass estimate will yield only a small overestimate of the losses.

The extracted losses being somewhat higher than theoretically expected may come from a lower slope efficiency due to heating in the smallest devices. Heating will lower the injection efficiency, but that effect is smaller than the roll-over created by the increasing threshold with temperature. In the devices with high loss, the injection efficiency could go down due to the increase in the carrier concentration in the active region necessary to create the higher gain. The higher than expected loss also may actually come from optical loss. The oxide could have excess roughness and create excess scattering, or the oxide could simply absorb light. However, this second loss mechanism, we will soon show is extremely small. Despite these discrepancies, the model provides a reasonable match with data and justifies the hypothesis that thinner (optically weaker) apertures and shorter cavities are enabling the scaling of the differential efficiency in actual devices.

Aperture Absorptive losses:

The aperture can absorb as well as scatter light creating additional size dependent losses. For oxides of AlGaAs, the material absorption is small enough around λ=1μm that accurate measurements of it have not been made,

but a relatively high upper bound on the absorption is α_{ox}=100cm^{-1}[22, 23] which is the measurable absorption in the UV from ellipsometry of thin films and estimated absorption in in-plane waveguides at 1µm[24]. Even with an absorption this high, the loss per pass is still estimated to be extremely small (negligible in comparison with scattering losses). In Figure 4-11, we show such an estimate which was made by using the effective index steps shown (Δn_d=0.004, 0.02 and 0.06) to calculate the mode for a step-index uniform waveguide. The fraction of power absorbed was determined from the overlap of the aperture and mode times $\alpha_{ox} t_{ox}$. (We're assuming the oxide is midway between a peak and null of the standing wave so that t_{ox} and the absorption scales linearly with Δn_d.) Although the lateral overlap of the aperture and the mode increases as the aperture gets thinner, the smaller thickness more than compensates so the overall absorption goes down. For the excess loss to be significant, the oxide thickness or the material absorption would need to be an order of magnitude higher.

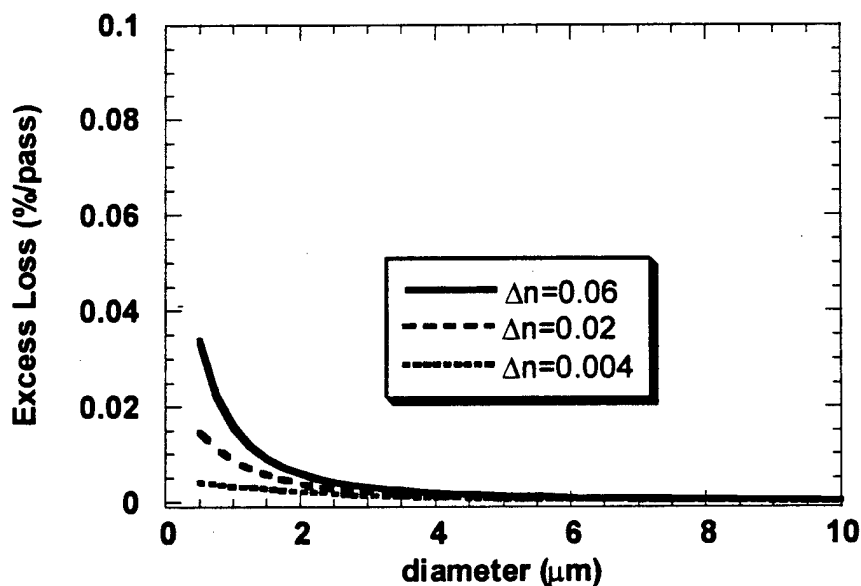Figure 4-11: Estimated absorptive loss if the oxide had 100cm^{-1} loss (for the purposes of estimating the mode an abrupt aperture was used). Notice the maximum of the vertical scale is only a fraction of the scale on the scattering loss graph.

Iterative Calculation of Mode and Scattering Losses

Although we found a simple estimate for the scattering loss from the coupling loss, we would like to verify the estimate and see what other subtleties of the problem there are to uncover. Unfortunately, the exact calculation of the mode and losses in the apertured VCL would require a full three-dimensional, vector solution of Maxwell's equations. A close approximation is to use a finite-difference approach to solve the 3-D scalar Helmholtz equation as is done in Ref. [25]. Other techniques which can be applied to the problem include finite difference beam-propagation [26] or the method of lines [27]. Here we will take a simpler approach, but account for the essential features of the problem not addressed by the single-pass coupling loss estimate: namely that the mode shape will be perturbed by periodic waveguiding and that the hard-mirror approximation is not exact. We follow a method analogous to the classic work of Fox and Li[28]. In that work, Fox and Li find the mode of a resonator formed by two mirrors and an opaque aperture. They propagate a scalar field (via the Fresnel integral) around an unfolded cavity until the field no longer changed shape (at which point it is considered a mode of the cavity). In this work, we will propagate a scalar field around a VCL cavity as shown schematically in Figure 4-12. This is an extension to two dimensions of the approach we took in [11].

To propagate the field in the mirrors and spacer regions, we decompose the field into its plane-wave Fourier components and multiply them by $R(k_x, k_y)$, the angular reflectivity spectrum of the DBR mirror *and* the spacer region. $R(k_x, k_y)$ is calculated using the transmission matrix method for a multilayer stack [29]. For simplicity, we have used equal mirror/spacer reflectivities. The multiplication in the Fourier domain is analogous to the diffraction of the mode through one cavity length (under the hard mirror approximation). Because the mode in a VCL is highly paraxial, the reflectivities for s and p polarized light are nearly equal. Nevertheless, to best approximate the actual polarization dependent problem, we used the *average* of the reflectivities for s-polarized and p-polarized waves, which is an accurate approximation for a linearly polarized, radially symmetric mode such as the fundamental lasing mode.

(Consider evaluating the integral in Eq. (32) in Ref. [7] for a radially symmetric mode.)

Absorbing boundary $l(x,y)$

$T(x,y)$

$R(k_x, k_y)$

Spacer+DBR

$R(k_x, k_y)$

$T(x,y)$

Phase Shift $\phi(x,y)$

Gain $g(x,y)$
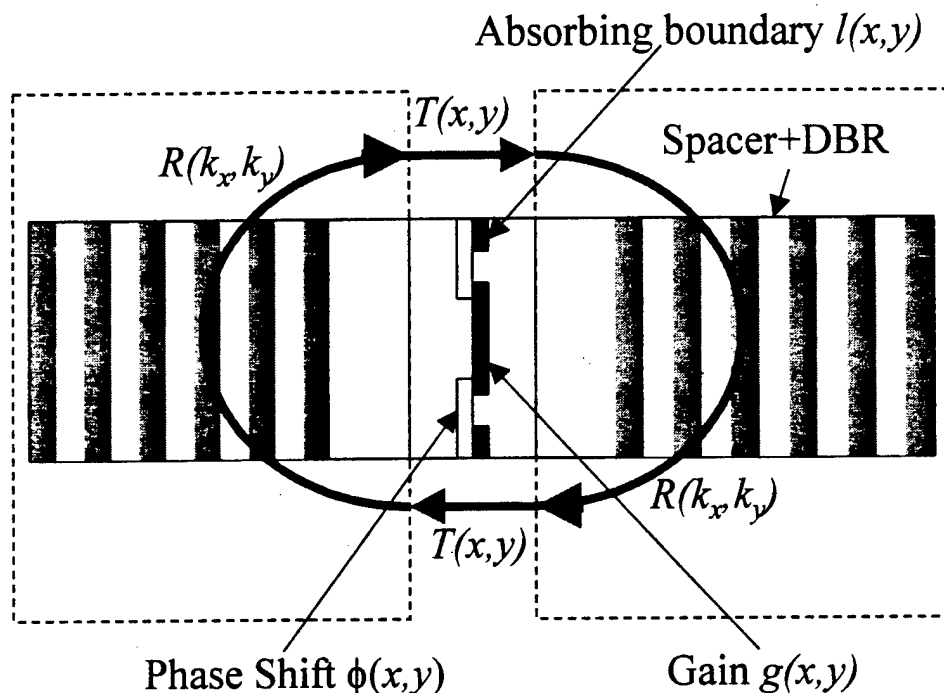
Figure 4-12: Schematic of the iterative model which incorporates the angular reflectivity spectrum of the DBR mirrors and a spatially dependent gain region in addition to the dielectric aperture. The arrows follow the path of the lateral field profile around the cavity. The field is alternately multiplied in the spatial domain by $T(x,y)$, and in the spatial frequency domain by $R(k_x, k_y)$, the angular reflection spectrum of the spacer region and the DBR mirror. The iteration ends when the lateral field profile changes only by a fixed phase shift from one pass to the next.

To propagate the field through the dielectric aperture, the field is given a position-dependent phase shift $\phi(x,y)$. At the same time, the field is passed through a position-dependent gain region $g(x,y)$ and an absorbing boundary $\ell(x,y)$. These position-dependent functions are contained in one factor

$$T(x,y) = \exp\left[g(x,y)/2 - \ell(x,y)/2 + j\phi(x,y)\right] \qquad (4\text{-}28)$$

We used a uniform gain i.e. $g(r < a) = g_0$ and $g(r \geq a) = 0$. As mentioned before the gain plays little role in the guiding. This was easily observed by setting $\phi(x,y)=0$ and obtaining a much larger mode. At the smallest sizes, g_0 will increase because the mode will expand beyond a. But this increase will not affect the modal gain which we will use to determine the scattering loss. The absorbing boundary is needed to prevent aliasing as a result of the FFT. The boundary is defined by $\ell(r < R_l) = 0$ and $\ell(r > R_l) = 0.2$. The edge of the boundary was adjusted based on the size of the mode so that moving it further away (increasing R_l) did not change the gain beyond the error in the calculation.

By sequentially diffracting the mode through the mirrors and passing it through the aperturing region, we propagate the mode around the VCL cavity (following the path shown in Figure 4-12). Formally, we can express sending the field through one round-trip as the operator, $\hat{Q}^2$

$$\hat{Q}^2 = \mathbf{F}^{-1} R(k_x, k_y) \mathbf{F}T\ (x,y) \mathbf{F}^{-1} R(k_x, k_y) \mathbf{F}T\ (x,y) \qquad (4\text{-}29)$$

To obtain the mode and gain of the VCL cavity, we begin by guessing the field, $\Psi(x,y)$, and then repeatedly propagating the field around the cavity (by applying $\hat{Q}$). During this process, the gain, g_0 is adjusted to match the losses. (We calculate the gain that will match the losses of the previous pass and then move the gain a fraction of the way to this value. In this manner, the gain is raised slowly so that higher order components and radiation not belonging to the lowest order mode will be stripped away.) The mode is propagated until the field only changes by a fixed phase from one pass to the next, i.e. $\Psi_{n+1} = \hat{Q}\Psi_n = e^{j\theta}\Psi_n$, where Ψ_n is the field after the nth pass and θ is a constant (spatially independent) phase shift. (This typically takes $1\text{-}4\times10^4$ iterations for the precision we desire for the gain.) At this point Ψ_n is considered to be a mode of the system. As in Fox and Li's analysis [28], we do not have fields simultaneously propagating left and right so resonance is not enforced (i.e. $\theta \neq 0$). As discussed in the section on lasing wavelengths, this sort of propagation leaves the wavelength fixed, but as far as diffraction is concerned, the error in the wavelength (around 0.1%) will not have a big effect.

Losses for abrupt apertures

The results for the scattering loss obtained from this iterative method (for abrupt apertures) are plotted as the solid lines in Figure 4-13. The scattering loss is defined relative to the loss, $\alpha_0 = 1 - |R(0,0)|^2$, for a plane wave at normal incidence. We determine the scattering loss, α_s, from the modal gain per pass, $G = \iint dxdy |\Psi_N|^2 e^{g(x,y)} - 1 = \alpha_0 + \alpha_S$ in which we have used Ψ_N, the normalized mode which satisfies $\iint dxdy |\Psi_N|^2 = 1$. During the simulation, we set the background absorptive losses in the mirror to zero. If included, we would also need to subtract these. See Eq. (4-16).

Figure 4-13 shows the loss vs. aperture radius for three different cases. In cases B and C, we use the *shorter cavity* of length L_C/n_0=0.327 µm, and for the case A, we use the *longer cavity* of length L_C/n_0=0.468 µm. The parameters for these cavities are given in Table 4-1. The lowest loss, case C, was produced with a small effective index step of Δn_d=0.02. From Figure 4-7, we see this step may be produced with a 12nm thick oxide aperture placed at the start of the first DBR layer. Case B, uses the same cavity length, but the index step is higher Δn_d=0.06 which could correspond to the same structure, but with an oxide aperture nearly filling the first quarter-wave layer (See Figure 4-7). This larger index discontinuity in case B leads to the higher losses.

In case A, we have a longer cavity length, increasing diffraction, but the index step is reduced to Δn_d=0.042 to yield the same phase shift per pass, ϕ, as in case B. Physically, this adjustment is the same as increasing the cavity length for a fixed aperture thickness.

From the cavity lengths and the index steps, we can determine the phase per pass, ϕ, and the Fresnel number, F, for a given aperture radius, and then compute the scattering loss based on the single-pass estimate presented in the previous section. The single-pass estimate for the scattering loss is shown by the dashed lines in Figure 4-13. The estimate matches to within ~10% with the iterative calculation even for different cavity lengths and index steps. One reason to expect a good match is because the modal overlap is better than 99%

between the lowest order mode of the uniform waveguide and the mode of the iterative calculation (even at the smallest aperture sizes).
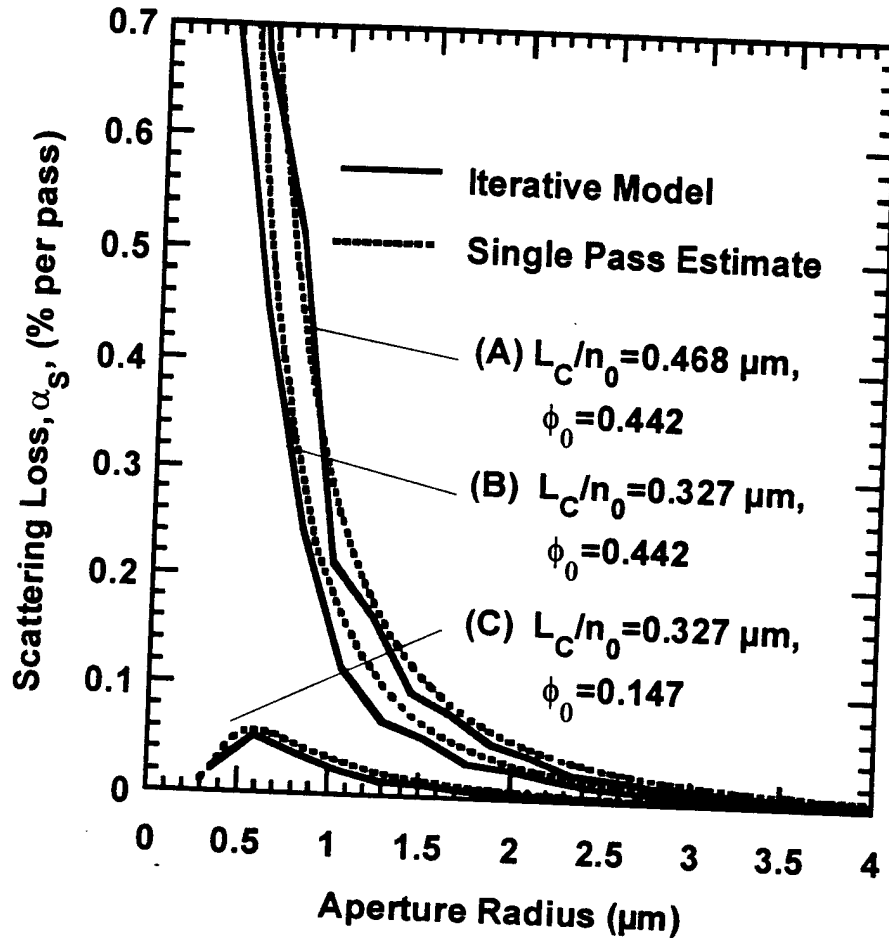

Figure 4-13: Comparison of the scattering losses calculated by the iterative model (solid lines) and by the single pass estimate (dashed lines). Cases (A) and (B) have apertures with the same effective phase shift per pass corresponding approximately to a 80nm oxide aperture in the first DBR layer.

Case (A) shows the loss for the *longer cavity* (See Table 4-1), which has a 1.5λ spacer region and $Al_{0.67}Ga_{0.33}As/GaAs$ mirrors. Case (B) shows the loss for the *shorter cavity*, (also in Table 4-1) which has a 1λ spacer region and binary AlAs/GaAs mirrors. Case (C) also uses the *shorter cavity*, but the aperture has a smaller phase shift per pass corresponding approximately to a 12nm oxide aperture placed at the first DBR interface.

Lastly, we should mention that the slight "bumpiness" in the curves is not due to lack of convergence or a limit to the spatial frequencies. Even more bumpiness is observed using hard mirrors in the iterative model. (In that case, losses also oscillates as a function of cavity length) The bumps are related to the lateral interference of waves and are also observed in other models. In fact, if you were to use the analysis by Marcuse[30] to compute the coupling from the fundamental mode of a uniform slab waveguide to radiation modes under a sinusodial perturbation along the z direction, you would see the coupling oscillate as a function of the aperture width and even drop to zero at some points.

	Shorter Cavity	*Longer Cavity*
Wavelength, λ (nm)	980	980
n_0	3.52	3.52
L_0	1λ	1.5λ
n_L	2.95	3.12
n_H	3.52	3.52
n_E	3.52	3.52
DBR Periods	21.5	30.5
L_C/n_0 (μm)	0.327	0.468

Table 4-1: Parameters for the cavities used in the iterative calculation

Losses for linearly tapered apertures

From the unfolded cavity picture, we know that the lowest scattering losses occur with a parabolic index profile. Although we cannot produce this in practice because the current also would be blocked, we can attempt to approach this ideal case by tapering the aperture.
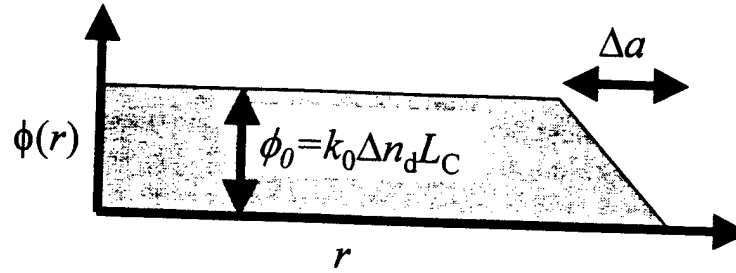
Figure 4-14: Phase shift for a linearly tapered aperture

For a linear taper we define the phase per pass as,

$$\phi(r) = \begin{cases} \phi_0 = k_0 \Delta n_d L & r < a \\ \phi_0 (a + \Delta a - r)/\Delta a & a \leq r < a + \Delta a \\ 0 & r \geq a + \Delta a \end{cases} \tag{4-30}$$

Pictorially, this equation is shown in Figure 4-14. Let us now compare different types and amounts of tapering. We would like to plot the loss vs. aperture size as before, but the radius of the aperture is not clear. We can make an appropriate comparison of optical loss if we compare modes of the same size. For the fundamental mode, we define the mode radius, a_m, by:

$$a_m = \sqrt{\frac{2}{\pi} \iint dx dy |\Psi|^2 / |\Psi(0,0)|^2} \tag{4-31}$$

For a Gaussian mode, a_m is the radius where the field^2 drops by $1/e^2$ from the peak. In Figure 4-15, we show the behavior of the mode radius vs. the inner aperture radius, a, for abrupt and linearly tapered apertures. For the abrupt apertures, we have also indicated with dots the size predicted from a uniform step-index waveguide model. Note how well it is able to predict the sizes except at the very smallest apertures. Also observe that the size of the mode will increase as the aperture closes for the smaller index step. This effect occurs as also expected in a uniform step-index waveguide.

With these considerations in mind, we now examine the scattering loss vs. the mode size for the two types of abrupt apertures, two apertures with different amounts of linear tapering and the ideal parabolic case. See Figure 4-16. For the abrupt aperture (Δa=0) with the larger index step, Δn_d=0.06, the mode size

scales with the aperture size and the losses increase for smaller sizes. For the smaller index step however, the mode size eventually expands at the smallest aperture size ($0.2\mu m$) and the losses decrease as also predicted from the single-pass coupling loss estimate. The aperture which is linearly tapered (as defined by Eq. (4-30)) over $\Delta a=0.7\mu m$ represents the best of both cases. Now the mode scales with the aperture size and the losses remain low. To compare designs, we ended the lines in Figure 4-16, at inner radius of a =0.2 μm. For the longer taper of $\Delta a=4\mu m$, the losses are low, but the mode does not shrink smaller than that of the lower, abrupt index step. We see if the taper is too short, then the scattering losses will approach the abrupt case. If the taper is too long, then the lateral confinement factor may become too small as the mode becomes much larger than the current aperture. Initially, this scenario is okay because the smaller active region will counter the lower confinement factor lowering the overall threshold current.
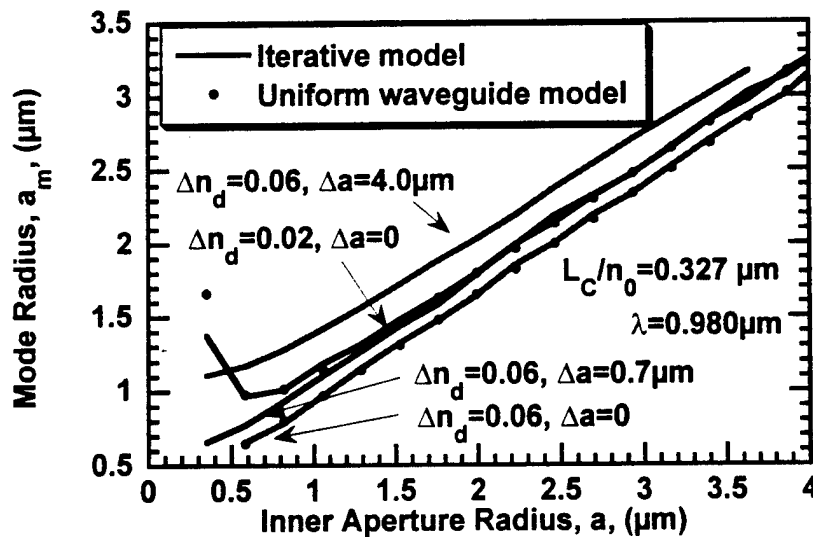
Figure 4-15: Mode radius vs. the inner aperture radius for abrupt and tapered apertures as calculated from the iterative model. The dots indicate the sizes predicted for modes of a step-index waveguide appropriate for the abrupt apertures

In practice, it is hard for a long taper to significantly lower the confinement factor because the current and carriers spread out. But a greater concern when making the taper long is the electrical resistance one will have for a given mode size. Another issue is the total thickness of the aperture - even when tapered - not because of the optical losses, but because of the multimodedness it creates. Even numerically it takes much longer to find the fundamental mode because the higher order modes want to stick around. But many modes all lasing in a small device may be desired when using multimode fiber. Here a thick tapered aperture is the way to go.

As mentioned in the discussion of the single pass coupling loss estimate, we can attempt to estimate the scattering losses for a tapered aperture using a step-index waveguide mode or a Gaussian. For the case of $\Delta n_d = 0.06$ and $\Delta a = 0.7 \mu m$, we can use the uniform waveguide mode found by assuming the same index step occurring exactly in the middle of the taper. For this mode, the losses were about a factor of two lower than those for the abrupt aperture, but still several times higher than those calculated with the iterative model. Using a Gaussian chosen with the same mode radius as in the iterative model, the losses are lower than the first estimate at the smallest size, but higher at the larger sizes. Though using the step-index uniform waveguide mode shows the correct trend, it appears one must turn to the iterative model for accurate calculation of losses with tapered apertures.
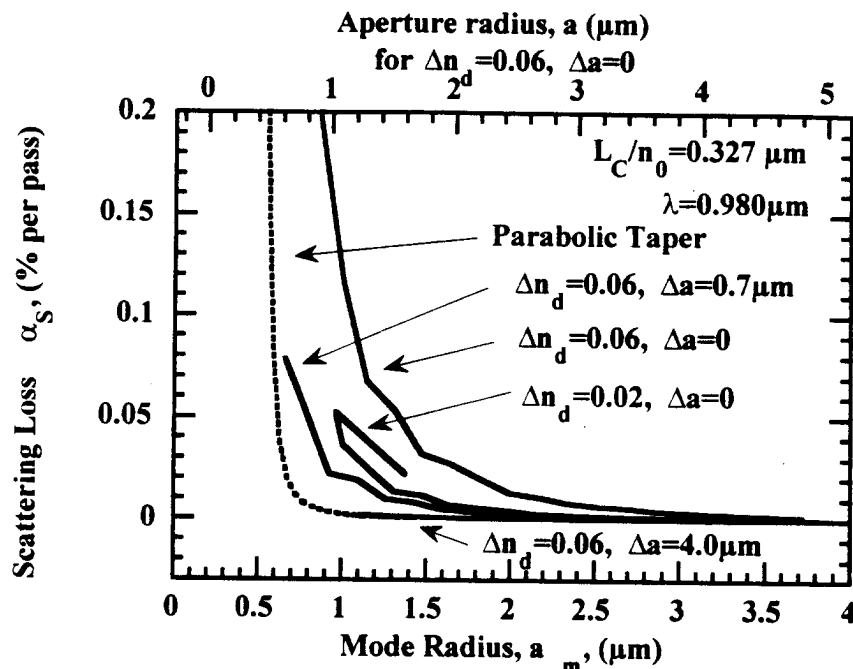
Figure 4-16: Scattering loss calculated for parabolic, linearly tapered and abrupt apertures using the *shorter cavity* (See Table 4-1). The upper two curves for abrupt apertures (Δa=0) are from the same calculations for cases (B) and (C) in Figure 4-13 plotted here vs. the mode radius. The curves above were generated by varying the aperture inner radius or shape (in the case of a parabola) calculating the mode radius and scattering loss. Although the doubled valued curve for Δn_d=0.02 looks odd, it can be explained as follows: As shown in Figure 4-15, the same mode radius may be created two different aperture sizes because under weak index guiding the mode starts expanding even as the size of the aperture is reduced. The larger mode diffracts less and therefore has lower scattering loss as is also predicted from the single pass estimate shown on curve (C) in Figure 4-13.

For the larger index-step (0.06) there is a one-to-one relation between the mode size and aperture size (for the sizes of interest) and so we have indicated in the upper axis this aperture radius. The losses for the parabolic taper increase rapidly below 0.5 μm since the mode diffracts at angles not strongly reflected within the first few DBR periods. The solid curve for the longer linear taper (Δa = 4.0 μm) initially overlaps the dashed curve for the parabolic taper; however, the aperture closes, and the long linear taper cannot produce the smallest mode sizes

Losses for a parabolic taper and the DBR angular stop band

The parabolic case (with $\phi(r) = -k_0 n_0 r^2/(2f)$ as discussed during the single pass coupling loss estimate of scattering loss) is indicated by the dashed line in Figure 4-16 which at larger sizes is overlapped by the solid line for the tapered case of Δa=4μm. As expected, the parabolic profile produces the least loss for the smallest size modes. However, the losses abruptly increase below a radius of 0.6μm. This corresponds to a Fresnel number around one, which we calculate using the mode radius for the characteristic size, i.e., $a=a_m$. This rise does not occur under the hard-mirror approximation since the cavity is still stable for this focal length. By examining the modal reflectivity from the DBR, we find this increase is caused when the mode size decreases so much that its angular spread exceeds the angular DBR stop-band. Examples of the reflectivity vs. angle are shown in Figure 4-17. We see that the apparent "stop-band" of the mirror is sometimes masked by the last interface. When the DBR ends on air, rays at steep angles are simply totally internally reflected. However, what also matters is how far the rays travel on average before being reflected. Effectively what happens is shown in Figure 4-18. The light that hits the last interface travels so far that it cannot recombine with the mode. Regardless of the final interface we can quantify the "correct" angular stop band, but we need to define yet another DBR penetration depth.
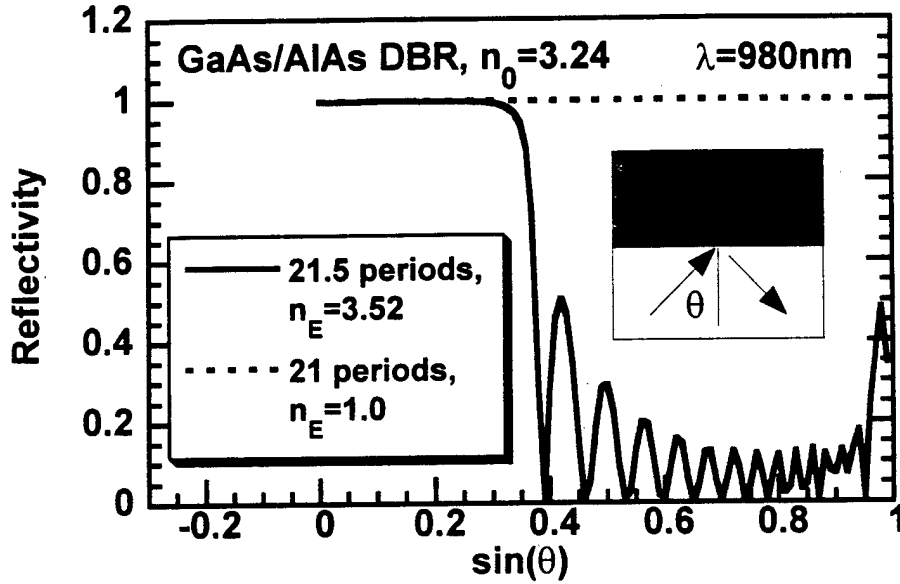
Figure 4-17: Reflectivity Spectrum vs. angle (as viewed from inside AlGaAs) for GaAs/AlAs DBRs ending on GaAs and on air

Aside: DBR mirror ray penetration depth

For small angles, the diffraction equivalent length of the mirror is defined from the change in phase of the reflection, $\Phi(k_r)$ vs. incident angle, θ, (see the inset of Figure 4-17) or equivalently the radial component of the incident k-vector, $k_r = k_0 \sin(\theta)$[7]. Consider a packet of rays pointing in the direction θ_0, but also localized in space say around $x,y=0$. Upon reflection from the DBR, the ray packet be localized away from the origin, say around $x=x_0, y=0$, and the packet will also spread out laterally. Of course, when θ_0 is zero, the packet only spreads laterally is still centered at $x,y=0$. As we know this spatial dispersion is found from the second derivative of the phase and that defines the diffraction

equivalent DBR length, $L_D = -\dfrac{k_0 n_0}{2} \dfrac{d^2\Phi}{dk_r^2}\bigg|_{k_r=0}$ [7]. For a packet of rays

pointing at $\theta_0 \neq 0$, the packet will be translated laterally upon reflection, and

the amount of translation will depend on the first derivative of the phase (as we know from Fourier analysis).

Total internal reflection
at air/semiconductor interface

Ray scattered
off-axis

Aperture

Re-circulating mode

Mirror with limited
angular stop-band
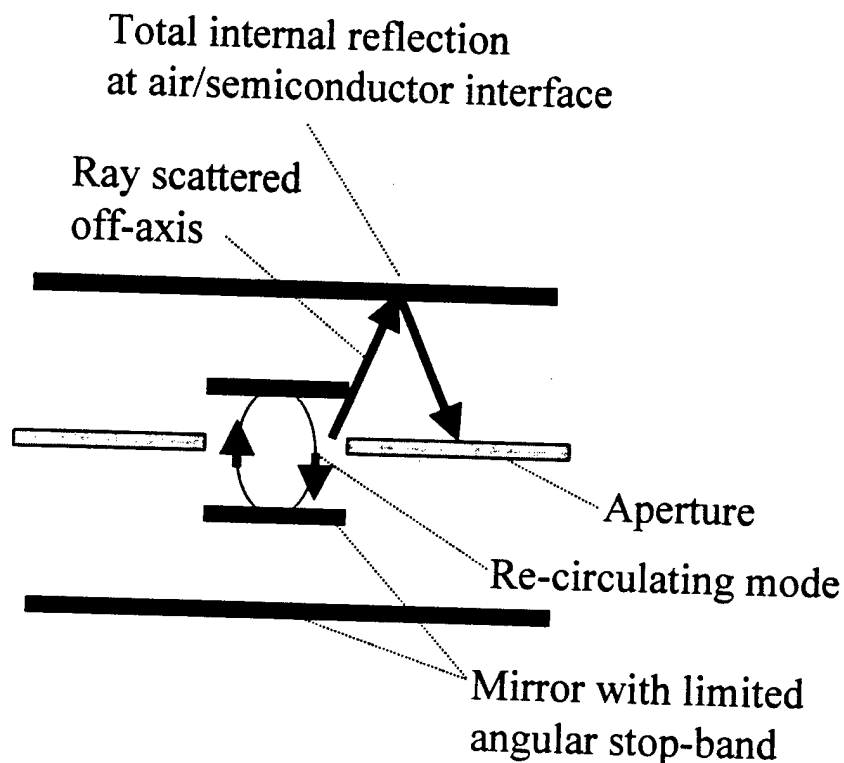
Figure 4-18: Ray trace of scattered light interacting with a real DBR with a limited angular stop-band. For AlGaAs/GaAs mirrors the angular stop-band is not much wider than about 16°. The light beyond this angle will travel through the DBR, but eventually will hit some air interface (either at the end of the mirror as shown or the bottom of the substrate) Light at such an angle will be totally internally reflected and move out laterally. (In the numerical model such light will be captured by the absorbing boundary.) For mirrors with a wider angular stop-band, higher angle rays (and hence smaller modes) can be confined better. For mirrors with an angular stop-band much smaller than a GaAs/AlAs DBR, one may be able to collect some of the scattered light so the slope efficiency will be higher than expected despite an increase in gain.

If the ray packet had traveled a distance L_R and back through a medium of index, n_0, then the phase shift and first derivative would be given by:

$$\Phi_{free} = 2k_z L_R$$

$$d\Phi_{free}/dk_r = -2k_r L_R/k_z \qquad (4\text{-}32)$$

where $k_Z = \sqrt{(k_0 n_0)^2 - k_r^2}$. Reversing the idea, we can find the equivalent ray penetration depth for a DBR mirror from, $L_R = -\dfrac{k_z}{2k_r}\dfrac{d\Phi}{dk_r}$. Although L_R is not defined precisely at $k_r=0$, as $k_r \rightarrow 0$, $L_R \rightarrow L_D$ for a DBR mirror (i.e. a reflector normal to the incident light). We have computed the ray penetration depth vs. $\sin(\theta)$ for the GaAs/AlAs DBRs we showed in Figure 4-17. Results of this calculation are shown in Figure 4-19.
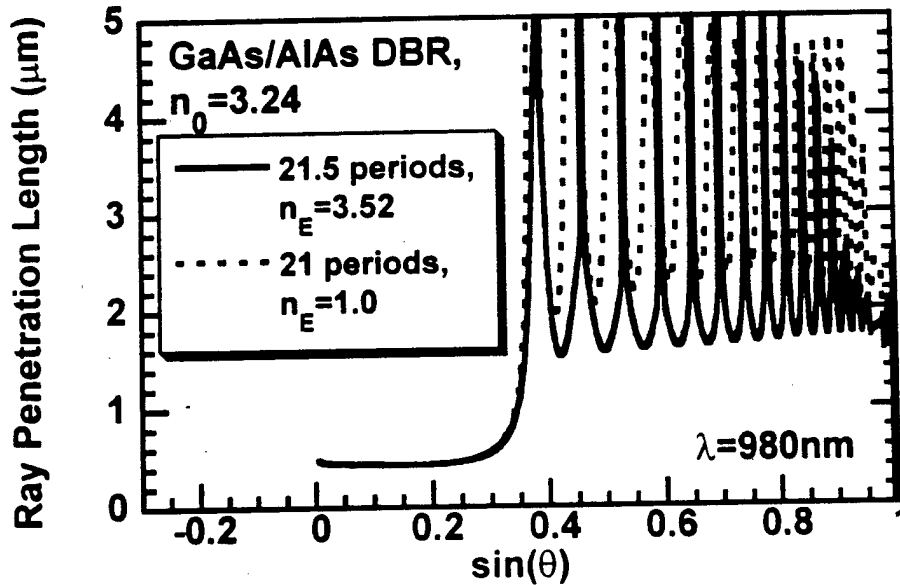
Figure 4-19: Ray penetration length of a GaAs/AlAs DBR vs. angle as extracted from the variation in the phase shift of the reflected wave vs. sin(incident angle). For small angles the cavity length is constant and thus may be approximated well as a reflection from a single surface. However, rays at large angles travel on average much further before being reflected.

As expected the penetration depth is relatively constant near θ=0, but much larger for steeper angles. We see now that the index of the ending material has little effect on the ray penetration length angular "stop-band".

This ray penetration length angular stop-band can be made larger by using a DBR with a higher index contrast and thus a shorter L_D. Figure 4-20 shows two examples using different dielectric mirrors.
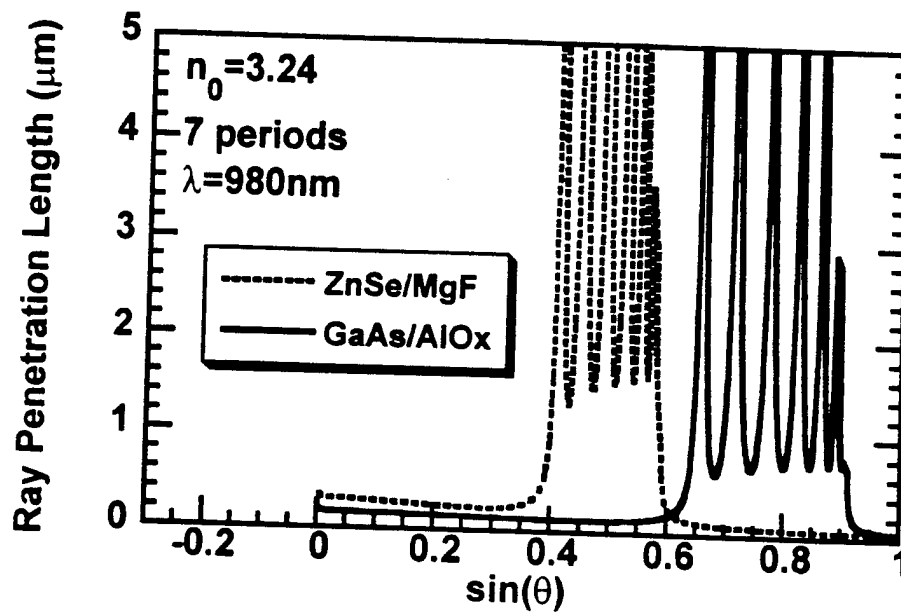
Figure 4-20: Ray penetration depth vs. angle for higher index contrast DBRs. The dashed line is for a seven pair quarter-wave stack with n_{ZnSe}=2.48, n_{MgF}=1.36. The solid line is for a λ/8 AlOx + 3λ/8 GaAs seven pair stack with n_{AlOx}=1.55, n_{GaAs}=3.52.

Although the rays are evanescent in the ZnSe above sin(θ)=0.55, they still tunnel through to the MgF where they can interfere and produce the oscillations shown. But above sin(θ)=0.76, the rays are evanescent in both the ZnSe and MgF so no oscillations are observed. For the AlOx/GaAs, the rays are never evanescent in the GaAs so this does not happen. Interestingly, the ZnSe/MgF mirror does not have a much wider angular stop band than the GaAs/AlAs mirror based on the ray penetration depth.

Other Optical Confinement Issues outside the Iterative model

Multiple Apertures

Using multiple apertures is one way around the problem of the DBR angular stop-band. One can add apertures to keep the mode focused as it moves into the DBR. However, extra apertures can also cause extra scattering. To have the iterative model work with two apertures in the mirrors would mean the mirror reflectivity could not be handled in the Fourier domain, among other complications, but we can turn back to the single pass coupling loss estimate to get a clue about the excess loss of multiple apertures.

For the case of two apertures in the cavity, then the amount of excess loss will depend upon the spacing of the apertures. We are still considering apertures placed symmetrically about the center. (See Figure 4-21) If the apertures are spaced by a cavity length or they are right next to each other, then they will effectively act like one thicker aperture, and consequently, scattering losses will be increased. However, when the apertures are evenly spaced (in the unfolded cavity), then the mode diffracts over only half a cavity length before being partially refocused by the aperture. One may treat two apertures in a cavity as two separate cavities of length L_S and L_C-L_s, with each cavity having an effective phase shift of $\phi_{1eff} = \phi_T L_s / L_C$ and $\phi_{2eff} = \phi_T (L_C - L_s) / L_C$. ($\phi_T$ is the total effective phase shift of both apertures.) The analysis ignores the variation of the aperture thickness, but accounts for the variation in the spacing. To first order, we can add the losses from the two cavities, and then the total loss is given by

$$\alpha_s = 2.28 \frac{\phi_T^{1.19}}{F^{1.3}} \exp\left[-\frac{0.206}{\phi_T F}\right]\left(\left[\frac{L_S}{L_C}\right]^{2.49} + \left[1 - \frac{L_S}{L_C}\right]^{2.49}\right) \qquad (4\text{-}33)$$

(a)

$$\phi_{2eff} = \phi_T (L_C - L_S)/L_C$$

$$\phi_{1eff} = \phi_T L_S/L_C$$

$$\phi_T = \phi_1 + \phi_2$$

(b)
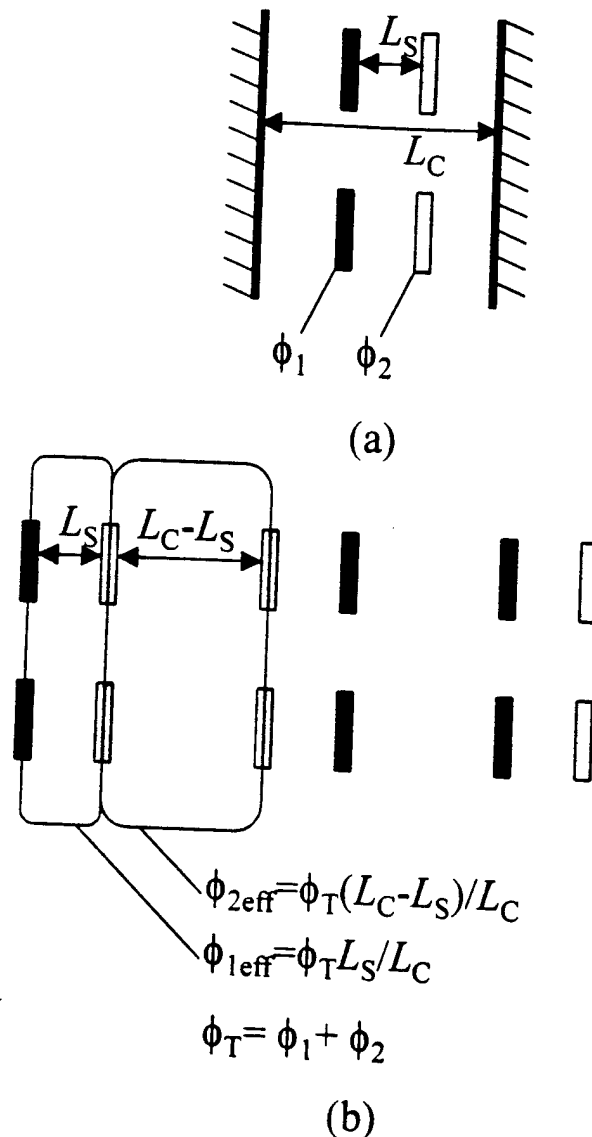
Figure 4-21: (a) Cavity with hard mirrors and two apertures (b) An unfolded double apertured cavity. The phase shifts can be distributed uniformly across two different cavities and then the scattering losses can be estimated from the single aperture model.

Figure 4-22 plots the relative scattering losses for various aperture designs. By distributing the total effective phase shift over two apertures (instead of one) scattering losses can be more than halved. However, simply adding a second

aperture to the cavity (and thereby doubling the total effective phase shift) generally gives higher losses unless the separation between apertures is close to half a cavity length.
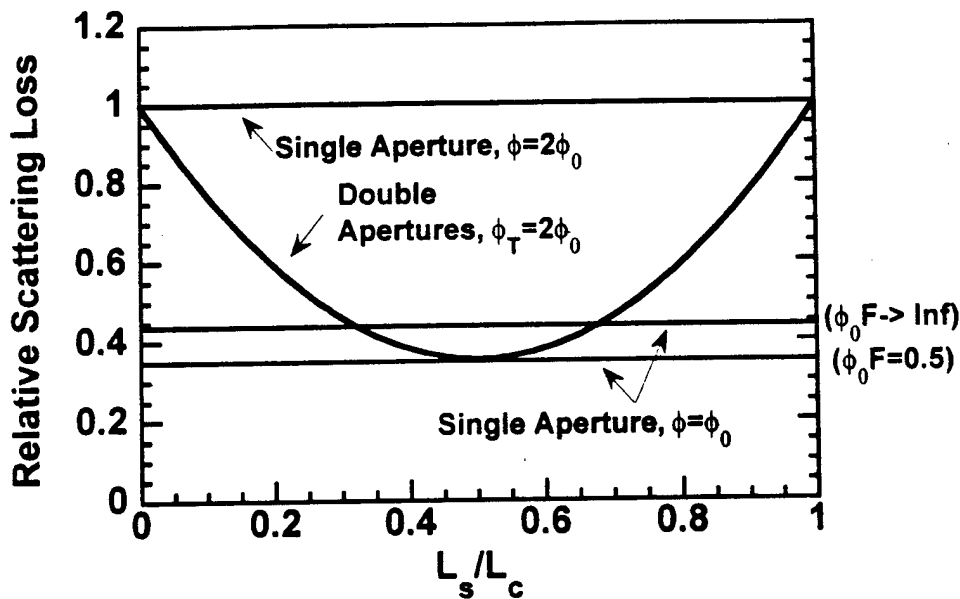
Figure 4-22: Estimate of the relative scattering loss for single vs. double aperture designs which depend on the relative spacing of the apertures

Strong Reflections off the aperture

Using the distributed index difference to calculate the phase shift per pass allows us to account fairly accurately for the essential effects of reflections off of the aperture. (As Jeff Scott shows in his thesis[31], the enhancement factor for a layer can be deduced from the left and rightward waves reflecting off a layer.) Even strong reflections will have similar effects and this approach will account (to some degree) for them. The main effect missed by only changing the phase is that the reflections from the aperture will lower the mirror transmission in the apertured regions. Essentially this is a form of gain (or loss) guiding, which is typically dominated by the index guiding. However,

the reflections from the oxide are more important when the oxide is in the output mirror. In that case the change in total mirror loss round-trip is much more dramatic than when the oxide is placed in the higher reflectivity mirror. This change in transmission can sometimes promote lasing under the oxide for higher order modes.

Potentially, reflections from a tapered aperture could create higher scattering loss as illustrated in Figure 4-23. But for an oxide/semiconductor interface to have total internal reflection, the angle would need to be $> 26°$. In addition, the aperture would need to be thick or the light will simply tunnel through instead of reflecting. The apertures in this work have taper angles $<\sim4°$ and relatively thin, so this effect does not come into play. Other simulations (which include the reflections) of properly designed tapered apertures have shown very low losses[32] indicating that in theory this angled reflection is normally not significant.

$\theta >\sim 26°$
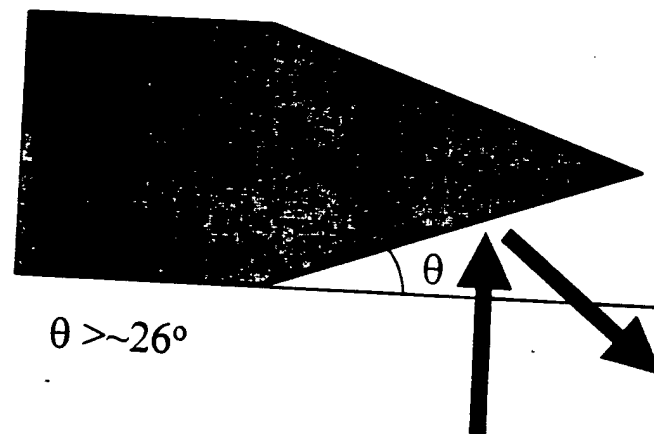
Figure 4-23: Strong reflections from thick, steeply tapered apertures could adversely effect optical confinement. (Angles used in this work are much smaller.)

Comment on Evanescent Rays

The iterative model considers only the energy travelling around the cavity and must use only propagating rays i.e. $k_r < k_0 n_0$. So the mode is not calculated to any higher spatial resolution than $\Delta x = \lambda/(2n_0)$. Waves evanescent in the semiconductor may compose the mode around the aperture (particularly to

match abrupt changes in index). However, it would not be physical to let these "propagate" around like rays in the unfolded cavity because they do not carry any power. If we were to by multiply these high Fourier components by $\exp(-ik_z z)$ when k_z is pure imaginary, then we would appear to diminish the power in the mode which is not what happens.

To handle these waves properly, we would need to consider reflections from the aperture. In the simplest of cases, when a plane wave hits a single interface above the critical angle, all the power in the plane wave gets reflected back, but transmitted "wave" is evanescent. Similarly, if a wave-packet containing only propagating waves hits the aperture and the transmitted wave packet contains evanescent waves, then to conserve power some propagating waves must be reflected. Thus, if we ignore reflections from the aperture, we must also limit the spatial bandwidth of the wavefunction.

Summary and Conclusions:

In this chapter, we have described the guiding in index apertured vertical cavity lasers. As far as the mode shape and the wavelength spacing, the guiding can very well be approximated as a uniform waveguide except at sizes around $1\mu m$ diameter (for $\lambda = 1\mu m$ VCSELs). However, if we think in terms of the modes of a uniform waveguide, then the fundamental mode of the actual apertured VCSEL will be some superposition of the lowest order uniform waveguide mode and higher order and radiation modes. A small coupling to radiation modes may mean little for the mode shape or wavelength, but it means much for the gain because the VCSEL needs such a high Q cavity. The calculations in this chapter showed that some of the first oxide VCSEL designs with 80nm thick apertures had significant scattering loss below diameters of $4\mu m$. From the picture of an unfolded cavity, we can see the scattering loss can be reduced by making the aperture more lens-like which would mean tapering the thickness. And we would also expect that if we could construct the equivalent waveguide, but with more frequent apertures the guiding would also be improved. These changes would mean shortening the cavity length and reducing the effective optical strength of the aperture. The calculations presented in this chapter verify these intuitions and furthermore allow us to state more strongly that simply by shortening the cavity length (despite

stronger effective guiding), the loss will be reduced. Reducing the optical strength of the aperture is equally effective at lowering scattering losses and easier in practice than shortening the cavity. The analysis presented allows one to estimate the scattering losses for single, abrupt apertures using a simple formula depending only on the Fresnel number and the effective phase shift of the aperture. As we described, this effective phase shift can be found from the aperture overlap with the standing-wave or, as done by Hadley[8], from the change in cavity resonance. This effective phase shift is highly dependent on the position of the aperture in the longitudinal standing wave.

These estimates of the scattering loss helped explain the drop in slope efficiency of small devices and led researchers here, like Thibeault[15], and Margalit[33], and elsewhere[3, 4, 34] to start using thinner or optically weaker apertures. An iterative model for the mode and scattering losses using the actual VCSEL mirrors showed the simpler single-pass coupling loss estimate is fairly accurate except for mode sizes around $1\mu m$ diameter which are so small that the finite angular stop band of a GaAs/AlAs DBR cannot support their wide k-vector spectrum. (To quantify this limit we introduced the ray penetration depth of a DBR).

Higher index contrast mirrors are one way to beat the limit on mode size or alternatively one may use multiple thin apertures. The reduction of scattering losses from additional apertures depends how well separated they are. If two apertures are too close, then they will have higher losses than a single, thinner aperture. We made a simple estimate for the loss by modifying the earlier estimate for single apertures. Given diffusion of carriers it may not be advantageous to confine modes smaller than $1\mu m$ unless you really want a microcavity. (In fact, the threshold can even be lower when a slightly larger mode is pumped in the center.)

In the remainder of the thesis, we will examine experimentally the use of tapered apertures for reduction of the scattering losses. (In addition, we will examine other issues such as aperture placement for current confinement and the improvements in wall-plug efficiency at lower optical powers.) As we calculated, tapered apertures (provided the index gradient is low enough)

should have much lower excess losses than abrupt apertures of the same thickness. As far as scattering losses for the fundamental mode, very thin apertures placed at a null have comparable losses. However, if one wants to guide higher order modes with low losses in order to make smaller multimode VCSELs for use with multimode fiber, then thick, tapered apertures have an advantage optically over thin apertures. As we will later describe tapered apertures also have an advantage for lower capacitance.

References:

[1]   B. J. Thibeault, "High Efficiency Vertical Cavity Lasers Using Low-Optical Loss Intra-Cavity Dielectric Apertures", Ph.D. Dissertation, Electrical and Computer Engineering, University of California, 1997

[2]   B. J. Thibeault, E. R. Hegblom, Y. A. Akulova, P. D. Floyd, J. Ko, R. Naone, and L. A. Coldren, "Electrical and optical losses in dielectrically-apertured vertical-cavity lasers," in *Proc. SPIE Photonics West '97*, Vol. 3003-12, 1997.

[3]   K. D. Choquette, W. W. Chow, G. R. Hadley, H. Q. Hou, and K. M. Geib, "Scalability of Small-Aperture Selectively Oxidized Vertical Cavity Lasers," *Appl. Phys. Lett.*, vol. 70, pp. 823-825, 1997.

[4]   A. E. Bond, P. D. Dapkus, and J. D. O'Brien, "Aperture Placement Effects in Oxide-Defined Vertical Cavity Surface-Emitting Lasers," *IEEE Photon. Tech. Lett.*, vol. 10, pp. 1362-1363, 1998.

[5]   R. H. Yan, Z. M. Chuang, S. W. Corzine, and L. A. Coldren, "Simultaneous gain and phase-shift enhancements in periodic gain structures," *J. Appl. Phys.*, vol. 67, pp. 4387-4389, 1990.

[6]   D. I. Babic and S. W. Corzine, "Analytic Expressions for the Reflection Delay, Penetration Depth, and Absorptance of Quarter-Wave Dielectric Mirrors," *IEEE J. Quantum Electron.*, vol. 28, pp. 514-524, 1992.

[7]   D. I. Babic, Y. Chung, N. Dagli, and J. E. Bowers, "Modal Reflection of Quarter-Wave Mirrors in Vertical-Cavity Lasers," *IEEE J. Quantum Electron.*, vol. 29, pp. 1950-1955, 1993.

[8]   G. R. Hadley, "Effective index model for vertical-cavity surface-emitting lasers," *Opt. Lett.*, vol. 20, pp. 1483-1485, 1995.

[9]   D. I. Babic, R. J. Ram, and J. E. Bowers, "Scaling Laws for gain-guided vertical cavity lasers with distributed Bragg reflectors," *Appl. Phys. Lett.*, vol. 64, pp. 1762-1764, 1994.

[10]   J. T. Verdeyen, Chapters 4 and 5 in *Laser Electronics*, 3rd. New Jersey: Prentice-Hall, 1995.

[11]   E. R. Hegblom, D. I. Babic, B. J. Thibeault, and L. A. Coldren, "Estimation of Scattering Losses in Dielectrically Apertured Vertical Cavity Lasers," *Appl. Phys. Lett.*, vol. 68, pp. 1757-1759, 1996.

[12]   M. D. Feit and J. A. Fleck, "Light Propagation in graded-index optical fibers," *Appl. Opt.*, vol. 17, pp. 3990-3998, 1978.

[13]   B. E. A. Saleh and M. C. Teich, Chapters 4 and 8 in *Fundamentals of Photonics*. New York: Wiley, 1991.

[14]   K. L. Lear, K. D. Choquette, R. P. Schneider, and S. P. Kilcoyne, "Modal analysis of a small surface emitting laser with a selectively oxidized waveguide," *Appl. Phys. Lett.*, vol. 66, pp. 2616-2619, 1995.

[15]   B. J. Thibeault, E. R. Hegblom, P. D. Floyd, R. Naone, Y. Akulova, and L. A. Coldren, "Reduced Optical Scattering Loss in Vertical-Cavity Lasers Using a Thin (300Å) Oxide Aperture," *IEEE Photon. Tech. Lett.*, vol. 8, pp. 593-596, 1996.

[16]   P. D. Floyd, B. J. Thibeault, E. R. Hegblom, J. Ko, and L. A. Coldren, "Comparison of Optical Losses in Dielectric Apertured Vertical-Cavity Lasers," *IEEE Photon. Technol. Lett.*, vol. 8, pp. 590-592, 1996.

[17]   D. B. Young, J. W. Scott, F. H. Peters, M. G. Peters, M. L. Majewski, B. J. Thibeault, S. W. Corzine, and L. A. Coldren, "Enhanced Performance of Offset-Gain High-Barrier Vertical-Cavity Surface-Emitting Lasers," *IEEE J. Quantum Electron.*, vol. 29, pp. 2013-2021, 1993.

[18]   R. L. Liboff, Chapter 13 in *Introductory Quantum Mechanics*, 2nd. Reading, Massachusetts: Addison-Wesley, 1992.

[19]   L. A. Coldren and S. W. Corzine, Chapter 6 in *Diode Lasers and Photonic Integrated Circuits*. New York: Wiley, 1995.

[20]   B. J. Thibeault, T. A. Strand, T. Wipiejewski, M. G. Peters, D. B. Young, S. W. Corzine, L. A. Coldren, and J. W. Scott, "Evaluating the effects of optical and carrier losses in etched post vertical cavity lasers," *J. Appl. Phys.*, vol. 78, pp. 5871-5876, 1995.

[21]   D. L. Huffaker, L. A. Graham, H. Deng, and D. G. Deppe, "Sub-40 µA Continuous-Wave Lasing in an Oxidized Vertical-Cavity Surface-Emitting Laser with Dielectric Mirrors," *IEEE Photon. Technol. Lett.*, vol. 8, pp. 974-976, 1996.

[22]   K. J. Knopp, R. P. Mirin, K. A. Bertness, D. H. Christensen, and R. A. Synowicki, "Optical Properties of Native-Oxide Antireflection coatings on GaAs," in *Proc. Electronic Materials Conference*, paper no. BB9, 1998.

[23]   K. J. Knopp, knopp@boulder.nist.gov, Personal Communication, 1998

[24]   A. Fiore, , Personal Communication, 1998

[25]   G. R. Hadley, "Optical Modeling of Vertical Cavity Surface Emitting Lasers," in *Proc. IEEE LEOS '96*, TuB1, 1996.

[26]   H. Bissessur and K. Iga, "FD-BPM modeling of vertical-cavity surface-emitting lasers," in *Proc. Photonics West '97*, paper no. 2994-13, 1997.

[27]   R. Pregla, "MoL-BPM method of lines based beam propagation method," in *Methods for Modeling and Simulation of Guided -Wave Optoelectronic Devices*, vol. PIER 11, *Progress in Electromagnetic research*, W. Huang, Ed. Cambridge, MA, 1995.

[28]   A. G. Fox and T. Li, "Resonant modes of a maser interferometer," *Bell Sys. Tech. J.*, vol. 40, pp. 453-473, 1961.

[29]   P. Yeh, *Optical Waves in Layered Media*. New York: Wiley, 1988.

[30]   D. Marcuse, *Theory of Dielectric Optical Waveguides*. Boston: Academic Press, 1991.

[31]   J. W. Scott, "Design, Fabrication and Characterization of High-Speed Intra-Cavity Contacted Vertical Cavity Lasers", Ph.D. dissertation, ECE Technical Report #95-06, University of California, 1995

[32]   R. Hadley, , Personal Communication, 1998

[33]   N. M. Margalit, "High-Temperature Long-Wavelength Vertical Cavity Lasers", Ph. D. Dissertation, ECE Technical Report #98-15, University of California, 1998

[34]   B. Weigl, M. Grabherr, C. Jung, R. Jager, G. Reiner, R. Michalzik, D. Sowada, and K. J. Ebeling, "High Performance Oxide-Confined GaAs VCSELs," *IEEE J. Selected Topics in Quantum Electron.*, vol. 3, pp. 409-415, 1997.

Chapter 5 :
Current Spreading

Introduction

As discussed in Chapter 2, scaling of the threshold current density in apertured vertical cavity lasers is limited by scattering losses, current spreading, and carrier diffusion. Here we discuss current spreading in more detail and derive the scaling relations previously used.

The simple analytic estimate we derive here for the increase in threshold has allowed several researchers here (Margalit[1], Thibeault[2], Akulova[3]) to make sense of the scaling of threshold current and to exclude other effects such as diffusion or lowering of the injection efficiency to explain their results.

Not only does the analysis yield a simple formula for the excess current at threshold, but just as importantly it shows that current spreading should only negligibly reduce the differential efficiency as implied by experiment.

In addition, the analysis of the spreading can be applied to double aperture active regions almost as easily as single apertured ones. This allows us to estimate the merit of current confinement on both sides of the active region.

We show the original application of the analysis to make sense of the excess threshold in the thin, abrupt aperture devices of Thibeault[4]. And in the next chapter, we will also analyze the tapered apertured devices featured in this work.

To prevent the current from spreading one simply could leave the region below the aperture undoped. However, it is desirable to dope next to the aperture for several reasons. One may wish to keep the intrinsic region short to avoid long transport times limiting the laser's speed.[5] Or as we found, it is necessary to ensure the grade down from the high aluminum content region with the aperture is doped to avoid high turn-on voltages. Thirdly, an oxide placed in an intrinsic region near the active layers can result in severe non-radiative recombination at the oxide semiconductor interface or perhaps shorter laser lifetimes. For these reasons, it is useful for the VCL designer to have a simple estimate for the effects of current spreading in order to evaluate the trade-offs in performance.

We consider a simplified version of the current spreading problem in which the region below the circular aperture is modeled as resistive sheet on top of a diode. This approach was first used for in-plane lasers to determine the increase in threshold due to spreading.[6-8] However, it has not been pursued to the same extent for VCLs.[9] So here we will find a simple form for the change in threshold for a radial geometry, examine the effect on the differential efficiency and then use the model to explain the scaling of the threshold current in a real VCL.

Electrical Model

Figure 5-1a. shows a schematic of a portion of the VCL structure. Current flows through an aperture of radius, R into a layer of sheet resistance ρ_s $(\Omega/\square) = \rho/t$ and through a layer with a diode J-V characteristic. (ρ is the resistivity and t is the thickness of the layer). The additional current necessary

to reach threshold may be estimated by assuming a uniform voltage across the aperture opening and then determining the current which flows beyond the aperture edge given the voltage, V_{IN}, at $r=R$.

(a)

(b)

(c)
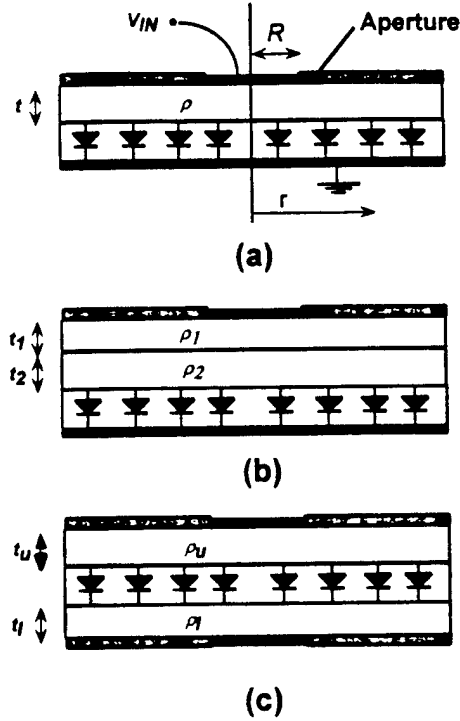
Figure 5-1: Schematics of the electrical structure around the active region in an apertured VCL with (a) a single resistive layer, (b) multiple layers, (c) double apertures

As the current moves radially outward through a small annulus (of width, dr), it encounters a voltage drop due to the resistive layer.

$$dV = -\frac{\rho_s dr}{2\pi r} I(r) \tag{5-1}$$

And the lateral current decreases due to current being sunk vertically by the diode.

$$dI = -(2\pi r)dr J_D(V(r)) \tag{5-2}$$

where $J_D(V) = J_o(\exp[qV/(\eta kT)] - 1)$ is the J-V characteristic of the diode layer.

Here we note that this formulation of the problem can be generalized by modifying ρ_s. For two (or multiple) resistive layers of resistivity ρ_1 and ρ_2 and thickness t_1 and t_2 as shown in Figure 5-1b, then we use the parallel sheet resistance of these layers,

$$\frac{1}{\rho_s} = \frac{t_1}{\rho_1} + \frac{t_2}{\rho_2}$$

(5-3)

Double Apertures

In the case of two apertures (as shown in Figure 5-1c), we need to consider the voltage drop through the upper the upper resistive layer and the lower resistive layer in Eq (5-1). So we simply have to use a sheet resistance which is the series combination of the resistance of the upper and lower layers

$$\rho_s = \frac{\rho_u}{t_u} + \frac{\rho_l}{t_l}$$

(5-4)

where ρ_u and ρ_l are the resistivities and t_u and t_l are the thicknesses of the upper and lower layers, respectively. Since the hole mobility is about twenty times less than the electron mobility in AlGaAs, we conclude that for similar doping levels and thicknesses, adding an aperture on the n-side provides less than a five percent increase in ρ_s and, as we will see below, less than a five percent reduction in the lateral leakage current.

Excess Current at Threshold

Eqs. (5-1) and (5-2) have been solved for several geometries including circular.[10] Once the boundary conditions are applied that $I=0$ as $r \to \infty$, and that $V(R) = V_{IN}$, one can determine the total lateral current, I_{OUT}, at $r=R$.

$$I_{OUT} = 2\pi J_{IN}\left(RL_s + L_S^2\right) = I_o/2 + \sqrt{I_o I_{IN}}$$

(5-5)

where we define a characteristic spreading length and characteristic spreading current as

$$L_s = \sqrt{\frac{2\eta kT/q}{\rho_s J_{IN}}} \quad \text{and} \quad I_o = 8\pi \frac{\eta kT/q}{\rho_s}$$

(5-6)

Rather than writing the current in terms of V_{IN}, we have expressed it in terms of $I_{IN} = \pi R^2 J_{IN} = \pi R^2 J_D(V_{IN})$ which is current injected within the aperture $r < R$ if the resistive drop in the center is neglected. The total current injected into the device is the sum of the current flowing within the aperture ($r < R$) and the spreading current: $I_{TOTAL} = I_{IN} + I_{OUT}$.

We have intentionally written the solution in two forms to reveal the scaling of the spreading current vs. device radius, R and vs. the current injected into the center of the device. When $R = 2L_s$, over half the total current is lost due to spreading, or alternatively, when $I_{IN} = I_0$, over half (3/5) of the total current is lost due to spreading.

The above solution Eq. (5-5) was found with the approximation that the -1 is dropped from the diode characteristic. Although that approximation will incorrectly predict the current and voltage *distribution* at radii much larger than the device radius (where the currents are small)[10], a numerical solution of the original equations shows the error on the *total* lateral current is negligible when the diode at $r < R$ is biased above turn-on (as is the case at threshold).

Effect on Differential Efficiency

With an estimate for the current injected in the center of the device at threshold one obtains the excess contribution to threshold current from spreading simply from Eq. (5-5). To find the change in the differential efficiency due to spreading, we must examine the *additional* current one must inject for $r > R$ relative to the *additional* current injects within the aperture. Thus we have,

$$\eta_i = \frac{\eta_{io} dI_{IN,\rho}}{dI_{IN,\rho} + dI_{OUT}} = \frac{\eta_{io}}{1 + (dI_{OUT} / dI_{IN,\rho})} \tag{5-7}$$

where η_{io} is the differential efficiency in the absence of spreading. Inside the aperture, the diodes are clamped so we cannot neglect the voltage drop due to the resistive layer above them, which yields

$$\frac{dI_{IN,\rho}}{dV} = \frac{\pi R^2}{\rho t} \tag{5-8}$$

(In this section, we are assuming the geometry of Figure 5-1a). Outside the aperture (where the diodes are not clamped) we need to inject an additional current found from differentiating Eq. (5-5) where we define $V_T = \eta kT/q$

$$\frac{dI_{OUT}}{dV} = \sqrt{\frac{I_o}{I_{IN}}} \frac{dI_{IN}}{dV} = \sqrt{\frac{I_o}{I_{IN}}} \frac{I_{IN}}{2V_T} = \frac{I_{OUT}}{2V_T} \qquad (5\text{-}9)$$

$$\frac{dI_{OUT}}{dI_{IN,\rho}} = \frac{dI_{OUT}/dV_{in}}{dI_{IN,\rho}/dV_{in}} = \frac{1}{R}\sqrt{\left(2t^3\rho J_{IN}\right)/V_T} = \frac{R_\eta}{R} \qquad (5\text{-}10)$$

Then the internal quantum efficiency above threshold is given by

$$\boxed{\eta_i = \frac{\eta_{io}}{1 + R_\eta/R} = \frac{\eta_{io}}{1 + D_\eta/D}}$$

$$(5\text{-}11)$$

where we can rewrite

$$R_\eta = \sqrt{2\rho t^3 \frac{J_{in}}{V_T}} \quad \text{and } D_\eta = 2\,R_\eta \qquad (5\text{-}12)$$

R_η (D_η) is the characteristic device radius (diameter) at which the internal quantum efficiency drops by 50%. To get a feel for the sizes, we can plug in some numbers typical for the InGaAs based 980nm VCLs at UCSB: $t=600\text{Å}$, $\eta kT/q=0.05$ volts, $J=500\text{A/cm}^2$ (a good current density at threshold for a 3QW device) and $\rho = 1/(q\mu n)=0.3$ Ω-cm for an $Al_{0.3}Ga_{0.7}As$ layer p-doped $2\ 10^{17}$ cm^{-3} with mobility $\mu=100$ cm^2/(V sec). Then we find $D_\eta=0.02\mu m$.

Using the same numbers, we find the diameter, $2L_S(1+\sqrt{3})$, at which half the threshold current is lost due to spreading is 3.5 μm. Comparing this to $D_\eta=0.02\mu m$, we see the effect of current spreading on the differential efficiency is really a second-order effect because the additional current injected above threshold spreads very little in comparison to the current that it takes to reach threshold. Essentially, the reduction in external quantum efficiency due to current spreading is an immeasurable amount. (See Figure 5-2.) This conclusion is in agreement with the scaling of the injection efficiency observed in oxide apertured VCLs[11] and in-plane lasers.[12]
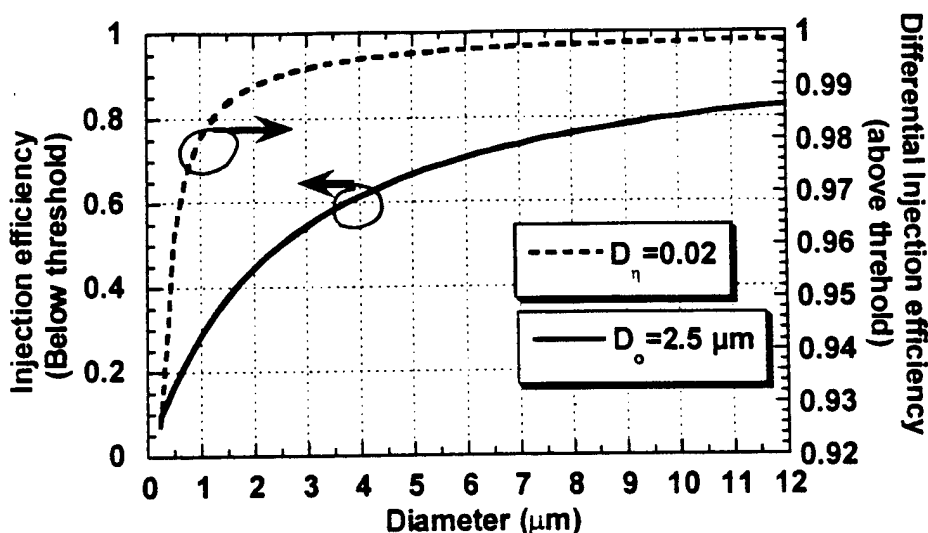
Figure 5-2: Scaling of injection efficiency below and above threshold
using some typical parameters which yield the characteristic
diameters indicated. Note the injection efficiency above
threshold barely changes.

Example of comparison with experimental results

To see if the above estimate for the increase in threshold is reasonable, we
examine the dependence of threshold current vs. device radius for a VCL
(described in [11]) with a thin (300Å) oxide aperture for lower scattering losses
than typical 80nm thick apertures. As we will discuss the scattering losses are
low enough that their contribution to an increased threshold current may be
neglected relative to current spreading; thus the estimate for the total current
only relies on two parameters: the broad area threshold current density and the
characteristic spreading current, I_0.

To estimate the broad area threshold current density, we use the output mirror
transmission of 0.7%, and η_i=0.8 (from in-plane laser measurements) to
determine the round-trip broad area losses from the measured external
differential efficiency η_{ext}=0.53, L+T = T (η_i / η_{ext})= 1% round-trip. Using a

gain-enhancement factor of 1.8 and an active layer thickness of 240Å, we obtain a material gain g= 1160 cm^{-1} per quantum well. The logarithmic fit to Scott Corzine's gain model g=1200 cm^{-1} log(J_w / 50A/cm^2)[13], gives J_w = 131 A/cm^2. So J_{IN}=J_{BA}=3J_w/ η_i = 490 A/cm^2.
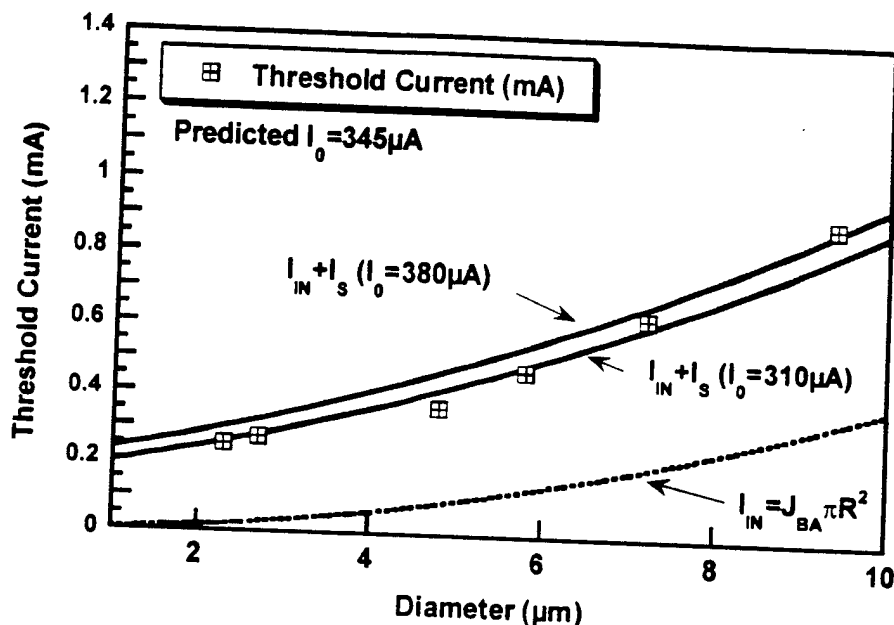
Figure 5-3: Comparison of threshold current data from the apertured VCL in Ref [11] to the threshold current expected with spreading

To estimate the characteristic spreading current, we need to consider several features of the device not previously described. Between the undoped region of the cavity and the aperture, there is a 72nm thick $Al_{0.3}Ga_{0.7}As$ layer doped 2.5 10^{18} cm^{-3}, a 6nm thick $Al_{0.3}Ga_{0.7}As$ layer doped 1.2 10^{19} cm^{-3} and a 10nm linear grade to a 25nm thick $Al_{0.9}Ga_{0.1}As$ layer estimated to be doped at 1 10^{18} cm^{-3} given the solid solubility limit of Be doping of AlAs grown at 600°C[14]. Although the layers were intended to be doped half those value, as described in [11], a Be doping calibration not long after the VCL growth revealed that the actual Be dopant concentration in the structure was double the intended value. The higher doping is also in agreement with the higher than expected absorption losses in the cavity which (as calculated from the differential efficiency) are ~0.36% per round-trip despite an undoped top mirror. The

aperture extends approximately 10 μm from the mesa edge. The hole mobility is effected both by the hole concentration and (to a lesser degree) by the Al mole fraction of the AlGaAs. From the mobilities in [15] along with the doping and thicknesses given above, the parallel combination of the sheet resistance of these layers is 4.6kΩ/□. Using $\eta kT/q$=0.052 volts, we find I_0=345μA. Admittedly, we cannot expect to know the actual doping concentration, mobilities, or diode ideality factor to great accuracy. However, all these contribute only to the characteristic spreading current I_0. So in Figure 5-3, we show the curves for the total threshold current based on I_0=345μA$\pm$10%.

The match with experimental results is especially good given the simplicity of the model and that fact that we did not use any fitting parameters. The model matches the data even at the smallest sizes. Here we might expect some scattering loss to start increasing threshold. In fact, the losses decrease η_{ext} to 0.43 for the smallest, 2.3 μm diameter, device. However, this only implies an increase in threshold of 1.4 μA. So neglecting the contribution from scattering losses was valid.

Spreading and Carrier Diffusion

In the previous analysis, we did not include any contribution to the threshold current from diffusion. However, when the current spreading is significant, the injected carrier profile is relatively flat at the edge of the active region (at the device radius, R). Consequently, the diffusion currents are small and contribute little to the increase in threshold.

In the opposite extreme, one may have very low doping beneath the aperture, in which case the boundary between the resistive layer and the diode is not distinct, and there may be significant diffusion in the intrinsic region of the diode. However, we should note that for the case that current is uniformly injected in the center of the device, (in the absence of size-dependent optical loss) the excess diffusion current also varies linearly with radius[16] which is the same size dependence as the excess current from spreading. So when neither effect is dominate, it may be hard to distinguish them simply by examining the variation of threshold current with device radius. Alternatively,

one can account for both current spreading and carrier diffusion by simply including some excess current which increases linearly with device size.

Conclusion

When scattering losses are low, current spreading can be an important contribution to the threshold current in apertured vertical cavity lasers, and this simple estimate has made sense of experimental data here and elsewhere. The analysis shows that not only that current spreading can be much greater than carrier diffusion, but also that current spreading has little effect on the injection efficiency above threshold.

We found the excess current at threshold (due to spreading) will vary linearly with radius assuming a constant threshold current density in the active region and the estimate only depends on the broad-area threshold current density and a characteristic spreading current. The analysis also allows one to examine the case of two apertures around the active region. In such a case, we estimate that because of the much higher electron mobility the benefit to lower excess current will be small (only about 5% less).

References:

[1]   N. M. Margalit, "High-Temperature Long-Wavelength Vertical Cavity Lasers", Ph. D. Dissertation, ECE Technical Report #98-15, University of California, 1998

[2]   B. J. Thibeault, "High Efficiency Vertical Cavity Lasers Using Low-Optical Loss Intra-Cavity Dielectric Apertures", Ph.D. Dissertation, Electrical and Computer Engineering, University of California, 1997

[3]   Y. A. Akulova, "Vertical Cavity Lasers for Cryogenic Optical Interconnects", Ph. D. Dissertation, ECE Technical Report #98-13, University of California, 1998

[4]   B. J. Thibeault, E. R. Hegblom, Y. A. Akulova, P. D. Floyd, J. Ko, R. Naone, and L. A. Coldren, "Electrical and optical losses in dielectrically-apertured vertical-cavity lasers," in *Proc. SPIE Photonics West '97*, Vol. 3003-12, 1997.

[5]   R. Nagarajan, T. Fukushima, M. Ishikawa, J. E. Bowers, R. S. Geels, and L. A. Coldren, "Transport limits in high speed quantum-well Lasers: Experiment and Theory," *IEEE Photon. Technol. Lett.*, vol. 4, pp. 121-123, 1992.

[6]   W. P. Dumke, "Current Thresholds in Stripe-Contact Injection Lasers," *Solid-State Electron.*, vol. 16, pp. 1279-1281, 1973.

[7]   W. T. Tsang, "The effects of lateral current spreading, carrier out-diffusion, and optical mode losses on the threshold current density of GaAs/AlGaAs stripe-geometry DH lasers," *J. Appl. Phys.*, vol. 49, pp. 1031-1044, 1977.

[8]   H. Yonezu, I. Sakuma, K. Kobayashi, T. Kamejima, M. Ueno, and Y. Nannichi, "A GaAs/AlxGa(1-x)As Double Heterostructure Planar Stripe Laser," *Jpn. J. Appl. Phys.*, vol. 12, pp. 1585-1592, 1973.

[9]   N. K. Dutta, "Analysis of current spreading, carrier diffusion, and transverse mode guiding in surface emitting lasers," *J. Appl. Phys.*, vol. 68, pp. 1961-1963, 1990.

[10] W. B. Joyce and S. H. Wemple, "Steady-State Junction-Current Distributions in Thin Resistive Films on Semiconductor Junctions," *J. Appl. Phys.*, vol. 41, pp. 3818-3830, 1970.

[11] B. J. Thibeault, E. R. Hegblom, P. D. Floyd, R. Naone, Y. Akulova, and L. A. Coldren, "Reduced Optical Scattering Loss in Vertical-Cavity Lasers Using a Thin (300Å) Oxide Aperture," *IEEE Photon. Tech. Lett.*, vol. 8, pp. 593-596, 1996.

[12] Y. Cheng, M. H. MacDougal, C. K. Lin, and P. D. Dapkus, "Confinement Effects of AlAs Native-Oxide Apertures Buried in Quantum Well Lasers," in *Proc. 15th International Semiconductor Laser Conference*, M3.1, 1996.

[13] L. A. Coldren and S. W. Corzine, *Diode Lasers and Photonic Integrated Circuits*. New York: Wiley, 1995.

[14] R. K. Kopf, E. F. Schubert, S. W. Downey, and A. B. Emerson, "N- and P-type dopant profiles in distributed Bragg reflector structures and their effect on resistance," *Appl. Phys. Lett.*, vol. 61, pp. 1820-1823, 1992.

[15] S. Adachi, *Properties of Aluminium Gallium Arsenide*. London: INSPEC, the Institution of Electrical Engineers, 1993.

[16]   L. A. Coldren and B. J. Thibeault, "Vertical-Cavity Surface-Emitting Lasers for Free Space Interconnects," in *Proc. SPIE Photonics West '96*, Vol. CR62, 3-34, 1996.

Chapter 6 :
Device Results

Introduction:

A major goal of improved scaling of device characteristics is improved wall-plug efficiency at lower output powers which is important for applications with arrays of VCSELs (like free-space interconnects or highly parallel laser printing). But, as discussed in Chapter 1, there are other important characteristics for free-space applications such as single-modedness, an operating voltage compatible with CMOS or BiCMOS drivers, and low threshold. When using integrated microlenses small modes are also desirable given the substrate thickness[1]. In addition, one would like designs easy to package which generally means they should be compatible with flip-chip bonding.

Noting these requirements, we begin this chapter by showing the state of the art results achieved here for small VCSELs and then go on further to examine how much of a difference design changes made in the device performance. And lastly, we describe what other design changes may be desirable in the future.

Key Performance Achievements:

Figure 6-1 shows a schematic of the best performing device in this work. It is a nominally 980nm VCSELs with a triple InGaAs quantum well active region and AlGaAs/GaAs mirrors. The most important feature is the tapered oxide aperture positioned at the first standing-wave null. The aperture position and design not only lowers the optical scattering loss, but also the proximity to the active region (about 50nm away) helps to better confine the current at small sizes.
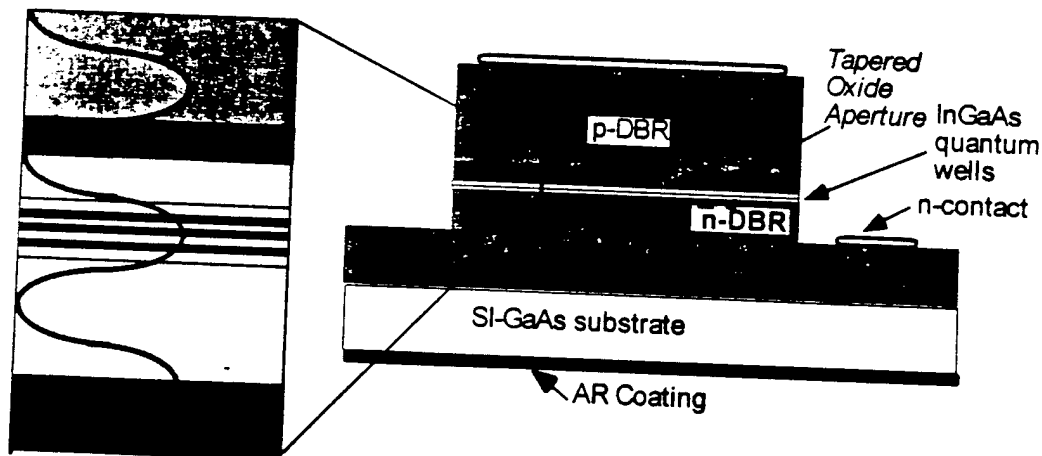
Figure 6-1: Schematic of the "1ˢᵗ Null" VCESL with a tapered aperture positioned at the 1ˢᵗ standing-wave null

To position the aperture at the first null the aluminum composition is increased but this lowers the index and creates a reflection out of phase with the other DBR layers. Although this violates normal DBR design, another mirror period can be added to compensate for the reduction in reflectivity.

This VCSEL is designed to be bottom-emitting because such structures are compatible with flip-chip bonding to connect arrays to circuitry (though the

performance we will describe could just as well be achieved using a top-emitting structure). Although the fabricated device does not have a planar structure, (which would be even more convenient for packaging), the layer structure is compatible with that type of processing as being developed here by Ola Sjolund and Duane Louderback (i.e. processing whereby via holes can be etched and the n-contact is brought up to the same level as the p-contact.) For improved optical efficiency of this bottom-emitting structure, a semi-insulating (SI) substrate is used. Naturally, this requires an n-intracavity contact which is fairly thick ($5\lambda/4$) so that when etching down to it (using reactive ion etching), the layer is exposed over the entire sample surface despite non-uniformity in the etch depth. Because of its thickness, the layer is positioned a few periods back from the active region in order to both reduce optical absorption losses and the cavity length. In addition, we used some of the doping design philosophy discussed in Chapter 3, so that the absorptive loss could be lowered without severely impacting the device resistance. We will discuss more details later about the layer structure, but for now let us simply show the final achievements.
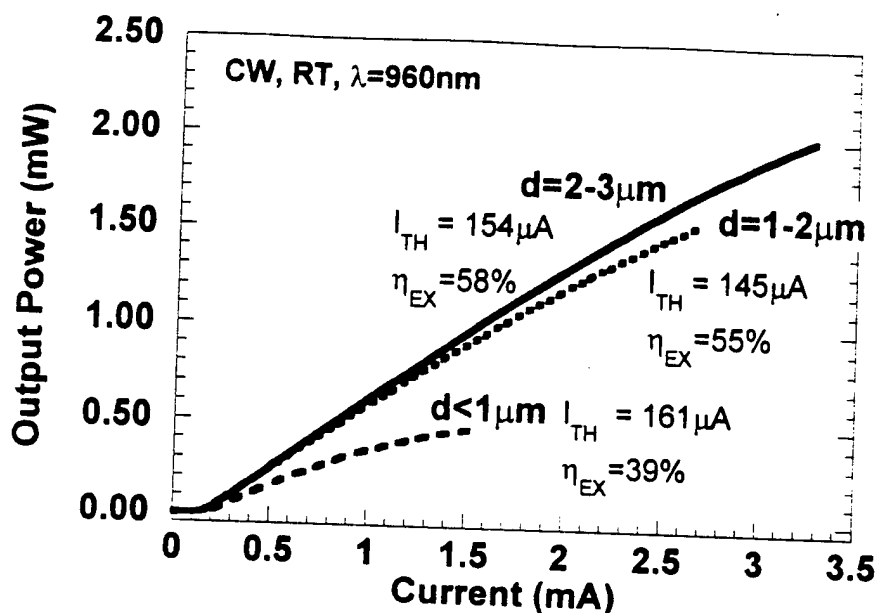
Figure 6-2: Output Power vs. current for the smallest of the "1ˢᵗ Null" tapered aperture VCSELs (*d*= diameter of the oxide opening)

Figure 6-2 shows the light vs. current characteristics of the smallest of the "1ˢᵗ Null" devices. The unusual combination of low threshold and good slope efficiency is due to the improved scaling of the broad-area device characteristics as we will soon discuss more thoroughly. The devices have record high slope and wall-plug efficiency for diameters <2µm.

If one has properly designed the vertical layer structure so there is a reasonable turn-on voltage given the amount of optical loss, then the improved scaling of the threshold and the slope efficiency should lead to improved wall-plug efficiency at lower powers as described more thoroughly in Chapter 2. In Figure 6-3, we plot the wall-plug efficiency vs. output power for the devices shown in Figure 6-2 (with the inclusion of a slightly larger device). The key

feature is that the wall-plug efficiency for the 2-3μm and 3-4μm devices[1] already reaches 20% at an output power of only 150μW.
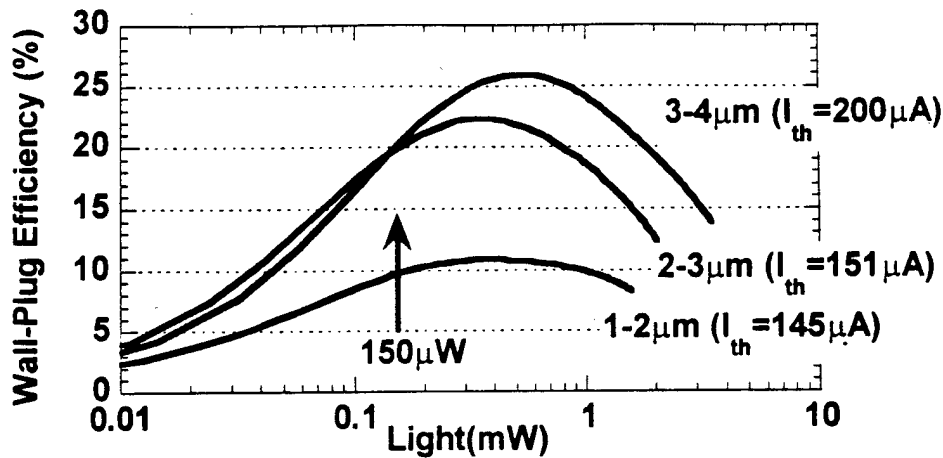
Figure 6-3: Wall-Plug efficiency vs. output power for several "1st Null" VCSELs (2nd processing run)

At this time, only one other VCSEL result has been published showing that high an efficiency at that low an output power[2]. However, that result was only achieved in one device[3]. In addition, the device was a much larger 7μm x 7μm - a size where single-mode operation generally does not occur. In any case, the key result of this thesis, is the improved scaling of broad-area device characteristics which lead to the improvements at smaller sizes and lower power. And we expect even further improvements when carbon doping (which should stay where we put it) rather than Be doping is used in conjunction with these designs. The wall-plug efficiency does drop for the 1-2μm size device shown in Figure 6-3. Although this size of device had the lowest threshold it also happened to be in a region of the sample which had photoresist interfering with the top contact and even larger devices in the same region had absurdly high turn-on voltages. However, an earlier processing run showed higher (in fact, record) 20% efficiency for this size device as shown in Figure 6-4. The

---

1 Boundaries on the device size (the diameter of the opening in the oxide) are determined by using an array of pillars with lithographically defined diameters which increase in steps of 1μm and observing which pillars do not pass current because they are closed-off by the lateral oxidation

threshold is somewhat higher for these devices than for those in the later processing run (in Figure 6-3). Most likely this is a combination of being slightly larger and in a different part of the wafer where the offset between the gain peak and lasing mode may be greater.
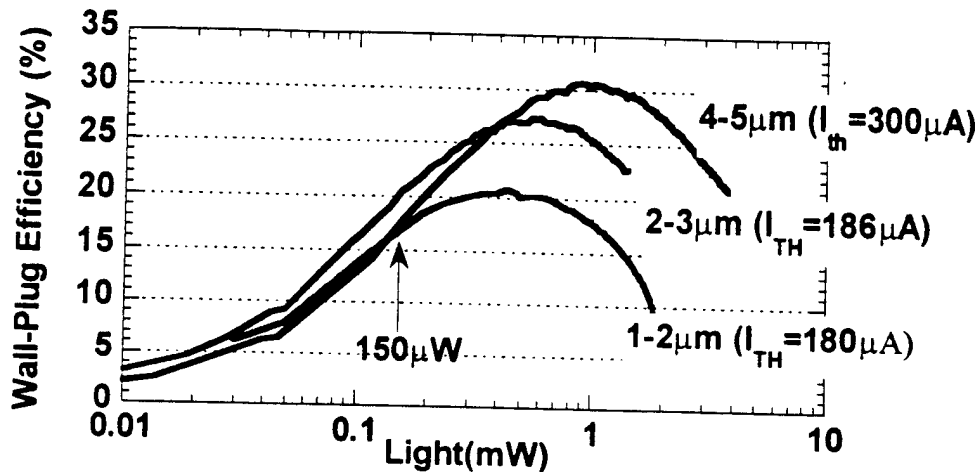
Figure 6-4: Wall-plug efficiency vs. output power for an earlier processing run of the "1st Null" devices. The efficiency is somewhat higher for a given size most likely because the devices are slightly bigger and have lower resistance than those in Figure 6-3.

Note, to compare the threshold from the earlier run (measured using an ILX current source) with the thresholds taken from the later processing run (which were measured on a more accurate HP4155 test setup) we subtracted a measured offset of 45μA - though to be conservative this offset was not used when we computed the wall-plug efficiencies in Figure 6-4. In our subsequent sections, we will be using efficiency and threshold data from the devices in the second processing run (those shown in Figure 6-2 and Figure 6-3)- though this will not change our conclusions.

In Figure 6-4, we see that the wall-plug efficiency again reaches 20% at only 150μW for the 2-3μm size device, and the highest efficiency breaks 30% around 0.9mW (not a world record, but a UCSB first for room temperature CW VCSELs).

For free-space interconnect applications, we need VCSELs which simultaneously satisfy several requirements. Consider the 2-3μm size device with the good efficiency at lower power. It has a peak output power over 2mW and as shown in Figure 6-5, is also single mode with a side mode suppression over 40dB at lower power and still stays single-mode up to around 1.5mW. (Larger devices were multimode and smaller devices did not achieve as high an output power.)
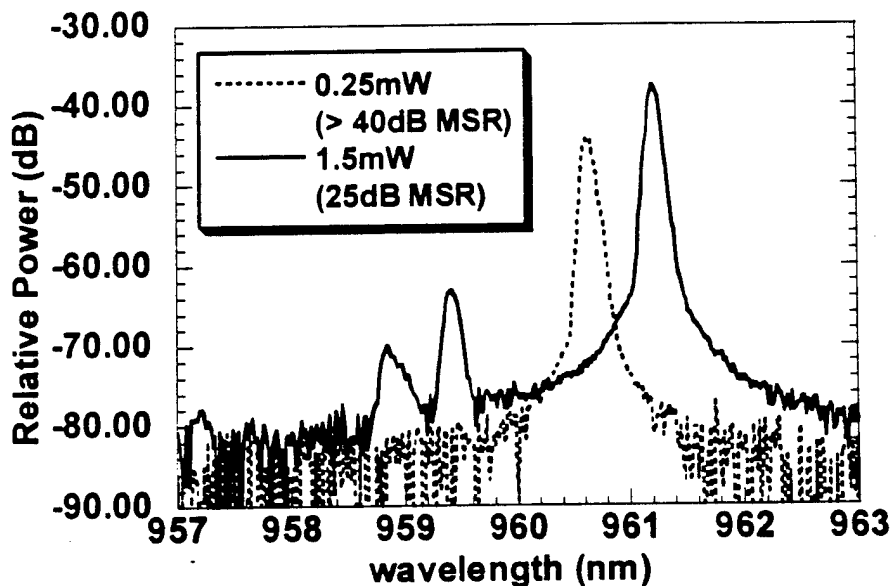
Figure 6-5: Optical spectrum from the 2-3μm, "1st Null" VCSEL showing single mode operation at output powers below 1.5mW

The other important requirement for a VCSEL in a short-distance interconnect application is the drive voltage which one would like to have low enough for CMOS driver circuitry (i.e. <2.5 volts for 3.3V CMOS.) Figure 6-6 indicates the drive voltage for a given output power from the 2-3μm device shown in Figure 6-2. For low output powers, the device meets this requirement, but one always desires lower voltages. And as we will discuss more thoroughly in the section on the scaling of the device resistance, we believe this voltage can be

lower (even while maintaining the efficiency and threshold) despite the increased resistance at smaller aperture diameters.
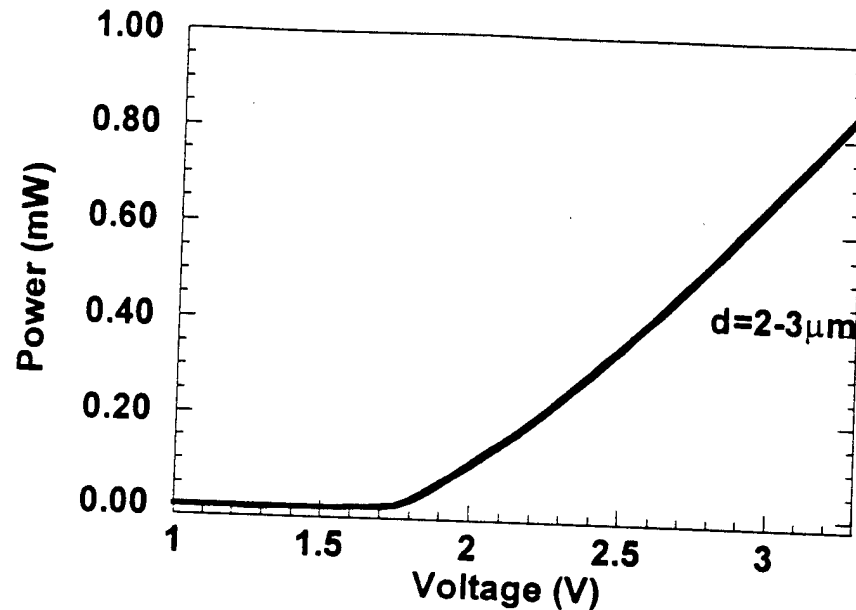
Figure 6-6: Output Power vs. Voltage for the 2-3μm "1st Null" Device. At the lower powers (<200μW) the voltage is low enough for 3.3V drivers. Despite the increasing resistance at small size, we still expect the voltage can be improved without additional loss.

Polarization

For free space interconnect systems which have some polarization selective element, the BER will be affected by any noise created by switching polarization states[4]. There are two ways to avoid this penalty: design a system without polarization selective components or stabilize the VCSEL polarization. By design, tapered apertures reduce the scattering loss for all the modes and in a circularly symmetric VCSEL, there is little anisotropy to force a polarization state. Measurement of the polarization shows little control. With the laser biased above threshold a polarizer in front of the photodetector was rotated until the maximum output power was found and the extinction

ratio relative to the perpendicular orientation was measured. Figure 6-7 shows the results. An angle of zero or 90° means the laser is polarized along the <011> or < 01 $\bar{1}$ > direction.
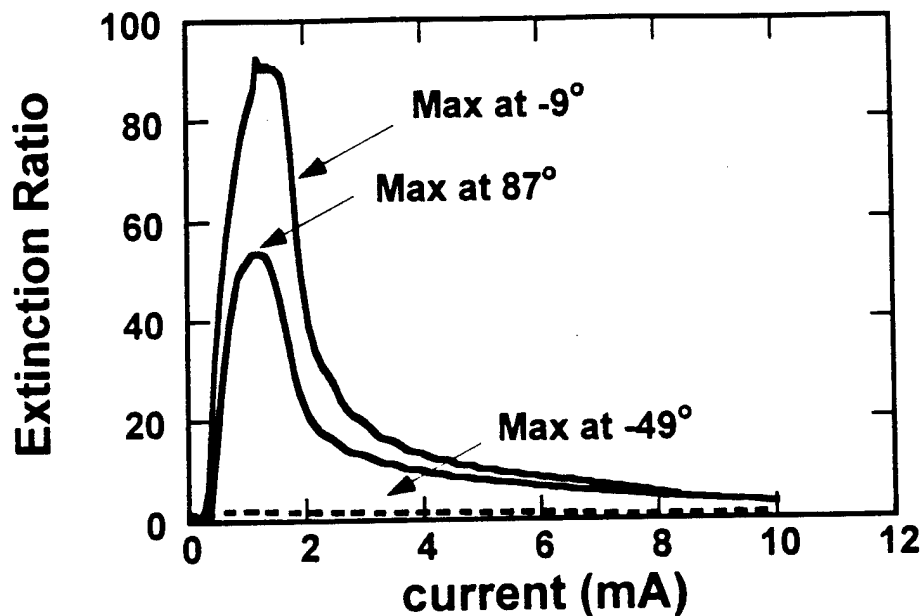
Figure 6-7: Extinction ratio vs. current for three different 2-3μm 1st Null VCSELs. The direction of polarization varies from device to device and in one case has low extinction (even at the angle for maximum extinction)

Various methods have been tried to control the polarization of VCSELs including anisotropic gain[5], asymmetric cavities[6, 7] and the use of a surface grating[8, 9]. Although these methods were shown effective in CW measurements they are less effective stabilizing the polarization under modulation[10]. For bottom-emitting VCSELs, probably an aggressive anisotropic change of the top mirror reflectivity is necessary for polarization stability under modulation.

Improvement to Scaling of Device Characteristics

Having summarized the key device results we achieved, let us now analyze these further and compare the scaling of characteristics to other devices and designs in order to quantify the impact of improvements in device design. In the following sections we will compare the results from the "1st Null" VCSELs we have just discussed to two other structures with different tapered aperture designs. A schematic of the central portion of these device structures is shown in Figure 6-8. All the structures are bottom-emitting VCSELs with 18.5 bottom GaAs/AlGaAs mirror periods. They all have the same calculated mirror transmission (0.7%) and the same number (three) and composition ($In_{0.18}Ga_{0.82}As$) for the quantum wells. The aperture is centered at different points in the standing wave: the first null from the active region, the first peak and the second null. The distance between the aperture tip and the active region varies from ~230nm in the "2nd Null" device to ~50nm for the "1st null" device. The tapers are created by oxidation of a thin AlAs layer adjacent to $Al_{0.9}Ga_{0.1}As$ as discussed in Chapter 7. For the 1st and 2nd Null devices the thin layer of AlAs is 10nm thick and for the 1st peak device the layer is 8.5nm thick. The 1st Peak and 2nd Null devices are not intracavity contacted and this impacts the broad-area slope efficiency because of some substrate absorption (but our comparison of scattering losses will not be effected). The 1st Peak device is carbon doped in the top mirror using a graphite filament in the MBE chamber. (However, as we discuss in Appendix A, excess doping and possible roughness in the top mirror periods caused by the doping and growth conditions lowered the slope efficiency - so the ideal performance was not achieved.) The top mirror in the 2nd null devices was Be doped and aside from the aperture layer, it used $Al_{0.7}Ga_{0.3}As$/GaAs top mirror as opposed to the other devices which used $Al_{0.9}Ga_{0.1}As$/GaAs top mirrors. (Unlike the 1st null devices, the mirror in the 2nd null devices was grown entirely at 600°C so the Be doping profile was far from ideal) Silicon doping was used in the bottom mirrors of all structures. Table 6-1 lists some the different measured parameters. In the subsequent analysis, we will attempt to account for changes in the broad-area device parameters so that the scaling is the salient feature.

<p align="center">(a)   (b)   (c)</p>
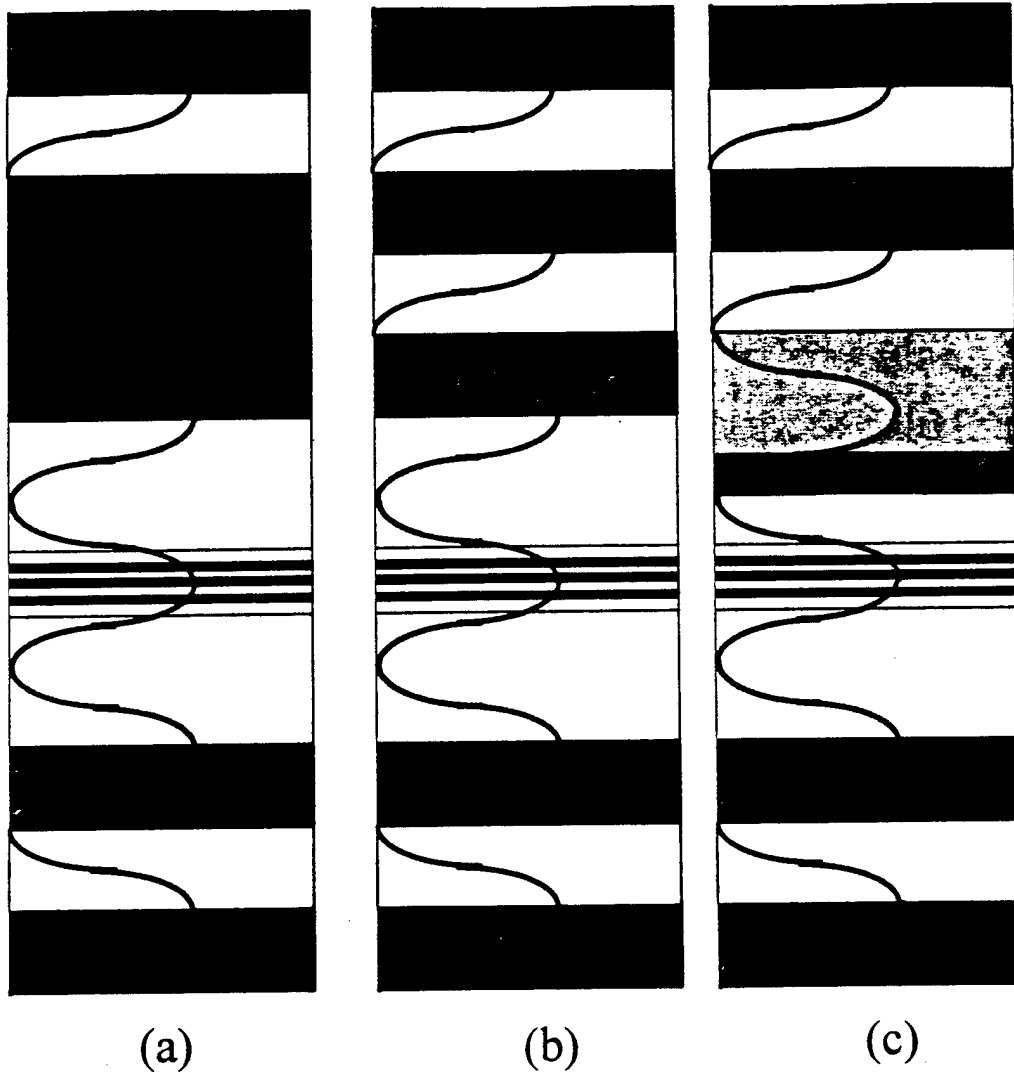
Figure 6-8: Schematic of the central portion of three VCSEL structures discussed in this work in which the aperture is positioned at (a) the 2nd null from the active region (b) the 1st peak and (c) the 1st null. The black areas indicate the oxide aperture, the lightest regions represent GaAs, the gray regions indicate AlGaAs except for the three stripes across the center which denote the three InGaAs quantum well active region. The oscillating line represents the standing-wave pattern. (Grading of the interfaces is not shown.)

Although some differences in doping change the background loss and resistance, the principle differences between the structures which affect the scaling of characteristics (aside from resistance which we are not comparing) is in the aperture design. We will first see how the apertures effect the waveguiding.

Aperture Position	2nd Null	1st Peak	1st Null
# Quantum Wells	3	3	3
Output Transmission	0.7%	0.7%	0.7%
Broad-Area Loss	0.12%/pass	0.37%/pass	0.10%/pass
J_{TH} (broad-area)	810A/cm^2	870A/cm^2	600A/cm^2
Est. doping between aperture and active	5e17 cm^{-3}	1e18 cm^{-3}	6e17 cm^{-3}
Dist. between aperture and active	210nm	130nm	50nm

Table 6-1: Parameters for the VCSELs under investigation

Optical Confinement

As described extensively in Chapter 4, the main reason for using tapered apertures is their lower scattering loss. But we must design the taper correctly. For tapered apertures, the degree of optical confinement depends critically not only on the position of the aperture in the standing-wave, but also on the gradient of the taper thickness which combine to give the gradient of the effectively index step. From scanning election microscope measurements of the tapers, one can determine the taper length though the exact taper profile is harder to determine. Nevertheless, we can estimate the index gradient if we assume the taper thickness varies linearly and a plot of the effective index step, Δn_d, vs. position taking into account the position in the standing-wave is given in Figure 6-9. The index step is calculated based upon the overlap of the dielectric perturbation with the standing-wave as discussed in Chapter 4. This calculation agrees with the index-step calculated based upon the change in the resonant wavelength except in the thickest regions where the perturbation of the oxide moves a second cavity resonance within the mirror stop-band. One

can see the taper positioned at the standing-wave peak has a much higher index gradient and this results in increased scattering losses.
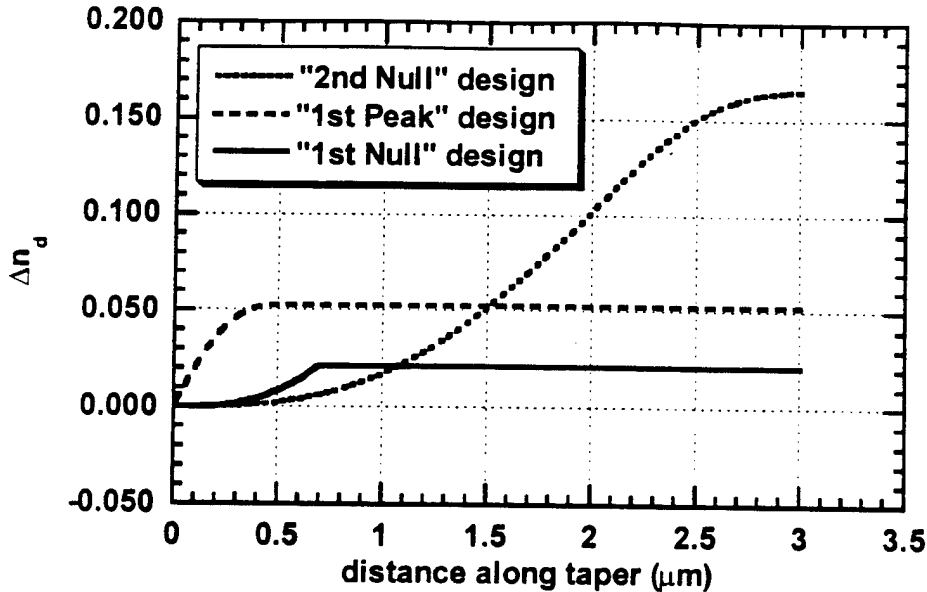
Figure 6-9: Effective index step vs. position for the three different taper aperture designs calculated assuming the thickness varies linearly with position

These losses are plotted in Figure 6-10. This excess optical loss is calculated by using the slope efficiency to extract the total optical loss and then subtracting the loss found in large (~20μm diameter) devices- a method used by Thibeault[4, 5]. Calculating the total optical loss, L_T (per pass)

$$L_T = \frac{T}{2}\left(\frac{T_s \eta_i}{\eta_{ext}} - 1\right) \tag{6-1}$$

relies upon calculating the output mirror transmission, T, estimating the injection efficiency, η_i, and the substrate transmission, T_s, which was lower for the highly-doped n-substrate under the "first peak" VCSELs. The substrate transmission can be directly measured by comparing the reflectivity in the stop band of the top DBR (effectively unity) with reflectivity from the bottom of the sample as described in Chapter 3.
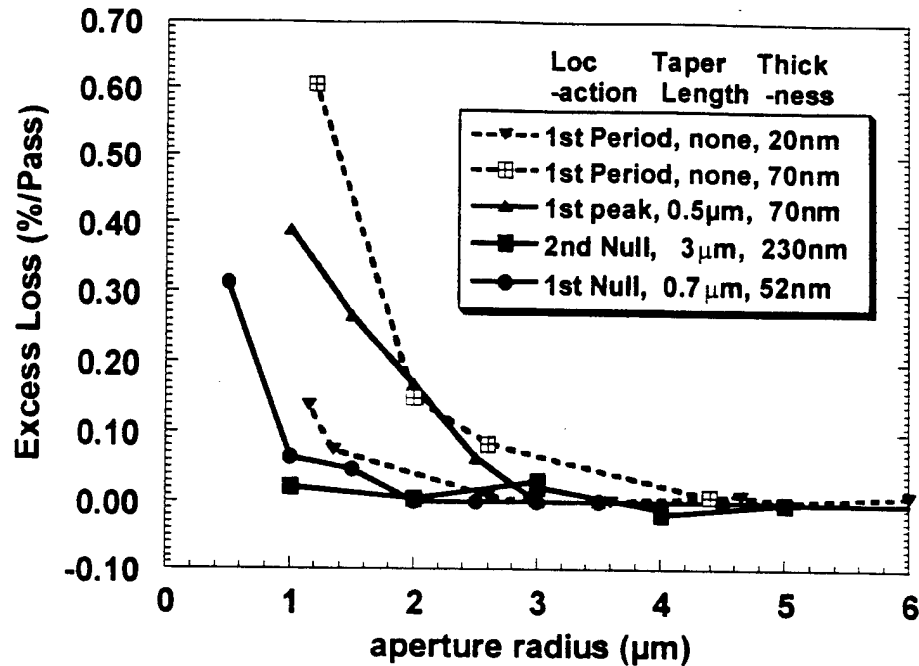
Figure 6-10: Summary of the excess optical "scattering" loss extracted from the change in the slope efficiency with size for three tapered aperture devices and two other VCSELs with abrupt apertures taken from [11, 12] which we analyzed in Chapter 4.

The injection efficiency is estimated to be 80% for the Be doped devices and 90% for the "first-peak" carbon doped device. (The injection efficiency is consistently measured higher for carbon doped in-plane lasers than for Be doped in-plane lasers with the same structure presumably due to diffusing of the Be around the active region. This diffusion would increase the voltage necessary for inversion and the resulting excess field could lower the conduction band barrier which normally keeps electrons from entering the p-side.) One also would like to correct for any injection efficiency changes with size. Unfortunately, this is difficult to do. But the theoretical estimate of the size dependence of the injection efficiency due to current leakage given in Chapter 5 indicates an assumption of a constant injection efficiency is adequate and the measurements of the clamping efficiency we later describe suggests this is correct. In addition, the excellent scaling of the slope efficiency of

tapered apertured devices sets an upper bound on the drop of less than 10% at 2μm. Despite this slight inaccuracy, our conclusions about the *relative* amounts of optical scattering from various aperture designs should be similar.
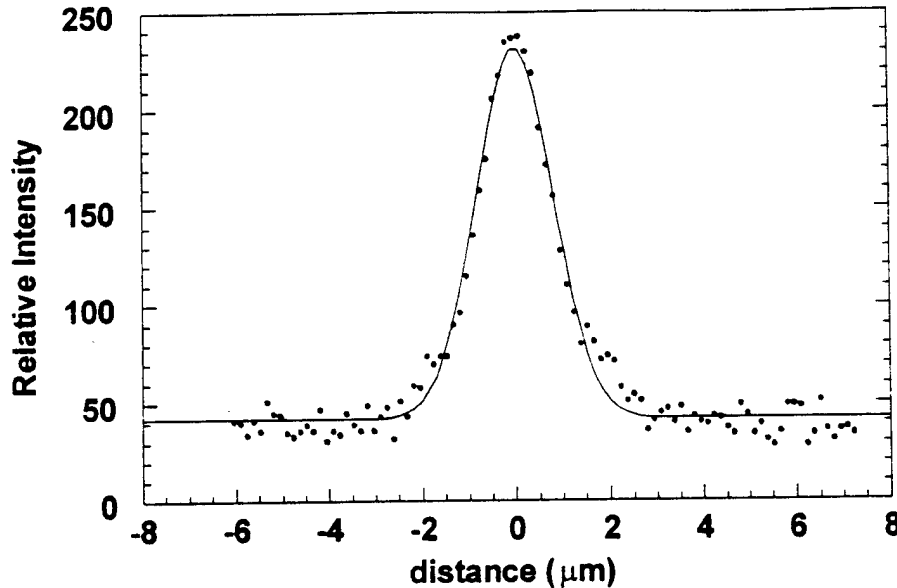
Figure 6-11: Near-field intensity vs. position for a mode from a "1st Null" VCSEL with a 2μm diameter opening

The size given for the abrupt aperture devices from [6, 18] in Figure 6-10 is calculated based upon the lateral mode separation and, as described, the size for the aperture opening for the tapered aperture devices is determined by the closing of the aperture for pillars below a particular diameter. We used the convention that a label of radius r_0 means the actual radius of the opening is between r_0-0.5μm and r_0. So the aperture size for the tapered apertures, maybe smaller than indicated. However, we should keep in mind, that because of the weaker guiding of both thinner apertures and tapered apertures, the mode is expected to be larger than the mode of an abrupt thick aperture of the same opening. Figure 6-11 shows a line-scan of the near field intensity in a "1st Null" device with a 1-2μm opening that shows about a $1/e^2$ diameter of 3μm. The system resolution was not taken into account and even though a high 0.75 NA lens was used, sharp features like the boundary of an etched mesa had a

boundary about 1μm wide. Thus, the actual diameter may be even smaller: approximately 2.8μm = $\sqrt{(3\mu m)^2 - (1\mu m)^2}$. Based on a vertically uniform waveguide analysis, one can calculate that for the mode guided by an 80nm thick, abrupt aperture (effective index step, Δn_d=0.06) to have a $1/e^2$ diameter of 3μm, the radius of the aperture opening should be ~1.8μm. But for this larger size, the excess optical losses of an abrupt, 80nm thick aperture are around 0.2%/pass which still is much greater than those for the 1-2 and 2-3μm diameter tapered and thin apertures. Thus, even at the same mode size thin or tapered apertures are preferable to quarter-wave thick ones. This result also agrees with theoretical calculations of the scattering loss vs. mode size presented in Chapter 4.

In chapter 4, we compared theoretical predictions for scattering loss to the loss for abrupt apertures, and saw that although the theoretical loss was lower than measured by experiment, it still followed the same trends. In Figure 6-12, we compare the scattering loss measured with that predicted using the iterative model (described in Chapter 4) for the various tapered apertures. Here we run into tougher problems being able to accurately compare theory and experiment because the reduction in loss depends on the taper profile which is difficult to precisely determine given the SEM resolution. Nevertheless, we used the estimates for the index profile found above to generate the curves. The 2nd null curve remains low, and then curves up at the smallest sizes unlike the 1st null curve. This effect has to do with the higher overall index step which can confine smaller modes. (The mode radius for these sizes is predicted to be smaller than for the 1st null curve.) The smaller modes at these sizes exceed the DBR angular stop-band. The location of this rise is very sensitive to the taper length and the DBR angular stop band. The measured mode radius ($1/e^2$) point for the 2nd Null device at 1μm radius was ~1.5μm suggesting that the effective index may change more slowly around the aperture tip than estimated. The simulation for the 1st null device suggests that because of the weaker index step, the DBR angular stop band should not be creating excess loss at the 1μm and 2μm diameter openings and this stipulation agrees with the measured mode size we showed above. (We will discuss this further at the end of the chapter.)

The devices tapered from the 1st peak show lower measured losses than the abrupt apertures of similar thickness (see Figure 6-10) and this trend is in agreement with the theoretical curves shown though the scattering loss is higher than predicted.
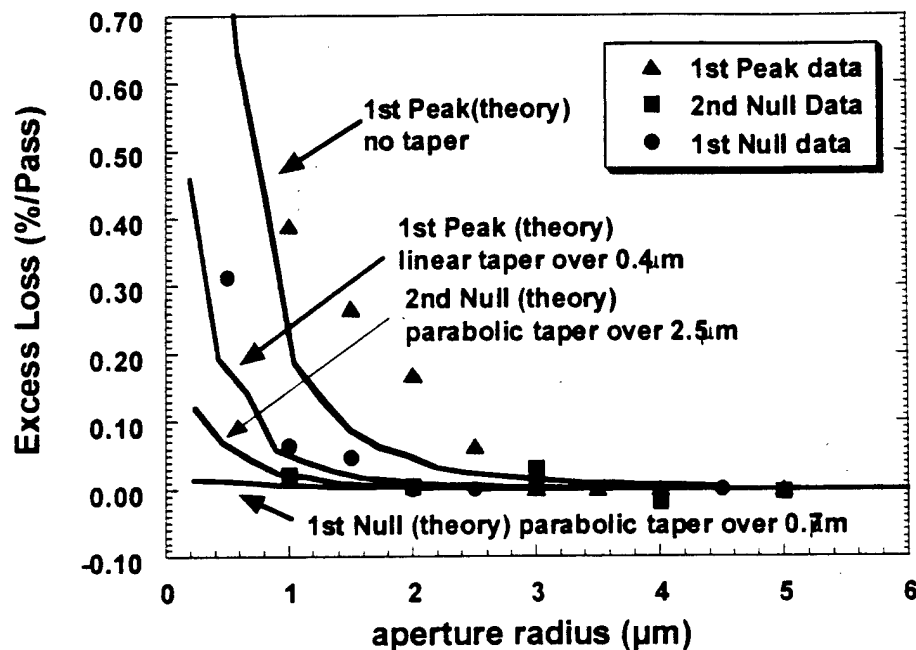
Figure 6-12: Measured and theoretical curves for the excess loss of various tapered apertures

Tapered vs. Thin apertures

One may also ask if tapered apertures are preferable to thin apertures when both are placed a standing-wave null. From the point of view of optical scattering losses for the lowest order mode there is little difference. However, there are situations where tapering is desirable. If one wishes to promote multimode operation in smaller VCSELs use of a thick, tapered aperture is preferable to a thin aperture which will not guide higher order modes. The tapered aperture lowers loss not only for the fundamental, but also for higher order modes. In fact, the losses were low enough in the 2nd Null device that it was still multimode at a 2μm diameter opening. Such a design is desired when

making lower threshold, but very multimode "medium sized" (~5-10µm diameter) VCSELs for coupling to multimode fiber. Further, tapering to greater thickness fairly far (>3µm) from the optical mode is desirable to reduce the parasitic capacitance through the oxide. Finally, tapering may occur as a result of other design conditions: It is typically necessary to drive current through the layers within the aperture. Apertures at the first null are within the cavity which is typically of high index, low aluminum content. However, if there is a large discontinuity in the aluminum composition, then one can incur a high drive voltage. This can be avoided with longer grading or surrounding the aperture by higher aluminum content which will frequently create a tapered aperture. And so one must be mindful of the index gradient to avoid higher loss.

Current Confinement

With size-dependent optical losses nearly extinct, the next major challenge for improving the scaling of characteristics is to reduce the lateral current and carrier
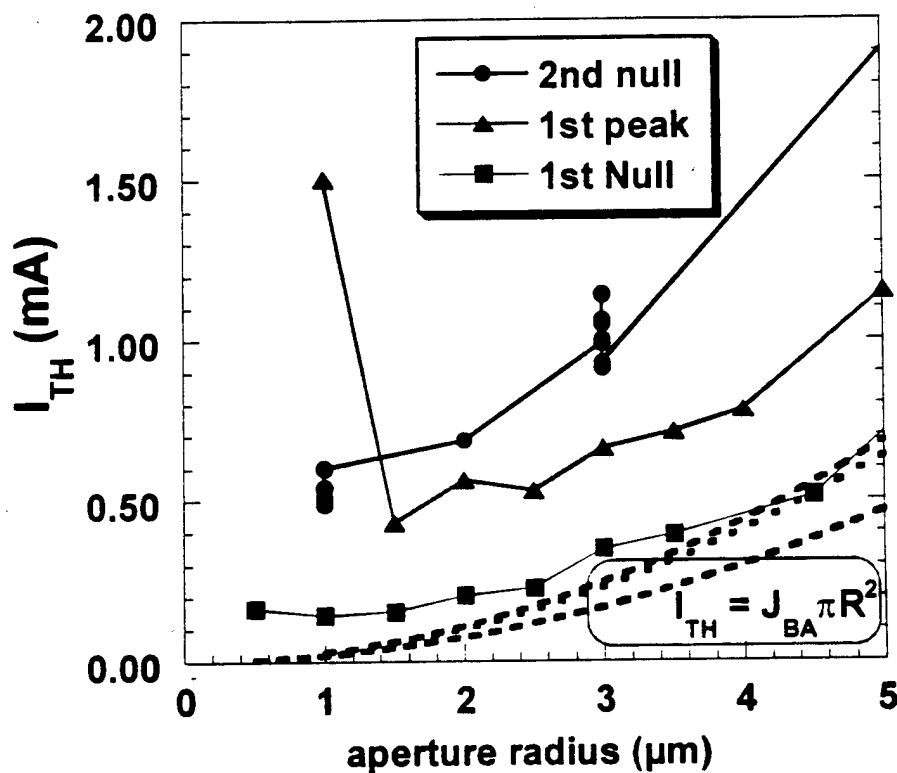
Figure 6-13: Threshold current vs. aperture radius for the three different taper designs. The dashed lines show the scaling based only on the broad area current density

leakage. We saw in Chapter 5 that current spreading can be a significant contribution to the threshold at small sizes even after scattering losses are removed. In Figure 6-13, we plot the threshold current vs. aperture radius for the three different structures. Although there is some difference in the broad area threshold current densities most of the reduction in the threshold can be

attributed to improved current confinement as the aperture is positioned closer to the active region. We see that even the close position of ~50nm is still beneficial.

For clarity, we have also plotted the ratio of the threshold current density to the broad-area threshold current density in Figure 6-14. Although the 1st Peak devices have higher scattering losses, the increase in the quantum well threshold current is small (except at the smallest size) given the size of the active region. Therefore, most of the change in threshold current density relative to the broad area threshold is due to current confinement only (Consider the main term in the threshold is $I_0/2$ - see below.)
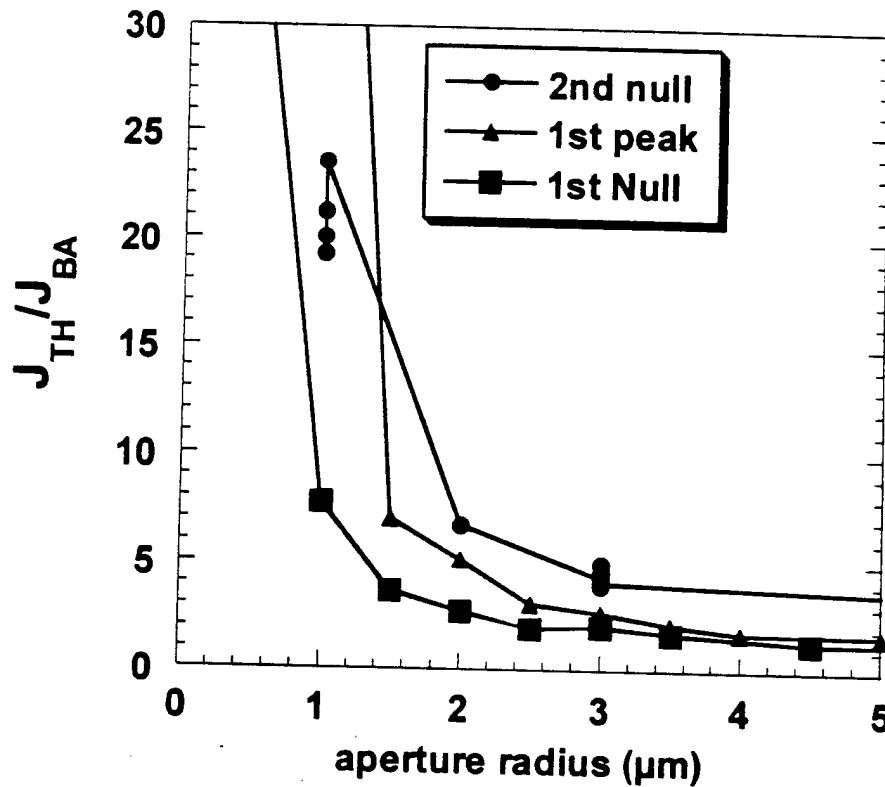
Figure 6-14: Threshold current density relative to the broad-area threshold current density for the three aperture designs

To better understand the current spreading it is useful to compare with the model developed in Chapter 5 for the spreading when there is a purely resistive region between the aperture and an active region with a diode J-V characteristic. Recalling the model, I_{TH} (in the absence of excess loss) should scale as:

$$I_{TH} = J_{BA}\pi R^2 + \frac{I_0}{2} + R\sqrt{\pi J_{BA}I_0} \tag{6-2}$$

where $I_0 = 8\pi(\eta kT/q)\dfrac{t}{\rho}$, for a layer of uniform resistivity, ρ, and thickness, t.

Figure 6-15 shows the threshold vs. size again where we have fit for the parameter I_0, but used the broad-area threshold current density from 20-30μm diameter devices.
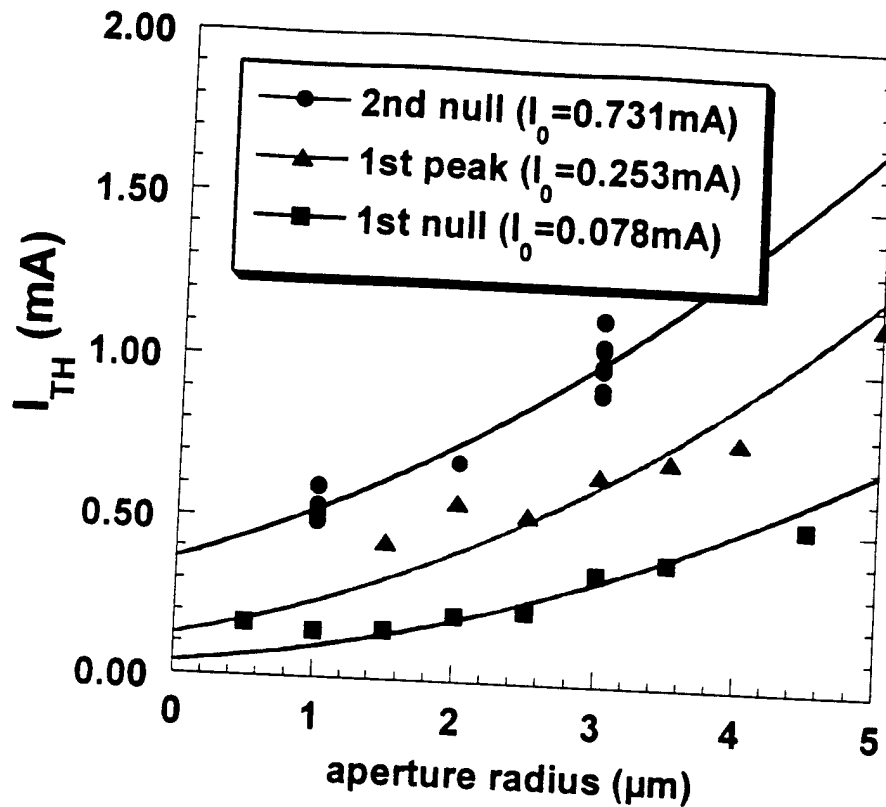
Figure 6-15: Fit of threshold current data to the current spreading model for a resistive layer between the aperture and the active region

(For the 1st peak device, we excluded one point where the threshold current increases due to scattering losses.) With the thickest region between the aperture and the active region, the 2nd Null devices show the highest I_0, but it is still almost four times higher than if the region were uniformly doped at $5 \ 10^{17}$ cm^{-3} - as approximately designed. One possible reason is that relatively low Be doping combined with movement during growth at the heterointerfaces creates a much higher vertical resistance forcing the current to spread further laterally. (The devices analyzed in Chapter 5 were so heavily doped with Be that, most likely, the heterointerface barriers were small.) The carbon doped 1st peak device are a better example. These were doped around $1 \ 10^{18} cm^{-3}$ between the aperture and active region which yields a predicted $I_0 \sim 0.2mA$. (noting the

lower mobility ~60cm^2/(V sec) expected for the higher doping in AlGaAs). We also observe the fit not matching as well for the 1.5 and 2μm radius devices and this is probably due to some scattering loss at these sizes that was shown in Figure 6-10. For the 1st Null device, the threshold scales the best but it is still much higher than expected at small sizes because we did not dope the region between the aperture and the active region. (And lateral diffusion current using an estimate like that in Chapter 2 is still too low to explain the results.) One possibility is that during growth of this region, which was at a substrate temperature of 600°C, Be moved beneath the aperture and is causing the higher than expected leakage. Secondary ion mass spectroscopy (SIM)s revealed that this is likely the case. Figure 6-16 shows the SIMs measurement made after the top mirror periods on the 1st Null sample were etched away. (The aluminum measurement was used as a marker to indicate location and its sputter efficiency depends upon the mole fraction; so it is not expected to match the designed mole fraction precisely.) The Be clearly has moved between the aperture and active region. (It is unlikely we have simply aligned the design and measured curves incorrectly because the Be also has moved into the GaAs region in the first top mirror period.) If we assume a hole concentration of 6 10^{17} cm^{-3} over this region, then we obtain I_0~70μA which is a reasonable match given the typical error in concentration and mobility. Lastly, we should observe a mismatch of the model and the measured current at the smallest two sizes for the 1st Null devices. At these sizes, the threshold model may not be accurate, but also the excess loss or possibly heating has raised the threshold current not only due to the increased gain required, but also because of the increased lateral leakage.
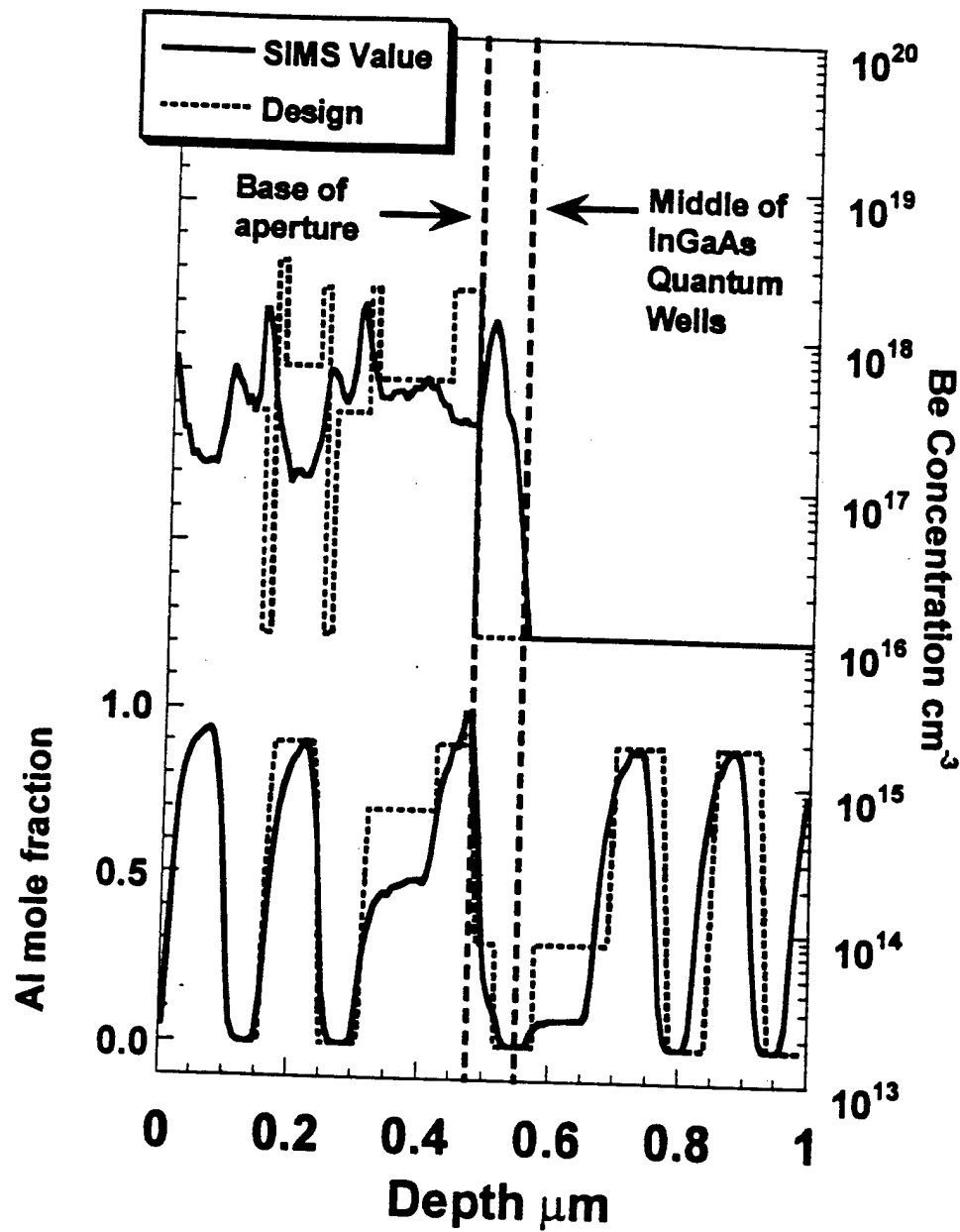
Figure 6-16: SIMs of the Be profile around the active region of the 1st Null sample (data taken by Charles Evans & Associates)

The other possibility to briefly consider is that the injected profile actually matches the aperture size in which case the injected current is smaller than the

mode for the 2μm size device and the lateral confinement factor is 50-70% (depending upon the true aperture size). However, this effect would only imply a factor of 1.4-2.4 higher threshold current density (assuming a logarithmic gain model with three quantum wells) needed in the active region which is still well below the observed factor of ten. We should note some reduction in confinement factor is not detrimental and, in fact, can make for a lower threshold current than one would achieve for a unity confinement factor of a mode of the same size because the power density in the mode is not uniform.

Scaling of electrical Resistance

As described in Chapter 2, the device resistance in theory scales approximately inversely with aperture radius and there is little with the aperture design we can do to change this. The increasing resistance is not desirable for trying to match to transmission lines. But if one had short connections as would VCSELs flip-chip
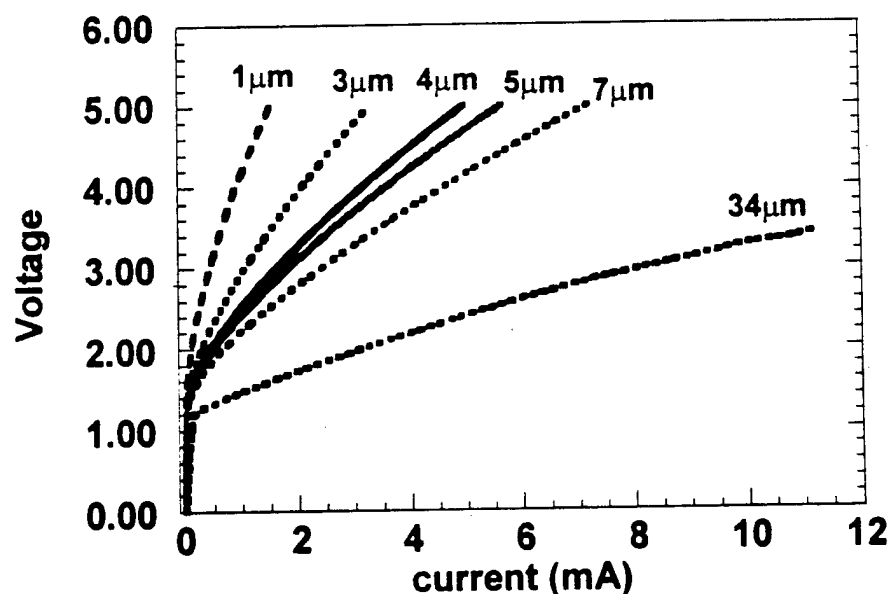
Figure 6-17: Voltage current characteristics for the 1st Null devices

bonded to circuitry, then the operating voltage rather than resistance is more of an issue. We showed the operating voltage vs. power previously for the 2-3μm

1st Null device. In Figure 6-17, we show the scaling of the voltage-current characteristics for these devices. Although the curves have a slight bend above turn-on, we can still extract the resistance vs. size which we show in Figure 6-18 along with the resistance vs. size for the carbon doped 1st peak devices. As expected resistance scales approximately with 1/(device radius).

$$y = 2512.4 * x^{(-0.70294)}$$
$$y = 843.5 * x^{(-1.1167)}$$

— 1st Null device
  Be doped

— 1st Peak device
  C doped
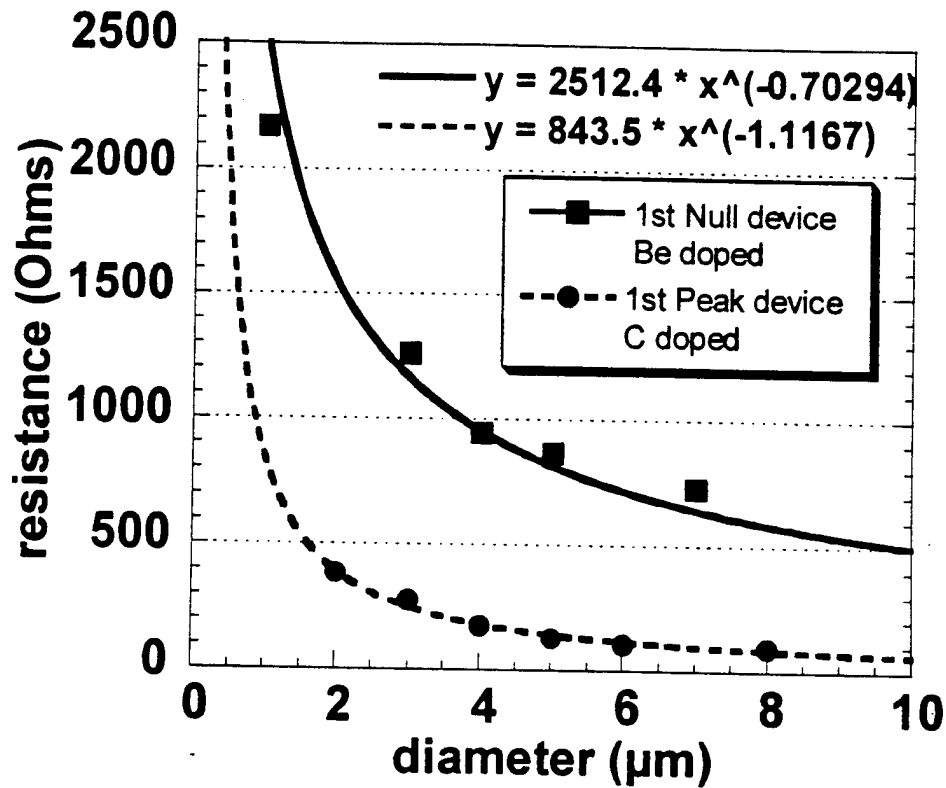
Figure 6-18: Scaling of resistance for the 1st peak and 1st null devices. Although the carbon doped 1st peak device has lower resistance optical loss was relatively high so the wall-plug efficiency was much lower than the 1st null devices. (Although we have labeled the designs by the aperture position, it has nothing to do with the scaling of the resistance.)

Sub-100Ω resistance was reached for the carbon doped devices. However the broad-area 1st peak devices had a slope efficiency of η_{EX} =40% as opposed to the lower background loss 1st Null devices with a broad area η_{EX}=63%.

Although slope efficiency was sacrificed for lower resistance in the carbon doped devices, it does not have to be. The 1st peak devices used the same doping profile in all of the top mirror periods. But the 1st null devices used lower average doping in the first few top mirror periods in order to have lower optical loss without adding significant voltage. (See Figure 6-19) These first few mirror periods were grown at a higher substrate temperature in order to reduce optical loss, and consequently the Be moved significantly in these layers as we showed in Figure 6-16.
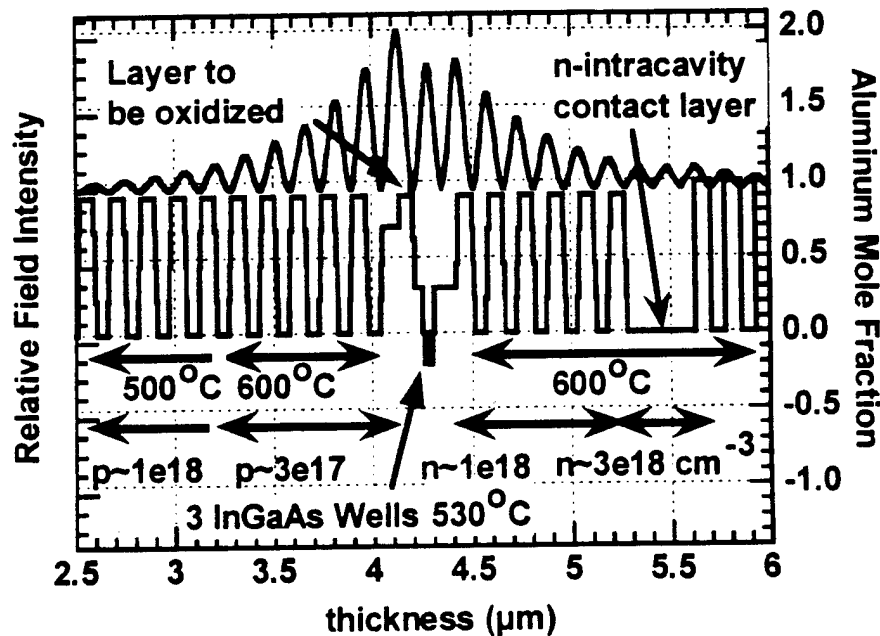
Figure 6-19: Structure, Substrate growth temperatures, average doping levels and standing-wave field^2 for the central portion of the 1st Null device

If low carbon doping was used in these first periods, then one should be able to circumvent this problem. (I tried this, but the devices had high threshold due to a large offset between the gain peak and lasing mode.) One also may be able to grow these first few mirror periods cold with Be. Last time that was tried (at UCSB) the losses went up[13], but that may have been simply been due to higher Be incorporation.

Scaling of the clamping efficiency

As previously discussed, we would like to have some idea of the scaling of the injection efficiency with size. One possible way to estimate this is to measure the clamping of the spontaneous emission. The thought here is that if carriers are moving laterally outside the region where they are "clamped" then this should show up as a relative increase in the spontaneous emission above threshold. To measure it, we placed a 930nm bandpass filter in front of the detector and recorded the light vs. current. At 930nm, we are measuring emission from upper states in the InGaAs quantum wells so we will not see carriers recombining in the barriers and cannot measure the total injection efficiency (by injection efficiency we mean the *above threshold* injection efficiency which multiplies the optical efficiency to yield the slope efficiency above threshold).
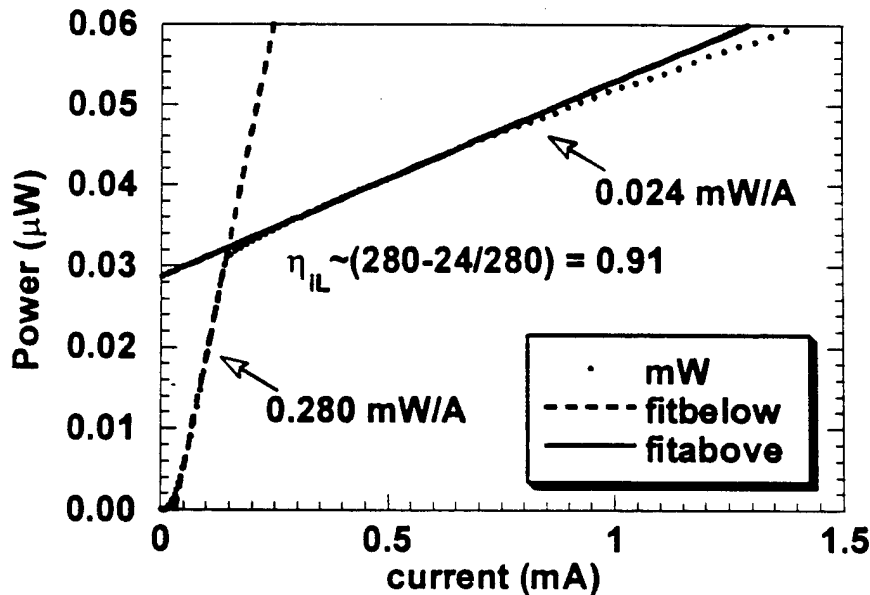
Figure 6-20: Clamping of the spontaneous emission in the 2-3μm diameter "1ˢ Null" device

Figure 6-20 shows the optical power of the spontaneous emission vs. current for a 3μm "1ˢ Null" VCSEL and we observe the expected change in slope at threshold. Independent of any changes in optical coupling, we can calculate

what we will call the *clamping* efficiency, $\eta_c = (\eta_b - \eta_a)/\eta_b$, where η_a and η_b are the slope efficiencies of the spontaneous emission above and below threshold, respectively. (Near Margalit used this clamping previously to estimate the injection efficiency in broad-area 1.55µm VCSELs.) Figure 6-21 shows this clamping efficiency vs. size. We see no strong variation with size which suggests that additional carriers injected above threshold going into unclamped regions relative to clamped regions changes negligibly with size. There are a number of assumptions which keep us from unequivocally concluding the lateral injection efficiency is not changing with size, but these data provide strong evidence that there is little variation laterally, which is in agreement with theoretical predictions in Chapter 5. Lastly, we should note that these measurements are on devices with low scattering losses. If one were to measure devices with high scattering losses, one might see a lowering of the *vertical* injection efficiency with size since the carrier density in the active region must rise with the additional loss.
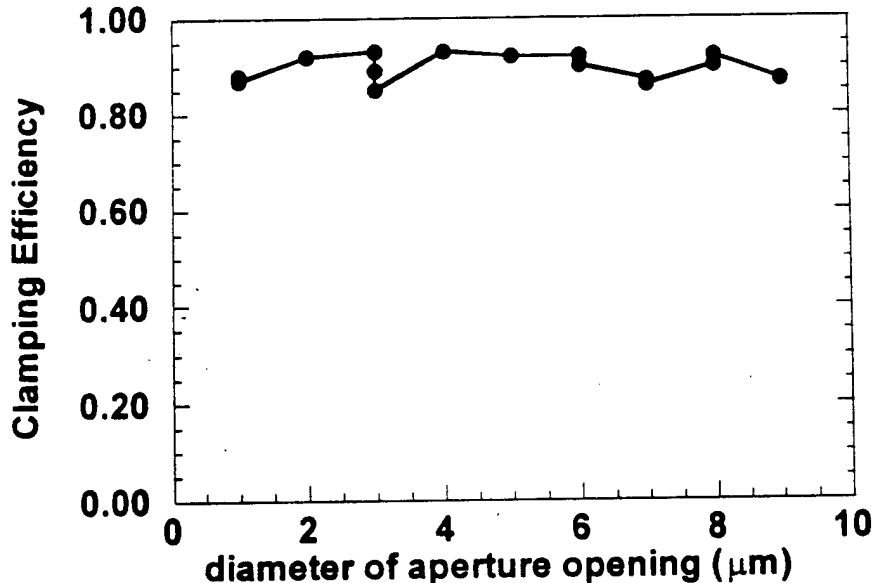
Figure 6-21: Extracted "clamping" efficiency vs. aperture size for the 1st null devices

However, these measurements beg another explanations for the small drop in efficiency at the smallest sizes in the 1ˢᵗ Null devices. The other possible causes are the thermal rollover or an increase optical losses. Part of the drop may also be accounted for by the mode becoming so small and divergent that it is difficult to collect all the light in the detector. Estimates of the mode size and measurement with a larger detector indicate that this accounts for about a 2% drop in the efficiency which still does not explain the drop from 55% to 39% slope efficiency in the smallest device. But the sharp roll-over of the 1μm diameter device even at a smaller power density that the 2μm device implies heating is responsible. (In theory, if leakage currents were removed then the heating will be lower even at a constant power density.)

Conclusions and Future Outlook:

Improvements to scaling from reduction of scattering losses with tapered apertures and with improvements to the current confinement have enabled small <2μm diameter VCSELs to have power conversion efficiencies over 20% and enabled 2-3μm diameter devices to reach 20% efficiency at output powers as low as 150μW. Such devices can combine several characteristics: low threshold, good efficiency, and singlemodeness all of which are desired for applications with dense arrays of VCSELs like free-space interconnects. Some sacrifice is made in resistance when shrinking device size, but we expect with better dopant control in the first few mirror periods that the resistance can be lowered without adding significant absorptive losses.

The designs we presented showed that current confinement benefited from bringing the aperture even as close as 50nm to the active region. It may be possible to obtain or surpass such improvements with better dopant control beneath the aperture although as we discuss in Appendix A some doping will probably always be necessary to dope the graded region beneath the aperture.

We demonstrated that tapered apertures are able to reduce scattering losses over abrupt apertures. And such reduction is also possible with thin apertures placed at a standing wave null. However, if one desires small (5μm-ish), very multimode VCSELs (for use with multimode fiber) then a thick, tapered

aperture is preferable. Although the objective here was to improve the smallest VCSELs, this different direction may be emphasized in the future.

References:

[1]   E. M. Strzelecka, G. B. Thompson, G. D. Robinson, M. G. Peters, B. J. Thibeault, M. Mondry, V. Jayaraman, F. H. Peters, and L. A. Coldren, "Monolithic Integration of Refractive Lenses with Vertical Cavity Lasers and Detectors for Optical Interconnections," in *Proc. SPIE Photonics West '96*, paper no. 2691-07, 1996.

[2]   K. L. Lear, K. D. Choquette, R. P. Schneider, S. P. Kilcoyne, and K. M. Geib, "Selectively oxidised vertical cavity lasers with 50% power conversion efficiency," *Electron. Lett.*, vol. 31, pp. 208-210, 1995.

[3]   K. D. Choquette, , Personal Communication, 1995

[4]   D. V. Kuksenkov, H. Temkin, and S. Swirhun, "Polarization Instability and Performance of Free-Space Optical Links Based on Vertical Cavity Surface Emitting Lasers," *IEEE Photon. Technol. Lett.*, vol. 8, pp. 703-705, 1996.

[5]   M. Takahashi, P. Vaccaro, K. Fujita, T. Watanabe, T. Mukaihara, F. Koyama, and K. Iga, "An InGaAs-GaAs Vertical Cavity Surface Emitting Laser grown on GaAs (311)A substrate having low threshold and stable polarization," *IEEE Photon. Technol. Lett.*, vol. 8, pp. 737-739, 1994.

[6]   K. D. Choquette and R. E. Leibenguth, "Control of vertical cavity laser polarization with anisotropic transverse cavity geometries," *IEEE Photon. Technol. Lett.*, vol. 6, pp. 40-42, 1994.

[7]   T. Yoshikawa, H. Kosaka, K. Kurihara, M. Kajita, Y. Sugimoto, and K. Kasahara, "Complete Polarization control of 8x8 vertical cavity surface emitting laser matrix arrays," *Appl. Phys. Lett.*, vol. 66, pp. 908-910, 1995.

[8]   J. H. Ser, Y. G. Ju, J. H. Shin, and Y. H. Lee, "Polarization stabilization of vertical cavity surface emitting lasers by inscription of fine metal-interlaced gratings," *Appl. Phys. Lett.*, vol. 66, pp. 2769-2771, 1995.

[9]   T. Mukaihara, N. Ohnoki, T. Baba, F. Koyama, and K. Iga, "A novel birefringent distributed Bragg reflector using a metal/dielectric

polarizer for polarization control of surface-emitting lasers," *Jpn. J. Appl. Phys.*, vol. 33, pp. L227-L229, 1994.

[10] D. V. Kuksenkov, H. Temkin, and T. Yoshikawa, "Dynamic Properties of vertical cavity lasers with improved polarization stability," *IEEE Photon. Technol. Lett.*, vol. 8, pp. 979-999, 1996.

[11] B. J. Thibeault, E. R. Hegblom, P. D. Floyd, R. Naone, Y. Akulova, and L. A. Coldren, "Reduced Optical Scattering Loss in Vertical-Cavity Lasers Using a Thin (300Å) Oxide Aperture," *IEEE Photon. Tech. Lett.*, vol. 8, pp. 593-596, 1996.

[12] P. D. Floyd, B. J. Thibeault, E. R. Hegblom, J. Ko, and L. A. Coldren, "Comparison of Optical Losses in Dielectric Apertured Vertical-Cavity Lasers," *IEEE Photon. Technol. Lett.*, vol. 8, pp. 590-592, 1996.

[13] D. B. Young, , Personal Communication, 1996

Chapter 7:
Tapered Fronts and other Oxidation Issues

Overview

Wet thermal oxidation of AlGaAs has been around since the late seventies but only recently has been employed in optoelectronic devices. A very comprehensive review of work in this area can be found in Ref [1] and more description can be found in Chapter 4 of Phil Floyd's thesis[2]. The purpose of this chapter is not to discuss this background, but to describe the oxidation technique for forming *tapered* oxide apertures and to mention some under emphasized issues about stress and oxidation.

Tapered Oxide Apertures

The oxidation rate for AlGaAs is highly dependent on Al composition. Even adding 5% Ga will drop the rate by an order of magnitude compared to the rate for pure AlAs[3]. Typically a single layer of uniform AlGaAs composition in

a vertical cavity laser structure is oxidized laterally to confine the optical mode and current.

GaAs

18nm linear grade

152nm $Al_{0.9}Ga_{0.1}As$

10.5nm AlAs

71nm $Al_{0.9}Ga_{0.1}As$

12nm linear grade

$Al_{0.3}Ga_{0.7}As$
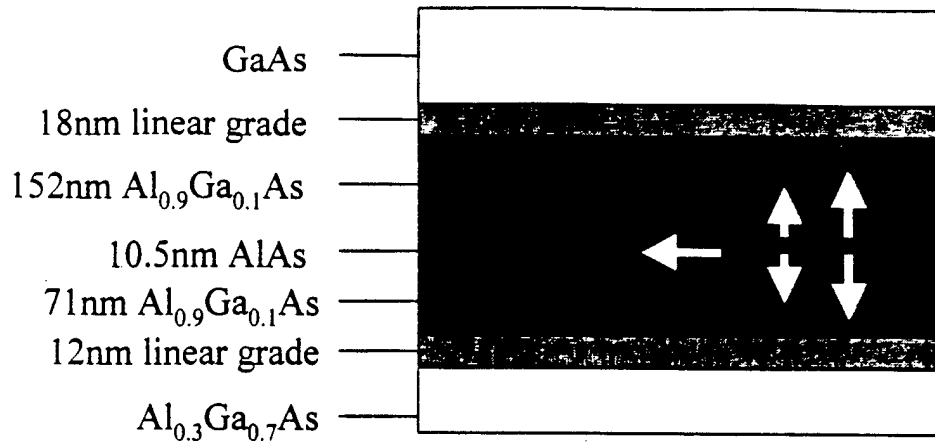
Figure 7-1: Schematic of a layer structure for a tapered aperture (This structure was used in the 2nd Null device discussed in Chapter 6.)
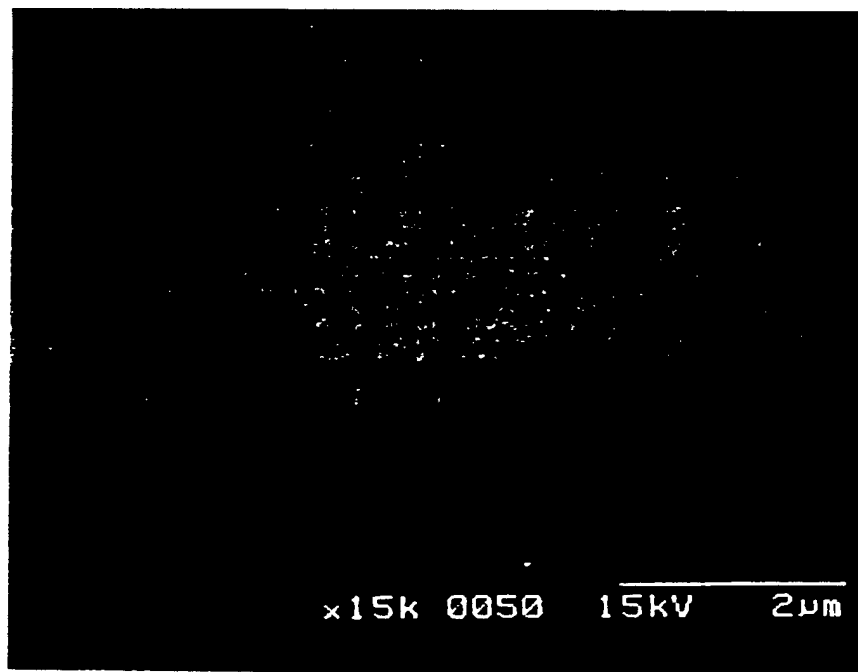
Figure 7-2: A scanning electron microscope image of a tapered oxide aperture formed by the layer structure in Figure 7-1.

The oxidation front in the thinnest (~20nm) of apertures does have some curvature, but this is usually only over a fraction of the thickness[4] and does little to affect the optical mode. Thus, we have considered such apertures completely abrupt. But to form a more lens-like optical element, one can taper the tip of the oxidation over a much longer distance. This is possible by a combination of fast lateral and slow vertical oxidation. As shown schematically in Figure 7-1, a layer of pure AlAs is imbedded in lower Al content AlGaAs. The oxidation proceeds quickly through the AlAs layer, and the oxidized layer supplies water vapor to the layers above and below which oxidize vertically forming the tapered shape. After the structure in Figure 7-1 was oxidized in a steam environment at 430°C for 15 minutes, the taper shown in Figure 7-2 was formed.
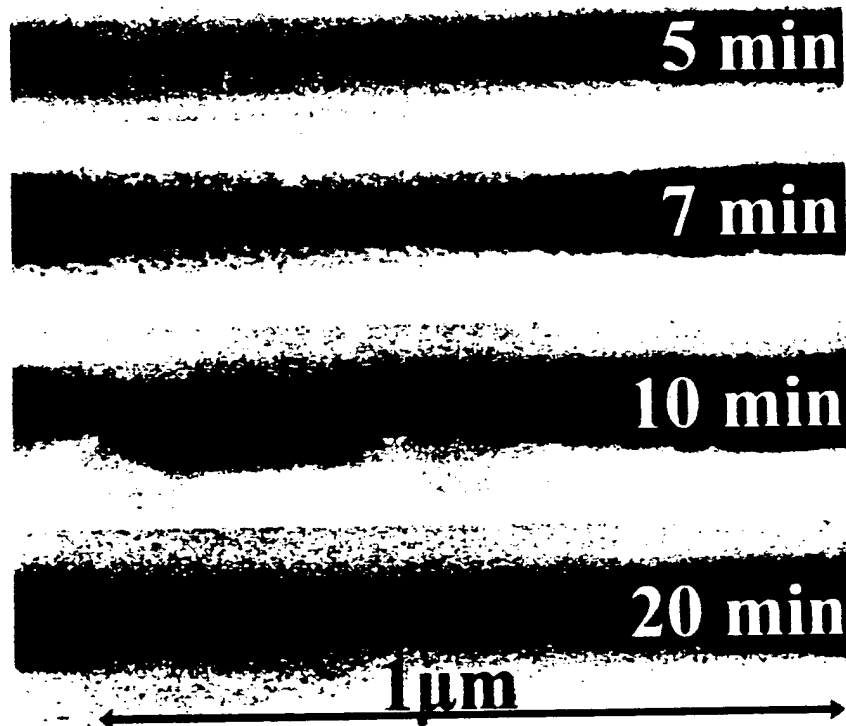
Figure 7-3: The evolution of a taper as characterized by R. Naone. Once formed, the taper shape does not change appreciably. (The sample was oxidized at 450°C using a water temperature of 95°C with N_2 flowing though it at 1 L/min.)

For the example structure, it was found that after the initial formation of the taper, the shape does not change appreciably even though the depth of the oxide front may vary by many microns. Ryan Naone characterized this aspect for the development of taper formed by a 20nm layer of AlAs sandwiched by $Al_{0.97}G_{0.03}As$. His results are shown in Figure 7-3.

The taper length is very sensitive to the oxidation rate of the supply layer relative to the surrounding AlGaAs. And in the examples shown, this AlAs supply layer is thin enough that the rate of oxidation depends on its thickness as Naone has measured and explained theoretically[4]. Thus, by varying the AlAs thickness, we can vary the taper length. Figure 7-4 shows a calibration test structure and the resulting taper lengths are plotted in Figure 7-5.

Comment on MBE digital alloys and oxidation

We should note that when the structure is grown by MBE that it is important to ensure that the digital alloying is done in the same manner in the test structure as in the real structure because this will effect how thick the AlAs layer is (depending. if the 90% Al layer below it ended on AlAs or GaAs). A detailed growth program for the 1st Null VCSEL is given in the Appendix C. Although digital alloys generally have a period of 2nm or less so that they appear electronically the same as the analog alloys, this makes it difficult to form a digital alloy for 98% Al 2% Ga (without using three cells) because the time to open and close the shutters is too short at 1μm/hr growth rates. Nevertheless, one can produce a 98% Al content layer by using a superlattice of 4.9nm AlAs/0.1nm GaAs/4.9nm AlAs. Although electronically this structure may not look exactly the same as a 98% Al analog alloy, the oxidation rate is considerably lower compared to AlAs. And typically all that matters is that material can be reproduced from a test structure to the actual device.

1000Å GaAs

160 Å Linear grade

600 Å $Al_{0.9}Ga_{0.1}As$

t   Å AlAs

120Å Linear grade

200Å $Al_{0.3}Ga_{0.7}As$
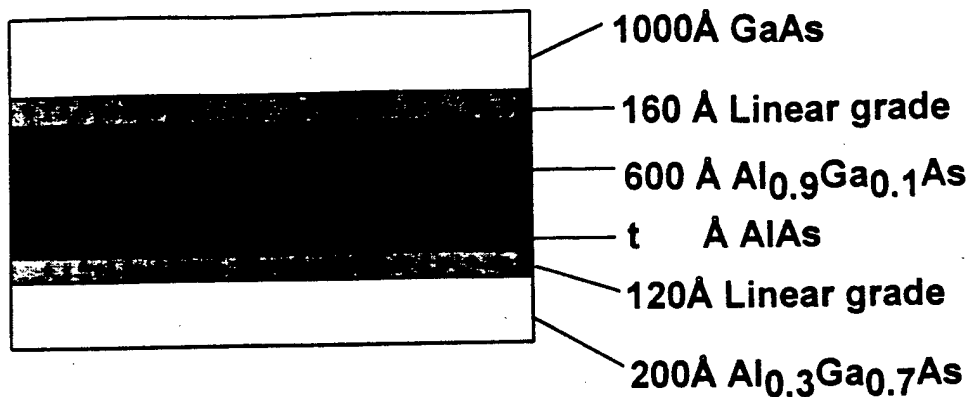
Figure 7-4: A test structure used the characterize the taper formation.
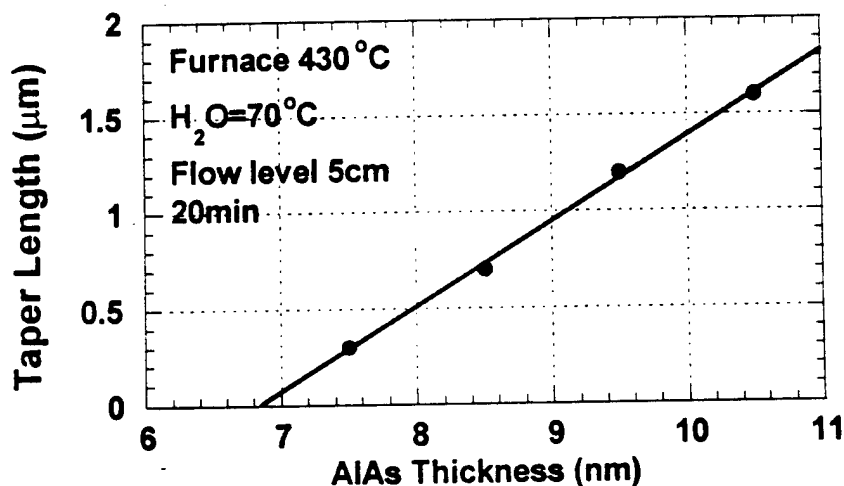
Figure 7-5: Taper length variation vs. the thickness of the AlAs layer in Figure 7-4.

The taper shape can also be controlled by using lower Al content in the supply layer or in the vertically oxidized layer. Naone has some examples of shorter tapers formed when the composition is varied[5]. And sometimes it is desirable to have very precise control over the amount of vertical oxidation when the oxide layer is used to control the resonant wavelength of a VCSEL. In that case, a 70% Al content cladding layer was used[6] adjacent to 10nm of AlAs. In fact, the 1ˢᵗ Null devices discussed in Chapter 6 use a 70% Al content layer above the 90% cladding layer used to form the taper. The 70% Al layer

will also oxidize vertically some distance near the edge of the sample ($\sim$10μm from the aperture tip). In the future designs it may desirable to raise the Al content of this layer in order to have the aperture be thicker near the edge of the device to reduce the parasitic capacitance. (See Figure 7-6.)
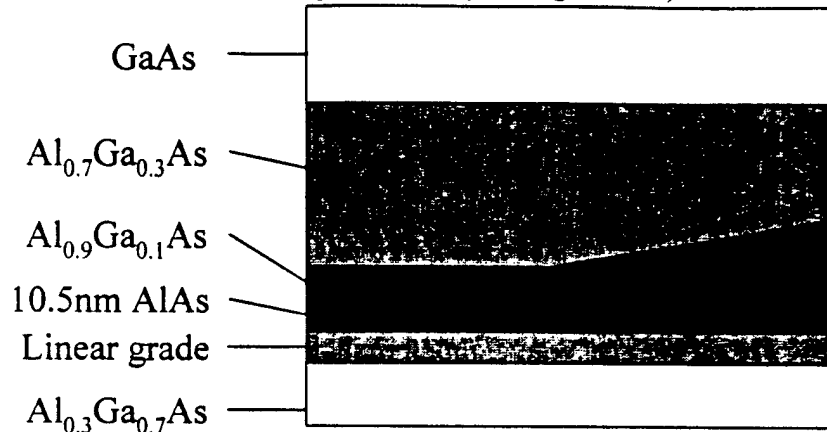
Figure 7-6: Schematic of a two tiered taper. The oxidation of the 70% (or a somewhat higher) Al content layer can be used to form a thick oxide layer well away from the optical mode purely for reducing the parasitic capacitance across the oxide. (The taper angles are exaggerated.)

Lateral oxidation rate Control

One must not only adjust the composition of the layers for the desired tapered shape, but also the oxidation rate should be reasonable and the rate for the aperture in 1st Null structure is given below (the layers oxidized are like those in Figure 7-4 with a 10nm thick layer of AlAs except the 90% Al content layer is clad by a 70% Al content layer - a precise structure is given in Appendix C).
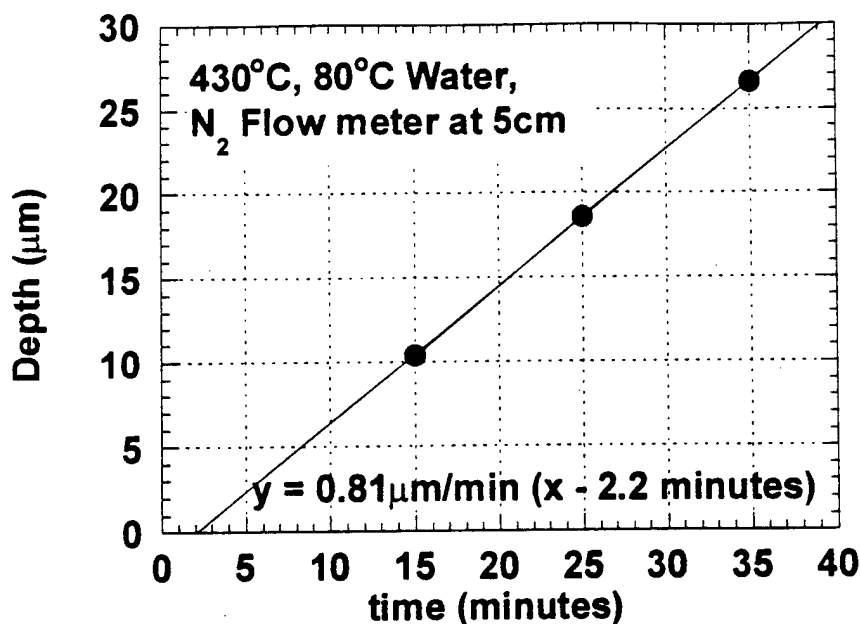
Figure 7-7: Oxidation depth vs. time for the 1ˢᵗ Null structure described in Chapter 6. Because the oxide was buried, the depth was measured using an SEM.

Although for the quick and dirty test above, all the points happened to lie on one line, generally at this rate the depth is controllable within +/- 1μm (from my experience closing off pillars in several processing runs). Before the oxidation of the full sample of VCSEL pillars, a portion of the sample is oxidized and a IR camera is used in conjunction with a 0.75NA lens to see which pillar sizes closed off. Then the rest of the sample is processed. Ideally, better control is desired especially in an industry environment. Control may be improved with oxidation at lower temperatures using lower Al content layers which oxidize more slowly. However, if possible one would like to re-oxide the layers. Unfortunately, my experiments trying to re-oxide layers seem to be more revealing about vapor and stress in the oxide than helpful to making devices.

Re-oxidation, Water and Stress in Oxide Films

If an oxidized sample (in this case one with a 20nm AlAs layer clad by GaAs) is left out in air (even for a few minutes), and one tries to oxidize it again, then a second oxide front eventually moves past the first, but in a non-uniform manner, and the semiconductor can break in regions over the first oxide front as shown in Figure 7-8.

Figure 7-8: A microscope image of the sample surface after attempting to re-oxidize a sample that was left in air for 15'. The oxide front (lighter region) moves, but in a non-uniform manner, and pieces of semiconductor break off where the first front was.

I tried several different intervening steps between oxidation and re-oxidation, but only keeping the sample in LN2 worked satisfactorily. We should also note that the first oxidation was 5' at 450°C and the second oxidation was for 10' at 450°C (both with a water temperature of 70°C), and the oxide front may be able to move after more time in the cases when we observed the front was "sealed".

Process Step Between Oxidations	Result
Air, room temp. 15'	partially sealed
Air, 200°C	sealed
Methanol (room temp)	sealed
Leave in furnace with N_2, no vapor	sealed
LN2 15'	re-oxidizes with smooth front
2' LN2 + 15' Room Temp	re-oxidizes, but surface cracks

Table 7-1: Various methods tested to promote reoxidation and their results.

"Sponge?" Theory of Wet Oxidation

It would be nice to have some understanding of the process preventing reoxidation and it appears because of the sample cracking that it has something to do with stress. In fact even single oxidations can bow the semiconductor surface as shown in Figure 7-9 and we know that in crystalline form the Al_2O_3 would like to be 20% thinner[1].

But thermal stress alone cannot be responsible because the sample left in the furnace without water vapor also is sealed. However, we can consider the oxide behaving like a sponge – I only mean by this statement that the water is keeping the oxide in a particular form (This is just my guess.). With vapor (or maybe just an overpressure of OH^- to keep $Al(OH)_3$ from turning into Al_2O_3) present, the oxide may be larger than without. Once the vapor is removed, the oxide compresses and makes it harder for vapor to come in and move the front. In air or especially in a solvent that loves to soak up the water, the water may leave very quickly. But when the sample goes immediately into LN2, the water stays inside and the re-oxidation can proceed like nothing happened. This hypothesis suggests that a water treatment before re-oxidation might help.

Andrew Huntington tried using doing this, but with only limited success. Lastly, we should remind ourselves that the layer tested in Table 7-1 was AlAs and layers with 2% Ga may not behave as badly when re-oxidized.
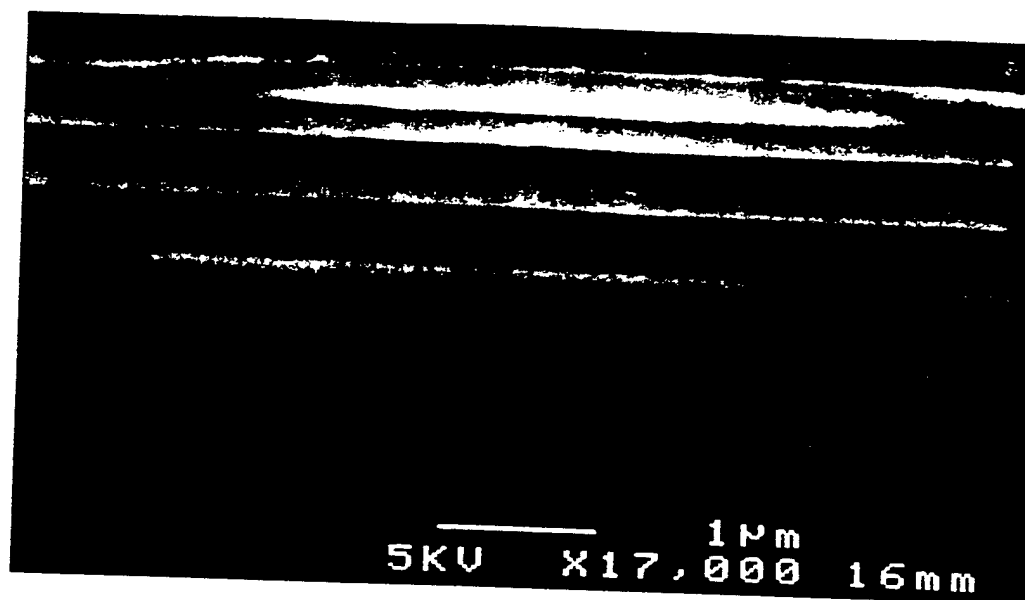
Figure 7-9: An SEM showing two oxide fronts can bow the semiconductor surface before closing off. (The fronts were closing off a 100μm wide mesa after being in the furnace for 30' at 450°C. The top AlGaAs layer is 246nm of 97.5% Al with a 10nm layer of AlAs in the middle. The layer is beneath 100nm of GaAs)

Potential Problems at Pillar Perimeters

Stress in pure AlAs oxide apertures has been shown to make oxidized pillars pop off[1] after a contact anneal, but that problem has not occurred in devices at UCSB which use thin layers of AlAs. While no pillars have popped off, de-lamination of the lower (90%) Al content layers at the edge of the pillar does occur. Although these layers oxidize about ten times shorter distance than the aperture, their total thickness is pretty high (as high as half the pillar height), and they are under more stress.
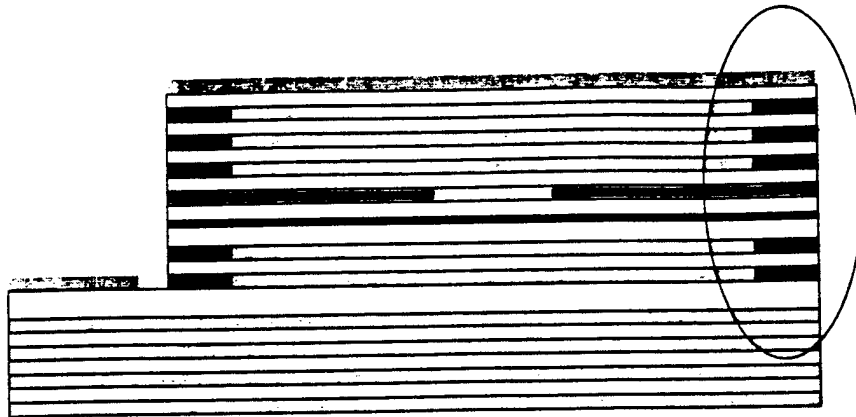
Figure 7-10: Oxidized layers at the edge of the pillar can delaminate after a contact anneal as shown in Figure 7-11.
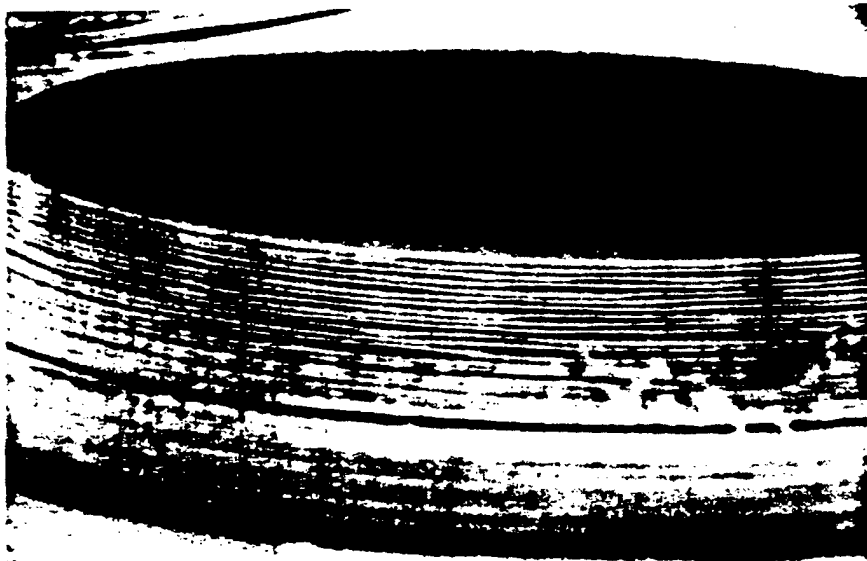
Figure 7-11: An SEM image showing de-lamination of the oxidized layers at the edge of the VCSEL after the contact anneal at 410°C for 30".

Despite the de-lamination at the pillar edge after the contact anneal, the VCSELs still lased and had state of the art performance. Perhaps this de-lamination is not a problem and may just look bad although it might lead to longer term reliability problems. To avoid or reduce this potential problem, the aluminum content could be reduced further in the mirror layers. Or these layers at the edge could be etched away before the contact anneal. Or both contacts could be annealed during the oxidation (using Ti/Pt/Au and Pt/Ge/Au contacts). Or perhaps under-etching rather than oxidation can be used to form the apertures in the first place.

Conclusions:

We demonstrated and characterized the formation of tapered apertures by the slow vertical oxidation of a lower aluminum content layer placed adjacent to a faster laterally oxidizing higher aluminum content layer. These apertures were successfully employed in several VCSELs resulting in lower optical scattering losses as discussed in Chapter 6.

We also showed some uglier aspects of oxidation created by stress in the layers which tends to inhibit their re-oxidation and can cause the surrounding semiconductor to bend or break off. These may cause reliability problems, but if delamination stays only at the pillar edge, it may never cause problems. Perhaps even a rapid thermal anneal is good since the stress is relieved afterwards and one can weed out any failures earlier. Industry will probably find out soon enough.

References:

[1]   K. D. Choquette, K. M. Geib, C. I. Ashby, R. D. Twesten, O. Blum, H. Q. Hou, D. M. Follstaedt, B. E. Hammons, D. Mathes, and R. Hull, "Advances in Selective Wet Oxidation of AlGaAs Alloys," *IEEE J. Selected Topics in Quantum Electronics*, vol. 3, pp. 916-926, 1997.

[2]   P. D. Floyd, "Vertical Cavity Lasers Fabricated Using Impurity Induced Disordering", Dissertation, ECE Technical Report #96-05, University of California, 1996

[3]   K. D. Choquette, R. P. Schneider, K. L. Lear, and K. M. Geib, "Low threshold voltage vertical-cavity lasers fabricated by selective oxidation," *Electron. Lett.*, vol. 30, pp. 2043-2044, 1994.

[4]   R. L. Naone and L. A. Coldren, "Surface energy model for the thickness dependence of the lateral oxidation of AlAs," *Submitted to J. Appl. Phys.*, 1997.

[5]   R. L. Naone, E. R. Hegblom, B. J. Thibeault, J. C. Ko, and L. A. Coldren, "Design of Graded AlxGa1-xAs Layers for Tapered Al-Oxide Apertures in Vertical Cavity Lasers," in *Proc. Electronic Materials Conference*, paper no. F3, p. 9, 1996.

[6]   A. Fiore, Y. A. Akulova, J. Ko, E. R. Hegblom, and L. A. Coldren, "Multiple Wavelength Vertical Cavity Laser Arrays Based on a Postgrowth Lateral-Vertical Oxidation of AlGaAs," *Appl. Phys. Lett.*, vol. 73, pp. 282-284, 1998.

Chapter 8 :
Conclusions and Outlook

Summary of Essentials:

This work has primarily focused on improving the properties of smaller vertical cavity lasers through changes in aperture design. With proper scaling of the broad-area threshold current density and slope efficiency, smaller VCSELs of course will have lower threshold, but they also will have higher wall-plug efficiency at lower powers and higher modulation current efficiency. And with lower operating powers being optimum in smaller VCSELs, the drive voltage and temperature rise can be lower depending upon aperture design even with increasing electrical and thermal resistance. (Table 2-1 provides a summary of the scaling of various characteristics under ideal conditions of constant current density and slope efficiency.)

Two major barriers to ideal scaling in apertured vertical cavity lasers were analyzed extensively in this work: optical scattering losses and current spreading.

Analysis of the guiding by abrupt index apertures showed that at sizes below $4\mu m$ diameter (for $\lambda{\sim}1\mu m$), scattering inherent to the aperture and cavity design (ignoring any roughness) would begin rising sharply and be comparable to the absorptive losses from the doping. The loss for abrupt apertures was formulated simply in terms of two parameters of the laser: the cavity Fresnel number and the effective phase shift of the aperture (accounting for the placement in the standing-wave). The predicted losses (although somewhat lower than, but on the same order as those extracted from actual devices) motivated and explained the improved scaling of the slope efficiency by employing thinner (or optically weaker) apertures. In addition, further analysis with an iterative model for the mode and losses not only confirmed the estimate of the loss from the simple two parameter model, but also showed considerably low loss for apertures with tapered tips which make a more lens-like optical confinement. Such tapered apertures were produced by taking advantage of the very sensitive dependence of oxidation rate upon Al composition and can be constructed by placing lower (e.g. 90%) aluminum content layers next to layers of higher content (e.g. AlAs) and relying on both lateral and vertical oxidation. VCSELs with sufficient index gradients demonstrated low excess losses slightly below those found in devices with 20-30nm thick apertures, and *trends* in improvement agreed with theoretical predictions as with abrupt apertures. *The low scattering losses provided by tapered apertures have enabled record high slope and wall-plug efficiencies for VCSELs with aperture diameters below $2\mu m$.*

This work also addressed current spreading between the aperture and active region with both theory and experiment. A simple estimate for the lateral spreading current was formulated in terms of two parameters that could be easily applied to existing structures and helpful to understand the threshold scaling. The estimate of spreading current in thin aperture devices, led us to try positioning the aperture much closer to the active region ($\sim$50nm) away.

The improvement in current confinement was confirmed by fabricating and testing other devices with apertures further from the active region.

While we still have not reached ideal scaling of the current density, we have nearly reached ideal scaling of the device slope efficiency through the use of thin and tapered apertures. The improvements to scaling of both parameters has led to improved wall-plug efficiency at lower output powers and at sizes small enough to be single mode. As we described in Chapter 6, the efficiency measured at powers <150μW (for the devices 2-3μm in diameter) is only matched by one other published result in a larger, 7μm, device[1].

Figure 8-1 shows wall-plug vs. size based upon fits to present device data for the 1st Null devices described in Chapter 6. In producing these curves, the slope efficiency was held constant (which has a minor error only at radii <1μm). The operating voltage fit to a current independent voltage, V_D, which varied as V_D=1.49+0.745$d^{1.56}$ (volts), where d is the aperture diameter in μm, and a series resistance, R_S, varying as R_S=2.51k$\Omega$$(1/d)^{0.7}$. The size-dependence of the threshold fit well to I_{TH} = 0.1mA/2 + (0.1mA $J_{BA}\pi)^{0.5}(d/2)$ +$J_{BA}\pi(d/2)^2$, where J_{BA}= 600A/cm^2.
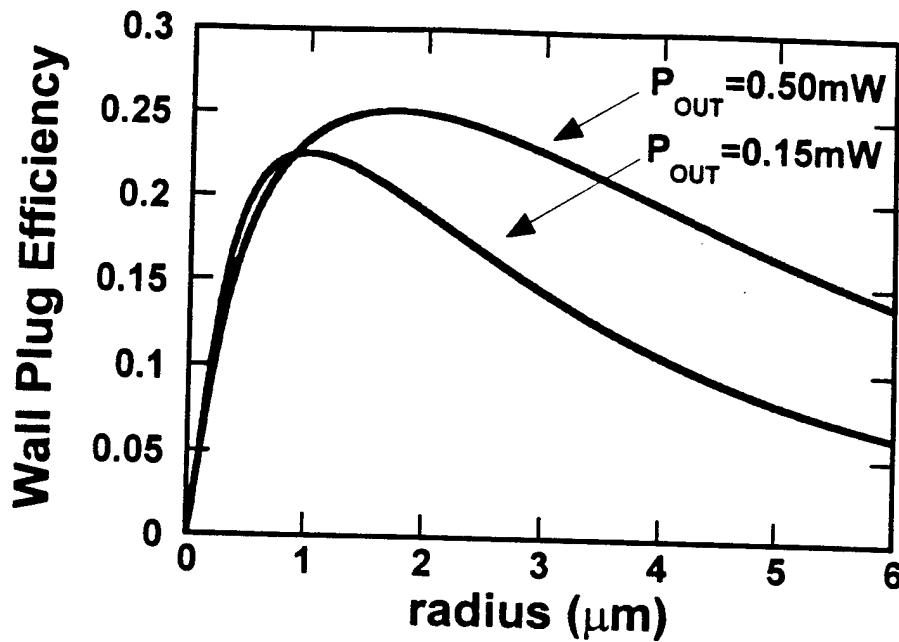
Figure 8-1: Wall-plug efficiency vs. device radius based upon fits to device parameters vs size for the best performing devices in this work

Future Potential Performance:

Even with improvements in current confinement, leakage still remains significant at the smaller sizes (as we discussed in Chapter 6). And due to the Be redistribution, the scaling of the voltage is likely worse that could be achieved with the same optical losses. Based on the estimates the improvements in the loss-resistance product discussed in Chapter 3 and based upon the loss-resistance products obtained in top performing carbon doped devices[1], use of a controlled doping profile (which is most important in the first few mirror periods where the doping is low) would probably give about a 30% lower resistance for the same optical losses. The expected improvements from removing leakage and from lowering the resistance are shown in Figure 8-2 for the cases of 0.5 and 0.15mW output power.
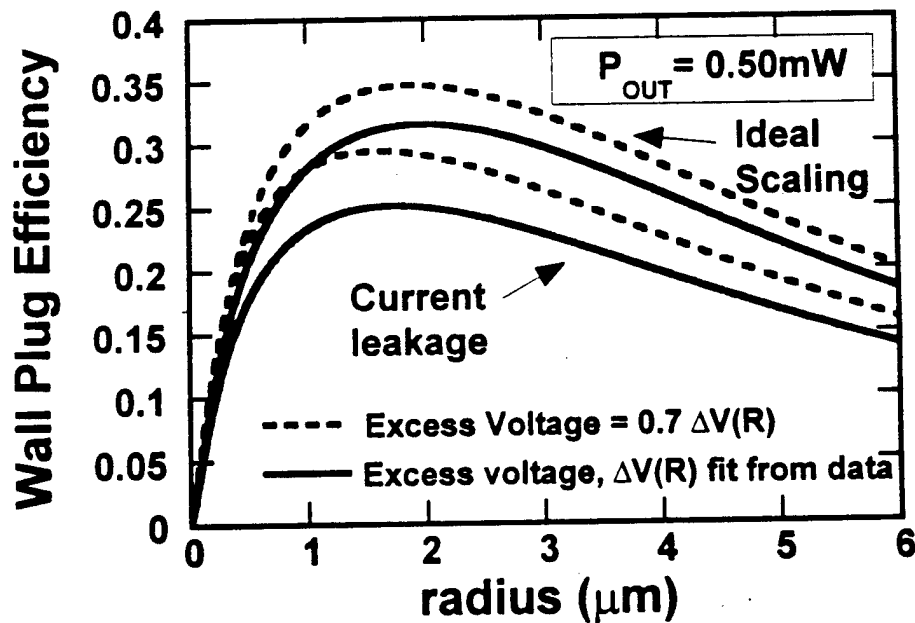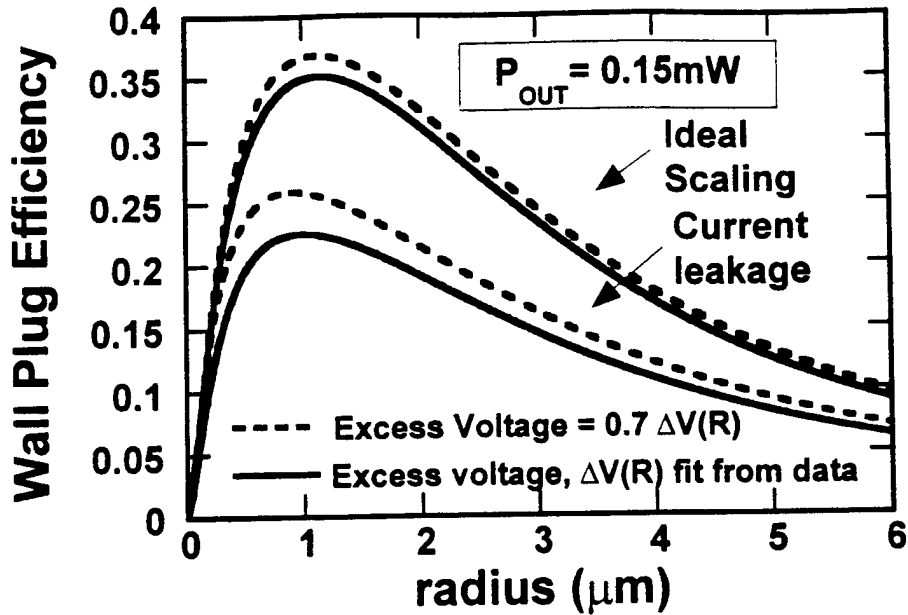
Figure 8-2: Scaling of the wall-plug efficiency at constant output power based on fitting the 1ª Null devices and the predicted improvement with current confinement and lower resistance.

We see that the most important improvement for higher wall-plug efficiency at lower output power is better current/carrier confinement and that by eliminating the excess current the peak efficiency will be higher even at lower output powers and smaller sizes - a trend we described in Chapter 2.

Future Opportunities:

Better Confinement

The improvements to scaling from better aperture design are desired for the smallest single-mode devices needed in the lowest power applications such as free-space optical interconnects chip-to-chip or board-to-board. And further improvement may be possible with techniques such as regrowth for carrier confinement or better dopant control just below the aperture.

Lower Capacitance

As we discussed, the parasitic capacitance can be reduced by using a thicker aperture away from the optical mode. Though the aperture in the 1st Null devices did have some longer tapering that extended over ~10μm from the optical mode all the way to the mesa boundary, the measured thickness change is not significant to change the capacitance across the oxide. As we described in Chapter 7, a slightly higher aluminum composition above the nominal aperture is desired to achieve this effect.

Small, Multimoded VCSELs

Much of this work focused on tapered apertures for lower losses for the fundamental mode in the smallest devices. But another possible opportunity for tapered apertures is to provide low scattering losses for many modes as desired when making smaller VCSELs for links using multimode fiber. Although thin apertures can provide low loss, they cannot guide as many modes as may be desired when the aperture becomes <~7μm diameter. Tapering is also useful at bunching lateral modes together spectrally which is desirable to squeeze more channels into a multimode WDM system. But such

potential benefits of tapered apertures have yet to be investigated experimentally.

References:

[1] K. L. Lear, K. D. Choquette, R. P. Schneider, S. P. Kilcoyne, and K. M. Geib, "Selectively oxidised vertical cavity lasers with 50% power conversion efficiency," *Electron. Lett.*, vol. 31, pp. 208-210, 1995.

Appendix A :
Graphite source carbon doping

Introduction

Carbon doping is very much desired for use in AlGaAs based vertical cavity lasers because unlike Be or Zn, C is a p-dopant that tends to stay in place during growth or any subsequent high temperature annealing. And the highest wall-plug efficiencies in VCSELs have been achieved in structures that use carbon doping. (In one case CBr_4 is used in an MBE system for the results of Ref. [1] and in another CCl_4 is used in an MOCVD system for results of Ref. [2].) As we discussed in Chapter 6, we even expect the scaling of the resistance to improve with carbon doping due to better control of doping in the more lightly doped first few mirror periods.

At UCSB, we have employed a heated graphite filament in an MBE system as the source for carbon. Matt Peters (in Appendix D of his thesis[3]) describes some background about the source along with initial doping calibrations,

contact resistance measurements, and in-plane laser characterization. Even for the same structure, the in-plane lasers tend to have lower threshold and higher injection efficiency (but also higher loss) than the best from system A (which uses Be) probably because the Be may move into the active region and raise the transparency current density and because the Be may not incorporate as well into the AlGaAs cladding resulting in lower loss, but also a higher field and lower barrier for electrons escaping the separate confinement heterostructure (SCH) and the quantum well region - this will lower the injection efficiency.

However, Peters attempts to make 980nm VCSELs or grow mirrors for wafer fused 1.55μm VCSELs were unsuccessful because of roughening of the layers. Under similar growth conditions of a 600°C substrate temperature and high As overpressure and 100 orientated GaAs substrates, other authors[4-7] using graphite filaments for carbon doping have only observed roughening of GaAs/AlGaAs structures at high doping levels ($>1e19cm^{-3}$) and not the moderate levels ($\sim 1e18cm^{-3}$) used for the mirror growths, but the structures grown in other works were not several microns thick as are VCSEL mirrors.

Optimized Growth Conditions for C doping

I tried several different growth conditions to avoid roughness in the carbon doped DBR mirrors (using a lower growth rate, lowering the Al content by 10%, using a substrate cut off-axis), but the most dramatic effects occurred when varying the substrate temperature. SEM images of the growths are shown in Figure A-1. These mirrors (designed for 1.55μm wafer fused VCSELs) are about 8μm high and the most challenging to grow smoothly. All the AlGaAs was grown by a 2nm period digital alloy and only step changes in doping were used (no delta doping), and the highest doping level was in the mid-$10^{18}cm^{-3}$. We can see the smoothest layers are produced at 675°C. (But as we will shortly discuss a somewhat lower temperature of 660°C is probably preferable.) At this high temperature the As flux was increased from its typical $0.9 \ 10^{-5}$ Torr beam equivalent pressure (BEP) to $1.3 \ 10^{-5}$ torr to ensure sufficient As incorporation[8]. (It is doubtful the increased As flux is responsible for smoothing the layers because I also grew an undoped mirror at 600°C using the usual (lower) As flux and observed no roughening.)
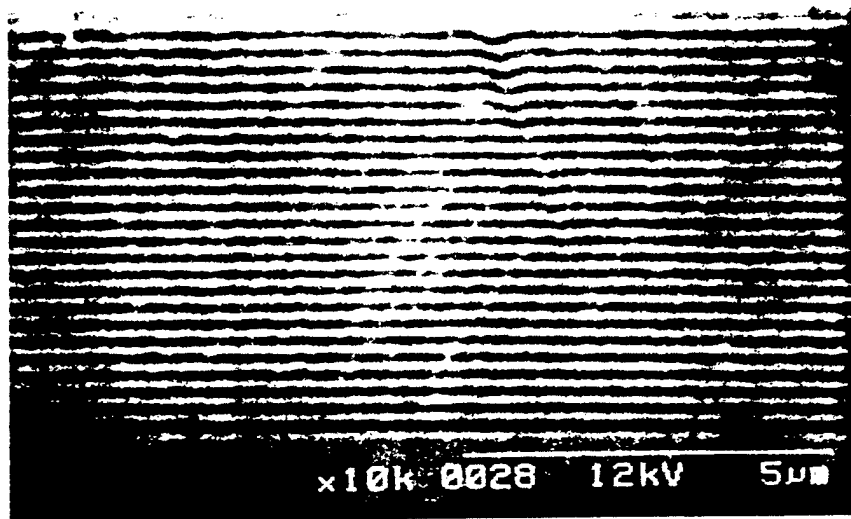
(a)
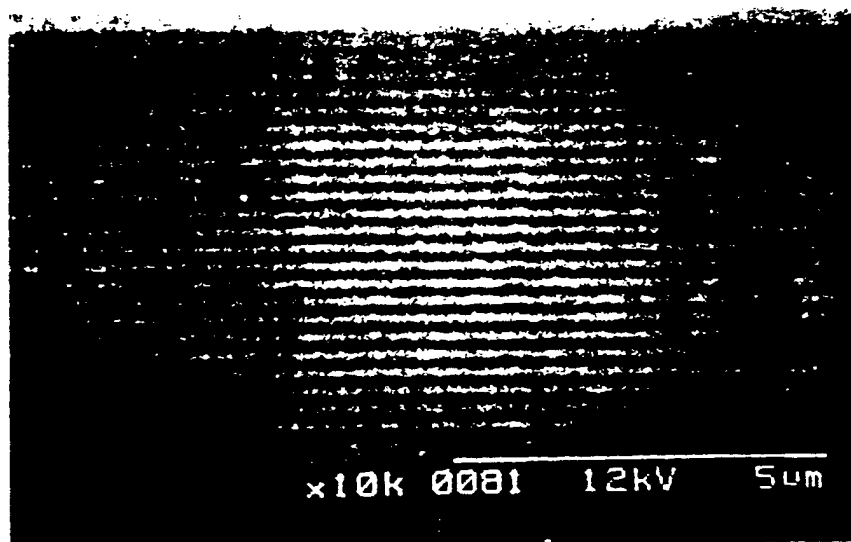
(b)
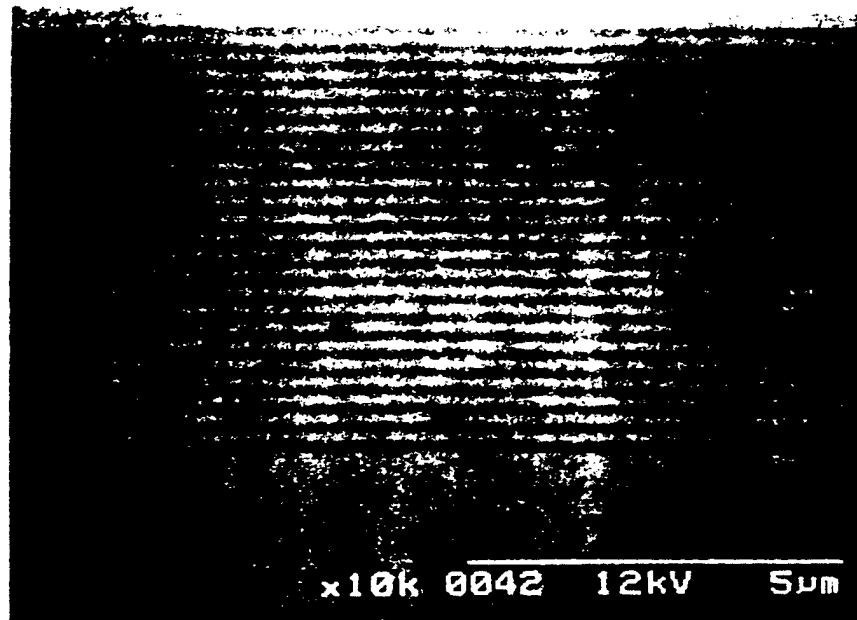
(c)

Figure A-1: Growths of $Al_{0.9}Ga_{0.1}As/GaAs$ mirrors centered around
1.55μm with an average carbon doping around $10^{18}cm^{-3}$ at
substrate temperatures of (a) 520°C, (b) 600°C, and (c) 675°C.
Roughening is removed in the highest temperature growth (but
this growth may be too hot as revealed by AFM)

Surface analysis

Although the hot growth at 675°C yielded a surface smooth to the eye and to
the SEM in cross-section, it still had odd defects on the surface as seen in an
optical microscope under Nomarski or by atomic force microscopy(AFM).
Such an image is shown in Figure A-2. One can see some pits and one large
bump in the image. These bumps were all over the sample. In the regions
without the pits and bumps, the surface is very smooth with an RMS roughness
of 0.169nm. A linescan over the bump is shown in Figure A-3. Interestingly
there is also a pit in the middle of this bump. We do not know the cause of the
bumps but the high growth temperature is suspected because the bumps did not
show up in a growth at 660°C and because the substrate temperature of 675°C
set just before growth likely means a 695°C temperature during growth due to
the radiation from the carbon filament (as we will discuss). Perhaps the bumps

are just a one-time artifact of the original sample surface. However, such bumps have not been observed in the microscope images routinely done of defect samples from the system.
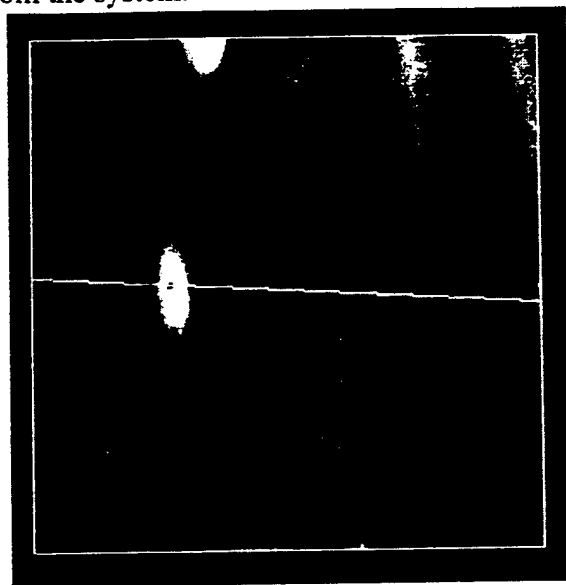
Figure A-2: 10x10μm AFM image of the surface of the carbon doped 675°C sample. The white line indicates the location of a linescsan below. (Measurement courtesy Jin Kim)
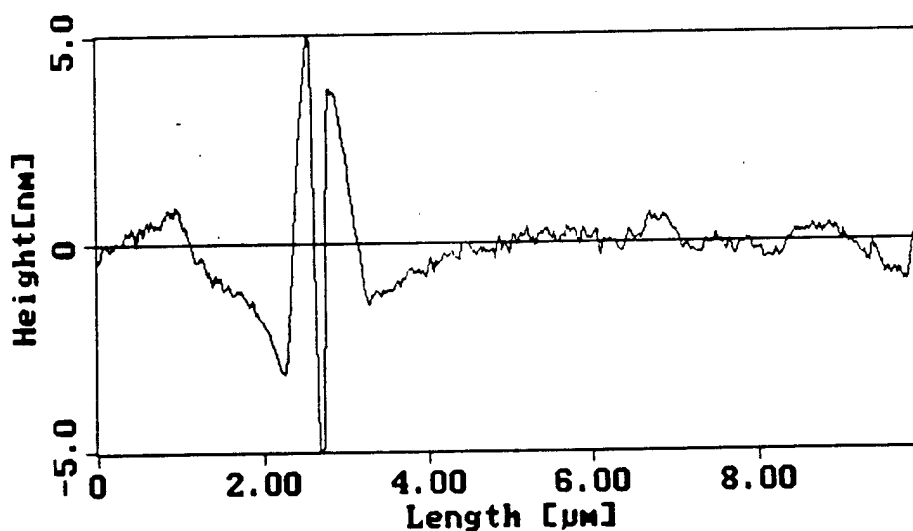
Figure A-3: Linescan of the bump shown in Figure A-2.
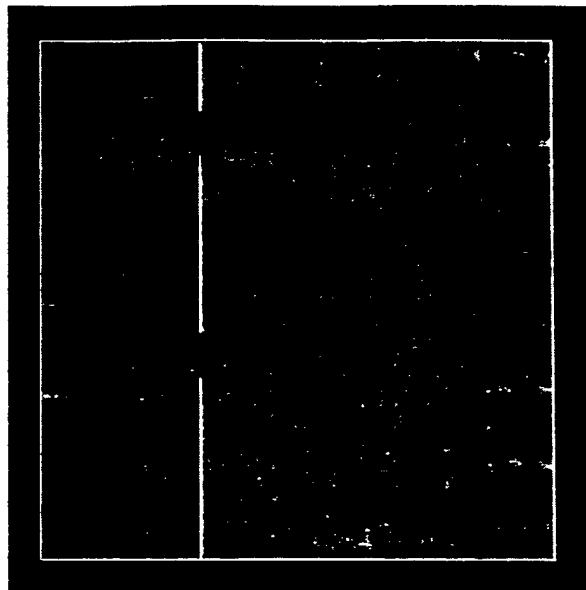
Figure A-4: 2x2μm AFM image of the surface of another 1.55μm mirror growth at 660°C. No bumps were observed, as in the 675°C growth, and no larger scale roughness occurred as in the 600°C growth, but pits remain over the sample. (Measurement courtesy Alexis Black.)
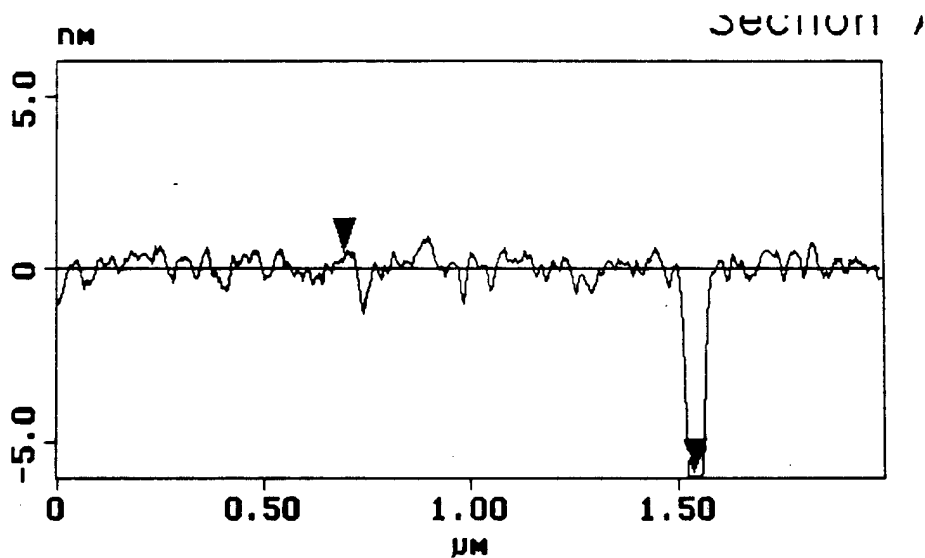
Figure A-5: Linescan of the pit shown in Figure A-4

Despite the bumps in the 675°C mirror, this mirror was smooth enough that Near Margalit could incorporate it in a wafer fused VCSEL which lased CW up to 45°C[9]. And these bumps did not appear in another 1.55μm mirror grown at a lower temperature of 660°C. We show this surface in Figure A-4. This mirror has an RMS roughness of 0.27nm in a pitless area and of 0.41nm over the whole image. We should point out that this mirror is much smoother than other λ~1.55μm, 7μm high Be-doped AlGaAs/GaAs mirrors (grown at 500°C) which have an RMS roughness of 2.5nm[10]! On the other hand, the 660°C carbon doped mirror is still not as smooth as the top of 980nm VCSELs which have 4μm high Be doped mirror grown at 500°C on top of 5μm of n-doped GaAs/AlGaAs grown at 600°C. Figure A-6 shows an AFM of the top of such a VCSEL. It shows no pits and has an RMS roughness of 0.25nm.
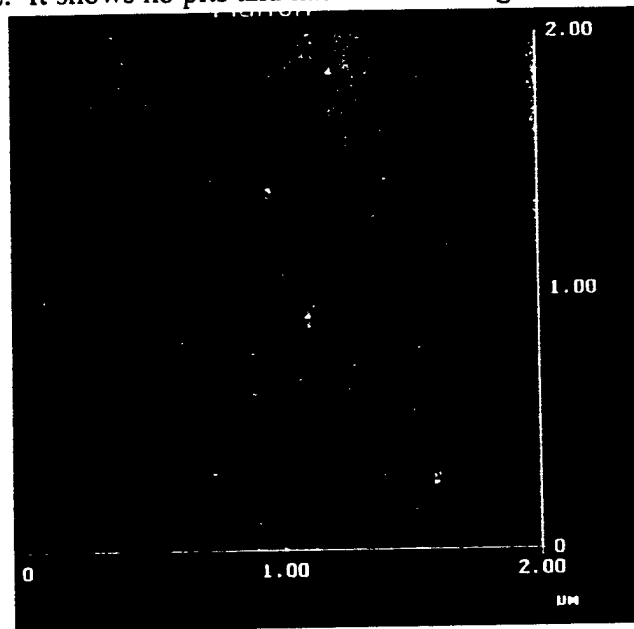
Figure A-6: AFM the Be doped 1ˢᵗ Null 980nm VCSEL shown for comparison. (AFM courtesy A. Black.)

Reasons for Roughness

Roughening at high doping levels (>1e19cm⁻³) is suspected to come from strain in the layers due to the larger size of C compared to As[7]. In that case, colder growth should help to keep the layers strained (and hence smoother). Roughening can also be caused by poor conditions for growing AlGaAs which

occur in a temperature range from 630-680°C when As_4 is used[8]. But at UCSB, we have used a cracker to produce As_2 and have not observed roughing of typical AlGaAs *digital* alloys at these growth temperatures. However, if the AlAs thickness within a period of the digital alloy exceeds about 5nm at a growth temperature of 680°C or if an analog alloy is grown, then facetting can be observed as described by Mirin[11]. (See also Chapter 5 in J. Ko's thesis[12.]) This facetting is due to too much surface mobility of the Al and occurs only along one crystal orientation. This roughness is avoided by using thinner Al layers and/or using lower substrate temperatures which reduce the Al mobility. Lastly, roughness can be due to impurities which limit the surface mobility. This is most likely the cause of the roughness in the mirrors because the higher substrate temperature increases the Ga and Al mobility. However, it is not clear that atomic carbon is alone responsible for the reduced mobility because DBR mirrors grown by MBE at 600°C with CBr_4 do not have this problem[13]. Both C_2 and C_3 will come off a graphite filament in vacuum though the rate is expected to be 10x less than atomic C[5]. Perhaps the carbon coming from the filament is in a higher, more reactive, energy state (not necessarily ionized) than the carbon that is created when a molecule like CBr_4 is cracked on the substrate surface. Or perhaps the Br acts as some surfactant (as does Sb even when the substrate is too hot for it to stick). But these are just guesses.

980nm C-doped VCSEL Results:

While lower voltage is the main reason touted for using carbon rather than beryllium doping, a better stated goal is lower voltage with the same or lower optical losses. Essentially, we are interested in a lower loss-resistance product at a given aperture radius. Although the threshold of devices may vary depending upon the offset between the gain peak and the mode, material quality and current confinement, we can examine the loss and resistance independently to see if the doping is optimized provided we are comparing devices large enough that the optical scattering losses from the aperture are not affecting performance.

We have made several generations of carbon doped VCSELs all with the same mirror transmission (0.7%). The L-I-V curves for 7μm diameter devices are

shown in Figure A-7 and Table A-1 shows a summary of the loss and resistances.
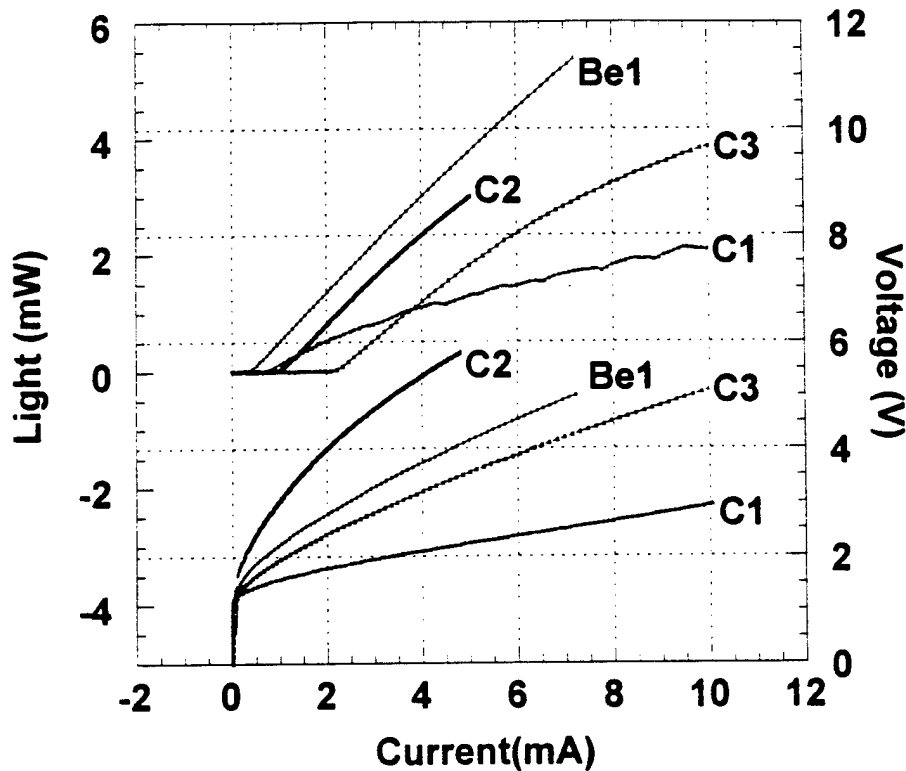
Figure A-7: L-I-V Curves of several generations (C1-C3) of C doped 7μm diameter VCSELs and the 7μm Be doped (Be1) 1st Null device shown for comparison (This device has the highest wall-plug efficiency).

Label	Alternate Sample name	Resist-ance Ω	Loss (%/RT)	R-L %Ω/RT	Comment
Be1	1st Null	491	0.28	137	Best for Be
C1	1st Peak	162	1.15	187	Doping high
C2	Vegas	723	0.29	212	Bad diode turn-on
C3	Monte Carlo	404	0.49	197	Large gain-offset

Table A-1: Summary of carbon doped 980nm VCSEL characteristics

The first generation (which we will call C1) were the "1st Peak" devices discussed previously in Chapter6 and compared to the Be1 "1st Null" devices. Due to an uncalibrated drift in the filament response, C1 VCSELs were heavily carbon doped (2e18 on average) and used a similar doping profile in all mirror periods. The loss-resistance is the lowest among the carbon doped devices, but the loss was too high for the mirror transmission; so the efficiency did not benefit. The second generation (C2) devices had low loss but a very high turn-on voltage (which was not due to high contact resistance). We expect the high turn-on is because the linear grade between the aperture and the Al$_{0.3}$Ga$_{0.7}$As that surrounds the active region was not doped. In the Be doped "1st Null" devices, this region was also undoped, but as discussed in Chapter 6, Be diffused into the active region. In the C2 devices it is unlikely the carbon moved into the grading region. In a study of p-i-n diode characteristics[3], Matt Peters showed that when the doping ends in a high Al content region, then the turn-on voltage can be very high. In generation (C3), the grading between the aperture and the active region was doped and the resistance was considerably lower, but a large offset between the gain peak and cavity mode raised the threshold considerably (Aside from causing some rolling over of the L-I curve, this should not effect the loss-resistance analysis.) Unfortunately, none of the carbon doped VCSELs matched or surpassed the best Be doped devices. Nevertheless, the material is good enough that reasonable performance can be achieved when one demands a dopant that will not diffuse during a high temperature (>800°C) anneal which might be used for disordering or for improving material quality.

Comment on Ga desorption and center wavelength:

Hot growth means there may be some Ga desorption; so the growth rate is not the same as we expect. I tried to test this by growing DBR calibration samples consecutively at 600°C, 660 and 600°C, but the variation in the growth rate during the day (0.5%) was larger than any change due to desorption causing the 660°C sample to be the longest wavelength. Probably a high As flux of 1.3e-5 Torr BEP helped reduce desorption. To be on the "safe" side during VCSEL growth, the first few periods of the top mirror above the active region

are grown at 630°C and the rest are grown at 660°C. In case there is desorption at 660°C, it should not change the wavelength considerably.

Other unique aspects of a filament source

Substrate Heating

The substrate temperature we have been quoting is the temperature measured by the pyrometer when the carbon source is closed. However it is worth noting that the carbon filament will radiatively heat the substrate.
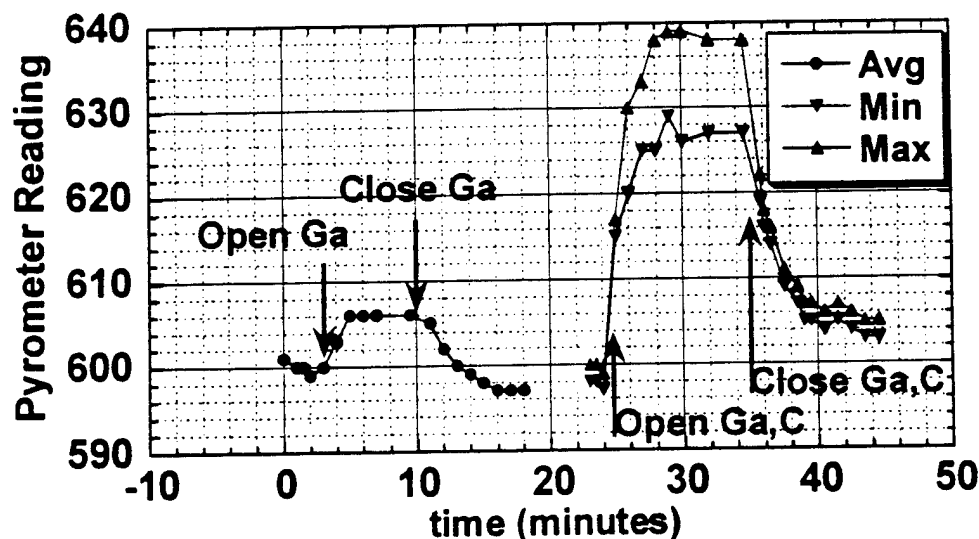
Figure A-8: Substrate Temperature vs. time after exposure to hot Ga and C sources. The C and Ga sources heat the substrate about 20°C

Figure A-8 shows a plot of the substrate temperature vs. time as the Ga and Ga and C are opened and closed. As the substrate rotates some light from the carbon filament can get reflected into the pyrometer and give a higher maximum reading, but you will notice that once the carbon shutter is closed the maximum and minimum converge, and it takes sometime for the temperature to decrease indicating the true substrate temperature was about 20°C higher when the C shutter was open.

Filament Temporal Response

One of the undesirable features of the carbon filament is that it takes sometime to change temperature. This adds a couple of hours extra delay to p-mirror growths (a minute or so per mirror layer is the minimum delay). Aside from the disadvantage for the grower (who may have to shut things off at 3am instead of 1am), the extra delay means it is not possible to precisely tailor the doping profile as we would like even though the carbon may stay put. And even with the one minute delay per mirror interface, it is still likely that the doping level is changing during layers that are supposed to be uniformly doped. With a valved gas source, changes in doping level would be virtually instantaneous and offer much more flexibility to the grower.
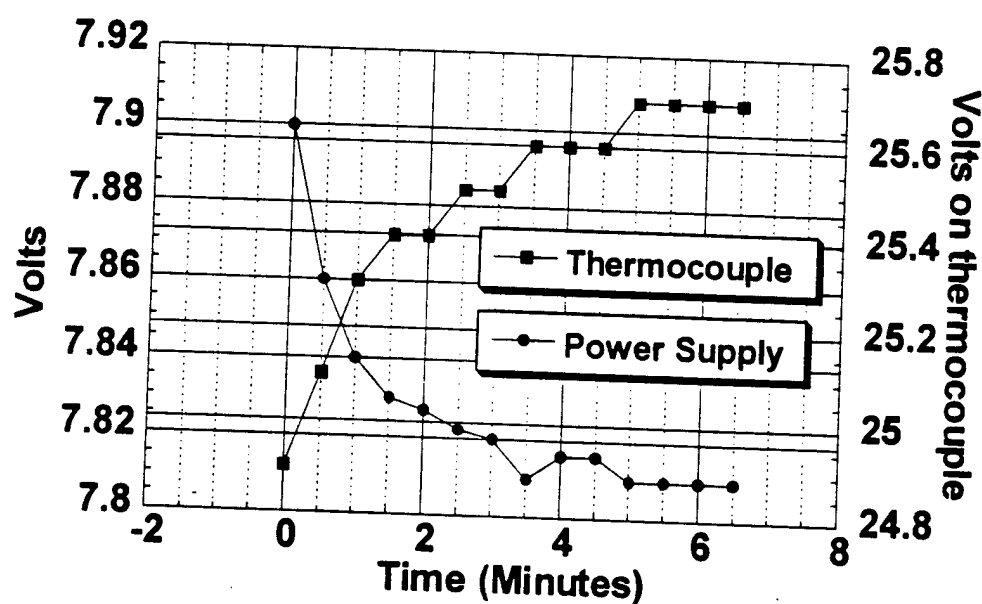
Figure A-9: Response of the carbon filament after the current source is changed from 73 to 77 amps. (The voltage on the power supply necessary to keep a constant current decreases because the resistance of the filament goes down as it heats up.)

Conclusions:

Use of a graphite filament for carbon doping in MBE has presented some difficulties in producing smooth layers. However, we found that by using a substrate temperature between 630-670°C, the layers become smooth - though they still have some pits over the surface. (Perhaps, as John English suspects, these pits are simply from thermal desorption of Ga and can be reduced with slightly lower temperature ~640°C and higher As flux.) Despite these pits, the mirror material for 1.55μm VCSELs is good enough that the fused VCSEL researchers achieved record high temperature (70°C) CW operation using it[14]. However, we were unable to improve the performance of 980nm VCSELs over the best achieved with Be doping. Perhaps this is due to some residual optical loss from the pits. Hopefully, gas source carbon doping will be available soon in the UCSB MBE lab and these problems will be solved.

References:

[1]   B. Weigl, M. Grabherr, C. Jung, R. Jager, G. Reiner, R. Michalzik, D. Sowada, and K. J. Ebeling, "High Performance Oxide-Confined GaAs VCSELs," *IEEE J. Selected Topics in Quantum Electron.*, vol. 3, pp. 409-415, 1997.

[2]   K. L. Lear, K. D. Choquette, R. P. Schneider, S. P. Kilcoyne, and K. M. Geib, "Selectively oxidised vertical cavity lasers with 50% power conversion efficiency," *Electron. Lett.*, vol. 31, pp. 208-210, 1995.

[3]   M. G. Peters, "Molecular Beam Epitaxy Growth of Vertical Cavity Lasers for Optical Communication", Ph. D. Dissertaion, UCSB, 1995

[4]   J. Nagle, R. J. Malik, and D. Gershoni, "A comparison of atomic carbon versus beryllium acceptor doping in GaAs grown by molecular beam epitaxy," *J. Crystal Growth*, vol. 111, pp. 264-268, 1991.

[5]   R. J. Malik, R. N. Nottenberg, E. F. Schubert, J. F. Walker, and R. W. Ryan, "Carbon doping in molecular beam epitaxy of GaAs from a heated graphite filament," *Appl. Phys. Lett.*, vol. 53, pp. 2661-2663, 1988.

[6]   R. J. Malik, J. Nagle, M. Micovic, R. W. Ryan, T. Harris, M. Geva, L. C. Hopkins, J. Vandenberg, R. Hull, R. F. Kopf, Y. Anand, and W. D.

Braddock, "Properties and applications of carbon-doped GaAs and AlGaAs layers grown by MBE with a pyrolytic graphite filament," *J. Crystal Growth*, vol. 127, pp. 686-689, 1993.

[7] W. E. Hoke, P. J. Lemonias, P. S. Lyman, H. T. Hendriks, D. Weir, and P. Colombo, "Carbon doping of MBE GaAs and Ga0.7Al0.3As films using a graphite filament," *J. Crystal Growth*, vol. 111, pp. 269-273, 1991.

[8] E. C. Larkins and J. S. Harris, "Chapter 2: MBE of High Quality GaAs and AlGaAs," in *Molecular Beam Epitaxy Applications to Key Materials*, R. F. C. Farrow, Ed. Park Ridge, NJ: Noyes Publications, 1995.

[9] N. M. Margalit, "High-Temperature Long-Wavelength Vertical Cavity Lasers", Ph. D. Dissertation, ECE Technical Report #98-15, University of California, 1998

[10] A. Black, , Personal Communication, 1998

[11] R. Mirin, M. Krishnamurthy, J. Ibbetson, J. English, and A. C. Gossard, "Observation of quasi-periodic facet formation during high temperature growth of AlAs and AlAs/GaAs superlattices," *J. Crystal Growth*, vol. 127, pp. 908-912, 1993.

[12] J. Ko, "High Performance 850nm Strained AlInGaAs/AlGaAs Vertical Cavity Lasers", Ph. D. dissertation, ECE Technical Report #98-11, University of California, 1998

[13] R. Michalzik, , Personal Communication, 1997

[14] K. A. Black, N. M. Margalit, E. R. Hegblom, P. Abraham, Y.-J. Chiu, J. Piprek, J. E. Bowers, and E. L. Hu, "Double-fused 1.5um vertical cavity lasers operating continuous-wave up to 70oC," in *Proc. 16th IEEE International Semiconductor Laser Conference*, 1998.

Appendix B
Theoretical Odds and Ends

Periodic and Uniform waveguiding:

In chapter 4, we described the propagation of a scalar wavefunction through an empty cavity with an aperture. When the cavity is unfolded, this periodic waveguiding (in the Fresnel approximation) is just like the BPM method commonly used to model waveguides. Of course, BPM (or periodic waveguiding) is only an approximation of a uniform waveguide and the difference between the wavefunctions depends upon where one picks the wavefunction in the periodic guide (i.e. just after the aperture or symmetrically between them.) Here we crank out that difference in terms of the cavity length.

Periodic waveguide equation

Recalling from Chapter 4, Eq. (4-18), passing a scalar mode, Ψ, through a cell of the periodic waveguide can be represented as the operator, $\hat{P}$.

$$\hat{P}\Psi = \hat{D}\exp\{j\phi(x,y)\}\hat{D}\Psi \qquad (B-1)$$

As we described in Chapter 4, $\phi(x,y)=k_0\Delta n_d(x,y)L_C$ where Δn_d is the effective index profile of the equivalent uniform waveguide and $\hat{D}$ is the free-space propagator for the wavefunction diffracting through half a cavity length. (This time we will use physical rather than normalized coordinates.) Again from Chapter 4, the $\hat{D}$ operator is defined (in the Fresnel limit) by:

$$\hat{D} = \hat{F}^{-1}\exp\{-jk_r^2 L_C/(4k_0 n_0)\}\hat{F} \qquad (B-2)$$

where the operator $\hat{F}$ is the Fourier transform defined by

$$\hat{F} = \iint dk_x dk_y \exp\{jk_x x + jk_y y\} \tag{B-3}$$

If Ψ is a mode of the periodic waveguide, then it is an eigenfunction of $\hat{P}$ whereby,

$$\hat{P}\Psi = \exp(jk_0 \Delta n_m L_C)\Psi . \tag{B-4}$$

Δn_{m} is a constant (spatially-independent) effective index step for the mode. Unlike the definition in Chapter 4, here we define Δn_{m} relative to the effective cladding index, $n_{\mathrm{d-min}}$, rather than the effective core index, $\Delta n_m = n_m - n_{d-\min}$, and n_{m} is the effective index for the mode. To make a comparison with the wave equation for a uniform waveguide, we need to start expanding this expression in terms of L_{C}. However, to keep the math compact, we will try to minimize the amount of expanding we do. For the $\hat{D}$ operator, we have:

$$\hat{D} = \hat{F}^{-1} \exp\{-jk_r^2 L_C /(4k_0 n_0)\}\hat{F} = \hat{F}^{-1}\left(\sum_{m=0}^{\infty}\left[-jk_r^2 L_C /(4k_0 n_0)\right]^m / m!\right)\hat{F} \tag{B-5}$$

And we note that when a function is multiplied in k-space by $-jk_x$ that this operation is equivalent to taking the derivative in real-space. Consequently, multiplying by $k_r^2 = k_x^2 + k_y^2$ in the Fourier domain, is the same as applying $\nabla_\perp^2 = \nabla_x^2 + \nabla_y^2$ to the function in real space. Thus, we can rewrite $\hat{D}$ as

$$\hat{D} = \hat{F}^{-1}\left(\sum_{m=0}^{\infty}\frac{1}{m!}\left[-jk_r^2 L_C /(4k_0 n_0)\right]^m\right)\hat{F} = \sum_{m=0}^{\infty}\frac{1}{m!}\left[jL_C /(4k_0 n_0)\nabla_\perp^2\right]^m \tag{B-6}$$

$$= \exp\left(jL_C /(4k_0 n_0)\nabla_\perp^2\right)$$

For those not comfortable with operators in the argument of an exponential, one can always undo the last step. Now let us rewrite the periodic waveguide eigenvalue equation:

$$\hat{P}\Psi = \hat{D}\exp\{j\phi(x,y)\}\hat{D}\Psi$$

$$= \exp\left(jL_C /(4k_0 n_0)\nabla_\perp^2\right)\exp\left(jk_0 \Delta n_d(x,y)L_C\right)\exp\left(jL_C /(4k_0 n_0)\nabla_\perp^2\right)\Psi \tag{B-7}$$

$$= \exp(jk_0 \Delta n_m L_C)\Psi$$

To write this more compactly, we define $\hat{A} = \dfrac{1}{4k_0 n_0}\nabla_\perp^2$ and $\hat{B} = k_0 \Delta n_d(x,y)$, then,

$$\hat{P}\Psi = \exp\left(jL_C \hat{A}\right)\exp\left(jL_C \hat{B}\right)\exp\left(jL_C \hat{A}\right)\Psi = \exp(jk_0 \Delta n_m L_C)\Psi \tag{B-8}$$

It looks tempting to simply add the arguments of the exponentials, but this would be a serious mistake because the derivative operator and multiplication by $\Delta n_d(x,y)$ are not operations that commute; i.e. you cannot multiply a wavefunction by $\Delta n_d(x,y)$ and take the derivative and expect the same answer if you did them in opposite order. This condition also prevents us from dropping all the jL_c factors in the exponentials.

Uniform waveguide equation

Now we will move to the wave equation which does not initially look much like (B-7). In a familiar form, the wave equation is

$$\left[\nabla_\perp^2 + k_0^2 n_d^2(x,y)\right]\Psi = k_0^2 n_m^2 \Psi \tag{B-9}$$

where, as mentioned, n_m is the effective index for the mode. We now make the approximation of small differences in the distributed index steps (which typically are pretty small $<2\% \ n_0$).

$$n_d^2(x,y) = \left[n_{d-\min} + \Delta n_d(x,y)\right]^2 \approx n_{d-\min}^2 + 2n_{d-\min}\Delta n_d(x,y)$$

$$n_m^2(x,y) = \left[n_{d-\min} + \Delta n_m(x,y)\right]^2 \approx n_{d-\min}^2 + 2n_{d-\min}\Delta n_m(x,y) \tag{B-10}$$

Without adding any first order errors in index step, we can also approximate the second term as $2n_{d-\min}\Delta n_d \approx 2n_0\Delta n_d$. Combining these approximations, the wave equation now looks like:

$$\left[\frac{1}{2k_0 n_0}\nabla_\perp^2 + k_0\Delta n_d(x,y)\right]\Psi = k_0\Delta n_m \Psi \tag{B-11}$$

We define $\hat{W} \equiv \frac{1}{2k_0 n_0}\nabla_\perp^2 + k_0\Delta n_d(x,y)$. Because $\hat{W}\Psi = k_0\Delta n_m \Psi$, we can operate on both sides with $\hat{W}$ and obtain $\hat{W}^2\Psi = \left(k_0\Delta n_m\right)^2\Psi$. We could keep doing this for any power of $\hat{W}$ and then add these equations together as the Taylor series for an exponential then we get a new form which we define as the $\hat{U}$ operator:

$$\hat{U}\Psi = \exp\left(jL_C\hat{W}\right)\Psi = \exp(jk_0\Delta n_m L_C)\Psi \tag{B-12}$$

L_C has been introduced here as a constant which could be dropped from both sides, but is needed to compare the order of the expansion. Using the previous definitions for $\hat{A}$ and $\hat{B}$, this becomes:

$$\hat{U}\Psi = \exp\left(jL_C\left[2\hat{A} + \hat{B}\right]\right)\Psi = \exp(jk_0\Delta n_m L_C)\Psi \tag{B-13}$$

Now this form of the wave equation, Eq. (B-13) looks very similar to the eigenvalue equation for the periodic waveguide, Eq. (B-8). If fact the right side is identical so we do not have to worry about it. But the exponentials on the left side are combined which we know is not quite the same.

Mathematical difference between periodic and uniform waveguiding

To determine the difference between the $\hat{U}$ operator (which has the same eigenfunctions as the uniform waveguide operator, $\hat{W}$) and the and the $\hat{P}$ operator (which has eigenfunctions of the periodic waveguide) is simply an exercise in Taylor series expansion. If the $\hat{P}$ and the $\hat{U}$ operators are expanded to second order in L_C, they will match. Then one can say that the eigenfunctions of the uniform waveguide will match the periodic waveguide. However, if the operators are expanded to third order in L_c, we find differences. Expanding the $\hat{P}$ operator gives:

$$\hat{P}\Psi = \exp\left(jL_C\hat{A}\right)\exp\left(jL_C\hat{B}\right)\exp\left(jL_C\hat{A}\right)\Psi$$

$$\approx \left(1 + jL_C\hat{A} - \frac{L_C^2\hat{A}^2}{2} - \frac{jL_C^3\hat{A}^3}{6}\right)\left(1 + jL_C\hat{B} - \frac{L_C^2\hat{B}^2}{2} - \frac{jL_C^3\hat{B}^3}{6}\right)$$

$$\left(1 + jL_C\hat{A} - \frac{L_C^2\hat{A}^2}{2} - \frac{jL_C^3\hat{A}^3}{6}\right) \tag{B-14}$$

And expanding the $\hat{U}$ operator gives:

$$\hat{U}\Psi = \exp\left(jL_C\left[2\hat{A} + \hat{B}\right]\right)\Psi$$

$$\approx \left(1 + jL_C\left[2\hat{A} + \hat{B}\right] - \frac{L_C^2\left[2\hat{A} + \hat{B}\right]^2}{2} - \frac{jL_C^3\left[2\hat{A} + \hat{B}\right]^3}{6}\right) \tag{B-15}$$

If we multiply out all these terms and collect them, we will find that $\hat{P} = \hat{U} + \Delta\hat{U}$ and that

$$\Delta\hat{U} = -jL_C^3/6\left[2\hat{A}\hat{B}\hat{A} - \hat{B}\hat{A}^2 - \hat{A}^2\hat{B} - 2\hat{B}\hat{A}\hat{B} + \hat{B}^2\hat{A} + \hat{A}\hat{B}^2\right] \tag{B-16}$$

which can be more compactly expressed using the notation $\left[\hat{\mathbf{A}},\hat{\mathbf{B}}\right]=\hat{\mathbf{A}}\hat{\mathbf{B}}-\hat{\mathbf{B}}\hat{\mathbf{A}}$,

$$\Delta\hat{\mathbf{U}}=-jL_C^3/6\left[\hat{\mathbf{A}}+\hat{\mathbf{B}},\left[\hat{\mathbf{B}},\hat{\mathbf{A}}\right]\right] \tag{B-17}$$

Because the operators are not very physically intuitive, lets get back to some physical variables. The difference term depends cavity length, wavelength, the total index step, and but such factors multiply $\left[\hat{\mathbf{B}},\hat{\mathbf{A}}\right]$ and if this term is zero then so is the difference term, $\Delta\hat{\mathbf{U}}$.

$$\left[\hat{\mathbf{B}},\hat{\mathbf{A}}\right]=\frac{1}{4n_0}\left(\Delta n_d(x,y)\nabla_\perp^2-\nabla_\perp^2\Delta n_d(x,y)\right) \tag{B-18}$$

We see that if we could just move the index step through the Laplacian, then we would be ok, and this can happen when the index profile is parabolic so that its second derivative is a constant. In that case $\left[\hat{\mathbf{B}},\hat{\mathbf{A}}\right]=0$.

Note on location of wavefunction in the periodic waveguide

The cell of the periodic waveguide we used started between the apertures and gave the operator this form:

$$\hat{\mathbf{P}}\Psi=\exp\left(jL_C\hat{\mathbf{A}}\right)\exp\left(jL_C\hat{\mathbf{B}}\right)\exp\left(jL_C\hat{\mathbf{A}}\right)\Psi \tag{B-19}$$

But if we had begun the cell of the periodic waveguide just before the aperture, then the operator would have the following form:

$$\hat{\mathbf{P}}\Psi=\exp\left(jL_C 2\hat{\mathbf{A}}\right)\exp\left(jL_C\hat{\mathbf{B}}\right)\Psi \tag{B-20}$$

If one then expands this operator to second order in L_C and compares it with a second order expansion of $\hat{\mathbf{U}}$, then there is difference, $\Delta\hat{\mathbf{U}}$ between the expressions and that difference

$$\Delta\hat{\mathbf{U}}=L_C^2\left[\hat{\mathbf{B}},\hat{\mathbf{A}}\right] \tag{B-21}$$

depends upon $\left[\hat{\mathbf{B}},\hat{\mathbf{A}}\right]$ as before. Thus, to obtain the best match between the uniform waveguide and the periodic waveguide, one should compare the wavefunctions centered between the apertures or in the center of the apertures.

Modified Expressions for Mirror Length

In Chapter 4, we gave expressions for the diffraction equivalent distance and phase penetration depths for DBRs which contained only quarter-wave layers

and had abrupt interfaces. DBRs in VCLs, however, often have graded interfaces or extra half-wavelength spacers (usually for the purpose of forming intra-cavity contacts). To determine the diffraction equivalent distance for an arbitrary DBR, one would determine the phase, Θ, of the mirror reflection vs. incident angle, α, using a transmission matrix approach[1], and then fit the response for small angles to the response of a hard mirror, $\Theta(\alpha) = \Theta(0) + k_0^2 \alpha^2 L_D / (k_0 n_0)$. But we would like to avoid this extra numerical calculation, if possible.

Adding Extra λ/2 spacers

If extra λ/2 spacer layers are added in the DBR, we find the change in the phase penetration depth, L_τ, by further manipulating the result in [2],

$$L_\tau = L_{\tau,QW} + \frac{\lambda}{2n_0} \frac{qp^{m-1}}{1 - \left(aqp^{m-1}\right)^2} \sum_{j=1}^{m} u_j p^{j-m} \left(1 - \left(ap^{m-j}\right)^2\right)$$

$$\approx L_{\tau,QW} + \frac{\lambda}{2n_0} \sum_{j=1}^{m} u_j qp^{j-1}$$

(B-22)

where u_j is an integer equal to the number of extra half-wavelengths in the jth layer. We number the layers of the DBR starting with the layer just after the incident interface (This is opposite of the convention used in [2]). m is the number of mirror layers, and $q = n_{LI}/n_{HI}$, $p = n_L/n_H$, and $a = n_{LE}/n_{HE}$ are the ratios (chosen less than 1) between the refractive indexes of materials at the incident, intermediate and exit interfaces, respectively. $L_{\tau, QW}$ is the penetration depth for the mirror without any spacer layers. ($L_{\tau,QW}$ was previously specified in Section II for the case of an infinite stack.) For a large number of layers (as in typical VCLs), $p^m \ll 1$ and the phase penetration depth may be approximated as in Eq. (B-22).

The diffraction equivalent distance depends on L_τ (which is proportional to the change in phase with frequency) and ξ (which is used to relate the shift in the center frequency to changes in the angle of incidence). We can assume that the change in the center wavelength of the DBR is still dominated by the quarter-wave layers, then the diffraction equivalent distance with an extra half-wave spacer is again given by $L_D = \xi L_\tau$, where the L_τ from (A1) is used.

Graded Interfaces

From the derivation in [3], one finds the phase penetration depth depends only on the reflectivity of the DBR interfaces and the phase delay between them. When graded interfaces are used instead of abrupt interfaces, the reflectivity will be reduced and the mirror lengthened. We use the result of [4] in which coupled mode theory is used to estimate the reduction in the reflectivity per interface due to the grading. (Note this is different from applying coupled mode theory to the whole DBR, which assumes the exit and incident media are equal to the average index). The result in [4] is that the inverse hyperbolic tangent of the interface reflectivity is reduced by a factor we will denote as γ, which is the ratio of the coupling constants for a graded profile to that of a square wave. The same reflectivity can also be produced by an abrupt interface with a higher index ratio, $p_{eff} = p^{\gamma}$ As noted in [4], $\gamma = \sin(f\pi/2)/(f\pi/2)$, for linear grading. f is the fraction of a mirror period which is graded. Thus to account for the effect of grading on L_{r}, we simply need to use the new index ratio p_{eff} instead of p. If the first interface is graded also, then we should modify the index ratio, q, in the same manner.

Graded interfaces will also change ξ, which relates the change in the center mirror frequency to the change in the angle of incidence. This change is determined from the requirement that the phase shift (for a ray traveling off-axis) across a mirror period equals π at the center mirror frequency. Using these requirements and following the approach in [5], we obtain $\xi = \frac{n_0^2}{2}\left(\frac{4}{\lambda}\int dz \frac{1}{n(z)}\right)$, where $n(z)$ is the longitudinal index profile and the integral is performed over one mirror period. One can obtain a closed-form expression in the case of linearly graded interfaces. However, if we consider a typical case of interfaces graded linearly over 20nm from n_H=3.52 to n_L=2.95 (at λ=1μm), then one finds the change in ξ is only 0.1%. For the same parameters, and n_0=3.52, the change in L_t is 3%, an order of magnitude larger.

Confinement Factor vs. V number
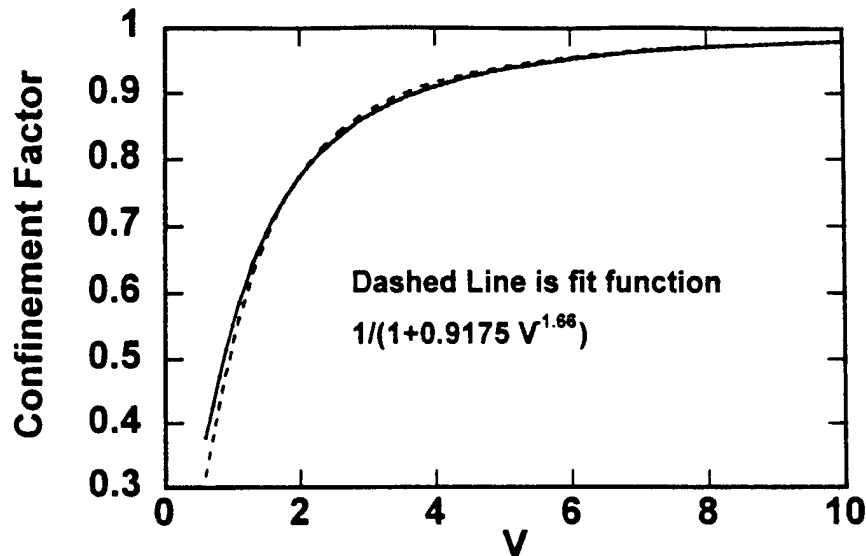
Figure B-1: Fraction of power confined within the core of a uniform step-index, circular waveguide along with a fitting function.

Mode Radius vs. V number

In Chapter 4, we defined the mode radius, a_m, for the fundamental mode by:

$$a_m = \sqrt{\frac{2}{\pi} \iint dx\,dy |\Psi|^2 / |\Psi(0,0)|^2} \qquad \text{(B-23)}$$

For a Gaussian mode, a_m is the radius where the field^2 drops by $1/e^2$ from the peak. This is sometimes more useful than using the standard deviation which can be too influenced by the tails of a distribution. Such a radius can be computed for the Bessel function modes of a step-index uniform waveguide and a simple fitting formula can be found as shown below.
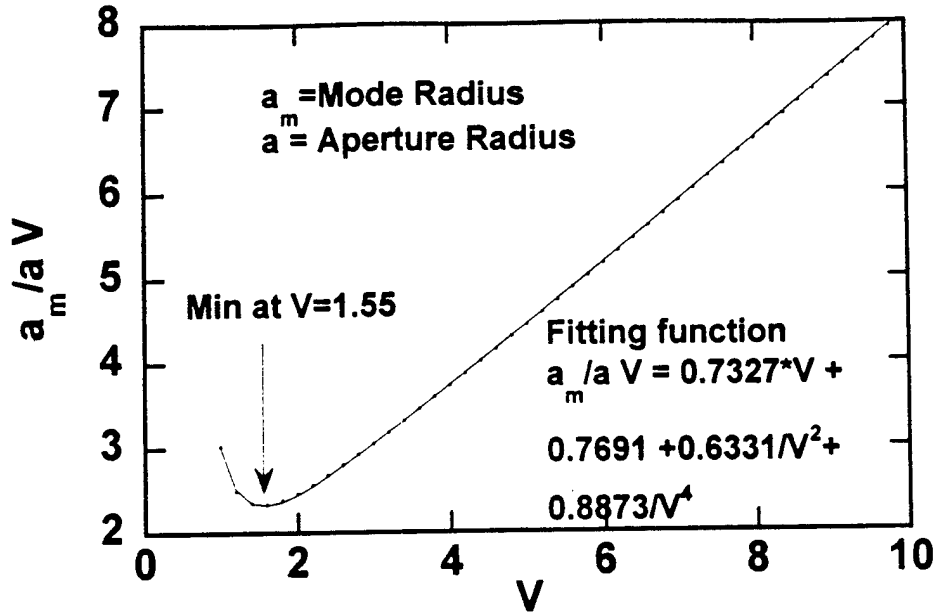
Figure B-2: Normalized mode radius vs. V number for a circular step-index longitudinally uniform waveguide

Generalized Optical Efficiency

Often the optical efficiency (stimulated photons out/stimulated photons generated) is calculated by looking at the transmission through the output mirror as viewed from the cavity and having some estimate for internal losses. But it is possible to find the optical efficiency just knowing the standing-wave field for the entire VCSEL structure without having to separately do calculations for the mirrors. This method is not as intuitive, but it is handy when one has the whole structure in a transmission matrix program and already found the threshold. (Or if someone flashes the standing wave at you, you can show off.) In his thesis[6], Scott Corzine derives the condition for optical power conservation inside the VCSEL cavity

$$\frac{dW_{TOT}}{dt} = 0 = \frac{1}{2}\omega\varepsilon_0 \int_{cavity} \varepsilon_I |E|^2 dV - \int_{surface\,bounding\,cavity} (\hat{n} \cdot \bar{S}) dA \quad \text{(B-24)}$$

where W_{TOT} is the energy density in the cavity, ε_I is the imaginary part of the dielectric constant, ω is the optical frequency (times 2π), $\vec{S} = \frac{1}{2}\text{Re}\{\mathbf{E} \times \mathbf{H}^*\}$ is the Poynting vector and $\hat{n}$ is the surface normal vector. In steady state, the power into and power out of the cavity are equal so $dW_{TOT}/dt = 0$. For clarity, these terms are:

$$\frac{dW_{TOT}}{dt} = 0 = P_{IN} - P_{ABS} - P_{OUTMIRROR1} - P_{OUTMIRROR2} - P_{SCATTER} \quad \text{(B-25)}$$

where

$$P_{OUTMIRROR1} = \int_{\text{surface of mirror1}} (\hat{n} \bullet \vec{S}) dA ,$$

$$P_{OUTMIRROR2} = \int_{\text{surface of mirror2}} (\hat{n} \bullet \vec{S}) dA ,$$

$$P_{SCATTER} = \int_{\text{surface excluding mirrors}} (\hat{n} \bullet \vec{S}) dA$$

$$P_{ABS} = -\frac{1}{2}\omega\varepsilon_0 \int_{\text{region where } \varepsilon_I < 0} \varepsilon_I |E|^2 dV$$

$$P_{IN} = \frac{1}{2}\omega\varepsilon_0 \int_{\text{region where } \varepsilon_I > 0} \varepsilon_I |E|^2 dV$$

The optical efficiency (out of mirror1) is then written as

$$\eta_{OPT} = \frac{P_{OUTMIRROR1}}{P_{IN}} \quad \text{(B-26)}$$

1-D Cavity

For the case of the simpler, one-dimensional cavity,

$$P_{OUTMIRROR1} = c\varepsilon_0 / 2 |E_{OUT}|^2 n_{OUT} \quad \text{(B-27)}$$

where E_{OUT} is the field at the output medium, and n_{OUT} is the real part of the index of the output medium. And

$$P_{IN} = \frac{1}{2}\varepsilon_0 c \int_{\text{active region}} g|E|^2 n_G dz \quad \text{(B-28)}$$

where c is the speed of light, g the material gain (in units of inverse length) of the active region and n_G is the real part of the index of the active region. Combining the expressions, we have

$$\eta_{OPT} = \frac{|E_{OUT}|^2 n_{OUT}}{n_W \sum_{wells} l_W g_W |E_W|^2} \tag{B-29}$$

where n_w is the real part of the index of the quantum wells, l_w is the length (thickness) of the wells, g_w is the gain of a quantum well (inverse length) and E_w is the field in the wells. Because we can also approximate the optical efficiency the usual way as $\eta_{OPT} = \frac{T}{T+L} = \frac{T}{2\Gamma_{enh} g_W l_W N_W}$, we can extract the field or photon density in the quantum wells if desired.

References:

[1]   P. Yeh, *Optical Waves in Layered Media*. New York: Wiley, 1988.

[2]   I. H. Tan, E. L. Hu, J. E. Bowers, and B. I. Miller, "Modeling and Performance of Wafer-Fused Resonant Cavity Enhanced Photodetectors," *IEEE J. Quantum Electron.*, vol. 31, pp. 1863-1875, 1995.

[3]   D. I. Babic and S. W. Corzine, "Analytic Expressions for the Reflection Delay, Penetration Depth, and Absorptance of Quarter-Wave Dielectric Mirrors," *IEEE J. Quantum Electron.*, vol. 28, pp. 514-524, 1992.

[4]   S. W. Corzine, R. H. Yan, and L. A. Coldren, "A tanh substitution technique for the analysis of abrupt and graded interface multilayer dielectric stacks," *IEEE J. Quantum Electron.*, vol. 27, pp. 2086-2090, 1991.

[5]   D. I. Babic, Y. Chung, N. Dagli, and J. E. Bowers, "Modal Reflection of Quarter-Wave Mirrors in Vertical-Cavity Lasers," *IEEE J. Quantum Electron.*, vol. 29, pp. 1950-1955, 1993.

[6]   S. W. Corzine, "Design of Vertical-Cavity Surface-Emitting Lasers with Strained and Unstrained Quantum Well Active Regions", Ph. D. Dissertation, ECE Technical Report #93-09, University of California, 1993

Appendix C
Layer Specifications

The following is a copy of the MBE programs used to grow the 1st Null VCSELs discussed in Chapter 6. There are three programs which are used in order. They could have been combined into one program but it would be too large for the old HP machine we use.

How to read the MBE program

The MBE programming language is relatively straightforward. Structures are subroutines as in most programming languages and are called by name. The first line executed is denoted with "!!! BEGIN HERE". The "!!!" are used for comments. Aside from calls to structures and the use of repeat loops, the only other commands are as follows:

COMMANDS IMPORTANT TO SPECIFYING EPITAXIAL LAYERS:

dope be (or dope si)	means that the Be shutter will be open during all the subsequent layers until an "end dope be" command is issued. I usually set the doping level just before by calling a structure like "p_2e18" to set the Be cell temperature corresponding to that doping level.
end dope be	See above
l ga t=80	short for layer ga thickness=80
	opens the Ga shutter long enough for 80A to be grown - (see growth rate). (The As shutter is always open during growth.)

The AlGaAs layers are grown by digital alloy with a period <=20A. So when you see

        repeat 10
                1 ga t=12
                1 all t=8
        end repeat

it effectively means that a 200A layer of $Al_{0.4}Ga_{0.6}As$ is grown.

COMMANDS ONLY IMPORTANT TO GROWERS

growth rate ga=2.83	specifies that when the Ga shutter is open for 1 second that 2.83A will be grown. This number is measured by the grower on the growth day and is irrelevant to anyone just wanting to know the epitaxial structure. Just read the "thickness=.." lines.
rotation 10	set substrate rotation to 10 RPM - again only relevant to the grower
valve As2 350	changes the arsenic value position - I usually state what flux this corresponds to.
close	closes all shutters - only growers need to worry about this command. It is mostly used to prevent commands being executed before they should be because of a quirk of the MBE programming language

Program for bottom of 1st Null VCSEL

!!! 12.5 periods of bottom of the structure
!!! and 1 lambda of the GaAs contact layer

structure si_2e18
        close
        temperature si=1250
end structure

structure si_3e18
        close
        temperature si=1265

```
end structure

structure si_5e18
        close
        temperature  si=1300
end structure

structure binaries
        !!! lambda=990nm
        !!! lambda/2.95/4 = 839A
        l al1 t=839
        !!! lambda/3.52/4 = 703A
        l ga t=703
end structure

structure contact  !!! grow 1 lambda
        si_3e18
        l al1 t=539
        dope si
        l al1 t=250
        end dope si

        l al1 t=50
        l ga t=100
        dope si
        l ga t=603
        l ga t=703
        l ga t=703
        si_2e18
        l ga t=703

        !!! in the next structure - still need to grow extra landa/4 - grade
        !!! to finish mirror period
end structure

!!! ******************** START HERE

growth rate ga=2.732
growth rate al1=2.864

rotation 10

l ga t=1000   !!! buffer layer

temperature  si=800   !!! warm up cell
repeat 11
        binaries
```

```
end repeat

si_2e18
binaries
!!! total 12 ga layers
contact
!!! total 13 ga layers

close
rotation 0
temperature  substrate=200
```

Program for middle of 1ˢᵗ Null VCSEL

```
structure si_5e17
        close
        temperature  si=1160
end structure

structure si_1e18
        close
        temperature  si=1200
end structure

structure si_5e18
        close
        temperature  si=1300
end structure

structure si_2e18
        close
        temperature  si=1230
end structure

structure be_2e18
        close
        temperature  be=880
end structure

structure be_1e18
        close
        temperature  be=855
end structure

structure be_5e17
```

```
        close
        temperature  be=835
end structure

structure cool520   !!! cool substrate to 520oC on pyrometer
        close
        temperature  substrate=650
        delay 1 minute
        temperature  substrate=620
        delay 1 minute
        temperature  substrate=600
        delay 2 minutes
end structure

structure warm600   !!! warm substrate to 600oC on pyrometer
        close
        temperature  substrate=660
        delay 1 minute
        temperature  substrate=690
        delay 1 minute
        temperature  substrate=715
        delay 2 minutes
end structure

structure loAs   !!! set As flux to 9e-5 Torr BEP
        close
        valve as2=360
end structure

structure hiAs   !!! set As flux to 1.0e-6 Torr BEP
        close
        valve as2=385
end structure

structure nup   !!! linear grade over 160A from GaAs to Al0.9Ga0.1As
            I al1 t=2
            I ga t=18
            I al1 t=4
            I ga t=16
            I al1 t=6
            I ga t=14
            I al1 t=8
            I ga t=12
            I al1 t=10
            I ga t=10
            I al1 t=12
            I ga t=8
```

```
        I al1 t=14
        I ga t=6
        I al1 t=16
        I ga t=4
end structure

structure ndn  !!! linear grade from Al0.9Ga0.1As to GaAs  over 160A
        I ga t=4
        I al1 t=16
        I ga t=6
        I al1 t=14
        I ga t=8
        I al1 t=12
        I ga t=10
        I al1 t=10
        I ga t=12
        I al1 t=8
        I ga t=14
        I al1 t=6
        I ga t=16
        I al1 t=4
        I ga t=18
        I al1 t=2
end structure

structure cavgrade  !!! grade over 120A from Al0.3 to Al0.9
        I ga t=12
        I al1 t=8
        I ga t=10
        I al1 t=10
        I ga t=8
        I al1 t=12 .
        I ga t=6
        I al1 t=14
        I ga t=4
        I al1 t=16
        I ga t=2
        I al1 t=18
end structure

structure endcontact
        si_2e18
        dope si
        I ga t=423
        si_5e18
        I ga t=200
end structure
```

```
structure nper
        nup
        si_5e17
        !!! lambda =9900A
        !!! lambda/4/3.00 - 160A = 665A = 505 + 150

        repeat 24  !!!480 here
                l ga t=2
                l al1 t=18
        end repeat
        l ga t=1.5
        l al1 t=13.5
        l ga t=1
        l al1 t=9
        si_5e18

        repeat 8
                l ga t=2
                l al1 t=18
        end repeat
        ndn
        si_5e17
        delay 1 minute

        !!! lambda/(4*3.52) -160 = 543 = 393+150
        l ga t=393
        si_5e18
        l ga t=150
end structure

structure nlast
        nup
        si_5e17
        !!! lambda/4/3.00=825;   825 - 160/2 - 100/2 = 695

        repeat 26  !!! 520 here
                l ga t=2
                l al1 t=18
        end repeat

        repeat 3  !!! 45A here
                l ga t=1.5
                l al1 t=13.5
        end repeat
        l ga t=1    !!! 10A here
        l al1 t=9
```

```
          repeat 6   !!! 120 A here
                  I ga t=2
                  I al1 t=18
          end repeat
          close
          si_5e18
          delay 1 minute

          !!! grade linearly from 90% to 30% Al over 100A
          I ga t=4
          I al1 t=16
          I ga t=6
          I al1 t=14
          I ga t=8
          I al1 t=12
          I ga t=10
          I al1 t=10
          I ga t=12
          I al1 t=8
          close
end structure

!!! length of spacer region
!!!  0.5*(9900(wavelength) - 3.52(600 = thickness of active) )/(3.33=index of 30%Al)
!!!  = 1169.4
!!!  n side:  1169.4 - 100/2 (grading thickness) = 1119.4
!!!  p side:  1169.4 - 120/2 (grading thickness) = 1109.4

!!! on n-side 300+820 = 1120A  - close enough
!!! on p-side 297.4 + 720 = 1017.4  (this growth)
!!!   + 92 A (next growth)  = 1109.4

structure ispacer  !!! 300A
          repeat 15
          I al1 t=6
          I ga t=14
          end repeat
end structure

structure nspacer  !!!820A
          repeat 41
          I al1 t=6
          I ga t=14
          end repeat
end structure
!!! savisg@us.ibm.com - microserfs
```

```
structure ipspacer !!!306A
        l al1 t=7.8
        l ga t=18.2
        repeat 14
        l al1 t=6
        l ga t=14
        end repeat
end structure

structure active   !!! 600A
        close
        l ga t=50
        loAs
        cool520

        l ga t=50
        close
        delay 5 seconds
        repeat 3
                l in,ga t=80
                close
                delay 5 seconds
                l ga t=80
                close
                delay 5 seconds
        end repeat

        warm600
        hiAs
        l ga t=20
end structure

structure aperture
        l al1 t=100
        repeat 17   !!! 420A of Al0.9Ga0.1As
                l ga t=2
                l al1 t=18
        end repeat

        be_5e17
        warm600
        repeat 4
                l ga t=2
                l al1 t=18
        end repeat

        !!! 1040A of Al0.7Ga0.3As
```

```
        repeat 50
                I ga t=6
                I al1 t=14
        end repeat

        be_2e18

        repeat 2
                I ga t=6
                I al1 t=14
        end repeat
end structure

!!! ******************** START HERE

growth rate ga=2.732
growth rate in,ga=3.37
growth rate al1=2.864

rotation 10

endcontact
!!! total 13 ga layers

repeat 5
        nper
end repeat
!!! total 18 ga layers

close
nlast
nspacer
close
end dope si
si_1e18
temperature  be=400
ispacer
active
ipspacer
close
be_2e18
cool520
cavgrade
dope be
aperture

close
```

end dope be
rotation 0
temperature in=350

Program for top of 1ˢᵗ Null VCSEL

!!! PROGRAM FOR TOP OF FIRST NULL VCSEL
!!! doping

```
structure p_2e19
        close
        temperature be=970
end structure

structure p_3e18
        close
        temperature be=890
end structure

structure p_2e18
        close
        temperature be=880
end structure

structure p_1e18
        close
        temperature be=855
end structure

structure p_1_3e18
        close
        temperature be=860
end structure

structure p_8e17
        close
        temperature be=850
end structure

structure p_6e17
        close
        temperature be=840
end structure
```

```
structure p_3e17
        close
        temperature  be=820
end structure

structure si_7e17
        close
        temperature  si=1190
end structure

structure cool   !!! lower substrate temperature to 500 as measured by pyrometer
        close
        temperature  substrate=650
        delay 1 minute
        temperature  substrate=600
        delay 1 minute
        temperature  substrate=570
        delay 2 minutes
        valve as2=360     !!! lower As2 flux to 9e-6 torr BEP for colder growth
end structure

structure firstgrade  !!! grade from 70% to 0 over 120A
        l al1 t=12
        l ga t=8
        l al1 t=10
        l ga t=10
        l al1 t=8
        l ga t=12
        l al1 t=6
        l ga t=14
        l al1 t=4    _
        l ga t=16
        l al1 t=2
        l ga t=18
end structure

structure grup1
        !!!  flat over 135-64=71A
        !!!  then linear grade over 64A (= half of parabolic grade) from GaAs to
        !!!  Al0.9Ga0.1As

        l ga t=71

        !!! linear grade
        l al1 t=1.4
        l ga t=14.6
```

```
        l al1 t=2.9
        l ga t=13.1
        l al1 t=4.3
        l ga t=11.7
        l al1 t=5.8
        l ga t=10.2
end structure

structure grup2  !!! parabolic grade from Al 0.5 to 0.9 over 135A
        l al1 t=7.5
        l ga t=7.5
        l al1 t=8.8
        l ga t=6.2
        l al1 t=10
        l ga t=5
        l al1 t=11
        l ga t=4
        l al1 t=11.8
        l ga t=3.2
        l al1 t=12.5
        l ga t=2.5
        l al1 t=13.0
        l ga t=2.0
        l al1 t=13.3
        l ga t=1.7
        l al1 t=13.5
        l ga t=1.5
end structure

structure grdn1 !!! parabolic grade from Al0.9 to Al0.5 over 135A
        l ga t=1.5
        l al1 t=13.5
        l ga t=1.7
        l al1 t=13.3
        l ga t=2.0
        l al1 t=13.0
        l ga t=2.5
        l al1 t=12.5
        l ga t=3.2
        l al1 t=11.8
        l ga t=4
        l al1 t=11
        l ga t=5
        l al1 t=10
        l ga t=6.2
        l al1 t=8.8
        l ga t=7.5
```

```
        l al1 t=7.5
end structure

structure grdn2   !!! total thickness 135A
        !!!linear grade from Al0.4 to GaAs over 64A
        !!! then 71A of GaAs

        l ga t=10.2
        l al1 t=5.8
        l ga t=11.7
        l al1 t=4.3
        l ga t=13.1
        l al1 t=2.9
        l ga t=14.6
        l al1 t=1.4


        l ga t=71
end structure

structure pgrupA   !!! grade Al composition up, use higher doping
        !!! grade is over 270A
        close
        end dope be
        p_3e18
        !!! flat + linear grade to 0.4 Al over 135A
        grup1
        close
        dope be
        !!! parabolic grade from 0.4 Al to 0.9 Al over 135A
        grup2
        p_2e18   !!! dope AlGaAs higher than GaAs due to lower incorporation of Be
        close
end structure

structure pgrupB  !!! grade Al composition up, use lower doping
        !!! grade is over 270A
        close
        end dope be
        dope si
        p_2e18
        !!! flat + linear grade to 0.4 Al over 135A
        grup1
        close
        end dope si
        dope be
        !!! parabolic grade from 0.4 Al to 0.9 Al over 135A
        grup2
```

```
        p_6e17   !!! dope AlGaAs higher than GaAs due to lower incorporation of Be
        close
end structure

structure pgrdnA  !!! grade Al composition down, use higher doping
        !!! grade is over 270A
        p_3e18
        !!! parabolic grade from 0.9 Al to 0.4 Al over 135A
        grdn1
        close
        end dope be
        p_1e18
        !!! linear + flat grade to 0.4 Al over 135A
        grdn2
        close
        dope be
end structure

structure pgrdnB  !!! grade Al composition down, use lower doping
        !!! grade is over 270A
        p_2e18
        !!! parabolic grade from 0.9 Al to 0.4 Al over 135A
        grdn1
        close
        end dope be
        p_3e17
        !!! linear + flat grade to 0.4 Al over 135A
        grdn2
        close
        dope be
end structure

!!! design for 990nm

structure lowqw
        !!! Al0.9Ga0.1As
        !!! 555A = lambda/(4*3.00) - 270A

        repeat 27  !!! 460A + 80 A here
                l al1 t=18
                l ga t=2
        end repeat

        !!! 15 A here
        l al1 t=13.5
        l ga t=1.5
end structure
```

```
structure hiqw
        !!! 433A = lambda/4/3.52 - 270A
        l ga t=433
end structure


structure topper    !!! upper mirror periods
        repeat 25
                hiqw
                pgrupA
                lowqw
                pgrdnA
        end repeat
end structure



structure botper   !!!bottom mirror periods
        repeat 5
                hiqw
                pgrupB
                lowqw
                pgrdnB
        end repeat
end structure



!!! *****************  BEGIN HERE

growth rate ga=2.732
growth rate al1=2.864

rotation 10

dope be
firstgrade  !!! over 120A
p_3e17
si_7e17
end dope be

l ga t=75  !!! 270A - 135A - 120/2 = 75A extra Ga to finish distance
close
dope be
botper

close
temperature  si=50   !!! idle si cell
```

```
cool

topper

p_3e18
hiqw
p_2e19
l ga t=135  !!! other half of grade
l ga t=455   !!! phase match layer to gold

close
end dope be

!!! IDLE EVERYTHING
temperature  substrate=200
rotation 0
temperature  be=50
temperature  ga=200
temperature  al1=1000
delay 15 minutes
valve as2=0     !!! shut off As – we are done - yippie
```